Imperial College London

Department of Mechanical Engineering

High Pressure and High Temperature Measurements on Diesel Sprays

by

Panagiotis Sphicas Dipl. Ing.

Submitted in partial fulfillment of the requirements for the degree of Doctor of Philosophy of Imperial College London

September 2013

Στους γονείς μου,

«τὰ πάντα ῥεῖ καὶ οὐδὲν μένει »

Ηράκλειτος

«Εν οίδα ότι ουδέν οίδα»

Σωκράτης

Declaration

I declare that this thesis is a record of the original work carried out by myself in the Department of Mechanical Engineering at Imperial College London during the period of June 2007 to September 2013. The thesis has not been presented elsewhere in consideration for a higher degree. Due acknowledgement must always be made of the use of any material contained in, or derived from this thesis

Panos Sphicas

Abstract

Environmental, financial and legal reasons demand the development of cleaner diesel engines. Atomization, evaporation and mixing phenomena observed during injection of Diesel fuel affect the produced emissions. To study these phenomena, under engine-like conditions (50bar, 1000K), a chemically preheated constant volume chamber was built. A system of sensors, driven in real-time by a FPGA (Field Programmable Gate Array) and controlled by a Real Time Controller, was built to monitor and control the operations. A modern common rail fuel injection system (Bosch CP3) was driven by a purpose-modified Hartridge 1100 test stand and controlled by the FPGA (Field Programmable Gate Array).

Chemical heating is a technique used widely to simulate the ambient conditions of an industrial combustor in a constant volume vessel. A flammable mixture is ignited in an optically accessible vessel, attempting to produce a post-combustion high pressure and high temperature environment. The flammable mixture usually consists of Hydrogen and a Hydrocarbon. Hydrogen is added, to assist with the ignitability of the pre-ignition mixture and to simulate the water present in industrial combustors as a result of exhaust gas recirculation. To this direction, the mole ratio of Hydrogen to Hydrocarbon and the mixture molecular weight were introduced as independent variables for the first time in the literature of constant volume combustion. An initial computer model, assuming perfect combustion, was used for calculation of adiabatic temperature and pressure. A second computer model investigated the effect of chemical dissociation by solving for the minimization of Gibbs energy and was compared to the former one. To verify the calculations, a dual pressure transducer technique and a High-Speed Schlieren technique were used to validate the combustion conditions inside the vessel

To further understand the atomization, evaporation and mixing phenomena in sprays, a Diesel spray was visualized using back-illumination and Schlieren High-Speed cinematography at high pressure and room temperature. To understand the evaporation behaviour of a spray and map the vapour fuel distribution, a tracer Laser Induced Fluorescence was applied on a Dodecane/Methyl-naphthalene spray under evaporating and non-evaporating conditions. To

compare the experimental findings to the theoretical models in literature, the evaporation of a single droplet in post-combustion vessel gases was simulated using a purpose-programmed FORTRAN code. A supercritical phase change was suggested to explain the sudden phase change and large differences between the theoretical model and the experimental results.

Acknowledgments

This thesis is the result of seven years of hard work, almost double than the typical PhD time and with me working long hours, it has taken as in Eindhoven three PhDs to reach this level of work. However, this work would not have been possible without the help of many people. In this section I will try to describe the help of all those people and thank them for their support. A second purpose of this section is to write down actions and behaviours that shouldn't be forgotten.

Firstly and most importantly I would like to thank my academic supervisor for giving me the opportunity to complete my work on this interesting research project. I am highly obliged to Professor William Jones, who volunteeringly accepted the supervision of this project at a very critical point. Professor Jones has been the voice of reasoning and hope and has offered the most thorough, useful and constructive academic supervision I have ever received.

Dr. Shaun Crofton and Dr. Peter Petrov have been the good Samaritans, whose paths crossed this work and I am very thankful for the generous help they offered. It was a rather bizarre coincidence that brought Dr. Crofton and me on a common path. Dr. Crofton was acting as coordinator between the department and the lab refurbishment contractors. On 11 May 2011, a Hydrogen incident in the lab brought Shaun to investigate the incident. Apparently the last person who had a similar event in this department, 20 years earlier, was Dr. Crofton himself. This will always connect me to Dr. Crofton. After that, Dr. Crofton with his expertise on material failure became my unofficial mentor and offered his knowledge in numerous occasions. It was in September 2011 that I met Dr. Peter Petrov, after the College Head of Safety pointed Peter as the most experienced person in College on Excimer Lasers. My group, a couple of years ago, had bought two Excimer Lasers, the one I commissioned was in storage for two years. The other Excimer was being used, but I was not allowed to operate my laser in the same way, so I had to design the exhaust, refilling and safety systems. Peter opened his lab

doors for me and let me copy his setup. The laser would have never operated if it was not for Dr. Petrov's help.

I would like to thank the last two consecutive heads of my department Professor Tony Kinloch and Professor Peter Cawley. They were an irreplaceable source of funding and hope. They both defended the good name of the college.

I am very grateful for the financial support from Honda R&D and Mr. Kazuaki and Mr. Yoshimi for their technical support and testing equipment. Also very grateful I am to the funding from Ford Motor Co and Mr. Tim Morris, Mr. Simon Peg and Mr. Khizer Tufail. At this point I should thank Professor Whitelaw for initiating the collaboration of Imperial with Honda and Ford some twenty years ago.

I would like to thank Dr. Frank Beyrau for all the advice on photochemistry, optics, lasers and cameras. His advice on lab and not lab related issues, was irreplaceable.

I am very thankful for all the technical and friendly support of Dr. Nikos Soulopoulos. Dr Soulopoulos was acting for many years as my unofficial supervisor and I have learned a lot from his lab experience.

I would like to thank Professor Peter Lindstedt and his student Henry Goh for their two emails that secured the Nd:YAG laser used in this work. Also I would like to thank Professor Peter Lindstedt and Professor Douglas Greenhalgh for being my examiners and giving me a unique opportunity to defend my work.

At this point I would like to thank Ilias Dodoulas, Florian Finger, Kostas Zarogoulidi, Bertrand Gillet, Kazuaki Matsuura and Tufail Khizer for making the right choice and showing me the path that I should had followed. Nikolaos Soulopoulos, George Charalampous and Sri Sahu we made the wrong choice. I would also like to thank Alexandros Charogiannis, Antonis Sergis and Dr Apostolos Pesiridis for the everyday support. Christina Nikita, Kyriakoulis Resvanis, Kostis Bergeles, Daniel Pearce, Juan Lian, Slava Stetsyuk and Constantinos Hadjiyiannis you are the next generation.

I would like to thank the technical staff of my department. Eddie Benbow has always been very helpful and very efficient. Without Eddie's perception of mechanical items and hands on approach, I couldn't have built my experimental rig. John Laker thank you for teaching me the basics of electronics in practise. Asanka Muhh thank you for building many electronics. Phil Proctor thank you for helping with the numerous moves. Mark Holloway thank you for uninterruptingly keeping the supply chain moving. Dr Niall McGlashan thank you for helping me specify the high pressure valves and the flame arrestors. I was very sad to hear that your experimental rig was given away.

This work wouldn't have been possible without the help of the Safety Department of College. Ian Gillett and John Luke thank you for all your help, time and effort you put into making my experiment safer. Also I would like to thank Colin Hale from ChemEng for his help with the HAZOP study.

The admin staff of the department supported this work. Serena Dalrymple I wish everyone was as helpful and efficient as you. Matt Smith, it's just impressive how, for at least a year, you were responsible for so many different things in the department. It was a pleasure being your friend both in the department and in the halls. Josie thank you for your help with the UG stuff.

I would like to thank Richard O'leary from Bronkhorst for helping me specify, configure and program the Mass Flow Controllers. Richard also helped me with various engineering components like the pneumatic valves, the solenoids, the non-return valves and many other that I now cannot recall.

I would like to thank from Radiant Dyes, Dr Mart Rahkema for delivering and demonstrating the excimer laser. When the excimer laser was damaged Dr Rahkema helped beyond the call of duty, despite his illness.

I would like to thank Colin Duncan from Andor for helping me set up the Andor Intensified Camera and the Mechelle spectrometer. Even though in the end the Mechelle

Spetrometer could not operate because of missing expensive focusing components, the Intensified camera was heavily used for imaging during this work.

I would like to thank Stuart Roberts and Adam Bakerhouse from National Instruments for providing documentation and support for setting up the FPGA system.

I would like to thank Daryll Spencer from KW for manufacturing the vessel used in this work.

I would like to thank Professor Maria Petrou for the support she provided during the development of the Proper Orthogonal Decomposition code.

I would like to thank Sam Tolhurst for helping with the movement of gas cabinets and all sort of other project-management jobs with the contractors in the lab. I don't know how many tasks would have been accomplished if it wasn't for Sam.

I would like to thank Dr Pat Leevers, Dr Fred Marquis, Professor Andy Heyes and Mr Keith Blackney for helping me run the undergraduate thermofluids teaching labs. I would like to thank Dr Fred Marquis for examining and correcting my MPhil transfer, which later on became the first few chapters of this thesis, also I would really like to thank Fred for his interest in my work and for keeping an eye on me. I would also like to thank Professor Andy Heyes for sponsoring my fees at the 13th UKHTC.

I would like to thank Dr Ferdinando Baena and Danieli Dini for their efforts to modernise the PhD student environment.

I would like to thank all the student reps, I believe that we did a great job in the PhD community. Richard Van Arkel, Sina Stapelfeldt, Ed Smith, Omar Al Fakir, Mike Kaye and Daniela Proprentner I am so proud for all the good changes we brought in the department. I hope the future generations will overpass our work.

My office mates Morad Karimpour, Ali Mehmanparast, Omar Al Fakir, Eri Kardoulaki, Nan Li, Liliang and Jingqi Wang, Dennis Politis, Shamshia Ngah, Aditya Narayanan, Junyi Lee, Yi Wang, Thomas Dunnett and Joseph Ahn thank you very much for offering me a nice working

environment. I couldn't have survived without the unique time we had together, I hope we keep in touch in the future.

My group friends Dehydys Pimentel, Bjorn Waldheim, Peter Krauss, Fabian Hampp, Thomas Sponfeldner, Benoit Fond and Chris Abram I really enjoyed our time in the division and in our conference in Sweden, despite the bizarre things happening in the lab during my absence. Michalis Hadjipanayis, Athanasios Chatzopoulos, Johannes Kerl, Sebastian Henkel, Alexandros Charogiannis and Thomas Jelly you should had joined too.

My friends Carmel, Anna, Anna, Kostas, Kostas, Dave, Peter, Paul, Panos, Angelos, Dimitris and Ibis thank you for making my stay abroad more enjoyable. Almost every time we met, I was a bit late because I had just left college, I hope you are not left with the impression that college was more important for me than your company. Also I would like to thank my Holland Club friends Arwen, Colin, Jack, Matt and Nasim. The spirit of Holland Club (and Clayponds) lives in people, not in buildings.

I would like to thank my cousin Professor Sarah Al-Khalili in Egypt, who is a mother, a wife, a politician and a scientist. How could I not receive courage out of my tough cousin? Also special thanks to my aunt Roula for spoiling me with her amazing cooking. Staying in the close family, I would like to thank my brothers Dr Dimitris Sphicas and Dr Nicolas Sphicas for all the great time we had.

I would like to thank my friends from Greece for offering me round the clock online Skype support, thank you Gregory Tsaggaris, Kostis Chatzopoulos, George Paliatsos, Nicholas Tsoumas, Giannis Moschos and Dr Alexandros Zymaris. Also I would like to thank my wise friend and lawyer Theodoros Patselis for his advice and long chats in the fields of life, law and entrepreneurship.

Finally and most importantly I would like to thank my mother and my father for everything.

Table of contents

Nomenclature

Roman symbols

V	axial velocity	[m/s]
L	length	[m]
d or D	nozzle diameter	[m]
D_{32}	Sauter Mean Diameter	
L/D	Nozzle length to diameter ratio	
h	enthalpy	[J/kg]
m	mass	[kg]
T	Temperature	[K]
k	heat conductivity	[W/Km]

Greek Symbols

ρ	Density	[kg/m^3]
θ	cone angle	[^{o}]
γ	heat capacity ratio	

Subscripts

inj	injection
b	break-up
l	liquid
a	ambient
f	fuel
vap	vaporization
b	boiling

Abbreviations

CCD	Charge-Coupled Device
CR	Common Rail
cRIO	compact Reconfigurable Input Output
CRU	Combustion Research Unit
CVV	Constant Volume Vessel
DMA	Direct Memory Access
ECU	Engine Control Unit
FIE	Fuel Injection Equipment
FIFO	First In First Out
FPGA	Field Programmable Gate Array
GUI	Graphical User Interface
LDV	Laser Doppler Velocimetry
MFC	Mass Flow Controller
PDA	Phase Doppler Anemometer
PIV	Particle Image Velocimetry
RTc	Real Time Controller
RTD	Resistance Temperature Detector
SAC	Type of injector nozzle
SMD	Sauter Mean Diameter
SoE	Start of energizing
SoI	Start of injection
VCO	Valve Covered Orifice
VI	LabVIEW code

Table of figures

Table of tables

1. Motivation

1.1 Introduction

This chapter will introduce the significance of Diesel Engines to modern life and will present their impact on public health. Some of the new technologies, used to reduce emissions, will be mentioned. Then this chapter will present the historic path to the development of the modern Direct Injection systems and will start presenting the focus of this work.

1.2 Significance and impact of diesel engines

Currently in the US there are about 13 million diesel engines in cars, buses, trucks, trains, ships and construction equipment, promoting transportation, commerce and in general supporting the economy. The emissions from the same engines are responsible for the premature death of 21000 people (EPA, 2009). This number is almost equal to the number of all students in Imperial College, or to a half full Stamford Bridge Stadium. Given that the average lifespan of a diesel vehicle is 30 years and that the number of diesel vehicles increases, the problem is severe.

Governments, in order to protect the public, legislate increasingly stricter emission limits, as shown in Figure 1. The most dangerous emission from a diesel engine is the particulate matter (PM), solely is responsible for the death of 15000 people annually and is highly carcinogenic. In Europe, in a period of five year, Euro 4 halved the allowed PM emissions of Euro 3. Four years after Euro 4, Euro 5 decreased again that limit 5 times. Similar laws are being applied to Nitric Oxide emissions (NOx), it is believed that Euro 6 will offer a 60-90% health benefit by reducing the NOx emissions by two-thirds (Commission, 2006). Similar policies are being followed in the United States with Tier regulations and generally worldwide.

In order for the automobile manufacturers to meet these regulations, a wide range of new technologies have to be implemented on the vehicles. For example, aerodynamic and power-

train loses are being constantly reduced, lighter materials are being developed to save vehicle weight and engine emissions keep reducing. To reduce engine emissions, engineers are developing exhaust gas after-treatment to absorb pollutants, but also try to improve combustion in the engine. Exhaust gas recirculation (EGR), Direct Injection (DI) and Turbocharging are the main technologies developed to improve in-cylinder combustion. This thesis will be focusing on the direct injection technology. The next section will present how the modern Direct Injection system was developed.

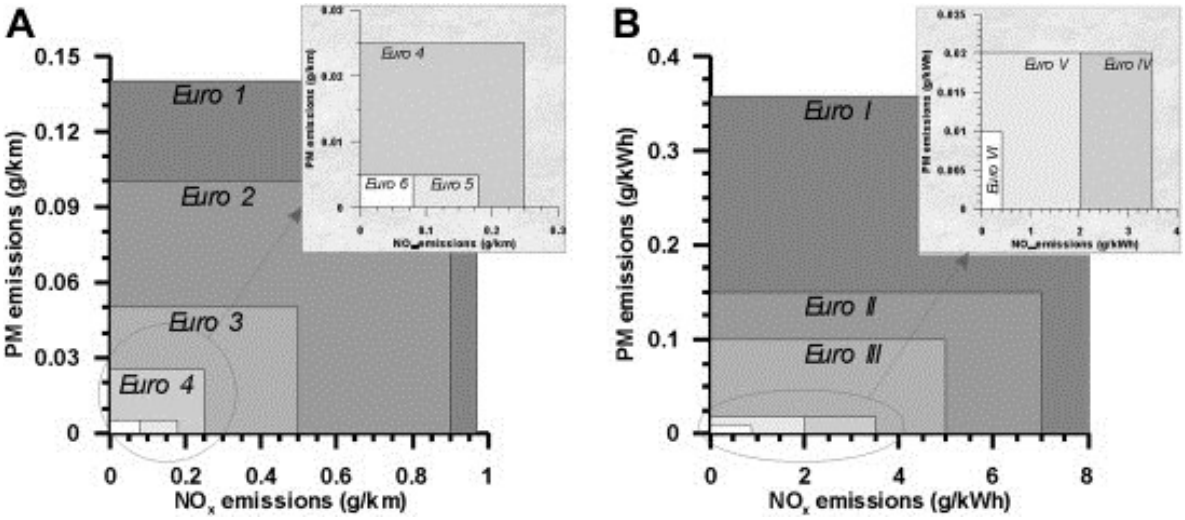

Figure 1 European emission standards comparison for, A) Diesel passenger cars B) Heavy-duty diesel engines (Gill et al., 2011)

1.3 The history of diesel injection

The diesel engine came to life in 1893 by Rudolf Diesel, who was almost killed by his engine when it exploded, but he had proved that fuel could be ignited without a spark. Though Diesel's cycle was less efficient than Otto cycle for a given compression ratio, Diesel's engine could achieve higher compression ratios and thus be more efficient than spark-ingnition-engines. By 1900 Diesel had presented a functional diesel engine at the Exposition Universelle (World's Fair in Paris) running on peanut oil.

Diesel's original engine injected fuel with the assistance of compressed air, which atomized the fuel and forced it into the engine through a nozzle. This injection technique, called air-blast injection, provides very efficient combustion at low-speed, high-load conditions even when using low-quality fuels. But it requires a big-sized, energy consuming multi-stage air compressor that made diesel engines large, heavy and reduced their power output.

When diesel engines found application on vehicles, the heavy air-blast injection was replaced by mechanical pumps that raise the pressure of the fuel. Initial injection systems of that type, known as jerk-pumps, were based on Pascal law. So, a cam-driven plunger would raise the pressure of the fuel in a small constant-volume chamber and since the fuel is incompressible, pressure will increase. A complicated system of weights, springs and helical grooves were used to determine the injected fuel mass. With this technology the mass injected was the independent variable and the pressure would adjust itself accordingly. Obviously for each cylinder, a jerk-pump is needed and the injection timings are directed by the cam-shaft (Ferguson, 1985).

To save costs and allow operation at higher speed, distributer-type pumps were developed. Unlike jerk-pumps, distributer-pumps have only one plunger for the whole engine, which meters and distributes the fuel to all the injection nozzles. However, even with the distributer-type pumps, the fuel-pressure is dependent on the engine speed and the injection timing/pattern is not flexible (Heywood, 1988).

In the early 1960s to further decrease cost and weight, a new approach was adopted on injection systems. A positive displacement pump would feed a pipe with a constant fuel-pressure. The injectors were connected on this pipe and were driven by the camshaft. With this configuration the independent variable is the rail-pressure and the delivered fuel-mass would adjust itself depending on the fuel pressure.

In the early 1980s with the development of electronically controlled diesel fuel injectors, the injection timings and patterns became fully independent of the camshaft. In combination to the common-rail system, the injected mass of fuel became independent of the fuel pressure.

These two innovations allowed for pre-, main and post-injections within the same engine cycle, that have proved so far to decrease noise and emissions.

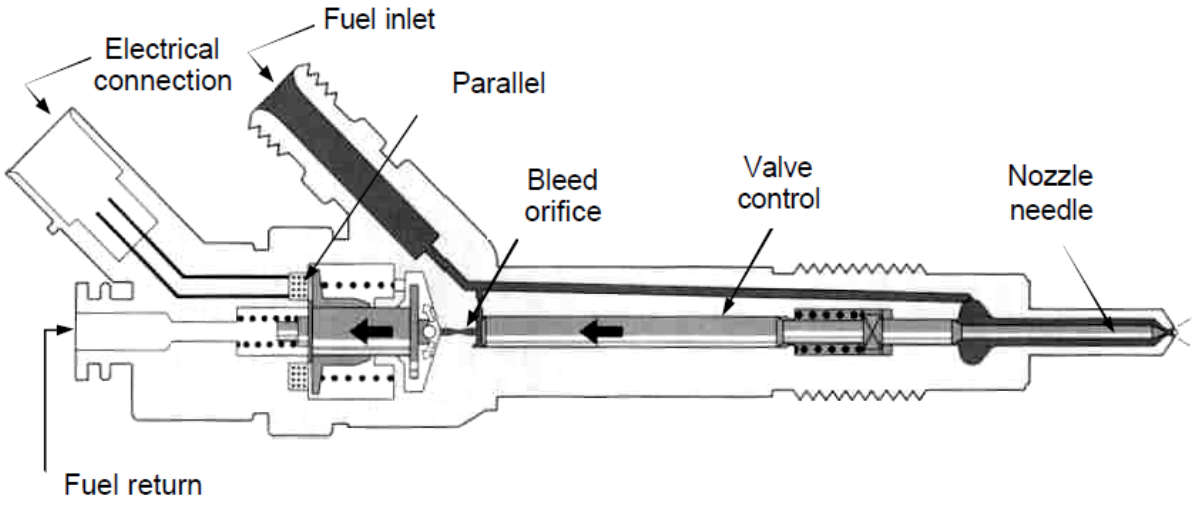

Figure 2 Bosch common rail injector (Bosch, 2005)

A modern typical plain orifice pressure-atomizer used in vehicles relies on the conversion of pressure into kinetic energy, Figure 2. A pump pressurizes the fuel to pressures up to 2500 bar, where the fuel behaves more like solid rather than liquid. Then the fuel is forced through a small conical hole typically of the order of 100 μm, where cavitation phenomena help to promote the atomization of the spray. When the fuel exits the orifice, a high-velocity liquid jet is formed that quickly disintegrates into a well-atomized spray. Air entrainment at the early stages of the jet promotes the mixing of fuel with air and thus the atomization of the spray and the evaporation of droplets. Improved fuel evaporation and air/fuel mixing, results in improved combustion and reduced emissions. The next chapter will thus present results from previous studies on sprays and will present the contribution of the current work.

1.4 Statement of aims

The main and broader aim of this work is to assist with designing cleaner and more efficient diesel engines. A way of achieving this broader aim is by improving the combustion of the fuel in the engine. Even though this work is not studying the combustion of a diesel spray, it focuses on the evaporation observed in sprays prior to combustion. It is well known that evaporation affects the combustion of fuel through different evaporation modes. The latter include flash evaporation as well as fuel distillation processes. To study the evaporative behaviour of a spray, the experiments, models and computational calculations of the following chapters were performed. Without going into more detail now, more information is provided along the chapters of this thesis.

2. Literature review in sprays

2.1 Introduction

In this chapter the behavior and general characteristics of a spray will be introduced. Some of the considerable amount of work in the literature will be summarized and the contribution of the current work will be presented. The outline of the thesis will complete the chapter.

2.2 Phenomena in a spray

Apart from the already mentioned fuel automotive applications, sprays are of paramount importance to many aspects of everyday life. All liquid fuel combustion systems are based, in one way or another, on injection of the fuel spray to a chamber. Other industrial applications include painting, spray drying and spray cooling. Medical applications are mainly focusing on nebulizers, which produce a mist inhaled into the lungs. Fire sprinklers and irrigation sprays are based on the atomization of a liquid jet in relatively large drops (Nasr et al., 2002, Bayvel and Orzechowski, 1993, Lefebvre, 1989). The jets of Ink Jet printers take advantage of the Rayleigh-break-up regime to deposit ink droplets on the paper (Bayvel and Orzechowski, 1993).

No matter what the industrial application, every spray can be macroscopically characterized by its penetration depth L_P, liquid length L_L, break-up length L_b and cone angle θ. Figure 3 shows these characteristic lengths on a typical spray. Penetration depth L_P refers to the maximum penetration of the spray, in vapor phase, in the ambient environment. Liquid core or break-up length L_b is the length up to which the fluid has not started breaking up to smaller formations. Liquid length L_L is the length up to which the liquid droplets of the spray have not evaporated. Finally cone-angle θ is the angle of the spray as measured from the orifice exit. The importance of each of these characteristics on diesel sprays will be discussed later.

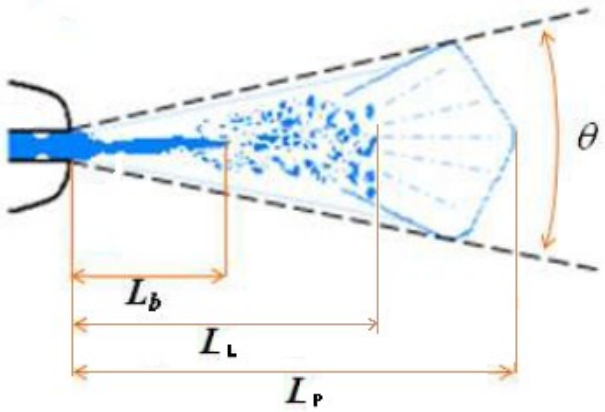

Figure 3 Spray Macroscopic characteristics, altered from (Heywood, 1988, Hiroyasu, 2000)

In the nozzle, the velocity profile is not a “top hat”, due to contact with the nozzle wall, but at the exit of the nozzle the velocity profile becomes a “top-hat”. This transition is called profile relaxation and is very important for atomization of laminar jets, as it can be very violent and cause the jet to burst, “bursting break up”. Though to a lesser extent than low velocity jets, even turbulent sprays like diesel sprays are affected by this profile relaxation (Lefebvre, 1989).

When the liquid exits the orifice, the surrounding air causes its surface to ruffle. It has been known for some time that there is a liquid core that is vibrating because of cavitation, profile relaxation and jet turbulence. Vortex structures are being disconnected from the liquid core. Also, waves on the surface of the liquid core create ligaments from which droplets are detached. This behavior is referred to as “primary atomization”. The liquid core disappears very quickly and the spray becomes a mixture of drops of fuel dispersed in the ambient air. The velocity of the spray is larger in the center, decreasing at the interface with the ambient air. These free-moving drops under their initial momentum and subjected to aerodynamic forces and surface tension are unstable and undergo further break up into smaller droplets, behavior known as “secondary atomization” (Lefebvre, 1989).

The Gaussian distribution observed for the spray velocity profile is also observed for fuel vapour concentration, where on the centerline there is almost pure fuel and towards the edge of the spray the fuel concentration drops.

The rest of this thesis will be focusing on the complete spray region, as the practical application of this work is diesel sprays. It will mainly focus on fuel sprays in high pressure and temperature environments, similar to those found in a diesel engine (50 bar, 1000 K). The following paragraphs will describe the macroscopic parameters of a spray and how these are affected by ambient and injection conditions.

2.2.1 Break-up length

In the literature there is a considerable amount of experimental and numerical work aiming to study the maximum value of the break up length of a spray. A summary of some semi-empirical correlations is presented in Table 1. The parameter that is always present is the spray velocity or injection pressure. Liquid surface tension, kinematic viscosity and density are either used directly in the correlations or hidden in the Reynolds, Weber and Ohnesorge number. Further detail about the definition, physical significance and typical ranges of these numbers is given in Appendix 1. Clearly all the aforementioned parameters are influencing each other.

The nozzle geometry is considered in the correlations as the diameter of the nozzle. The length of the nozzle is usually ignored but, as will be presented later, it is an important parameter.

Initial models ignored the importance of ambient conditions on spray formation and especially on the break-up length (Grant and Middleman, 1966, Lefebvre, 1989). Later models took into account the ambient gas density (Arai et al., 1984), but it was with the use of constant volume vessels that it was realized that ambient pressure and “ambient-gas-density” are two different parameters that can be altered separately and both affect the liquid length (Yule and Filipovic, 1992, Hiroyasu and Arai, 1990). Chapter 4 will present how in a constant volume vessel, ambient pressure and “ambient-gas-density” can be independently altered with the use of different pre-ignition mixtures.

So far, no break-up length model has focused on the ambient temperature as an influence on the break-up length; this information is implied in the ambient gas density, according to the gas law, and mainly affects droplet evaporation (Spalding, 1979). As demonstrated in later work (Siebers, 1998) and as will be presented later in this work, ambient temperature has an influence on break-up length.

Expression of break-up length	Range	Researcher
$L_b = V_{inj}^2 \left(ln\frac{d}{2\delta_o}\right)\left[\left(\frac{\rho_l d^3}{\sigma}\right)^{0.5} + \frac{3\mu_L d}{\sigma}\right]$ Or $L_b = dWe^{0.5}(1+3Oh)ln\frac{d}{2\delta_o}$	laminar jet at ambient conditions	(Weber 1931)
$L_b = dWe^{0.5}(1+3Oh)ln\frac{d}{2\delta_o}$ $ln\frac{d}{2\delta_o} = 7.68 - 2.66Oh$ $L_b = 19.5dWe^{0.5}(1+3Oh)^{-0.28}$	laminar jet at ambient conditions	(Grant and Middleman, 1966)
$L_b = 8.51dWe^{0.32}$	turbulent jet at atmospheric conditions	(Grant and Middleman, 1966)
$L_b = 7.15d\left(\frac{\rho_l}{\rho_a}\right)^{0.5}$	Diesel fuel, ambient pressure 1-40 atm, injection pressure up to 166 atm	(Reitz and Bracco, 1979)
$L_b = 15.8\sqrt{\frac{\rho_l}{\rho_a}}d$ $t_b = 28.6\frac{\rho_l}{\sqrt{\rho_a}}\frac{d}{\sqrt{\Delta P}}$	Ambient pressure 1-30 bar, room temperature, injection pressure 110-190 bar	(Arai et al., 1984)
$L_b = 5381dWe^{0.5}Re^{-0.625}$	water at atmospheric	Baron (Lefebvre, 1989)

	conditions	
$L_b = 7d\left(1+0.4\frac{r}{d}\right)\left(\frac{Pa}{\rho_l V_{inj}^2}\right)^{0.05}\left(\frac{L}{d}\right)^{0.13}\left(\frac{\rho_l}{\rho_a}\right)^{0.5}$	Diesel fuel, ambient pressure 1-50 bar	(Hiroyasu and Arai, 1990)
$L_b = 2.8d \times 10^4 We_b^{-0.46}$ $We_b = \frac{\rho_a V_b^2 d}{\sigma_l}$ $t_b = 7D\left(1+0.4\frac{r}{d}\right)\left(\frac{P_a}{\rho_l V_{inj}^2}\right)^{0.05}\left(\frac{L}{d}\right)^{0.13}\left(\frac{\rho_l}{\rho_a}\right)^{0.5}$	For $Re_b < 10^5$ (Lacoste, 2006). At room temperature, ambient pressure 5-50 bar and injection pressure 215-300 bar (Yule and Filipovic, 1992).	(Yule and Filipovic, 1992, Lacoste, 2006)

Table 1 Models of break-up length of spray

2.2.1.1 Injection Velocity/Pressure effect on breakup length

To understand the effect of injection pressure on the break-up length of a spray, consider a nozzle through which fluid is exiting, the magnitude of the velocity of the fluid at the exit of the nozzle will determine the shape of the liquid core of the spray, as shown in Figure 4. Researchers normally calculate the exit velocity based on the injecting pressure, assuming a top-hat velocity profile across the orifice and a steady frictionless flow.

As shown in Figure 4 and Table 2, if the pressure or velocity is very low, separated small droplets will be formed, this is called dripping flow and is similar to the flow of an almost shut tap. By increasing the exit velocity, a laminar continuous flow column is formed in the laminar flow region. Increasing the exit velocity leads to longer liquid length. In this region, the jet disintegrates due to surface tension forces and the drops produced are fairly similar. This mechanism was initially studied by Lord Rayleigh and Sir G. I. Taylor (Taylor, 1949, Rayleigh, 1878). By increasing the exit velocity even further, a maximum of liquid length is observed at

$We_l = \frac{1.74 \times 10^4}{Re^{0.5}}$ or $Re_{cr} = 3.25 \times Oh^{-0.28}$ (Grant and Middleman, 1966) or $Re_{cr} = 12{,}000 \times \left(\frac{l}{d}\right)^{-0.3}$ (Van De Sande and Smith, 1976) for convergent 3 mm nozzles.

From this point on, it has been observed that aerodynamic forces cause symmetric waves on the column, area known as transition flow region or first wind-induced mode (Haenlein 1932; Ohnesorge 1936; Reitz and Bracco 1979; Weber 1931). After a minimum in liquid core length is reached, the core length starts increasing again with exit velocity, in the region known as the turbulent flow regime or the second wind-induced mode. Here the drops produced are smaller than before and the liquid column is turbulent and characterized by asymmetric waves, the turbulent flow region ends at $We_l = \frac{9.4 \times 10^5}{Re^{0.5}}$. Further increase in the exit velocity produces a spray. As mentioned earlier, a spray has a cone angle and drops of various sizes. Hiroyasu and Arai classified sprays into two categories, incomplete if the liquid length is decreasing with increasing exit velocity and complete if cavitation has appeared in the nozzle, that decreases the liquid core and makes it relatively insensitive to the exit velocity (Hiroyasu and Arai, 1990).

Typical modern diesel injectors, including those used in this work, operate at injection pressures around 1700 bar. The spray exit velocity is above 100 m/s, under these conditions the spray is in the complete spray regime.

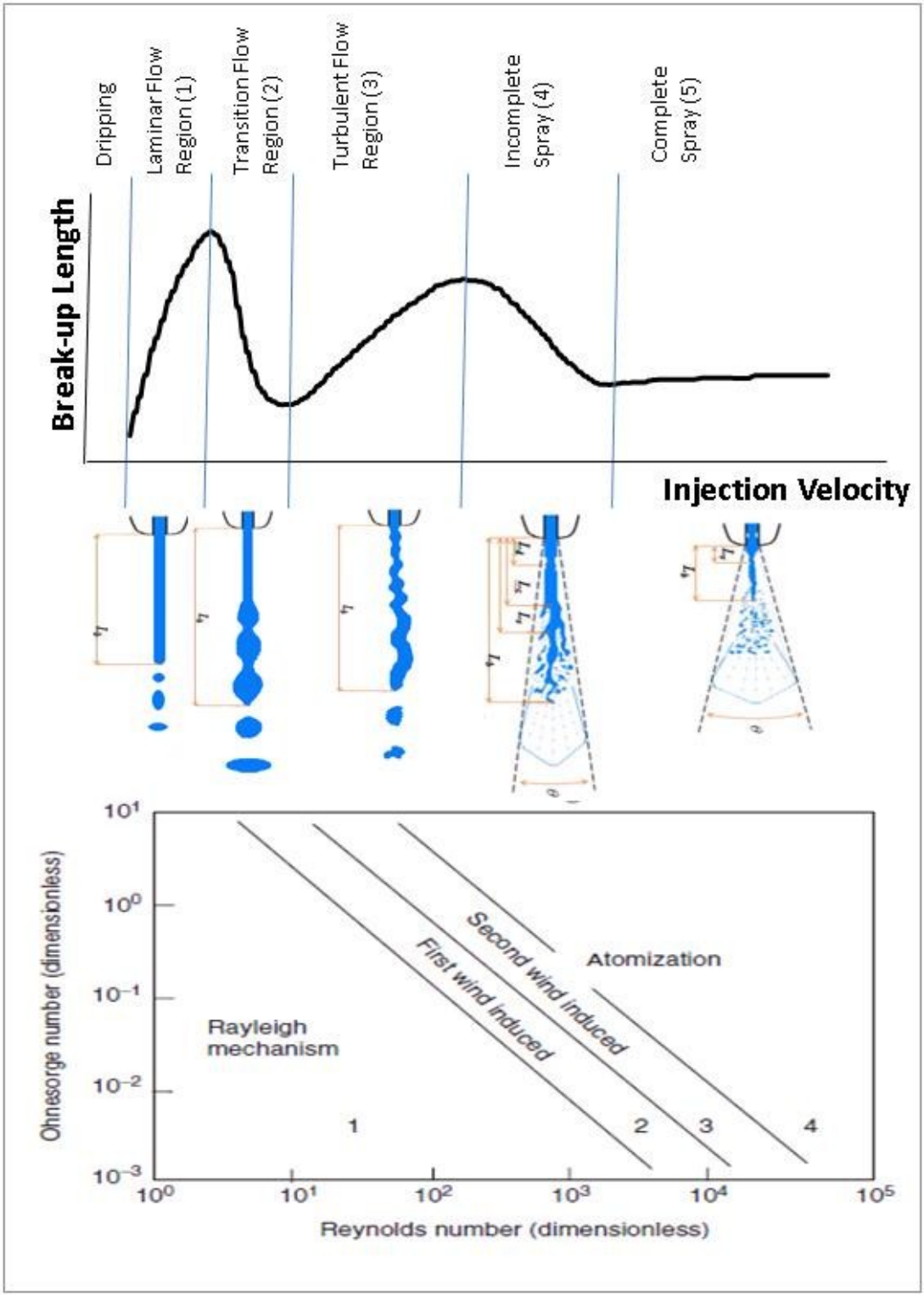

Figure 4 Break up length of jet as a function of calculated sectional average across the orifice injection velocity. Compilation and enrichment of figures from literature (Hiroyasu and Arai, 1990, Heywood, 1988, Karimi, 2007, Crowe, 2006)

Spray regime		Characteristics
1	Laminar flow region	Break up due to surface tension, Rayleigh regime, quasi mono-disperse drops
2	Transition flow region	Begins at $We_l = \frac{1.74\times10^4}{Re^{0.5}}$. Symmetric waves, first wind-induced mode
3	Turbulent flow region	Asymmetric waves, second wind-induced mode, smaller drops, ends at $We_l = \frac{9.4\times10^5}{Re^{0.5}}$, radial velocity component causes column to disintegrate.
4	Incomplete spray	Poly-disperse drops, cone angle appears.
5	Complete spray	Cavitation appears in the nozzle and the liquid core length is drastically reduced

Table 2 Spray regimes

2.2.1.2 Ambient Pressure and Gas density effect on breakup length

As aforementioned, especially in the early break-up models, a parameter commonly ignored was the ambient gas density. Ambient gas density can be varied independently of ambient pressure. If the ideal gas law is considered: $\mathrm{PV} = nRT \rightarrow \mathrm{PV} = \frac{m}{MW}RT \rightarrow \mathrm{P} = \frac{m}{V}\frac{1}{MW}RT$, where MW is the mixture molecular weight. For example, in a diesel engine in the compression stroke, after the valves have closed, the "ambient mass m" does not change. However, because of volume V decrease the ambient gas density increases, the same for the ambient pressure P. The only way to change the "ambient mass m" of this diesel engine is to add more air before closing the valves (turbocharging/supercharging).

If a constant volume vessel is considered, where a pre-combustion technique takes place to increase the ambient pressure, the volume V is clearly constant. But the "ambient mass m" is dictated by the mass of gases entered in the vessel and does not change during the pre-combustion technique, because of conservation of mass. So the ambient gas density, which is the ratio m/V is dictated only by the mass present in the vessel. However, the amount of combustible fuel, will control how much heat will be produced that will increase the pressure. So in a constant volume vessel, ambient pressure and ambient gas density can in principle be altered independently at will: more on that will be presented in Chapter 4.

In 1990, Hiroyasu and Arai studied the effect of ambient pressure and gas density on the breakup length as shown in Figure 5. At the time they concluded that “the density of the surrounding which gives the shear stress to the liquid column is considered as the last important factor for the disintegrating process” (Hiroyasu and Arai, 1990). However, their measurements took place at low ambient pressures, up to 10 bar, and low injection pressures, up to 150 bar, which could explain why no effect of ambient gas density was observed on the breakup length.

Yule and Filipovic, at injection pressure of 210-312 bar and ambient pressure of up to 50 bar, did observe a correlation between breakup length and ambient gas density as shown in Figure 6 (Yule and Filipovic, 1992). However the ambient pressure was not constant, but was the dependent variable of ambient gas density.

The liquid-core of a diesel spray is difficult to observed due to the dense droplet cloud formed, so planar optical techniques cannot give an insight of the spray core. Some research has been done in illuminating the liquid-core of the spray, passing a laser beam through the atomizer, thus illuminating the liquid continuity of the spray core. However this work was done at low injection pressure at ambient environment (Charalampous et al., 2009). The lack of liquid core visualization of typical modern diesel sprays in the literature is apparent.

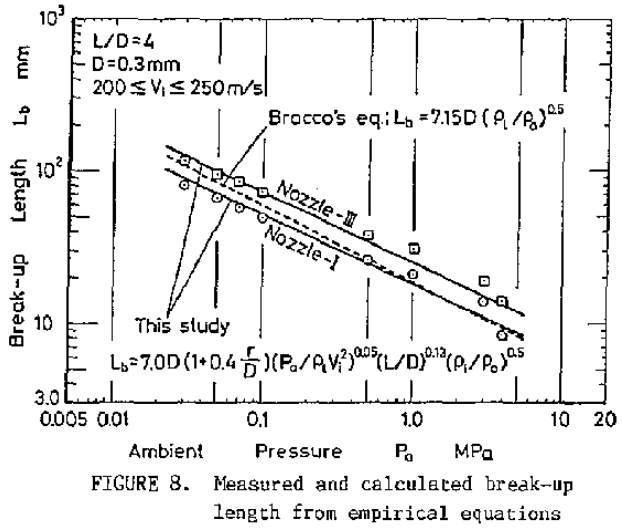

Figure 5 Break-up length as a function of ambient pressure for constant orifice geometry and L/D, adaptation from (Hiroyasu and Arai, 1990)

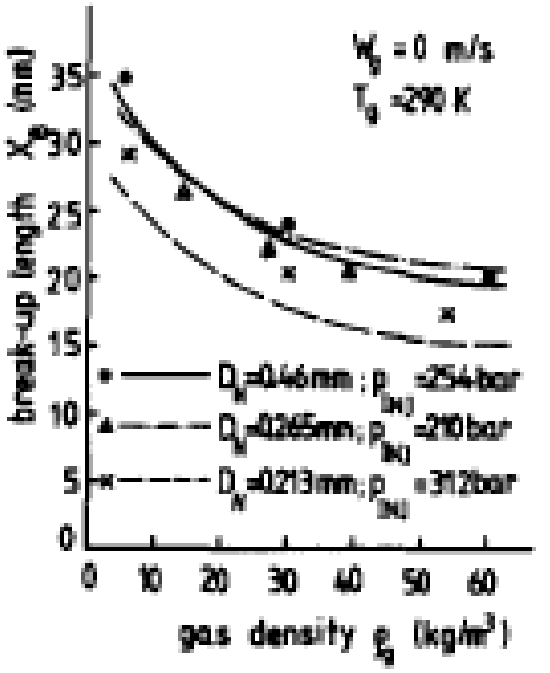

Figure 6 Break-up length as a function of ambient pressure for constant orifice geometry and L/D, adaptation from (Yule and Filipovic, 1992)

2.2.1.3 Cavitation effect on breakup length

Though ignored untill recently, the atomization of a spray can start in the nozzle. At upstream parts of the nozzle, as the fluid velocity increases suddenly, the local static pressure can drop below the fuel vapour pressure. So clouds of vapour bubbles are formed. This vapour generation process is promoted by the fact that the injector tip is at high temperature, thus giving high vapour pressure (Stone, 1985). Soteriou noticed that cavitation starts as an annular bubbly flow around the liquid core (Soteriou et al., 1998). At more severe cavitation conditions, bubbles are formed across the whole of the nozzle entrance but after the smallest cross-section of the flow, cavitation only appears in the boundary layer. Regardless of the severity of cavitation, it will induce fluctuation to the fluid.

Many researchers have created “super-scale” models of diesel injectors to study cavitation. However this approach does not allow for cavitation to be studied under realistic engine pressure and temperature condition. Still there is much work to be done on how exactly

cavitation affects the spray development, both in steady-state and in transient operation. Additionally the engine-like environment at the nozzle exit cannot be simulated.

2.2.1.4 Nozzle geometry effect on breakup length

Cavitation promotes spray break-up, but needs high injection pressure that is translated to high power absorbed by the fuel pump. However recent research has shown that using a nozzle with variable cross-section can disturb the liquid flow and initiate cavitation at lower injection pressures. Tamaki experimented with a mesh installed upstream of the nozzle or in the nozzle and observed enhanced atomization (Tamaki et al., 2001).

In the simplest case where the nozzle is a hole of constant diameter with sudden contraction and expansion at the entrance and exit of the flow, it is known that the longer the length of the nozzle, the more laminar the flow of the liquid core, which deters atomization. It has been observed that increasing the ratio of nozzle length to diameter L/D increases the break-up length (Hiroyasu and Arai, 1990). A too small L/D ratio is not for structural reasons. This increase of break-up length with increasing L/D, diminishes as the ambient pressure is increased as shown in Figure 8. However if the injection pressure and the L/D are held constant and only the nozzle diameter is increased, the break up length increases, Figure 7.

Many researchers have compared sharp and rounded inlets, in order to evaluate the effect of the inlet shape of the nozzle on cavitation. It has been observed that in the laminar flow, transition flow and turbulent flow regions, round corners promote atomization. However at the incomplete and complete spray regions, due to cavitation, the sharp corners promote atomization. A phenomenon observed by Hiroyasu is that with sharp edged nozzles, in the incomplete spray region, a hysteresis appears explained by different cavitation modes (Hiroyasu, 2000). However later work (Soteriou et al., 2010, Laoonual et al., 2001, Sou et al., 2007) did not observe similar behavior, as the injection pressure was much higher, bringing the operating regime in the complete spray region.

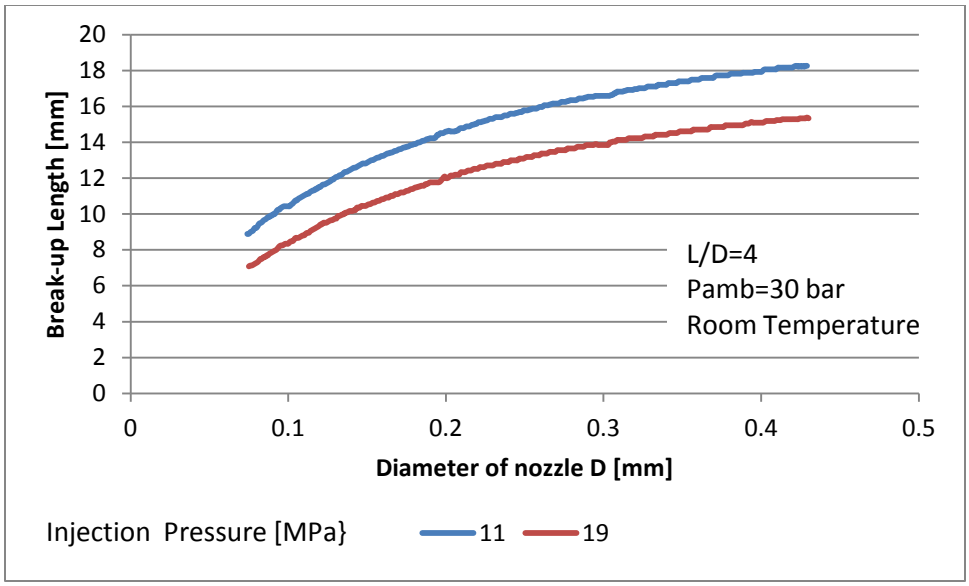

Figure 7 Break-up length as a function of the nozzle diameter at different injection pressures, with constant ambient pressure and L/D, adapted from (Hiroyasu and Arai, 1990)

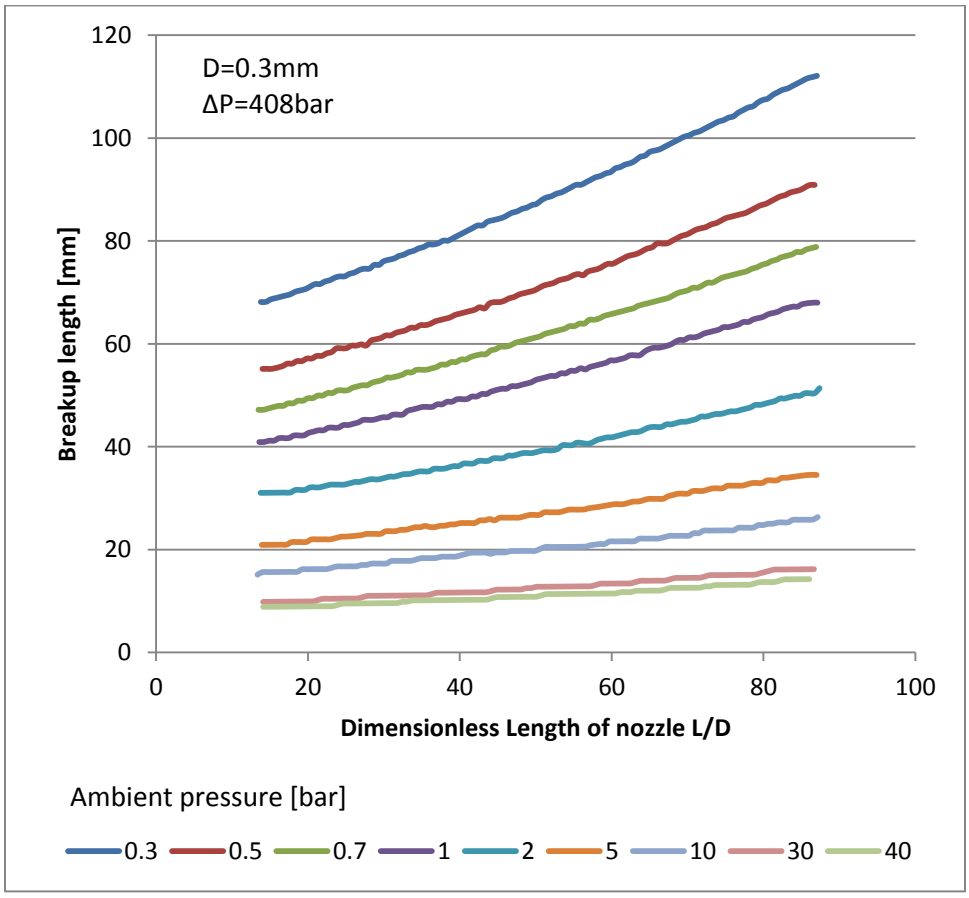

Figure 8 Effect of dimensionless length of nozzle on break-up length with ambient pressure as parameter, adapted from (Hiroyasu and Arai, 1990)

2.2.2 Liquid Length

Expression of liquid length		
$L_b = dkA^{\alpha}B^{\beta}$ $A = \frac{\rho_l}{\rho_a}$ $B = \frac{\sum m_i h_{vap,i} + (T_{b,max} - T_f)\sum m_i c_{p,l,i}}{C_{p,a}(T_{b,max} - T_f)\sum m_i}$ k=10.5, α=0.58, β=0.59	700-1300 K ambient temperature, 3.6-59 kg/m^3 ambient gas temperature and 1400 bar injection pressure	(Higgins et al., 1999)

Table 3 Models of liquid length

2.2.2.1 Injection Velocity/Pressure effect on Liquid Length

Kamimoto and Yeh have observed that the liquid penetration is approximately constant for injection pressures between 260 and 1100 bar (Kamimoto et al., 1987, Yeh et al., 1993), the same observation was observed by Verhoeven in a constant volume vessel for injection pressure up to 1500 bar (Verhoeven et al., 1998) and by Siebers for injection pressure up to 1750 bar (Siebers, 1998).

2.2.2.2 Ambient Pressure and Gas density effect on Liquid Length

Though many researchers have observed temporal spray tip penetration development, very little work has been done on the maximum spray penetration and liquid length. Temporal development of the spray is very important for high-speed automotive diesel engines, but cannot offer information about the maximum length and diameter of the spray, which is very important in selecting the dimensions of the combustion chamber. Siebers studied the liquid phase of a diesel spray and presented Figure 9, where it was observed that “the ambient gas density has a strong, non-linear effect on liquid length. As the gas density increases, the liquid length decreases, but at a decreasing rate with increasing density.” (Siebers, 1998). Knowing the composition of his post-combustion gases, the equivalent ambient pressure was calculated

and the liquid length as a function of ambient pressure with parameter the gas density was plotted, Figure 10. It is apparent that as the gas density increases, the effect of ambient pressure on the liquid length decreases.

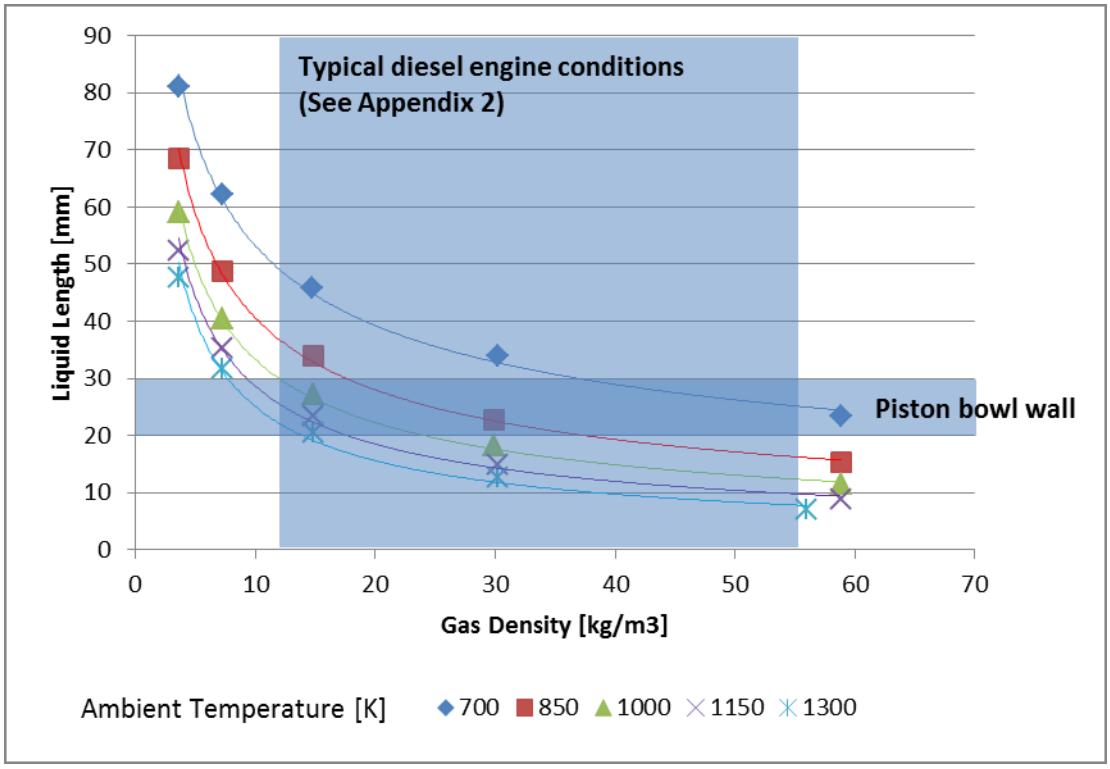

Figure 9 Liquid length of diesel spray as a function of gas density with temperature as parameter, adapted from (Siebers, 1998)

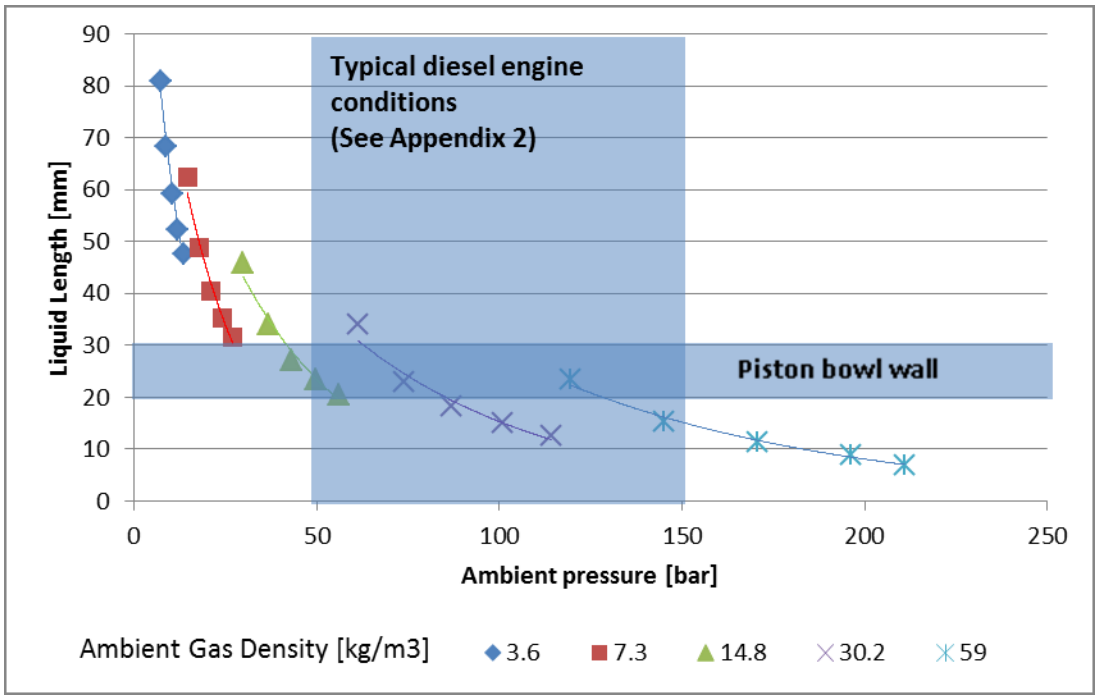

Figure 10 Liquid length of diesel spray as a function of ambient pressure with ambient gas density as parameter, data calculated from (Siebers, 1998)

2.2.2.3 Ambient temperature effect on Liquid Length

Siebers, in a constant volume vessel using Mie scattering, found a strong effect of temperature on the liquid length: more precisely it was observed that as the gas temperature increased, the liquid length decreased. It was suggested that higher ambient temperature increases vaporization rate and shortens the required length of spray to entrain enough hot gas to vaporize the fuel. He also noticed that the general trend of decreasing liquid length with increasing temperature is decreasing at higher temperatures and ambient gas densities (Siebers, 1998). In another work, it was observed that the effect of temperature on liquid core decreases with increasing gas density (Higgins et al., 1999).

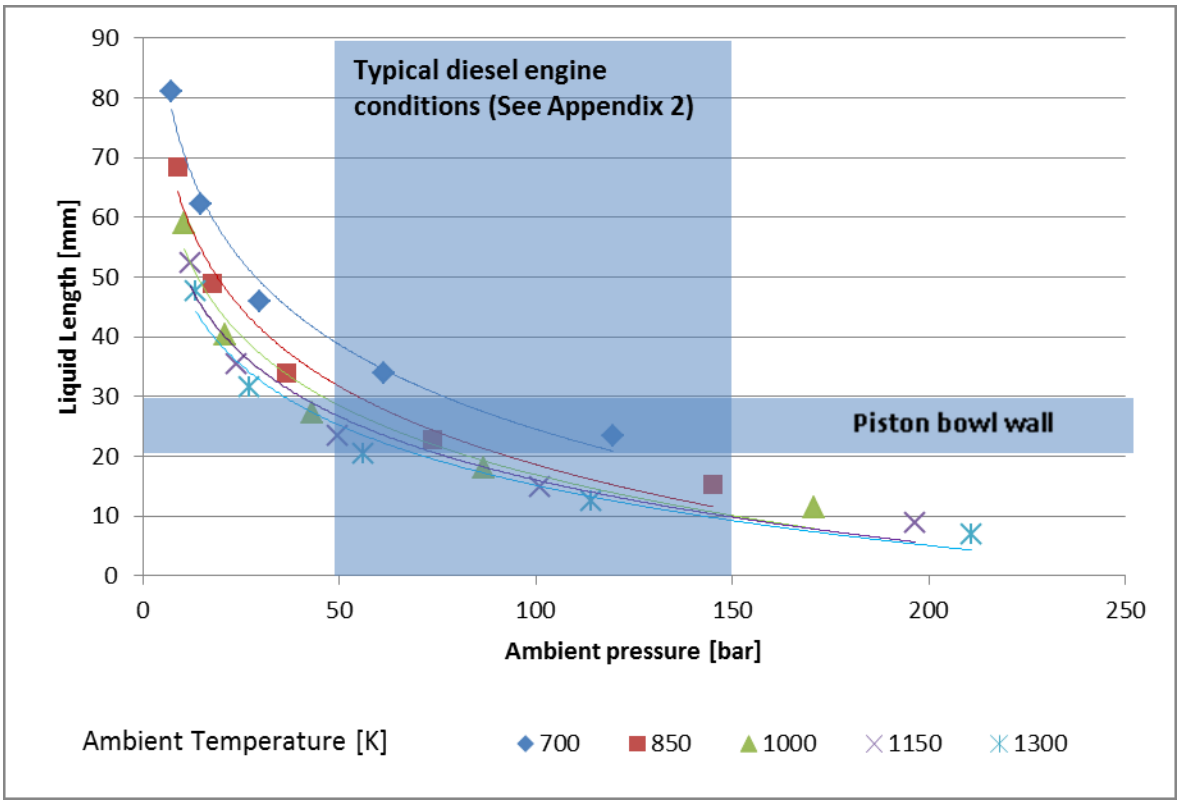

Figure 11 Liquid length as a function of ambient pressure with ambient temperature as a parameter, data calculated from (Siebers, 1998)

2.2.2.4 Nozzle Geometry effect on Liquid Length

The liquid length of a diesel spray has been observed to be linearly dependent on the orifice diameter. Independently of all the other parameters examined (ambient gas temperature and density, injection pressure, fuel and orifice aspect ratio), a change in the orifice diameter results in a directly proportional change in the liquid length (Siebers, 1998)

2.2.2.5 Fuel Temperature effect on Liquid Length

Siebers observed that as fuel temperature increases, the liquid length decreases linearly. This effect was found to be more significant at low ambient-gas-density and temperature conditions (360-460 K, 7-14 kg/m^3). It was suggested that as the fuel temperature increases, the energy required to heat up and vaporize the fuel decreases, thus the liquid length decreases (Siebers, 1998). Increasing temperature increases the liquid vapour pressure, which demotes cavitation, which is an important factor affecting the liquid length. But

increasing temperature, decreases fuel surface tension which promotes droplet breakup and thus leads to shorter liquid length. Especially as commercial diesel is a blend of hydrocarbons, it is very difficult to analytically quantify the effect of fuel temperature on the liquid length.

2.2.2.6 Fuel Volatility effect on Liquid Length

Browne and Siebers have noticed that lower volatility fuels have longer liquid lengths. This was explained as a lower volatility fuel needs more energy to heat and vaporize, so as the entrainment rate of energy to the spray is limiting the vaporization, the requirement for more energy to heat and vaporize a less volatile fuel, leads to longer liquid length (Siebers, 1998).

2.2.3 Temporal spray penetration development

Due to the experimental difficulty in observing the time-development of the liquid-core of a spray, in the literature there is limited work documenting the break-up length development (Verhoeven et al., 1998). Also this information is of limited use to the engine-designers. However, the temporal development of the spray-tip is very important in high-speed diesel engines. In a typical automotive diesel engine, maximum power appears at around 4000 rpm, at this rotational speed the whole compression cycle lasts 7.5 msec, allowing the spray limited time to develop, mix, evaporate and ignite. Too slow penetration will not allow for good mixing of fuel and air in the cylinder and will lead to high soot formation. Too rapid penetration will cause the spray to impact the wall and may even disallow the stratified operation of the engine. Table 4 presents some semi-empirical correlations which describe the temporal evolution of a spray tip penetration

It has been suggested that spray penetration follows a two stage development. In the first stage, up to time t_b, the tip development is linear with time, but after time t_b the penetration is proportionate to the square root of time (Reitz and Bracco, 1979, Hiroyasu and Arai, 1990).

So far all the proposed models of spray-tip penetration consider the injected-fuel quantity to be a dependent variable. So the fuel quantity is not taken into account in the correlations, Table 4. Clearly the information of spray-tip penetration is of little value if the fuel quantity injected leads to non-realistic air-to-fuel ratios (i.e. AFR<0.7 or AFR>1.3). As will be presented later, some researchers have included this parameter in models describing the generated droplet size distribution.

Hiroyasu and Arai (1990) measured the temporal development of spray penetration of a diesel spray using a purpose built instrument with light transmitting LED and receiving phototransistors. For pressures below 20 bar, they noticed that temporal spray penetration development is insensitive to ambient temperature. However, at the time they could not reach realistic diesel-engine temperature values, Appendix 2.

Almost a decade later, researchers started investigating fuel sprays in constant volume vessels using pre-ignition techniques that allowed them to better control ambient conditions. In this way, observation of evaporating, non-combusting sprays was possible and engine-like values of ambient conditions could be reached. Newer models started including more parameters as shown in Table 4.

Expression for temporal spray tip penetration	Method	Researcher
$L_P = (2C_V)^{0.25}\left(\frac{\Delta P}{\rho_a}\right)^{0.25}\left(\frac{d \cdot t}{tan\theta}\right)^{0.5}$	based on the momentum theory that air entrained into fuel.	(Wakuri et al., 1960)
$L_P = 3.07\left(\frac{295}{T_a}\right)^{0.5}\left(\frac{\Delta P}{\rho_a}\right)^{0.25}(d \cdot t)^{0.5}$	For limited geometry and injection condition	(Dent, 1971)
$L_P = 390\left(\frac{2\Delta P}{\rho_l}\right)^{0.5} t$ for $0 < t < t_b$	For ambient pressure of	(Hiroyasu and Arai, 1990)

$L_P = 2950\left(\frac{\Delta P}{\rho_a}\right)^{0.25}(d\cdot t)^{0.5}$ for $0 < t < t_b$ $t_b = 28.65\frac{\rho_l d}{\sqrt{\rho_a \Delta P}}$	10-100bar, temperature 22-320oC	
$L_P = 3.8\left(\frac{\Delta P}{\rho_a}\right)^{0.25}(d\cdot t)^{0.5} tanh[(t/t_b)^{0.6}]$	For $Re_b < 10^5$ (Lacoste, 2006). At room temperature, ambient pressure 5-50bar and injection pressure 215-300bar.	(Yule and Filipovic, 1992)
$L_P = 1.26\cdot \dot{M}_o^{1/4}\rho_a^{-1/4}\cdot t^{1/2}\cdot tan^{-1/2}(\theta/2)$ Where the momentum flux $\dot{M}_o = \rho_f \frac{\pi}{4} \mathrm{d}^2 U_o^2$		(Desantes et al., 2006)
$L_P = k\cdot\rho_a^{\alpha}\cdot\Delta P^b\cdot t^c$ K=0.018, α=-0.256, b=0.516, c=1.044 $L_P = k\cdot\rho_a^{\alpha}\cdot\Delta P^b\cdot t^c\cdot tan(\theta/2)^d$ K=0.00243, α=-0.218, b=0.575, c=0.997, d=-0.197		(Payri et al., 2008a)
$L_P = a\cdot t^b$		(Verhoeven et al., 1998)

Table 4 Models of temporal spray tip penetration

2.2.3.1 Injection Velocity or injection pressure effect on spray tip penetration

As expected, increasing the injection pressure leads to faster liquid phase evolution and reduces the time needed for the spray to reach maximum length, Figure 12 (Verhoeven et al., 1998, Yu and Bae, 2003, Zhang et al., 1997). Even though the rate of tip penetration increases

with increasing pressure, it has not been explicitly noted that this effect of increasing spray velocity with increasing pressure has a decreasing rate with increasing injection pressure.

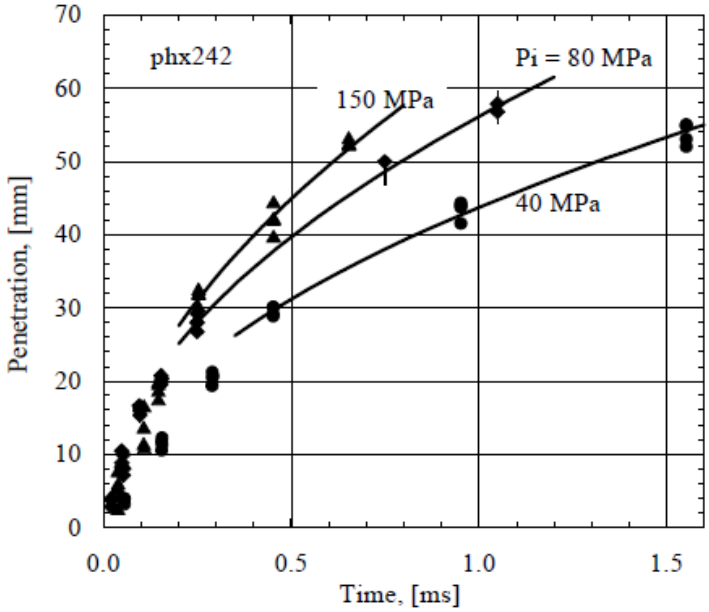

Figure 12 Spray-tip temporal penetration rate with injection pressure used as parameter, adapted from (Verhoeven et al., 1998)

2.2.3.2 Ambient Pressure or gas density effect on spray tip penetration

Many researchers imply the effect of the ambient pressure in the pressure difference, ΔP, between the inlet and outlet of the nozzle, Table 4. This ΔP term also implies an influence of the injection velocity. Injection velocity is calculated considering a uniform velocity distribution across a nozzle cross-section and using the injection pressure difference. So the "Bernoulli" speed is calculated as $u = \sqrt{2\Delta P/\rho}$, however the nozzle geometry and cavitation within the nozzle are being ignored.

2.2.3.3 Ambient Temperature effect on spray tip penetration

It is known that even if ambient temperature increases from room temperature to 590K, the spray-tip penetration is not significantly affected(Hiroyasu and Arai, 1990). However the spray cone angle is noticeably decreased, due to the evaporation of the droplets at the spray periphery (Karimi, 2007).

2.2.3.4 Nozzle geometry effect on spray tip penetration

Baik et al. (2001), using deep X-ray lithography and electroplating, created exceptionally small diameter nozzles, up to 40 µm, and noticed that for a constant injection pressure the smaller the diameter of the nozzle, the slower the spray development Figure 13. Similar behavior was observed in the previous paragraph 1.2.2.5. However, the L/D ratio was not kept constant, which, as described earlier, promotes a laminar flow.

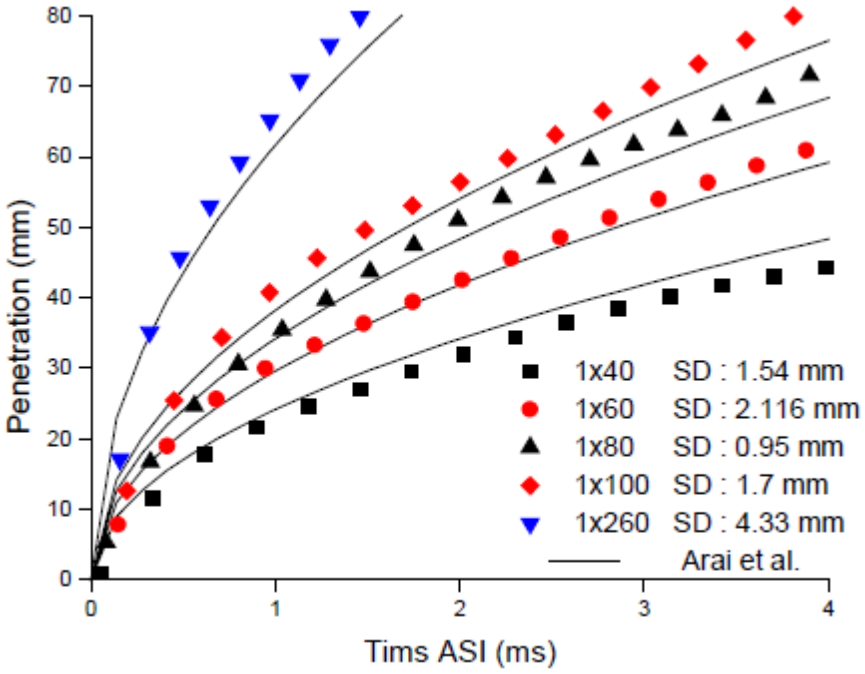

Figure 13 Temporal spray-tip penetration with nozzle diameter used as a parameter, adapted from (Baik et al., 2001)

2.2.4 Spray cone angle

The spray cone angle provides a measure of spray mixing with ambient air. Naber has named the cone angle "spray dispersion angle" (Naber and Siebers, 1996). Arai even

characterized a complete spray as the region where the cone angle becomes relatively insensitive to the injection velocity as shown in Figure 14 (Hiroyasu and Arai, 1990). Reitz regarded the "jet divergence" as an important parameter of the mechanism of atomization (Reitz and Bracco, 1982).

In a room temperature study of atomization, Reitz and Bracco (1982) altered the ambient pressure and gas density independently by using mixtures of air, Helium, Xenon and Nitrogen and noticed that the increase in spray divergence was caused by the increase in gas density and not the increase in pressure. However, similar observation has not yet been made for the tip-penetration and the break-up length, especially in an evaporating spray. Also they noticed that fuel viscosity has insignificant effect on the cone angle. It was observed that higher L/D decreases the cone angle. Though they appreciated that rounded inlet nozzle should stabilize the flow, they failed to detect this effect experimentally.

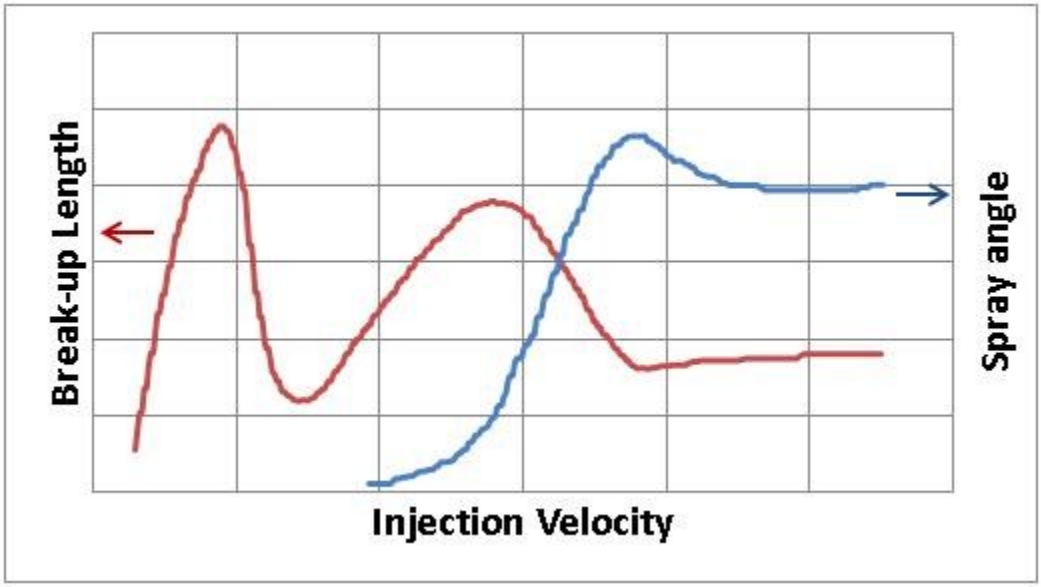

Figure 14 Jet regimes as a function of spray angle, adaptated from (Hiroyasu and Arai, 1990), as discussed in Figure 4

It is known that rapid actuation of the needle, as in piezo-injectors, does not affect the tip penetration, but leads to larger spray cone angles. Experiments have measured up to 10^{o} larger cone angles than arise in equivalent solenoid-injectors. This is believed to be the result of the rapid increase of the injection flowrate (Park et al., 2006). However, in that work the

triggering pulse was the same for both the piezo and solenoid injectors and the injected fuel quantity was not kept constant.

Expression of cone angle	Researcher
$\theta = 83.5\left(\frac{L}{D}\right)^{-0.22}\left(\frac{D}{D_o}\right)^{0.15}\left(\frac{\rho_a}{\rho_l}\right)^{0.26}$	(Hiroyasu and Arai, 1990)
$tan\left(\frac{\theta}{2}\right) = 0.40\left(\frac{\rho_a}{\rho_l}\right)^{0.19}$	(Naber and Siebers, 1996)

Table 5 Empirical correlations of spray cone angle

2.2.5 Drop size distribution

Figure 15 shows some typical drop sizes appearing in everyday life. In combustion systems, the main purpose of the atomizer is to mix the fuel-vapour with the oxidizer quickly and homogenously; this is achieved by breaking down the fuel into small evaporating droplets. It can be easily shown that for a specific volume of fuel "broken down" in droplets, by decreasing the droplets diameter N times, the surface area increases according to N^2. This increase in surface area is beneficial to the evaporation of the fuel and the mixing of the fuel vapour with air. For this reason, it is very important to quantify the size of the generated droplets.

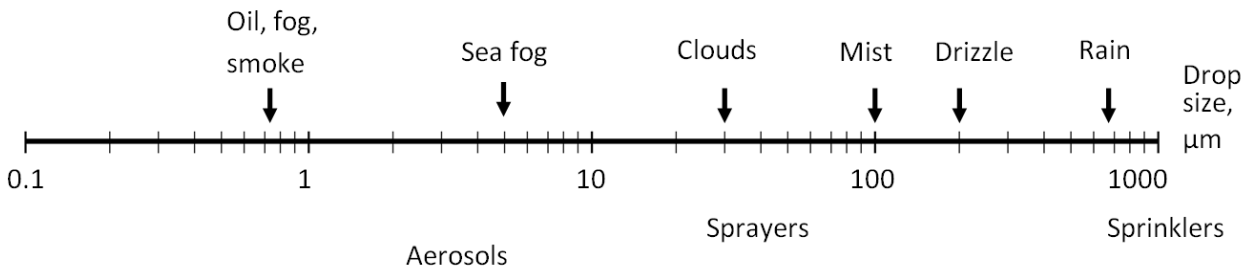

Figure 15 Spectrum of drop sizes, adaptated from (Lefebvre, 1989)

For the study of atomization, evaporation and combustion of fuel sprays the Sauter Mean Diameter has extensively been used. It is defined as the ratio of the volume of the produced drops by their surface area, $D_{32} = \left[\sum_{i=1}^{i=N} D_i^3\right] / \left[\sum_{i=1}^{i=N} D_i^2\right]$. In Table 6, some models describing the SMD of fuel sprays are presented. A difference from the previous models of spray characteristics is that the injected fuel quantity is a parameter that was previously ignored. The dependence of SMD on the injecting velocity/pressure and fuel characteristics is quite obvious. The SMD is decreasing with an increase in ambient pressure, as higher gas density causes higher We, which promotes droplet break up. It has even been practically proven that atomizers can only produce fine sprays $D_{v0.5} = 30$ microns or less only by injecting to high gas density ambient conditions 10 kg/m^3 or more (Nasr et al., 2002).

Expression of SMD of spray	Researcher
$\dot{m}_{p,ev} = 2\pi r_p (\rho D)_g Sh_o ln(1+B)$	(Sirignano, 1999)
$D_{32} = 3.98 \cdot 10^7 \frac{d}{\nu}\left(\frac{\sigma}{\rho_\alpha}\right)^{0,25} \sqrt{\gamma}\left(1 + 3{,}34\frac{\mu\sqrt{g}}{\sqrt{\sigma\rho_l d}}\right)$	(Tanasawa and Toyoda, 1954)
$D_{32} = 1.605 \cdot 10^6 Q'^{0.131} \nu^{0.215} \Delta P^{-0.458}\left(\frac{A_{orf}}{A(t)_{eff}}\right)^{0.916}$	Knight (Knight, 1955)
$D_{32} = 2.33 \cdot 10^3 Q^{0.131} {\rho_a}^{0.121} \Delta P^{-0.135}$	(Hiroyasu and Arai, 1990)
$D_{32} = 3.08 \cdot 10^6 \nu^{0.358} \sigma^{0.737} {\rho_l}^{0.737} {\rho_a}^{0.06} \Delta P^{-0.54}$	(Elkotb, 1982)
$D_{32} = 6156 \cdot \nu^{0.385} \sigma^{0.737} {\rho_l}^{0.737} {\rho_a}^{0.06} \Delta P^{-0.54}$	(Ejim et al., 2007)

Table 6 Models of SMD of sprays

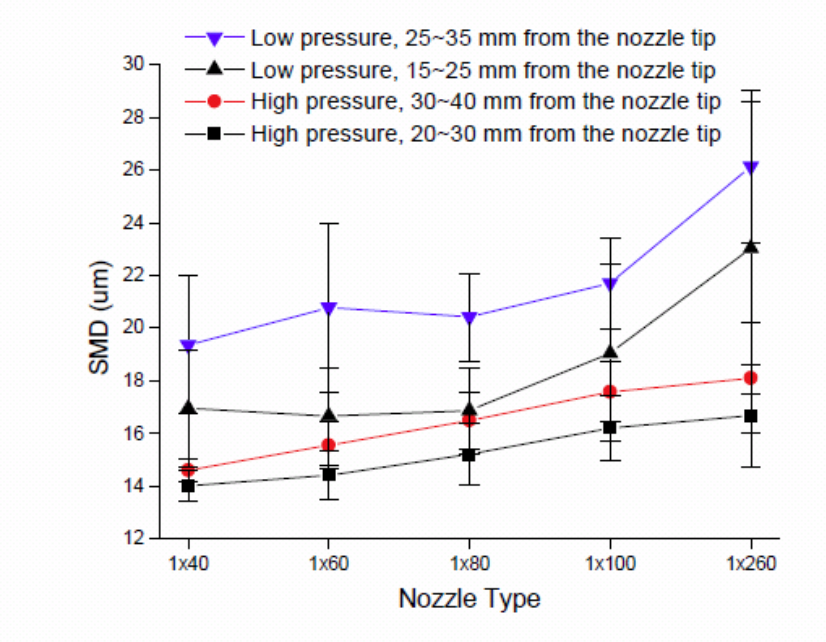

Figure 16 Drop size of single orifice nozzles, adaptated from (Baik et al., 2001)

It has been observed (Baik et al., 2001) that the SMD of piezo injectors is smaller than that of solenoid injectors. Piezo injectors have quicker response than solenoid injectors, especially in short energized durations such as the pilot injections, so they create higher injection velocities. These higher injection velocities mean that the droplets have a higher Weber number, thus an enhanced break-up, Figure 16.

As will be presented in Chapter 7, the smaller the droplet the easier it evaporates. For example, a 50% reduction of droplet size, means that the droplet will evaporate four times faster. In perspective to the limited time available between injection and ignition of a diesel spray, this means that the smaller the fuel droplets, the better the air-fuel mixture, thus the less the soot emissions. Chapter 7 will also mathematically demonstrate the influence of the ambient-gas heat capacity and heat conductivity on the evaporation of a single droplet. It will also be shown how these conditions can be achieved.

2.3 Atomizer efficiency

As discussed by Yule and Dunkley (1994), in principle atomization is a process with very low efficiency; however the necessity of sprays in industrial and every-day life makes it an irreplaceable process. Efficiency of an atomizer is the theoretical energy needed to break down a volume of liquid into droplets, divided by the actual energy delivered to the atomizer. The plain orifice atomizer is one of the most efficient atomizers but still efficiency lies between 5 to 20%. The theoretical energy needed to atomize a jet can be calculated as the product of the surface tension of the liquid and the surface area produced by the atomizer.

$$E_\sigma = \sigma S = \sigma \sum_{i=1}^{i=N} \pi D_i^2$$

Neglecting the need to overcome viscous forces during breakup, the input energy will be the product of pressure drop along the nozzle by the volume of fluid flowing through the nozzle. The volume can be calculated as the sum of the volume of the produced drops, so the theoretical efficiency n_σ is:

$$n_\sigma = \sigma \left[\pi \sum_{i=1}^{i=N} D_i^2 \right] \Big/ \left[\Delta P \left(\frac{\pi}{6} \right) \sum_{i=1}^{i=N} D_i^3 \right]$$

Or

$$n_\sigma = 6\sigma / (\Delta P \cdot SMD)$$

Though ignored by almost all researchers, the efficiency of an atomizer is of paramount significance in industrial applications, especially in the automotive industry, where the atomizer energy has to be produced by the engine. For instance a modern Diesel Common-Rail pump, used to compress fuel at 1700 bar, requires a maximum power of 9 kW, which is about 10% of the engine output. However to calculate the atomizer-efficiency one needs to find a quantitative way of measuring the Sauter Mean Diameter.

2.4 Objectives of this work

The present work has recognized that supercritical evaporation of the liquid can occur in real Diesel engines as well in the combustion chamber designed as part of the current work. The fuel injector produces fuel droplets with different diameters. So under the latent heat evaporation assumption, larger droplets would take longer time to evaporate. However, it has been experimentally observed that the evaporation of a spray is complete roughly at the same distance from the nozzle exit, thus all droplets evaporate at approximately the same time. At engine-like conditions, ambient pressure and temperatures are greater than the critical pressure and temperature of typical hydrocarbons usually found in the diesel fuel blend. It is known that supercritical evaporation of a mixture composed of liquid and vapour phase, takes place without latent heat absorption, but as an instant transition from the two phase mixture to the vapour phase. However, the fuel injected in the cylinder through the injector is in liquid phase and is instantly being surrounded by gases at pressure and temperatures, which are at supercritical conditions for the liquid fuel. In order for the supercritical transition to commence, the droplets will first have to be at supercritical temperature. It is obvious that the liquid is always in supercritical pressure, as the common rail pressure is well above the cylinder pressure, which is at supercritical pressure. However, the injected fuel initially is in subcritical temperature and, when injected in the cylinder, cools down the supercritical ambient environment. So, the core of the spray is in subcritical temperature and needs time to warm up. This might be the reason why droplets survive in the sprays for some time after injection and then evaporate all together. To support the proposed mechanism, it should be emphasized that all computational approaches in predicting fuel evaporation are based on the assumption of latent heat absorption evaporation, as described by the D^2 law. However, the D^2 law over-predicts the time required for evaporation as will be demonstrated in Chapter 7.

As will be shown in Chapter 3, most of the previous experiments in the literature did not include advanced electronic control of the operation of the high pressure chamber, which increases the uncertainty of the measured quantities and reduces the probability of good repeatability between different realizations of the injection process. An important advantage of the current research is that real-time multilevel-architecture monitoring and controlling

equipment was custom-built. A reprogrammable National Instruments FPGA connected to a Real-Time-Controller was programmed in LabView, to receive information from sensors and send commands to a series of actuators. This improved control of the rig allows for better control of the experimental conditions

In previous similar experiments, described in Chapter 3, the pressure vessels were filled with a desired amount of gas by monitoring the pressure through a manometer, which allowed the mass of the gas mixture components to be calculated from the equation of state. In this work an alternative method, Bronkhorst mass flow controllers programmable from LabView, was used.

The Fuel Injection Equipment of the current work is also more efficient than those described in the literature. A dual common rail system has been used. The older common rail systems were equipped with a pressure control valve. In the newer common rail systems, to save energy from pressurizing and then returning to tank excess fuel, a by-pass valve is installed prior to the high-pressure pump and is controlled by a pressure sensor on the rail. However, with the later configuration the control of pressure in the common rail suffers from a time-lag. Since, in this work, a new type common rail system is tested, the pressure in the rail was measured by the pressure sensor on the new-type rail and a dummy old-type common rail was used to control the fuel pressure by the pressure regulating valve. Both pressure regulating valve and low-pressure by-pass valve were controlled by custom made National Instruments electronics. This approach achieved stable fuel pressure in the common rail during injection and thus the fuel mass injected was less susceptible on the pressure wave in the rail. Clearly, it was not in the scope of this work to program the FIE system to save energy, but it could be easily done with this dual-rail configuration.

2.5 Outline of the thesis

To simulate the conditions in a diesel engine cylinder, a constant volume vessel (CVV) was built, which, unlike the cylinder of an engine, allowed for full development of the spray,

without wall restrictions. Additionally spray ignition due to high pressure and temperature was prevented by not allowing Oxygen to be present in the ambient gas. Chapter 3 will describe how the vessel was designed, built and controlled.

The pre-ignition technique used to create a high-pressure and high-temperature environment will be presented in chapter 4. Two chemical models were developed to calculate the post-combustion conditions (pressure, temperature, heat capacity and heat conductivity). The initial model was based on the assumption of perfect combustion and the second model investigated the effect of chemical dissociation by solving for the minimization of Gibbs energy. Additionally, a High-Speed Schlieren technique and a dual pressure transducer method were used to validate the combustion conditions.

Chapter 5 will present the tracer-Laser Induced Fluorescence (LIF) technique used in this work. A literature survey of the current LIF techniques and tracers will initially be presented. Finally the chapter will explain the reasons behind the selection of the Methyl-Naphthalene tracer as the most appropriate for these conditions.

The macroscopic behaviour of a non-evaporating Diesel spray at ambient and elevated pressure is presented in Chapter 6. For this purpose, a back-illumination High-Speed Cinematography and a High-Speed Schlieren technique were used. Some semi-empirical correlations of temporal spray characteristics, presented in Chapter 2, will be evaluated in Chapter 6. However, more importantly the results of Chapter 6 will be then compared to the evaporative spray measurements of Chapter 7.

Chapter 7 will initially present a numerical study of single droplet evaporation. The influence of the ambient-gas heat capacity and heat conductivity on the evaporation of a single droplet, as well as of the ambient pressure and temperature, were investigated. Subsequently, the tracer-LIF technique was applied to the evaporative spray to measure the fuel vapour distribution. Finally, a numerical single-droplet-evaporation model was compared to the tracer-LIF results.

3. Design and operation of high pressure and high temperature constant volume chamber

3.1 Introduction

As evaporation and mixing phenomena of a spray (Chapter 2) depend on ambient conditions, it is important to study these phenomena at conditions typically found around the Top Dead Center of a diesel engine. To achieve this, in a constant volume vessel, temperature and pressure were increased using a chemical-preheating technique (Chapter 4).

The current chapter will present how previous researchers created high pressure and temperature environment and will describe the design of the vessel used in this work. For the precision of the experimental conditions and results, a series of sensors and actuators were used on the vessel, the Fuel Injection Equipment (FIE), the laser and the camera. The operation of those controls and sensors was time and safety critical, so the controlling software was physically compiled on a real time Field Programmable Gate Array (FPGA) chip. This chapter will finish by describing the software and hardware developed for this experiment.

3.2 Literature review of methods for creating high temperature and pressure conditions

To recreate high temperature and high pressure condition in the lab, various types of experimental rigs have been built. The most common ones are shock-tubes, rapid compression engines and constant volume chambers; each of these devices has disadvantages and advantages.

A shock tube is a closed tube, of rectangular or circular cross-section, separated by a thin diaphragm into two parts. One part, at low pressure, is filled with the test gas. The other part is filled with a high-pressure, driver gas. At a specific time, the diaphragm is burst mechanically and a pressure wave propagates through the low pressure testing volume.

Usually, as driver gas, an ignitable mixture is ignited at the high pressure part of the shock tube and the diaphragm bursts due to the high pressure created after the ignition. Shock-tubes are a key device for studying chemical kinetics. However, test times are typically limited to a few milliseconds and boundary layer growth can present a problem (Bradley, 1962, Ferri, 1961, Gaydon, 1963, Wright, 1961, Zel'dovich and Raizer, 1962, Hanson, 1997, Bowman and Hanson, 2000, Hanson 2013).

In a rapid compression machine (RCM) one or two pistons move rapidly to create a high pressure and temperature environment. Such machines have a compression ratio of 9-15, so even if adiabatic compression is considered, $P_2 = P_1 \left(\frac{V_1}{V_2}\right)^{\gamma}$, the final pressure cannot exceed 40 bar. The maximum temperature is also limited by adiabatic compression to a value given by $T_2 = T_1 \left(\frac{V_1}{V_2}\right)^{\gamma-1}$, which even with electrical preheating, does not exceed 1000 K as reported in the literature (Merola and Vaglieco, 2004b, Donovan et al., 2004, Minetti et al., 1994, Mittal and Sung, 2006, Merola and Vaglieco, 2004a).

A continuous flow vessel (CFV) is a vessel where preheated pressurized gases flow through the vessel in a steady state at a low speed, usually around 1-2 m/sec. Major benefits of this technique are the steadiness of the conditions in the test volume and the relatively short time needed to purge the vessel and prepare it for the successive test, which is usually of the order of a few seconds. However, as the conditions are steady, a robust construction of high strength materials is needed, which makes this an expensive experimental setup. The most important drawback of this technique is that the steady flow of air in the test volume, swipes the fuel-vapour away from the spray and artificially promotes spray evaporation.

Constant Volume Vessels (CVV) can achieve high temperatures and pressures with quite good repeatability and relatively low cost. A CVV is based on the principle that if an amount of oxidant-fuel is ignited in a constant volume chamber, the pressure and temperature will increase. This ignition is called pre-ignition as it might precede a potentially second ignition of the injected diesel fuel by the diesel injector. The fuel used for pre-ignition is usually a combination of gaseous fuels (i.e. H_2, C_2H_2) selected to create a desired post-combustion

environment in the vessel. Table 8 summarises the previous work performed in constant volume vessels.

3.3 Design

Some of the most important problems associated with designing and building a CVV include heat transfer, repeatability of operating conditions, robustness of the structure, optical access, control of processes and safety issues. These issues will be discussed in this sub-chapter.

3.3.1 Dimensioning and shaping the vessel

As discussed in Chapter 2, the purpose of this work is to observe the spray development and evaporation. Thus any interaction of the spray with the vessel wall is unwanted. As shown earlier, a typically fully developed diesel spray is around 60 mm long. In a typical modern diesel injector, the spray exits the injector at an angle of 15^{o} from the horizontal level, as shown in Figure 17. So, ideally the vessel should be large enough to accommodate the spray and the recirculation vortices created around the spray during injection. However, in terms of cost and safety, the volume should be as small as possible. The largest dimension of the vessel determines the largest lengthscale of the flow.

The Pressure Equipment Directive (97/23/EC) was adopted by the European Parliament to harmonise national laws of Member States regarding the design, manufacturing, testing and conformity assessment of assemblies of pressure equipment. The Directive among other pressure equipment, concerns items such as the constant volume vessels used in this work. Figure 18 shows the conformity assessment of pressure vessels. Clearly for volumes up to 1 L and nominal pressures up to 200 bar, only sound engineering practice is required. This simplifies the testing, certification and regular inspections of the experimental rig.

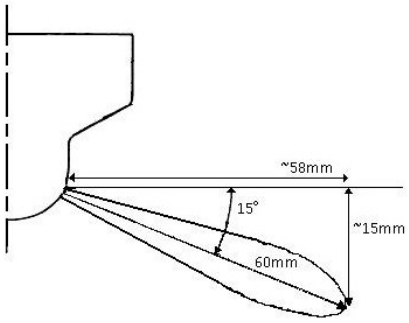

Figure 17 Typical dimensions of a modern diesel spray

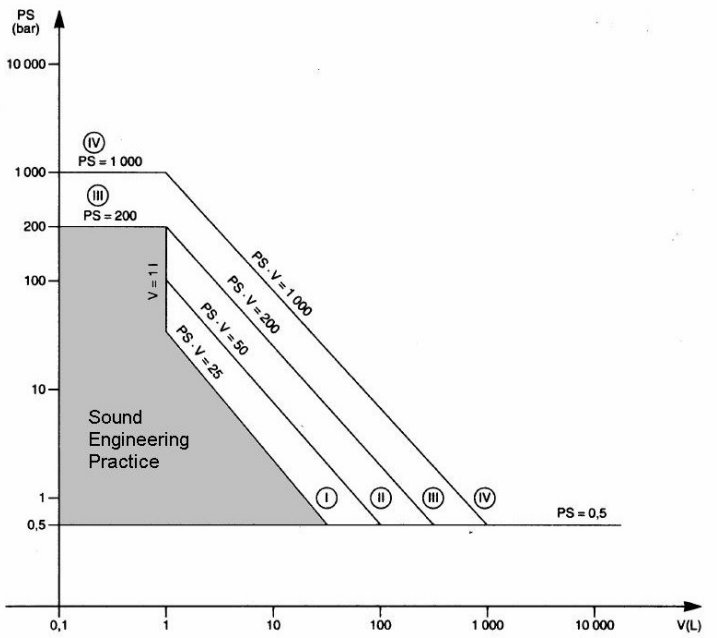

Figure 18 Conformity assessment graph, Sound Engineering Practice, adapted from 97/23/EC (council, 1997)

In the end, balancing the above factors and taking into account previous similar work in the literature, Table 8, a compromise was struck at a volume of around 1 L. Further detail can be found on the engineering drawings of the vessel, Appendix 4.

The dominant constant volume vessel shapes in the literature are either cubical or cylindrical. There has been a spherical combustion vessel, Table 8. Cubical and spherical vessels are very expensive to manufacture and do not offer an experimental advantage.

3.3.2 Repeatability of injection conditions

Accurate and precise repeatability of the temperature and pressure conditions into the vessel are of vital importance to the validity of the measurements. In this direction, many parameters need accurate control, such as the materials and insulation used, the initial temperature of the vessel, the mass of fuel being used for the pre-ignition, the heat losses of the vessel and the flow within the vessel.

After ignition, pressure and temperature in the vessel keep decreasing. However, during the time of fuel injection, pressure and temperature conditions can be considered nearly constant, as the vessel cooling down timescale is 100 times longer than the injection time.

3.3.3 Windows design and material

3.3.3.1 Optical properties

The most common window materials used in the literature, Table 8, are quartz, fused silica and sapphire. The expensive sapphire is UV and IR transparent but can have a bipolar behavior at high temperature. Quartz and fused silica, though cheaper, are not IR and UV transparent respectively. As will be discussed in chapter 5, for this work a UV laser was used, so the transmittance of fused silica as shown in Figure 19 is satisfactory. The surface of the window was polished with an accuracy of λ/4, where λ is the average wavelength of visible light.

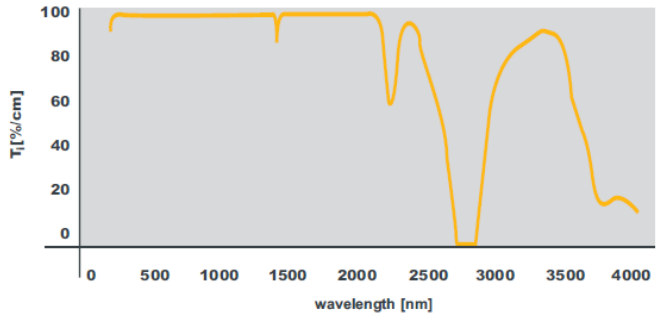

Figure 19 Internal transmittance of fused silica used in the experiment (Corning Inc 2003)

3.3.3.2 Thermal properties

Since the windows occupy most of the vessel's surface area, the glass material is responsible for most of heat losses. Out of the three aforementioned most common materials used in the literature for optical windows, sapphire has very high heat conductivity and fused silica and quartz have very similar values of heat conductivity as shown on Table 7. So sapphire, in terms of heat loses, has very poor performance.

Fused silica has lower heat conductivity than stainless steel, Table 7, which means that fused silica has higher heat resistance. So it would be expected to have higher heat loses per unit of surface area through the steel. As the stainless steel part of the vessel is electrically preheated and insulated, the heat loses per unit of surface area are lower than heat loses from the fused silica. Detailed calculations are given in Appendix 3. A simple and novel way to overcome the problem of heat losses through the windows, is the use of double glazing that was adopted in this work.

Window matter	Elastic Modulus	Shear Modulus	Bulk Modulus	Tensile strength	Modulus of s	Maximum service temp	Heat Conductivity
Sapphire	350	145	250	400	350	Not recommended	25
Fused Silica	73	31.4	35.4	52.4	52.4	1650	1.3
Quartz	74	31	36.9	50	50	1300	1.4
Stainless steel 316L	200	82		485			16.3

Table 7 Table of mechanical properties of typical window materials, values from (Corning Inc 2003) @ 25°C

3.3.3.2 Mechanical/Chemical properties

The windows are the most fragile part of the vessel, as they have less strength (lower tensile strength) than steel, Table 7. So the vessel peak pressure is dictated by the strength of the windows. Contact surface areas between the window and the metal, required for supporting the window and sealing the vessel, are loading the window, as shown in Figure 20. The cross-section of the window appearing on the right plug of the vessel in Figure 20 is made of steel, these steel "blank" windows were made for non-optical measurements. As steel is ductile, the blank-window deforms and the stresses are higher in the center of the surface facing the inside of the vessel. The window on the left is made of fused silica and the stresses appear more uniform. Care was taken to remove sharp edges that would act as stresses

concentration-points, so the window was shaped as shown in Figure 97 in Appendix 4. A series of gaskets and O-rings had to be improvised to ensure sealing and decrease stresses on the window, as shown in Figure 21. Further detail on the gaskets and O-rings can be found on the vessel's engineering drawings in Appendix 4 and especially in Figure 96.

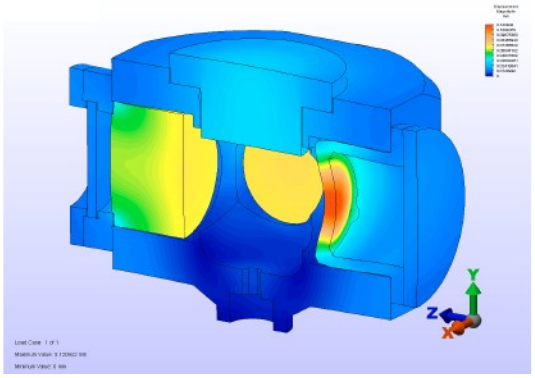

Figure 20 Stresses on vessel as calculated on Solidworks

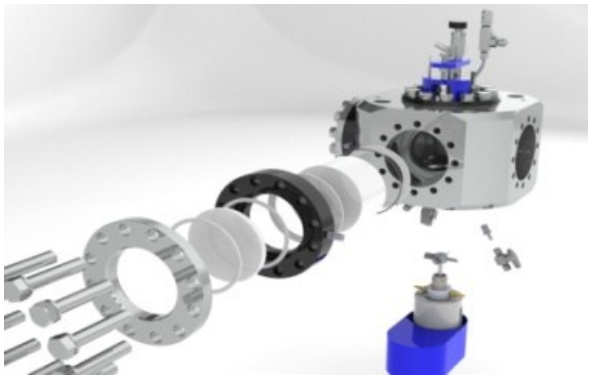

Figure 21 Cartoon reconstruction of sealing gaskets and O-rings

As shown on Table 7, sapphire has higher strength (tensile strength and bulk modulus) than fused silica and quartz. Sapphire's strength is almost equal to the strength of the stainless steel that the vessel was made of. However, sapphire is very brittle (has high elastic and shear modulus and low tensile strain), property unwanted in this application. Whereas, the lower strength quartz and fused silica are very tough (they can absorb more energy than sapphire before breaking).

3.3.4 Heat Insulation/Vessel material

Stainless steel is the dominant material for pressure vessels, because of its strength, low cost, relative ease in machining, good magnetic behavior and stainless property. However, stainless steel has large heat conductivity and high heat capacity, properties not desired in this application. High heat conductivity means that there are heat loses from the vessel to the environment, Appendix 3. In order to overcome this problem, vessels in the literature are insulated and electrically heated, Table 8. High heat capacity means that the metal absorbs

heat produced by the pre-combustion, a simple solution to reduce this problem is to preheat electrically the vessel.

The CVV used in this study was made of stainless steel 316L and fitted with four 500watt cartridge electric heaters. The heaters were controlled by the cRIO FPGA using a variable frequency and duty-cycle, pulse width modulation signal, which was triggering a solid-state high-power relay. As condensation on the windows was not a problem to this study, the heaters were not used.

3.3.5 Diesel injection system

The injector can be either top or side mounted on the vessel depending on the type of measurement. As the spray develops, due to air-entrainment through its edges, a recirculation zone is being formed. To keep this recirculation zone interacting as little as possible with the spray and the vessel wall, the injector nozzle is mounted at a distance of 2 mm from the wall, which is a common practice (Naber and Siebers, 1996, Verhoeven et al., 1998). Detailed engineering drawings presenting the geometry of the injector position are given in Figure 95 in Appendix 4.

Figure 23 shows the experimental setup that was used to drive and trigger the injector. A lift-pump was used to increase the fuel pressure and pass it through a particulate filter, before sending it to the high-pressure common rail pump. A Hartridge 1100 test stand drove an automotive Bosch CP3 pump. The fuel-flow rate to the high-pressure common rail pump was controlled by a valve upstream of the pump, as opposed to downstream in previous pump generations (Bosch, 2005). To be able to control the pressure in the associated common rail (which is factory-equipped with a pressure relief valve only), an additional dummy common rail (with a pressure-regulating valve downstream of the pump) was attached. As a safety measure, should the valves fail (thus deliver full flow), we retained the injectors on the dummy rail with their integral spill paths. As the fuel return from the injectors, rail and pump was at high

temperature, 80^{o}C, a water cooled heat exchanger cooled the fuel before returning it to the fuel tank. In this way, the fuel in the tank was kept at 25^{o}C.

As will be discussed later in this chapter, the vessel, pump and injection operation were controlled by LabView software and all operations were monitored and controlled in real time by a National Instruments cRIO FPGA system. Briefly, and regarding only the fuel injection equipment (FIE), the pressure sensor on the associated common rail was feeding the cRIO with information about the pressure in the common rail. The user defined the rail pressure in the custom-made LabView code and the cRIO was controlling the pressure by modifying the signals sent to the pressure-regulating valve upstream of the pump and the pressure-regulating pump on the dummy rail, using a feedback loop. The user had to manually adjust the pump speed from the Hartridge test stand and the injector was triggered from cRIO through a custom made injector-drive box, which was kindly provided by Honda R&D. A water-cooled jacket was built to keep the injector within working-temperature range. However, as the vessel wall temperature was measured to be about 25^{o}C during experiments, the injector-cooling jacket was not used, Chapter 4 will provide more detail.

3.3.6 Mixing of pre-ignition gases (Magnetic fan)

The mixture of combustible gases has to be very well mixed, before ignition, in order to have repeatable post-combustion pressure and temperature conditions. A magnetically coupled fan was used to control the flow and enhance mixing in the vessel. The austenitic nature of stainless steel 316L allowed for the magnetic couple to be used, thus avoiding leaks. The operation of the fan was controlled automatically by LabView, more specifically; a digital output from the cRIO was used to drive a 24V solid-state-relay, which in turn was used to drive a contactor, which acted as an ON/OFF switch for the fan-speed-controller as shown in

Figure 24. The speed and direction of the fan could be adjusted manually. This “3-layer” technique, (digital output, 24V solenoid and high voltage contactor), was used extensively in the rig in order to isolate high power mains from sensitive low voltage and power electronics. Also in terms of safety an adaptor had to convert the power supply to the fan speed controller,

from 220V AC to 50V DC, as high voltage electricity tends to create sparks, which could be dangerous in combination to vapour fuel.

During the filling of the vessel with gases, the fan was on, to enhance the mixing of the gases and homogenize the temperature in the vessel. During the first tests of combustion of the gases, the fan was left on to increase the flame speed and most importantly keep a uniform temperature distribution in the vessel, technique adopted from Sandia Labs (Naber and Siebers, 1996). However, High-Speed-Schlieren cinematography applied during combustion proved that the rotating fan led to flame extinction and re-ignition. Any disturbance of the combustion process due to physical obstacles or in-vessel-flow, will alter the combustion duration from experiment to experiment. It will also produce different post-combustion pressure and temperature conditions and cause dissociative combustion products, which will be studied in Chapter 4. So, the fan was powered off three seconds before the ignition, this period of time was enough for the swirl to dissipate as observed by using smoke visualization in the vessel. More on this topic and the experimental results will be described in Chapter 4.

3.3.7 Ignition

In this work a low-voltage glowplug was used to provide ignition. The glowplug was powered by a commercial automotive battery and controlled by a digital cRIO output through a 24V DC solenoid relay. Alternative methods of ignition have also been explored in the literature and include sprak-plug and laser ignition (Naber and Siebers, 1996, Verhoeven et al., 1998).

3.3.8 Control, supply and extraction of gases (Mass Flow Controllers and pipes)

In the literature, poppet valves are used to seal the vessel from the input and output lines, Table 8. In this work to avoid the cost and complexity of building, running and maintaining poppet valves, commercial solenoid valves, provided by Bronkhorst UK Ltd, were used. There are two input lines to the vessel, one for purging air and one for the pre-ignition gases, as shown schematically in Figure 22. On the input lines, non-return valves were used to protect

the solenoid valves from high pressure and temperature conditions in the vessel, so the input solenoid valves had low pressure and temperature specifications. A specially designed manifold system, that is shown in Figure 101 of Appendix 4, was built to allow for better mixing of the input gases and minimize the “dead” volume. Non-return valves and flame-arrestors were used to protect the Mass Flow Controllers. However, on the output lines, for safe extraction of high temperature and pressure gases, high pressure and temperature solenoids had to be used, which were pneumatically driven from a Nitrogen cylinder.

Usually the filling of similar vessels is achieved based on the principle of partial pressures of the gaseous components, either in the vessel itself (Verhoeven et al., 1998, Naber and Siebers, 1996), or in a separate mixing tank which in turn “feeds” the vessel. However, in both cases the effect of temperature drop, caused by the pressure drop of the gas from the high pressure cylinder to the chamber, is ignored. For this reason (Klein-Douwel et al., 2007) used Mass Flow Controllers to fill the vessel. The importance of accurate and precise metering of the pre-ignition gases is discussed in Chapter 4.

A purpose-built LabView code, also known as VI, executed from a dedicated computer, controls the filling of the vessel with the pre-ignition gases by the Bronkhorst Mass-Flow-Controllers, as will be presented in Section 3.5.4. The “dead” volume between each mass-flowmeter and its corresponding non-return valve was calculated and automatically added to the mass of each injected gas. The “dead” volume between the nitrogen mass-flowmeter and the vessel’s inlet solenoid valve was calculated and automatically added as a purging mass of Nitrogen at the end of the filling procedure. However, after experimentation, it was found that transient operation of the Mass Flow Controllers, results in large errors (of the order of 2% in the delivered mass), even after compensation for the opening and closing operations. For reasons explained in Section 4.5, vacuuming and filling the vessel with the gaseous fuels was

Setup of gas pipes: 1)Gas cylinders, 2)Mass Flow Meters, 3)Check Valves, 4)Solenoid Valves, 5)Constant Volume Vessel, 6)Cyclone, 7)Vacuum Pump, 8)Safety quick release valves, 9)Techni-measure pressure transducer

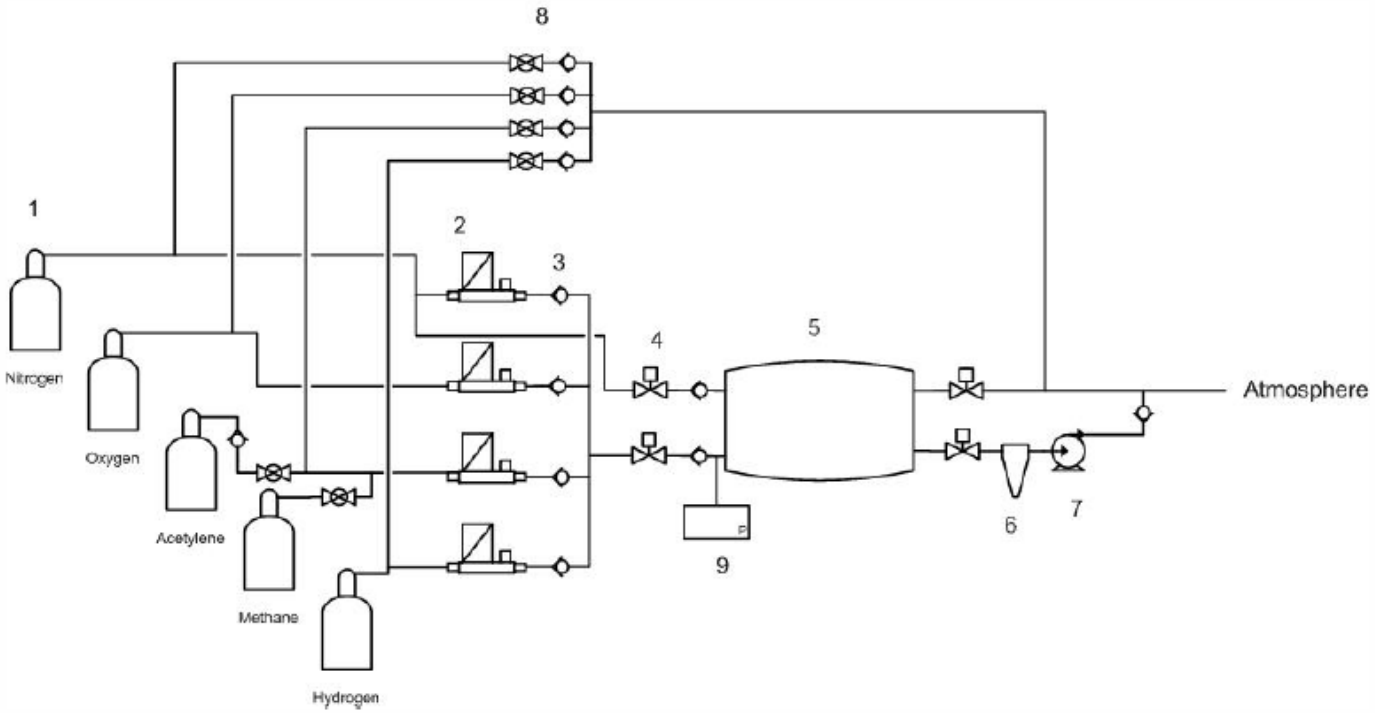

Figure 22 Supply and extraction of gases

not producing as repeatable results as continuously purging the vessel with the gaseous fuels. Further detail about the filling software and procedure can be found in Section 3.5.

3.3.9 Thermocouples and RTD

Four K-type thermocouples were installed at the four corners of the vessel, to provide temperature reading of the vessel walls, Figure 99. Though this temperature differs significantly from the gas temperature, it provides feedback to the heaters and prevents the vessel from thermal stresses. If, for example, the temperature at one corner is higher than the temperature of another corner, the controlling software will turn off the heaters to prevent development of thermal stresses, which could crack the windows or the vessel itself.

In the literature correlation of wall temperature T_w to gas temperature T_c has been attempted. It was shown that: $\frac{T_c}{T_b} = 1 + a\left(1 - \frac{T_w}{T_b}\right) + b\left(\frac{T_b}{T_w} - 1\right)$, where T_b is the mass-averaged gas temperature, and constants a and b were empirically determined. The second term on the right accounts for cooler, higher density gases in the boundary layers, while the third term on the right accounts for cooler, higher density gases in the crevices and corners of the vessel (Siebers, 1998).

In this work an RTD (Resistance Temperature Detector) was installed in the center of the vessel, measuring the gas temperature of the core. It has to be noted that, as with thermocouples, RTDs have a slow sampling rate of up to 10 samples per second. Also, due to their cladding, RTDs and thermocouples have a slow response to temperature changes. In the literature work with fine thermocouples 0.050 m has reported high-frequency sampling (Heitor and Moreira, 1993), but this falls outside of the scope of this work. For these reasons, in this work, the mass-averaged temperature of the gases in the vessel was calculated from pressure reading using the ideal gas law. The RTD gave the core temperature of the gases before ignition, which is equal to the mass-averaged temperature because of well stirring and which was then used to calculate the mass of the gases and thus the post-combustion conditions as will be shown in Chapter 4.

Organisation	Pressure	Temperature	Observation Method	Extra Heating	Orifice	Laser	CR injection pressure	Fuel	Publications
Aachen (Chalmers University)	73 – 90 bar	900 K	Rayleugh scattering, LII	N/A	CR injection system with one hole	Nd:Yag	N/A	n-Dodecane IDEA mix	(Vogel et al., 2005)
Aachen	5 MPa	800 K	PDA	N/A	8 holes D=0.13-0.131mm Ks=1.3 and 3	N/A	60, 90 and 135 MPa	Diesel	(Weber et al., 2006)
RWTH Aachen	Up to 5 MPa 21.4 kg/m^3	700 K	Simultaneous Mie and Shadow imaging	24 kW electrical, constant airflow	Bosch CR with 5 holes, L/D=7.25	Ruby laser (694nm) and flash lamp	135 MPa	Ethanol	(Spiekermann et al., 2009)
ACE Institute Co. Ltd (N2 pressurized)	1.5 MPa	Room	PIV	none	Single hole D=0.17 L/D=7.82	Nd:Yag	27, 106, 201 MPa	n-tridecane	(Sasaki et al., 1998)
Australia	25 bar	1100	Two-colour-	none	Bosch	none	180 bar	Ethanol, diesel,	(Kostas et al.,

LTRAC (CRU from Lund)		K	pyrometry		CR, five-hole injector, D=0.2mm			various mixtures of bio-oil	2009)
Brighton (rapid compression)	Up to 12 MPa	Up to 720 K	LII	none	Single-hole VCO D=0.2 mm	Nd:Yag	100, 140 and 160 MPa	Esso AF1313 and 2-ethylhexyl nitrate	(Crua et al., 2003)
Bosch (GDI)	Up to 2 MPa, 0.12 & 0.56 MPa	Up to 400^{o}C, 80 & 180^{o}C	Diethylketone-LIF, Stroboscopy Sclieren, Mie	Electrical	Several types of atomizers were tested	excimer	8MPa	Premium unleaded and iso-octane/diethylketone	(Preussner et al., 1998)
Chalmers University of Technology	Up to 100 bar	Up to 900 K	Nonanone-LIF, LII, Mie , Rayleigh scattering	Electrical preheating and chemical heating	Standard diesel injector	Nd Yag, tunable KrF excimer	Standard diesel injector	n-decane	(Schulz et al., 2004)
Chungbuk University	1 and 30 bar	300 and	Shadowgraph, Mie	preheating and	D=0.22 mm	Nd:Yag	400 bar	DME	(Lim et al.)

		600 K		chemical heating					
Chungbuk University (pressurized N2)	0.6 – 1.5 MPa	room	shadowgraph	none	D=0.2, 0.3, 0.4 mm	none	35 MPa	DME	(Hwang et al., 2003)
CMT-Motores Termicos	5 and 7 MPa	800, 950 K	stroboscopy		3 different conicity 6-hole injectors	none	30, 80, 160 MPa	Repsol CEC RF-06-99	(Payri et al., 2008b)
Colorado Labs	12.5 atm	873 K	FTIR (Fourier Transform Infrared Spectrometry)	Heating cartridge packed bed heater	D=160 µm, L/D=4	none	150 MPa	Diesel, dodecane and methyl-oletate	(LABS and PARKER, 2007)
Doshisha-Kawasaki	0.5-1.5 MPa	298 K	Shadowgraph	none	0.3, 0.7, 1 mm	none	6-12 MPa	Hydrogen	(Tsujimura et al., 2003)
Doshisha University	5.3 kg/m^3 and 30 kg/m^3	700 K	LIF	Electrical Heater	D=0.2 mm L=0.8 mm	Nd:Yag	42 MPa, 72 MPa and 112 MPa	i-octane, n-dodecane and n-hexadecane	(Myong et al., 2008, Fujimoto et al., 2005b)
Doshisha University	16.2 kg/m^3	1200 K	LII	Electrical Heater	D=0.2 mm	Nd:Yag	70 MPa	DBE, DGP, DGE, DGM,	(Fujimoto et al., 2006)

					L=0.8 mm			BA, EA	
Doshisha University	2.55 MPa 12.3 kg/m^3	700 K	Exciplex Fluorescence	Electrical preheating and chemical heating	D/L=0.2/1	Nd:Yag	72 MPa	n-tridecane doped with naphthalene and TMPD	(Yeom et al., 2001)
Doshisha University (optical engine with a swirl chamber)	N/A	N/A	Natural emission of OH radical	none	Port injection	none	14.7 Mpa	JIS second class gas oil	(Fujimoto et al., 1999)
Eindhoven TU	Up to 7 Mpa	Up to 905 K	Shadowgraphy	Electrically up to 200^{o}C	8-hole Bosch D=0.184 mm L/D≈5	none	150 MPa	Diesel	(Klein-Douwel et al., 2007)
Erlangen (GDI)	0.3 MPa	Up to 433 K	Rotational coherent anti-Stokes Raman Scattering (RCARS)	Heated by constant air flow	D=53 mm, L=116 mm	Nd Yag and Dye laser	4, 8 and 10 MPa	Iso-octane	(Hildenbrand and Schulz, 2001)

Georgia Institute of Technology	Up to 100 atm	Up to 650 K	LIF calibration	Electrical heating	none	Nd Yag	None	Acetone seeded in nitrogen	(Tran et al., 2008)
Huazhong University of sience and technology	0.1, 2, 3 MPa	Room temperature (28^{o}C)	High-speed photography	none	0.18, 0.25 and 0.32 mm	none	15, 20, 25 MPa	LPG, Diesel and LPG/Diesel fuels	(Helin et al., 2006)
IFP	12, 25 and 30 kg/m^{3}	387, 800 and 1100 K	Mie scattering, Schlieren and high-speed cinematography	Electrical preheating and chemical heating	Single hole Φ=0.2 mm	Ruby laser	40, 80, 150 MPa	n-dodecane and 1% commercial lubricant	(Verhoeven et al., 1998)
IFP	12, 25 and 30 kg/m^{3}	387, 800 and 1100 K	Mie scattering, radicals-LIF, LII		Ganser Hydromag single holed injector L/D=0.2/0.8mm	Nd:Yag, Rudis, dye	40-160 MPa	Heptane, Dodecane and Diesel	(Bruneaux et al., 2004, Bruneaux, 2001b, Verhoeven et al., 1998, Bruneaux, 2001a)

IFP (compression machine)									(Bruneaux et al., 1999)
Imperial College London	10-40 bar	Room temperature	PDA			N/A	20 MPa	Diesel	(McGlashan, 1997)
Instituto Motori (rapid compression)	50 bar	20 – 500^{o}C	Scattering	Electrical heating	L/D=1/0.18 mm	Nd:Yag	120 MPa	ISO 4113 calibration fuel	(Andreassi, Ubertini, & Allocca 2007)
Instituto Motori (extra chamber)	N/A	N/A			Single and 6-hole injector				(Merola and Vaglieco, 2004b)
Korea Advanced Institute of Science and Technology	1, 15 and 30 bar	30^{o}C	High-speed digital camera	none	10 D=0.32 mm	none	2000 bar	diesel	(Bae and Kang, 2000, Yoon et al.)
Lucas diesel (2stroke optical engine)	N/A	N/A	Shadowgraph	none	5hole D=0.15 mm	Nd Yag	200-1600 bar	Diesel	(Kunkulagunta, 2000)

Lund Institute of Technology	25 bar	700 – 800 K	LIF		6x0.4 mm	Tunable excimer	190bar		(Franke et al., 2005)
Lund Institute of Technology	Atmospheric	400 K	Acetone-LIF and NO and OH LIF	Electrical heating		KrF excimer and Nd Yag			(Franke et al., 2005)
MAN based on Hiroyasu design	Nitrogen up to 50bar	room	High Speed photography	None	Single hole nozzle	none	Up to 350 bar	DME	(Sorenson et al., 1998)
Paul Scherrer Institute	8 MPa	850 K	Flashlight shadowgraphy, Laser Elastic Scattering, LII and Chemiluminescence imaging	4x2 kw 6x800 w	Single hole, D=0.15 mm, L/D=4	Nd:Yag	150 MPa	low aromatic diesel fuel	(Bougie et al., 2005)
Queen Marry (combustion system)	2.1 MPa by up to 10 MPa	N/A	Filter papers	none	D=0.2 mm, L/D=2	none	24 MPa	Diesel	(Crookes et al. 2003)
Sandia	7.3 – 30 kg/m^3	350 – 1100	Flame Luminosity, LII		100 µm limitations	Nd:Yag	43-184 MPa	Diesel fuel	(Pickett and Siebers, 2004),

		K			for 180 µm				(Naber and Siebers, 1998, Siebers and Higgins, 2001)
Sandia	7.3 – 60 kg/m^3	800-1300 K	OH chemiluminescence/ Mie scattering	Electrical	D=100-363 µm	He:Ne	40-190 MPa	Philips #2 diesel	(Higgins and Siebers, 2001, Siebers, 1998)
Sandia and CMT	42bars, 14.8 kg/m^3	1000 & 1100 K	PLII and Laser extinction	Electrical preheating and chemical heating	180 µm	He:Ne	1380 bar	T70	(López and Pickett, 1)
Sandia	14.8 kg/m^3	850-1200 K	OH – chemiluminescence, LII and laser extinction	Electrical preheating and chemical heating	Single hole Φ=0.180, 0.100, 0.071 and 0.050 mm	Nd Yag for chemiluminescence and HeNe for laser extinctio	138 MPa	Number 2 diesel fuel	(Pickett and Siebers, 2002)

						n			
University of Hiroshima	3.1 MPa	773 K	Pyrene-LIF	Electrical heating	Single hole Φ=0.15 mm, L/D=5.3	Nd Yag	31 MPa	n-hexadecane	(Yoshizaki et al., 1996)
University of Hiroshima	Up to 4 MPa	Room	High speed movie camera and reflector lamp	none	Droplet maker	none	Droplet maker	n-heptane, n-decane, n-dodecane, n-hexadecane, iso-octane and light oil	(Kadota and Hiroyasu, 1981)
University of Wisconsin Madison (fast compression)	Up to 4 MPa Details in ref(L.Hermant, 2001, Froba et al., 1998)	N/A	Flame Luminosity	Electrical preheating and chemical heating	D=0.66 mm	none	250 kPa	propane	(Plackmann et al., 1998)
University of Wisconsin	17.97 kg/m^3	293 K	Light Extinction Method (LEM)	none	6 hole Φ=0.16	Pulsed copper-	900 and 1200 bar	diesel	(Tennison et al., 2009)

Madison					mm, L/D=6.25	vapour			
University of Wisconsin Madison	Argon up to 18.9 kg/m^3	Room tempe rature	Laser illumination	none	14 purpose built 40, 60, 80,100 and 260 microns nozzles	Cu-vapor	20-25 and 70-80 MPa	California diesel fuel	(Baik et al., 2001)
Waseda University (Apart from combustion vessel, a single-cylinder DI engine was used	1.8 MPa, 8 kg/m^3	800 K	High-speed video-photography	Chemica lly ethylene, Oxygen and Nitrogen	Single hole Φ=0.25 mm	Copper laser	40, 60, 80 MPa	Base and Light diesel	(Lee et al., 2002)
	3.5, 6, 8 kg/m^3	300, 600, 800 K	LIF of OH-radicals from combustion and	Ethylen, Oxygen, Nitrogen	Single hole Φ=0.35	Nd:Yag	40 MPa	Liquid petroleum gas	(Lee, Kusaka et al. 2001)

			NO-combustion??		mm				
Waseda University	3.5, 6, 8 kg/m^3	300, 573, 873 K	High-speed video-camera	Ethylen, Oxygen, Nitrogen	Single hole Φ=0.3 mm	Copper laser	40 MPa	n-dodecane, DME, LPG	(Lee et al., 2001)
		Light extinction, LIF							(L.Hermant, 2001)
PSA centre technique de Velizy(cold)	15.4 to 16.6 kg/m^3	Up to -25^{o}C	High speed camera	none			250 and 400 bar	n-heptane and diesel	(Vergnes et al., 2007)

Table 8 Previous work on high pressure and high temperature vessels used for spray study.

Experimental setup of Diesel injecting system: 1)Fuel tank, 2)Lift pump and filter, 3)Bosch CP3, 4)Rail will pressure control valve, 5)Tested modern rail with pressure relieve valve, 6)Injectors for over spilling fuel in case of valve failure, 7)Tested injector, 8)Fuel cooler

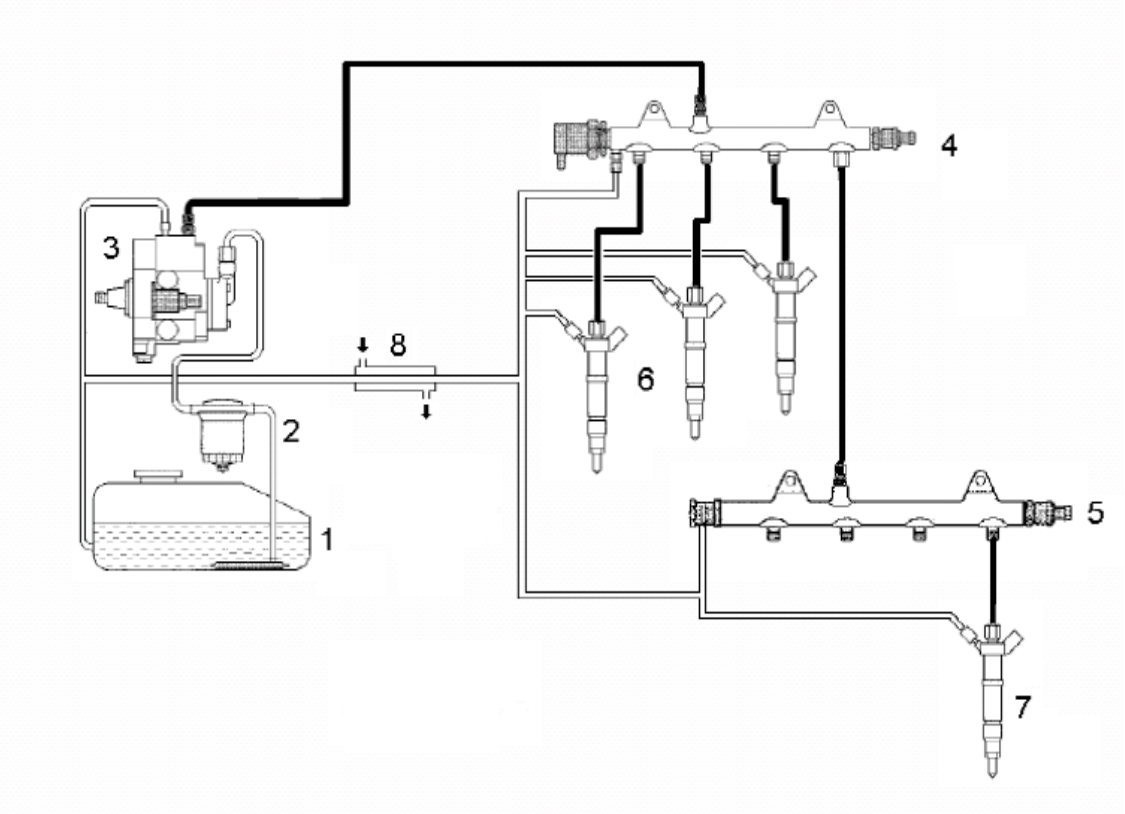

Figure 23 Setup of Diesel Injection System

Setup of electrical connections: 1)Mass Flow Controllers, 2) Solenoid Valves, 3)Glow-plug, 4)Injector, 5)Injector drive, 6)Heaters, 7)Kistler Pressure Transducer, 8)Thermocouples, 9)Motor magnetically coupled to fan, 10)Vacuum Pump, 11)Techni-measure Pressure Transducer

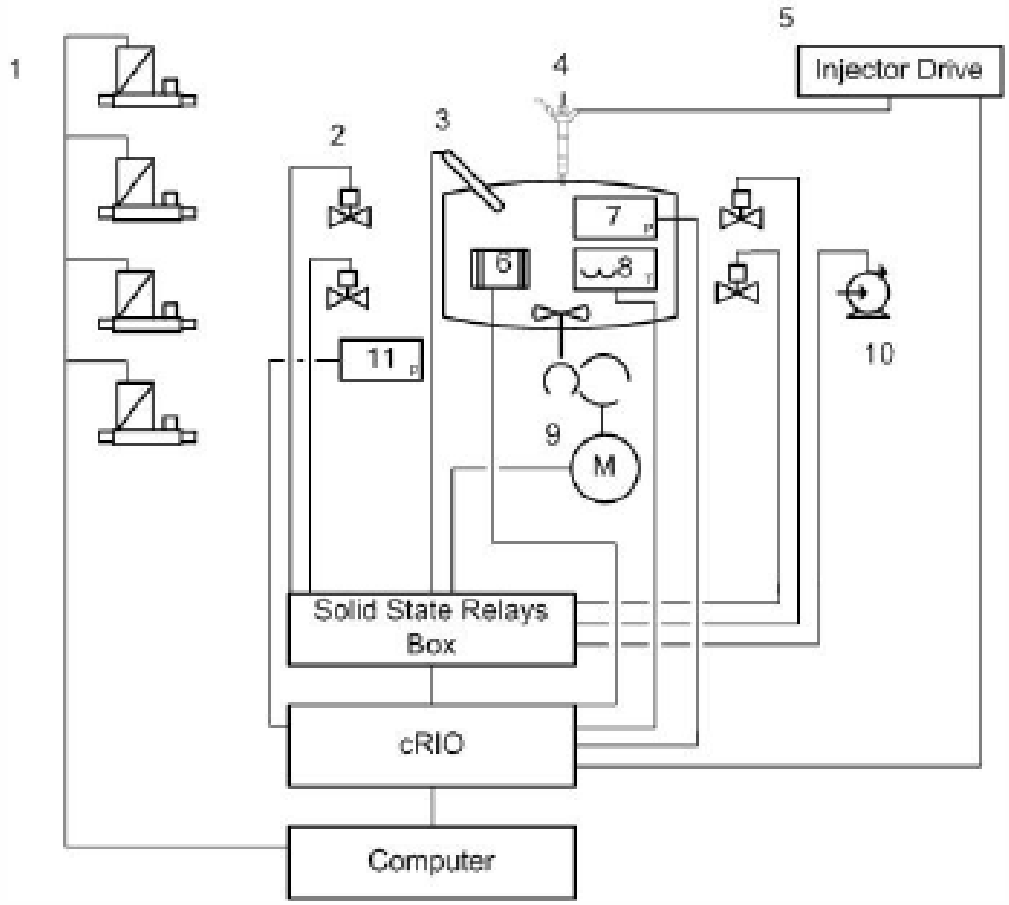

Figure 24 Set-up of electronic controls

3.5 Controlling Software and electronics

3.5.1 Introduction

In the previous sub-chapter the experimental setup was described, clearly it is a very complicated system that has to be finely tuned and synchronized. Also many components are dangerous to the user (high pressure, high temperature, high voltage, flammable and suffocating gases and liquids) and could prove lethal. For the above reasons the operation of the vessel and the Diesel-Common-Rail-System was monitored and controlled by a National Instruments compact Reconfigurable Input Out (cRIO). As shown in Figure 28, in the "heart" of the cRIO there is a Field Programmable Gate Array (FPGA), controlled by a Real-Time controller (RTc) and both programmed and executed by a PC on LabVIEW codes, also known as VIs. This sub-chapter describes the programming architecture and the software developed to control and operate the CRU and the Diesel Common Rail System.

3.5.2 FPGA

The cRIO is equipped with a Xilinx Virtex-5 FPGA, where the controlling software is physically compiled on the chip for faster and safer operation. The FPGA consists of logic blocks, programmable interconnects and I/O blocks Figure 28. The logic blocks are a collection of digital components such as lookup tables, multipliers and multiplexers. Programmable interconnects are routing signals from one logic block to the next or to the I/O blocks. The I/O blocks are connected to the pins on the chip for two-way communication to surrounding circuitry through the cRIO modules. Because LabVIEW FPGA VIs are synthesized down to physical hardware gates connected by programmable interconnects, firstly the LabVIEW FPGA VI generates a VHDL code and passes it to the Xilinx compiler. Then the Xilinx compiler synthesizes the VHDL and places and routes all synthesized components into a bitfile. Finally, the bitfile is downloaded to the FPGA Figure 28. So the FPGA was programmed through LabView graphical environment and acted as digital hardware (National Instruments Corporation 2009).

FPGA, though adding programming complication, offers many advantages. Having the software as a hardware chip is highly reliable. FPGAs do not use any operating systems,

so this minimizes reliability concerns with true parallel execution and deterministic hardware dedicated to every task, up to 25 ns timing accuracy of critical components can be achieved. Because an FPGA implements parallel code as parallel circuits in hardware, there is no limitation from the number of processor cores; therefore, every piece of parallel code in an entire FPGA application can execute concurrently. Finally, FPGA chips are highly reconfigurable (National Instruments Corporation 2009).

Time and safety critical subroutines were programmed on the FPGA chip and were independent of the Real Time Controller and the Computer. Loops running at 40 MHz were checking the Pressure, Temperature and the Panic Button; if these values were above a user-set critical value then the FPGA automatically initiated the shut down procedure. Also the shutdown procedure was compiled on the FPGA, so when the shut down flag was raised, no interference was required by the RTc or PC. Additional Watchdog routines were checking for uneven heat distribution on the vessel that would cause thermal stresses and for extraction fan malfunction. Similarly, a routine drove the injector when the required pressure had been reached in the vessel.

3.5.3 Real Time Controller

Compiling the software on FPGA cannot cover all the needs of this experiment. The FPGA chip has no memory, so any data-logging had to take place on the RTc's embedded 2GB memory. In order to achieve that, an FPGA subroutine, initiated by the RTc, started acquiring data from the cRIO modules and sent them by Direct Memory Access (DMA) to the RTc using a First-In-First-Out (FIFO) protocol. Also FPGA does not offer a Graphical User Interface (GUI), so commands had to be passed from the PC to the RTc and then to the FPGA, so routines that required user interface had to be programmed on the RTc.

The real-time controller (Figure 28) contains an industrial processor that reliably and deterministically executes LabVIEW Real-Time applications. It is also equipped with onboard 2GB solid state memory used for data logging and software upload and is responsible for communication between PC and FPGA and supplying the FPGA with power (National Instruments Corporation 2009).

As discussed above, routines that required GUI had to be programmed on the RTc. So the basic software (Figure 25) was programmed on the RTc and called the FPGA VI. In the FPGA VI, some subroutines were called by the RTc. Clearly the Watchdog subroutines in the FPGA VI were event-driven and called without RTc intervention. Figure 25 shows the flowchart of the main program and Figure 26 the flowchart of the shut-down procedure, that will be discussed later.

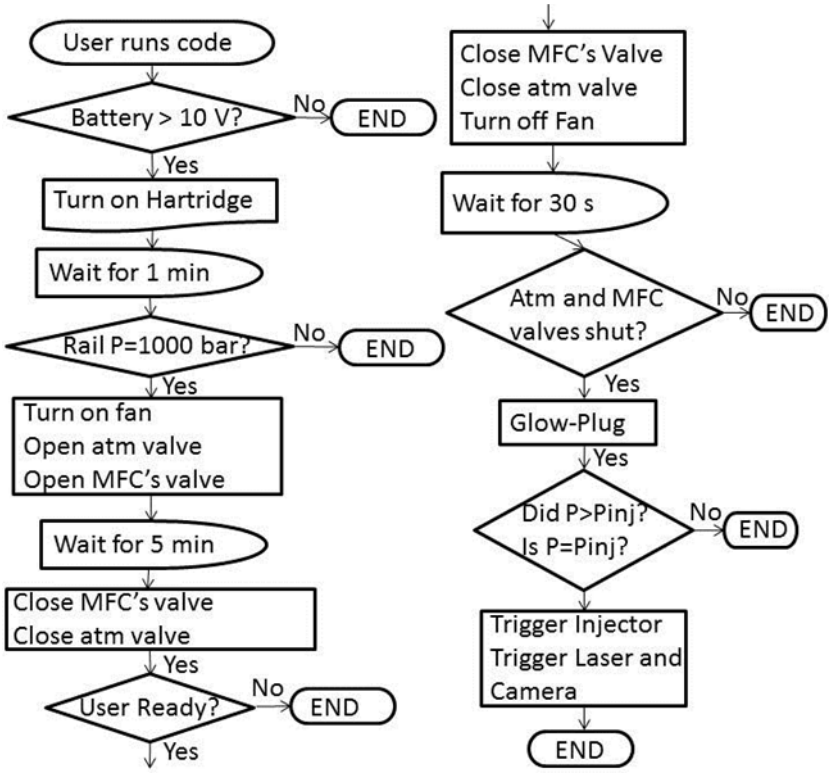

Figure 25 Flow-chart of control software

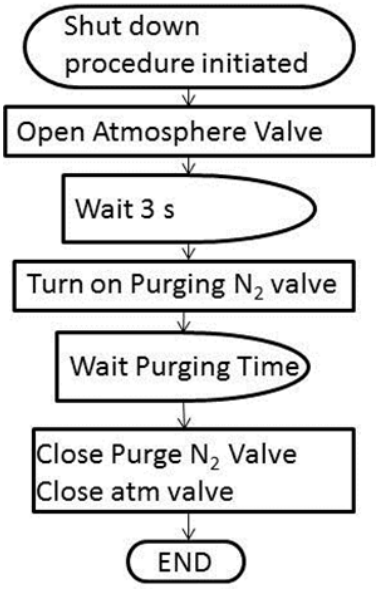

Figure 26 Flow-chart of shut-down procedure

3.5.4 Computer Setup

In principle, the Real Time controller in combination with the FPGA can provide an autonomously working unit. However, this was not sufficient for the current application. The RTc has limited memory that is used both for storing the RTc VI and the logged data. After each run the data were transferred to the PC's hard drive. More importantly, the RTc VI has to be called from the computer, allowing for GUI. The cRIO was connected to the PC

over Ethernet. If this connection to the computer was lost, the RTc “timed out” the software execution as no input was given by the user. The FPGA VI, including the Watchdog routines, continued running normally after loss of computer until the shut-down flag was raised either because of timing out or of emergency stop.

The Bronkhorst Mass Flow Meters were connected and controlled by a dedicated computer, as described in Section 3.3.8. The Real Time Controller cannot offer communication to other devices, so the computer was used to connect the MFCs via RS-232 interface and to call the MFC VI. The RTc VI as shown in Figure 25 would at some point pause the operation and wait for the user to execute the MFC VI and then order the RTc VI to proceed with ignition. FlowDDE, a commercial software package provided by Bronkhorst UK Ltd, allowed for communication between the MFCs and the PC. The MFC VI was following the filling sequence described in the next section.

3.5.5 Guided Description of the program

In this section, Figure 25, which is the backbone of the controlling software, will be described. The user starts the software by opening the LabView Project and executing the RTc VI. On the front panel of the software the default values are saved. The user can alter them at this stage and then press the start button. The default values were semi-empirically chosen after checking every subsystem independently and were optimised for the specific operating conditions. It is not recommended that inexperienced users alter them. Table 9 shows these values.

After the start button is pressed the software will check the voltage level of the battery feeding the glowplug. The next check is that the pressure of the common rail has reached the user defined value. Then the atmosphere and the MFC valves are opened and the fan turned on. This will last for a predefined purging time, which is sufficient for the combustion mixture to purge all unwanted substances from the vessel. Subsequently, the atmosphere and MFC valve will close but will leave the fan on. At this stage the vessel is fully charged, waiting for the user to proceed. When the user presses the “Glowplug” button, the fan will stop, the RTD will start logging the vessel’s gas temperature and the Kistler-pressure transducer will start logging pressure. All these measurements are clearly

referring to the pre-ignition conditions in the vessel. Three seconds later, time long enough to allow for the vortices of the combustible mixture to dissipate, the glowplug will be activated.

Following activation of the glowplug, as will be shown in Chapter 4, depending on the composition of the mixture, deflagration of the mixture will initiate three to eight seconds later. The FPGA monitors (at 70 kHz) the pressure in the vessel to first exceed the pressure that the user has selected for injection and then drop again at the desired value of the "injection pressure", at which point, injection will take place. Should the deflagration never take place or never generate pressure higher than the injection pressure, the operation will time out after 15 seconds without triggering neither the injector nor the laser and camera system. In the usual occasion where deflagration happens as expected, pressure increases in the vessel. The laser has to be triggered at a fixed rate of 10Hz, to keep the flashlamp at a specific temperature and avoid damage due to temperature gradients. During the cooling-down of the post-combustion gases, the ambient pressure at which the spray-injection is required to take place will be reached. At the next pulse of the laser, the FPGA will trigger the injector, allowing time for the spray to develop. At the second next pulse, the FPGA will trigger the camera and log the vessel pressure at the time of imaging. Five seconds later, the "shut down" routine will be called. More detail on the camera and laser signals and triggering setup will be given in Chapter 7.

3.5.6 Controls used in control software (NI cRIO RTC and FPGA)

Figure 27 illustrates the front panel of the controlling software. On the front panel there are some controls and some indicators. Though the previous section offered a described guide of the software, this section will offer a description of the controls on the front panel and the values that were selected for these controls, Table 9. The controls can be divided into four general groups, controls that set values to initiate the experiment, controls that adjust the data-logging process, controls that allow the user to control the progress of the software execution and controls that regulate the watch-dog routines

As mentioned, some controls are used to initiate the experiment. The control "Initial Ambient Temperature [K]" should not be mistaken with the wall temperature, this is the gas

temperature in the vessel as measured by the RTD and acquired by the cRIO RTD module. The user defines this value after consulting GasEq solutions (Morley, 2005) and Chapter 4. Once this temperature condition is met, the code will continue. The control “Purging Time [s]” is the time that the vessel will be purged for. Knowing the purging-gases flow-rate, the value of this control, was calculated as 100 times the vessel volume. The user can set the pressure value of the common rail at which injection is to take place in the control “Rail Pressure [bar]”. The fuel injector system used in this work is optimized for operation at 1700 bar, so all the measurements were performed at this value of rail pressure and this controlled was set at 1700 bar. In the Diesel common rail system used in this work, the rail pressure is controlled by a Pulse Width Modulation (PWM) signal feeding the upstream pass-by valve to the CP3 pump and by a pressure-control valve on the common rail. The “Pump Frequency [Hz]” control is the frequency of the PWM signal feeding the pump pass-by valve and “Duty Cycle Pump [%]” is the duty cycle of the PWM signal, since the pass-by valve is normally closed, 100% should bypass all the fuel to the fuel tank. “Rail Frequency [Hz]” is the frequency of the PWM signal feeding the Common Rail pressure control valve, according to manufacturer this value should be around 60 kHz. The equivalent duty cycle is controlled by “Duty Cycle Rail [%]”. As the pressure control valve on the common rail is normally open, 100% builds up the maximum pressure in the rail. The control “Glowplug time [ms]” sets the time the Glowplug will stay ON. This depends strongly on the pre-combusted mixture and should in no case exceed 10sec, according to glowplug specifications. The user can specify the value of the pressure of gases in the vessel at which the spray injection will take place. This is done by the control “Injection Ambient Pressure at start of injection [bar]”. However, as the signal from the pressure transducer contains natural high-frequency noise, a 5 point running average was proved empirically and by frequency response calculations to be sufficient to cut down unwanted noise.

Some other controls of the program are used to control the data-logging. The control “RTD time [s]” is the duration for which the temperature acquisition from the RTD will be logged. Logging initiates at pressing the Glowplug “ON” button. This value should be of the order of 5sec, to avoid filling the memory of the RTc with meaningless data. Logging will stop if the “shut down” procedure is called. The control “Number of memory elements” dictates the size of buffer used for Direct Memory Access between the FPGA and the Real

Time controller. This value can vary between 400 and 10000. National Instruments recommends a value of around 1000 elements. The Read FIFO method on the Real Time controller returns data only when the Number of Elements is available. “DMA Cycles” is the control referring to the number of cycles that the RTc will read the FIFO DMA at a period of 10msec. Empirically optimised value for this field is 100 cycles. The FPGA clock is running at 40MHz, the control “Count [FPGA ticks]” is the sampling rate of the Kistler preamplifier connected to the Kistler pressure transducer. The maximum sampling value of the sensor is 571 processor ticks, each corresponding to 25 ns.

Some controls are used to regulate the progress of the software execution. The “Start” button is what the user has to press, after making necessary alternations to the values of the controls, in order to run the flowchart of Figure 25. “Panic Stop”, as the name suggests initiates the shut-down procedure once pressed. The “Stop Kistler” button stops the pressure logging from the Kistler pressure transducer. However the software is not terminated when this control is pressed. The control “Fan OK MFC VI” was placed so that the cRIO will wait for the user to visually check that the fan is rotating, then execute the MFC VI, and then press this button to proceed.

Finally some controls allow the user to regulate the watch-dog routines. Generally, it is not recommended for the user to manually override the software. However, if parts of the software need to be tested, then the user will have to restart the software and press the “Manual Override” control before pressing Start. This will override the flowchart of Figure 25 and will allow the user to manually control every operation, apart from the watch-dog routines, which will keep running normally. “Override Battery” overrides the battery voltage check. If the “Override Inj Pres” is “true”, the cRIO will trigger the injector immediately after the glowplug, without waiting for the desired pressure in the chamber to be reached, it is only recommended for tests without using the chemical pre-heating technique. For example, for the measurements at high-pressure Nitrogen environment, this control had to be activated. The watch-dog routines for peak pressure, peak temperature and thermal stresses can be overridden by the controls “Override Pressure”, “Override Temperature” and “Override Thermal Stresses” respectively. Even though the vessel is protected against overpressure by the pressure-relief valve, it is not recommended to override watch-dog routines. The control “OverrideRail Pressure”, overrides the rail pressure check. The

common rail, as described in Chapter 3, is equipped with a pressure-relief valve to protect the fuel injection equipment against overpressure, however if the injector is activated at low rail pressure, the injector might get damaged.

3.5.7 indicators used in control software (NI cRIO RTC and FPGA)

In Figure 27, where the user interface of the software is shown, it is clear that there is a number of indicators. These are placed there, to help with the monitoring of the vessel and the operations happening, Table 10. As with the controls described in Section 3.5.6, the indicators can be divided into four groups, indicators that present the current condition of the vessel, indicators related to the data-logging, indicators that present the progress of the software execution and indicators related to the watch-dog routines.

Indicators that present the current condition of the vessel are usually in the form of a numerical output. The indicator marked as “Battery Voltage” presents the charge of the battery feeding the glowplug. A resistance bridge is used to decrease the battery voltage by 10 times connected to the cRIO to protect the Analogue Input module from high voltage. Expected values should be between 0 and 1.3 V. This is important for informing the user if the battery will be able to initiate the ignition of the chemical heating. “Initial Ambient Temperature [K]” presents the ambient temperature of the vessel before pre-ignition. “Rail Pressure [bar]” is showing the signal of the pressure sensor mounted on the Common Rail, powered by the purpose built common rail control box. The output of the sensor was fed, through the common rail control box, to the Analogue Input of the cRIO. Calibration curve was provided by Bosch GmbH. Expected values, when the sensor is powered, lie between 0.45 and 5 V or 0 to 2000 bar. The indicator “Current Pressure [bar]”presents the current pressure in the vessel. Note that, due to communication between FPGA, RT-controller and PC, there is an insignificant lag. Critical pressure-triggered operations happen on the FPGA in real time without user intervention.

As mentioned, there are indicators related to the data-logging. The “RTD” indicator is lit up when data-logging from the RTD is taking place. When the “Kistler” indicator is “ON”, data is being logged from the Kistler pressure transducer. The “Error out” indicator will return any error in the data-logging process. The “Elements Remaining” indicator shows the

number of elements remaining in the host memory part of the DMA FIFO (RTc). The Write method on the FPGA returns Empty Elements Remaining when the data is written. This output should be greater than zero.

There is a number of indicators that present the progress of the software execution. The indicator “Armed” will light up after the user has pressed the glowplug button and pressure has exceeded the injection pressure. The “T initial OK” indicator shows that the gas temperature has reached the desired initial temperature and the software has proceeded to the next step of the flowchart presented in Figure 25. Similarly, the “Rail Pressure OK” indicator shows that the common rail pressure has reached the desired value. The “Injection pulse” indicates that a pulse is trigerring the injector. It should be “ON” just for an instant. Similarly, the “Glowplug” indicator shows that the glowplug is “ON”. The “Panic Stop” indicator will indicate the initiation of the shutdown routine. For safety reasons a manually operated panic stop button is located next to the Hartridge panic stop button. If this button is pressed a 100 Ohm resistance is isolated from the RTD module of the cRIO, so the FPGA detects an open circuit and initiates the shut-down procedure, indicating “Hardware Panic Stop”. If the shut-down procedure is called for any reason, then this output of the “Shut down” indicator will become “true”.

Indicators related to the watch-dog routines are usually of red colour to attract attention. If the vessel pressure exceeds maximum allowed pressure, the shut-down procedure will be initiated and the “Overpressure” indicator will light up. This operation, as the rest of the watch-dog routines are executed at 40 MHz. If the wall temperature exceeds the user set maximum allowed temperature, the shut-down procedure will be initiated and the “Over Heat” indicator will light up. The wall temperature is measured by four J type thermocouples connected to the thermocouple module of the cRIO. If the wall-temperature readings of the four thermocouples vary between themselves by more than 5%, the shut-down procedure will be initiated to secure the vessel from thermal stresses and the “Thermal Stresses” indicator will light up.

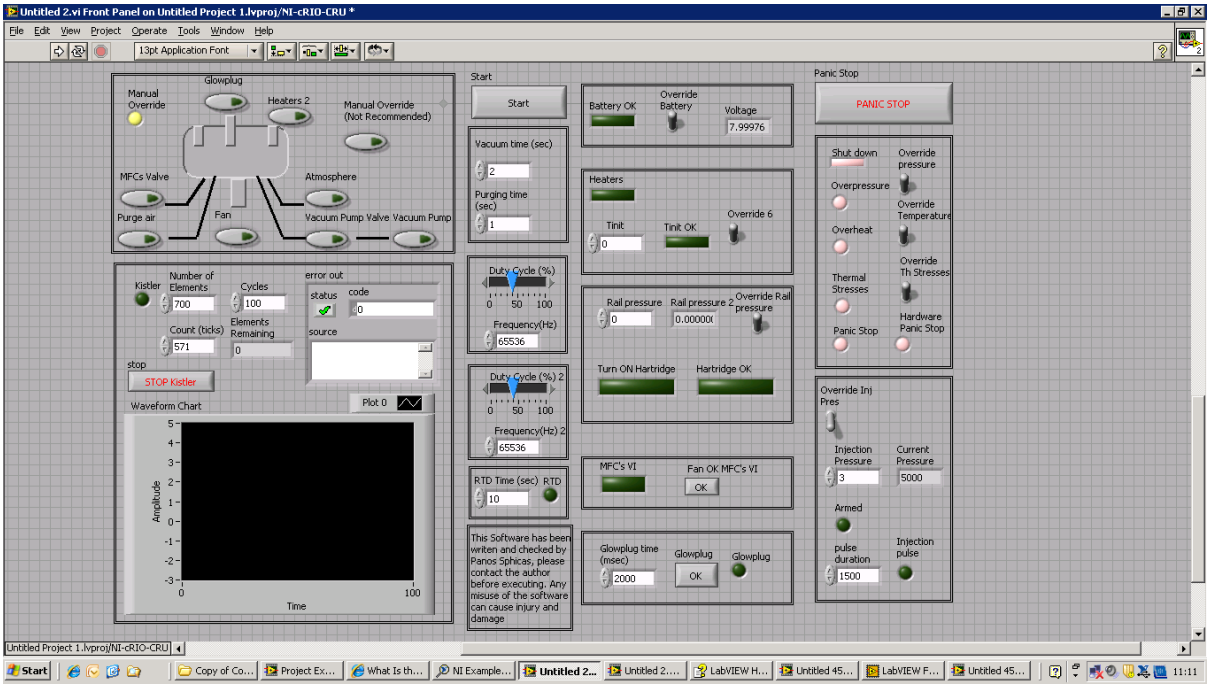

Figure 27 User interface of control software of CVV

This chapter presented the design and operation of the vessel. However, in order for the vessel to operate, the appropriate mixture of gaseous fuels has to be filled in the vessel and subsequently ignited. The next chapter will investigate the selection of this appropriate mixture and the post-combustion environment created.

Control Name	Short Description
Initial Ambient Temperature [K]	Not to be mistaken with the wall temperature, this is the gas temperature in the vessel as measured by the RTD and acquired by the cRIO RTD module. The user defines this value after consulting *GasEq* solutions and Chapter 4. Once this condition is met, the code will continue.
Purging Time [s]	Knowing the purging-gases flowrate, this was calculated as 100 times the vessel volume.
Rail Pressure [bar]	The user-set pressure value of the common rail at which injection is to take place.
Pump Frequency [Hz]	The frequency of the Pulse Width Modulation (PWM) signal feeding the upstream pass-by valve to the CP3 pump. According to manufacturer this value should be around 1000Hz
Duty Cycle Pump [%]	This is the duty cycle of the PWM signal feeding the CP3 pass-by valve. The valve is normally closed, so 100% should bypass all the fuel to the fuel tank.
Rail Frequency [Hz]	The frequency of the Pulse Width Modulation (PWM) signal feeding the Common Rail pressure control valve. This value should be around 60kHz
Duty Cycle Rail [%]	The duty cycle of the PWM signal feeding the rail pressure control valve. The valve is normally open, so 100% should build up maximum pressure in the rail.
Glowplug time [ms]	The time the Glowplug will stay ON. This depends strongly on the pre-combusted mixture and should in no case exceed 10sec according to glowplug specifications.
Injection Ambient Pressure at start of injection [bar]	The user specified value of the pressure of gases in the vessel at which it is required that injection will take place. A 5 point running average was proved empirically and by frequency response calculations to be sufficient to cut down unwanted noise.
RTD time [s]	The duration for which the temperature acquisition from the RTD will be logged. Logging initiates at pressing the Glowplug “ON” button. This value should be of the order of 5sec. Logging will stop if “shut down” is called.
Number of memory elements	The size of buffer used for Direct Memory Access between FPGA and Real Time controller. This value can vary between 400 and 10000. National Instruments recommends a value of around 1000 elements. The Read FIFO method on the Real Time controller returns **data** only when the **Number of Elements** is available.
DMA Cycles	The number of cycles that the RTc will read the FIFO DMA at a period of 10msec. Empirically optimised value for this field is 100 cycles.
Count [FPGA ticks]	The FPGA clock is running at 40MHz, this value controls the sampling rate of the Kistler preamplifier connected to the Kistler pressure transducer. The maximum sampling value of the sensor is 571 processor ticks, each corresponding to 25ns.
Start	After executing the RTc VI, the user can alter the values of the control and then press start to run the flowchart of Figure 25.
Panic Stop	Once this button is pressed the shut-down procedure is initiated.

Stop Kistler	This stops the pressure logging from the Kistler pressure transducer. However the software is not terminated.
Manual Override	It is not recommended for the user to manually override the software. However if parts of the software need to be tested, then the user will have to restart the software and press this control before pressing Start.
Override Battery	Overrides the battery voltage check
Override Inj Pres	If “true” the cRIO will trigger the injector immediately after the glowplug, without waiting for the desired pressure in the chamber to be reached. Recommended only for tests with the glowplug unplugged.
Override Pressure	If “true” will override the pressure watchdog routine, not recommended.
OverrideTemperature	If “true” will override the temperature watchdog routine, not recommended.
Override Th Stresses	If “true” will override the temperature watchdog routine, not recommended.
OverrideRail Pressure	Overrides the rail pressure check
Fan OK MFC VI	The cRIO will wait for the user to visually check that the fan is rotating, then execute the MFC VI, and then press this button to proceed.

Table 9 List of Controls used in control software (NI cRIO RTC and FPGA)

Indicator Name	Brief Description
Battery Voltage	A resistance bridge is used to decrease the battery voltage by 10 times connected to the cRIO to protect the Analogue Input module from high voltage. Expected values should be between 0 and 1.3V.
Initial Ambient Temperature [K]	The ambient temperature of the vessel before pre-ignition
Rail Pressure [bar]	A pressure sensor is mounted on the Common Rail, powered by the purpose built common rail control box. The output of the sensor was fed, through the common rail control box, to the Analogue Input of the cRIO. Calibration curve was provided by Bosch GmbH. Expected values, when the sensor is powered, lie between 0.45 and 5 Volts or 0 to 2000bar.
Current Pressure	This indicates the current pressure in the vessel. Note that, due to communication between FPGA, RT-controller and PC, there is an insignificant lag. Critical pressure-triggered operations happen on the FPGA in real time without user intervention.
Elements Remaining	The Elements Remaining output contains the number of elements remaining in the host memory part of the DMA FIFO (RTc). The Write method on the FPGA returns Empty Elements Remaining when the data is written. This output should be greater than zero.
Overpressure	If the vessel pressure exceeds maximum allowed pressure, the shut-down procedure will be initiated and this indicator will light up. This operation, as the rest of the watch-dog routines are executed at 40MHz.
Over Heat	If the wall temperature exceeds the user set maximum allowed temperature, the shut-down procedure will be initiated and this indicator will light up. The wall temperature is measured by four J type thermocouples connected to the thermocouple module of the cRIO.
Thermal Stresses	If the wall-temperature readings of the four thermocouples vary between themselves by more than 5%, the shut-down procedure will be initiated to secure the vessel from thermal stresses.
Panic Stop	This panic stop indicator is on the VI front panel and will indicate the initiation of the shutdown routine.
Hardware Panic Stop	For safety reasons a manually operated panic stop button is located next to the Hartridge panic stop button. If this button is pressed a 100Ohm resistance is isolated from the RTD module of the cRIO, so the FPGA detects an open circuit and initiates the shut-down procedure.
Shut down	If the shut-down procedure is called for any reason, then this output will become “true”.
RTD	This indicates data-logging from the RTD

Kistler	When this indicator is “ON”, data is being logged from the Kistler pressure transducer
Armed	This indicator will light up after the user has pressed the glowplug button and pressure has exceeded the injection pressure.
Glowplug	Indicates that the glowplug is “ON”
Injection pulse	Indicates that a pulse is trigerring the injector. It should be “ON” just for an instant.
Error out	This will return any error in the data-logging process
T initial OK	Indicates that gas temperature has reached the desired initial temperature
Rail Pressure OK	Indicates that the common rail pressure has reached the desired value

Table 10 List of indicators used in control software (NI cRIO RTC and FPGA)

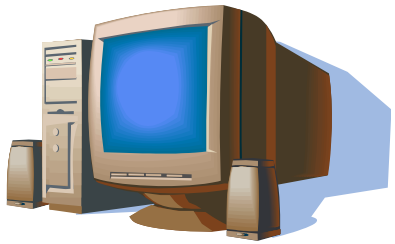

Figure 1.7 NI cRIO-9014 Real-Time Controller

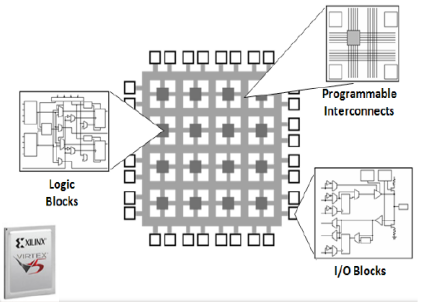

Figure 6.2. An FPGA is composed of configurable logic and I/O blocks tied together with programmable interconnects.

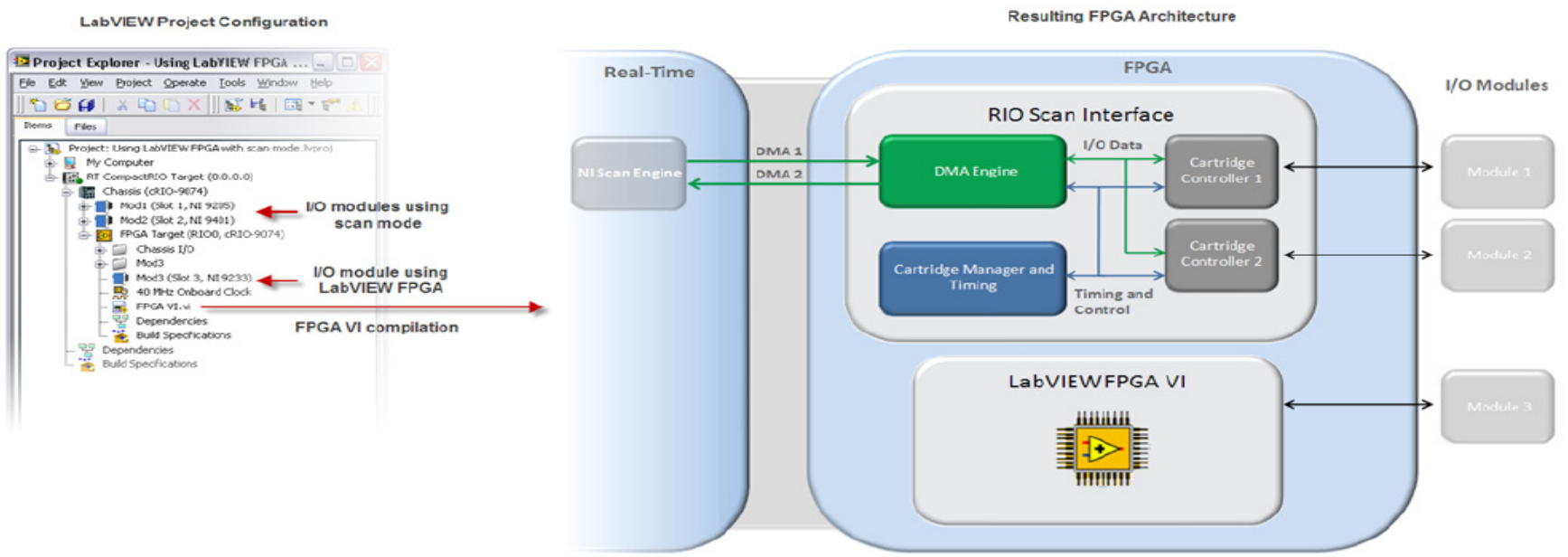

Figure 6.1. You can supplement the capabilities of the scan mode with custom LabVIEW FPGA code.

Figure 28 Control electronics and software architecture, compilation from (Corporation, 2009)

4. Isochoric combustion

4.1 Introduction

The previous chapter described the design and control of the constant volume vessel. This chapter will present the pre-ignition technique used to create a high-pressure and high-temperature environment in the vessel. An initial computer model, assuming perfect combustion, will provide results on post-combustion conditions. Then a second computer model will investigate the effect of chemical dissociation by solving for the minimization of Gibbs energy and will be compared to the former one. At the end of the chapter, measurements with a High-Speed Schlieren technique and a dual pressure transducer method will validate the combustion conditions inside the vessel.

4.2 Chemical heating

The chemical heating technique is based on the isochoric combustion of a mixture of gases that increases the temperature and pressure in that volume. By carefully selecting the composition of the combustible mixture, the composition of the final mixture after pre-ignition can be controlled. Usually, it is desired to have a post-combustion high-pressure-temperature environment with composition similar to atmospheric air or EGR (Exhaust Gas Recirculation) atmosphere in the vessel. So, the flammable mixture usually consists of Hydrogen and a Hydrocarbon. Hydrogen is added, to assist with the ignitability of the pre-ignition mixture and to simulate the water present in the engine cylinder as a result of exhaust gas recirculation.

Most researchers, Table 8, have combustion product gases forming a mixture of CO_2, H_2O, O_2 and N_2. However, for the purposes of this study oxygen is not wanted in the final mixture, as it would cause ignition of the injected liquid fuel and will strongly quench the Laser Induced Fluorescence (LIF) signal for fuel vapour concentration measurements, Chapter 5. H_2O, CO_2 and N_2 do not cause quenching of the LIF signal. So the pre-ignition-mixture has to be

slightly rich, but not too rich as to form soot which would stick on the windows and prevent good quality imaging.

Apart from the final composition, the combustible gas mixture needs to be selected so that the target temperature and pressure are met. Also, the post-combustion mixture needs to have thermal conductivity and heat capacity close to those found in typical diesel engine conditions during fuel injection, Appendix 2, since these parameters affect the fuel evaporation, as discussed in Chapter 2.

So the amount of fuel used for pre-ignition is perhaps the most important parameter to keep the post-ignition environment (pressure, temperature, mass density, composition, heat capacity and heat conductivity) as constant as possible from experiment-to-experiment. For this purpose, Bronkhorst mass-flow-controllers were used. Their working principle is the observation of the temperature of a very thin metal cable heated by constant electrical current and being cooled by the flow. Their accuracy is of the order of 1 per-cent of the total mass flow for steady flow operation.

4.3 Perfect-combustion chemical model of the pre-ignition

A reaction of a general hydrocarbon C_aH_b, Hydrogen, Oxygen and Nitrogen was considered to take place in the vessel. The number of moles of each abovementioned molecule is denoted as X_i.

The ratio of Hydrogen moles to the hydrocarbon moles is written as A, where:

$$A \equiv \frac{X_{H_2}}{X_{C_aH_b}}$$

Any potential dissociation of the reaction is ignored in this section, so the only products formed are CO_2, H_2O and N_2. In Section 4.4, the assumption of perfect combustion will be

investigated. Perfect combustion implies that the Hydrogen and hydrocarbon fuel are fully burnt, without excess of Oxygen. So, in order to have conservation of molecules it is:

$$X_{C_aH_b}C_aH_b + X_{H_2}H_2 + X_{O_2}O_2 + X_{N_2}N_2 \rightarrow X_{CO_2}CO_2 + X_{H_2O}H_2O + X_{N_2}N_2$$

And

$$X_{CO_2} = aX_{C_aH_b}$$

$$X_{H_2O} = \frac{b}{2}X_{C_aH_b} + X_{H_2}$$

$$X_{O_2} = \left[\left(a + \frac{b}{4}\right) + \frac{A}{2}\right]X_{C_aH_b}$$

Assuming ideal gases, gas density gasD in g/L or Kg/m^3, and n number of moles in the vessel before the ignition, it can be shown that:

$$X_{C_aH_b} = \frac{gasD - 28n}{(16a + 2b - 28) - 24A}$$

$$X_{H_2} = AX_{C_aH_b}$$

$$X_{O_2} = \left[\left(a + \frac{b}{4}\right) + \frac{A}{2}\right]X_{C_aH_b}$$

$$X_{N_2} = n - \left[\left(a + \frac{b}{4} + 1\right) + \frac{3A}{2}\right]X_{C_aH_b}$$

Where

$$n = \frac{P_{init}V}{RT_{init}}$$

This is because the number of moles n of the initial mixture in the vessel is dictated by the equation of state, where P_{init} is the initial pressure in the vessel, T_{init} the initial temperature, V the volume of the vessel and R the ideal gas constant.

From the above equations the concentration of gases in the vessel was calculated using a custom made C++ code.

In order to calculate the pressure and temperature conditions in the vessel after pre-ignition, the following algorithm was followed.

From the first law of thermodynamics for adiabatic, isochoric combustion:

$$U_{reac}(T_{init}, P_{init}) = U_{prod}(T_{ad}, P_f)$$

$$H_{reac} - H_{prod} - V(P_{init} - P_f) = 0$$

Where H is the enthalpy, U the internal energy of the system, P_f the final pressure of the system and T_{ad} the final adiabatic temperature.

Applying the ideal-gas law to eliminate the V term:

$$P_{init}V = \sum_{i=reac} N_i R T_{init} = N_{reac} R T_{init}$$

$$P_f V = \sum_{i=prod} N_i R T_{init} = N_{prod} R T_{ad}$$

Thus:

$$H_{reac} - H_{prod} - R(N_{reac}T_{init} - N_{prod}T_{ad}) = 0$$

Where

$$H_{reac} = \sum_{i=reac} N_i \overline{h_\iota} = \sum_{i=reac} N_i \left(\overline{h^o_{f,\iota}} + \overline{c_{p,\iota}}(T_{init} - 298)\right)$$

and

$$H_{prod} = \sum_{i=prod} N_i \overline{h_\iota} = \sum_{i=prod} N_i \left(\overline{h^o_{f,\iota}} + \overline{c_{p,\iota}}(T_{ad} - 298)\right)$$

Where N_{init} and N_f are the number of moles before and after the combustion. H_{reac} and H_{prod} is the enthalpy of the reactants and products respectively. The enthalpy of the molecules in the pre and post combustion mixtures, at the equivalent temperature, is denoted as $\overline{h_i}$. The formation enthalpy of the molecule i at standard conditions is $\overline{h^o_{f,i}}$ and heat capacity, which is a function of temperature is denoted as $\overline{c_{p,i}}$.

According to the National Institute of Standards and Technology (NIST) tables, the heat capacity $\overline{c_{p,i}}$ of each molecule can be considered solely a function of temperature, as the influence of pressure on its value is minor, so $\overline{c_{p,i}} = \overline{c_{p,i}}(T_{ad})$.

Solving with iterations the above equation, T_{ad} is calculated. The final pressure in the vessel after combustion, ignoring heat loses, is:

$$P_f = \frac{T_{ad}}{T_{in}} \frac{N_f}{N_{init}} P_{init}$$

4.3.1 Pressure and Temperature results of the perfect-combustion chemical model

The plots in Figure 29 show the post-combustion temperature and pressure in the vessel, for a mixture of Acetylene, Hydrogen, Oxygen and Nitrogen predicted by the model described in the previous section. Acetylene has been used extensively in the literature (Klein-Douwel et al., 2007, Bruneaux, 2007) because of the high ratio of Carbon to Hydrogen, which translates to a low Water to Carbon Dioxide ratio in the post combustion mixture. Appendix 2 and this section later on, will show why keeping in the vessel a low Water to Carbon Dioxide ratio simulates more accurately a Diesel engine with EGR.

On the horizontal axes of the plots in Figure 29, the initial vessel pressure is plotted. This variable is important because, in conjunction with the initial pre-ignition temperature, it dictates the total mass in the vessel. As will be shown from measurements in the vessel, in Figure 42, the initial pre-ignition temperature was almost always equal to the room temperature. Thus, the initial vessel pressure dictates the gas density in the vessel. Assuming that there is no mass escaping the vessel (Section 4.4.2), and because of mass conservation, the

gas density does not change after ignition. As described in chapter 2, gas density is an important parameter for spray characteristics.

In the previous section the ratio of Hydrogen moles to the moles of hydrocarbon was introduced as the parameter A, where $A \equiv \frac{X_{H_2}}{X_{C_aH_b}}$. A given initial pressure and temperature, assuming ideal gas law, corresponds to a specific number of gas moles in the vessel. As mentioned in the previous section, it was assumed that the Oxygen present in the mixture is as much required for the Hydrogen and hydrocarbon to get fully oxidized. Since the rest of the mixture consists of Nitrogen, the parameter A is of great importance to show how many times more moles of Hydrogen, than moles of Hydrocarbon, exist in the mixture. The parameter A is also used to determine in the post-combustion composition which is the ratio of Water to Carbon Dioxide. It can be easily shown that: $\frac{X_{H_2O}}{X_{CO_2}} = \frac{b+2A}{2a}$, where a and b are the number of Carbon and Hydrogen atoms, respectively, in the Hydrocarbon molecule C_aH_b. The water to Carbon Dioxide ratio is indicative of the Exhaust Gas Recirculation (EGR) of an engine. A typical modern Diesel engine has up to 11% Carbon Dioxide and 7% combustion produced Water in the cylinder air (Appendix 2). On the plots of Figure 29, the post-combustion pressure and temperature is plotted with the value of the parameter A used as a constant for each plot.

The parameter A describes how many times more moles of Hydrogen, than Hydrocarbon moles, exist in the pre-ignition mixture. However, it does not implicitly quantify the actual number of moles, neither of the Hydrogen nor of the Hydrocarbon. For a given initial pressure and parameter A, the mixture molecular weight has a unique solution as to the number of Hydrogen and Hydrocarbon moles (see Appendix 5). For this reason, on the vertical axes of the plots of Figure 29, the Mixture Molecular Weight is plotted. On the left-hand-side column of Figure 29, the maximum pressure appears and the adiabatic temperature on the right-hand-side column. From top to bottom rows, the parameter A has been varied and the considered values are 0.2, 0.5, 1, 1.5 and 8.

The black squares represent the points that the custom-made C++ code solved, the rest of the contour area was triangulated based on these calculations using a triangle keep factor of

0.25. Triangles of factor 0 are three collinear points, while triangles of factor 0.5 are equilateral. Any triangles with a factor lower than 0.25 were dismissed from the plot. So, any triangles with an angle smaller than 30 degrees were ignored.

It can be easily observed that as the mixture molecular weight increases, the adiabatic temperature and pressure increases. This is because more heavy Oxygen is present in the pre-ignition gases.

As the parameter A increases, for a specific initial pressure value, there are more black squares on the plots. This is because more combinations of Hydrogen and Acetylene can “fit” in the initial conditions. Hydrogen needs less Oxygen to get ignited. It has to be noted that a mole of Hydrogen requires less Oxygen than a mole of Acetylene, that is why as the parameter A increases, the plots move to lower molecular weights.

As the parameter A increases, higher pressure and temperature are achieved at lower mixture molecular weight. This is because as parameter A increases, there is more Hydrogen in the pre-ignition mixture. The lower calorific value of Hydrogen has been reported to be 121,000 kJ/mole and much less for Acetylene at 1,300 kJ/mole.

For a given initial pressure, as the mixture molecular weight increases, the post-combustion pressure and temperature increases too. It can be observed that the maximum mixture molecular weight is less than 30. This is because Oxygen is the heaviest molecule in the mixture with molecular weight of 32, Nitrogen follows with 28, Acetylene with 26 and Hydrogen with 2.

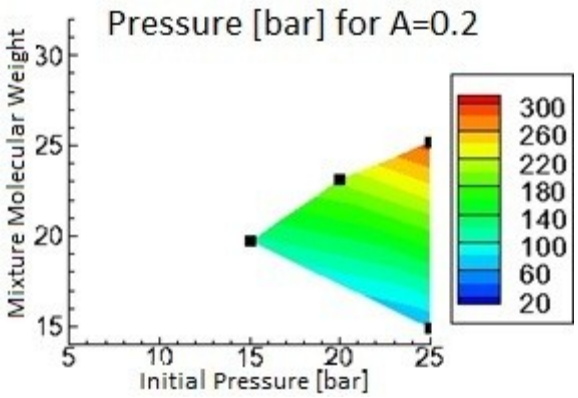
Pressure [bar] for A=0.2
Mixture Molecular Weight
Initial Pressure [bar]
300
260
220
180
140
100
60
20

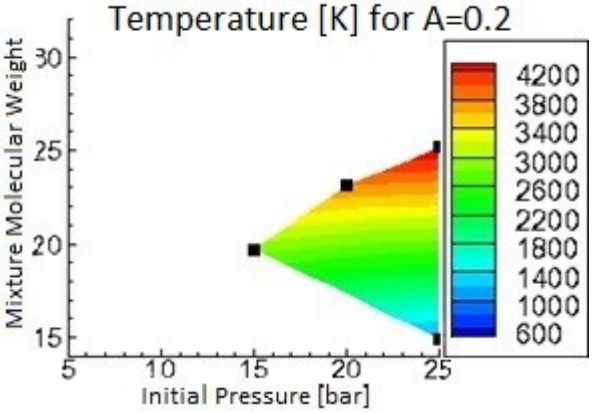
Temperature [K] for A=0.2
Mixture Molecular Weight
Initial Pressure [bar]
4200
3800
3400
3000
2600
2200
1800
1400
1000
600

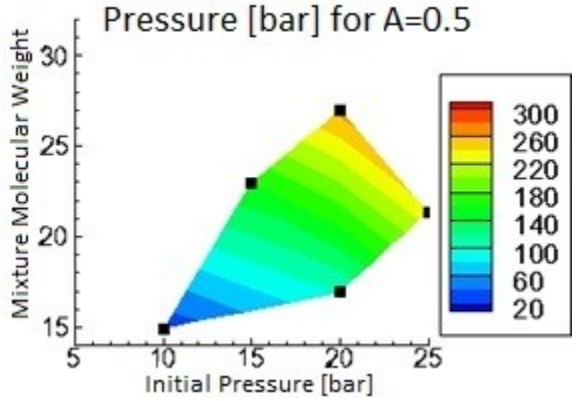
Pressure [bar] for A=0.5
Mixture Molecular Weight
Initial Pressure [bar]
300
260
220
180
140
100
60
20

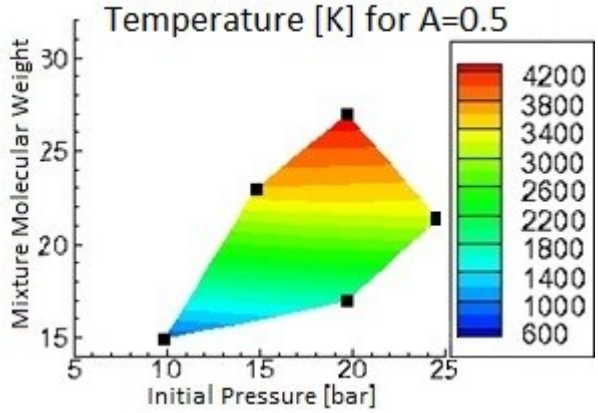
Temperature [K] for A=0.5
Mixture Molecular Weight
Initial Pressure [bar]
4200
3800
3400
3000
2600
2200
1800
1400
1000
600

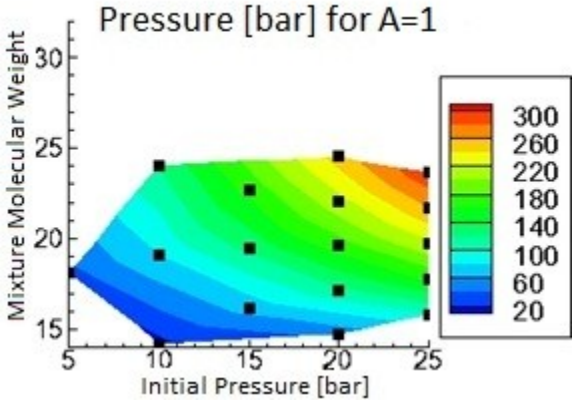
Pressure [bar] for A=1
Mixture Molecular Weight
Initial Pressure [bar]
300
260
220
180
140
100
60
20

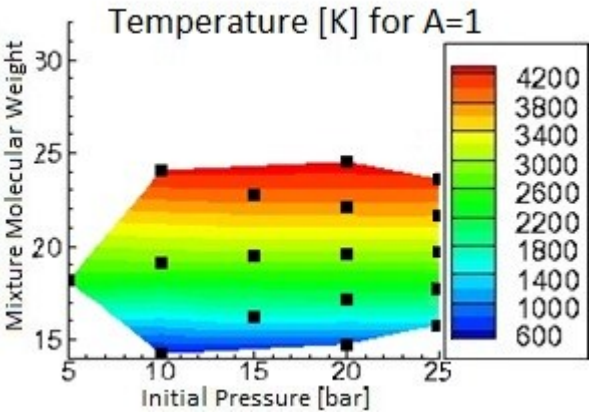
Temperature [K] for A=1
Mixture Molecular Weight
Initial Pressure [bar]
4200
3800
3400
3000
2600
2200
1800
1400
1000
600

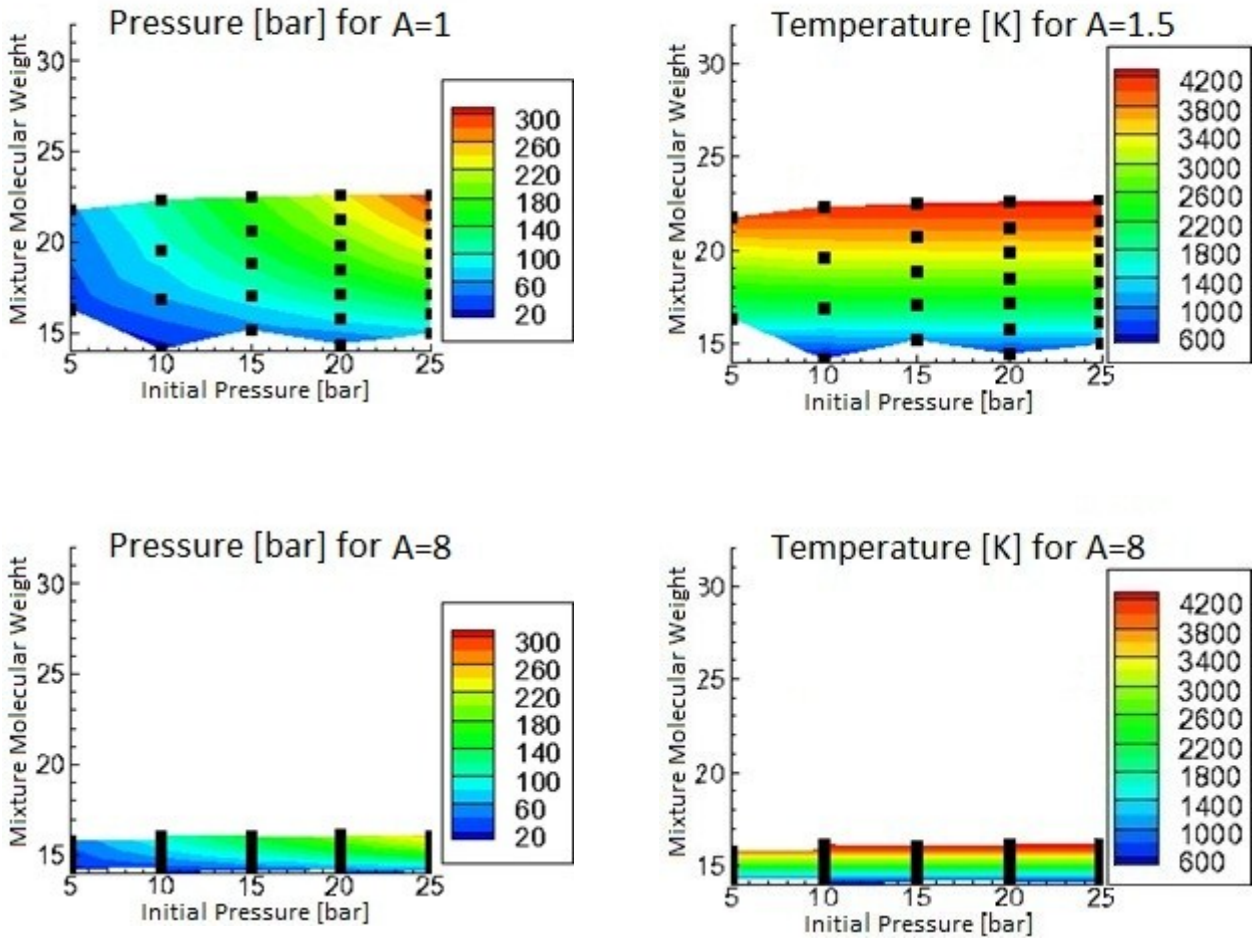

Figure 29 The left column presents the calculated post-combustion pressure and the right column the calculated adiabatic temperature of the post-combustion gases as a function of the initial pressure and mixture molecular weight. These graphs act as an operating map of the vessel.

The vessel used in this work had a maximum operating pressure of 30 bar. It can be easily observed on the left hand side column of Figure 29 that the area not exceeding this pressure value is very small. Also a small increase of the pre-ignition mixture molecular weight or of the initial pressure, results in an unproportional increase of the post-combustion pressure, which, in most of the cases, creates post-combustion-pressure exceeding the maximum vessel operational pressure. For this reason, it was necessary to investigate pre-ignition mixtures of lower initial pressure, which would not create unsafe post-combustion pressure. The plots of Figure 30 have the same layout as Figure 29, with the exception that the plotted initial pressure has values from 1 to 5 bar. The post-combustion pressure and temperature are now within safe operating regions. It is therefore clear that even with an initial pressure of 5 bar, the pressure

and temperature conditions found at the top-dead position of an engine cylinder can be recreated in a constant volume vessel. The next section will investigate the heat conductivity and heat capacity of the post-combustion mixture, properties important for the evaporation of the liquid fuel.

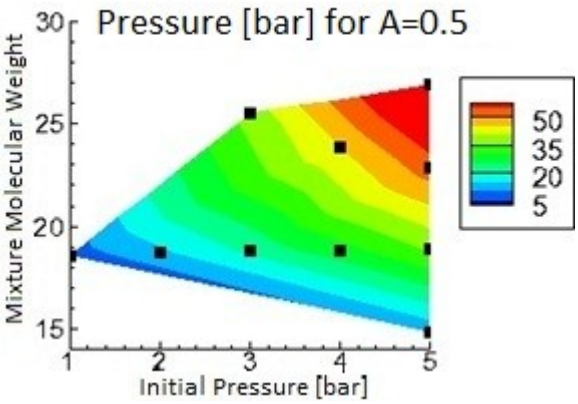

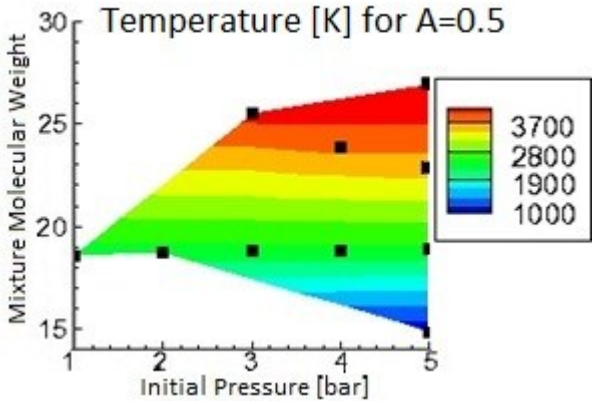

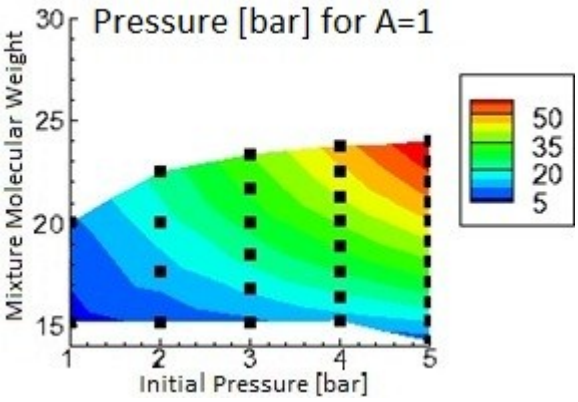

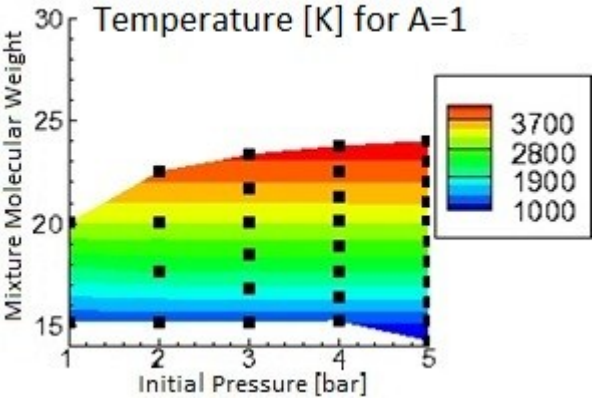

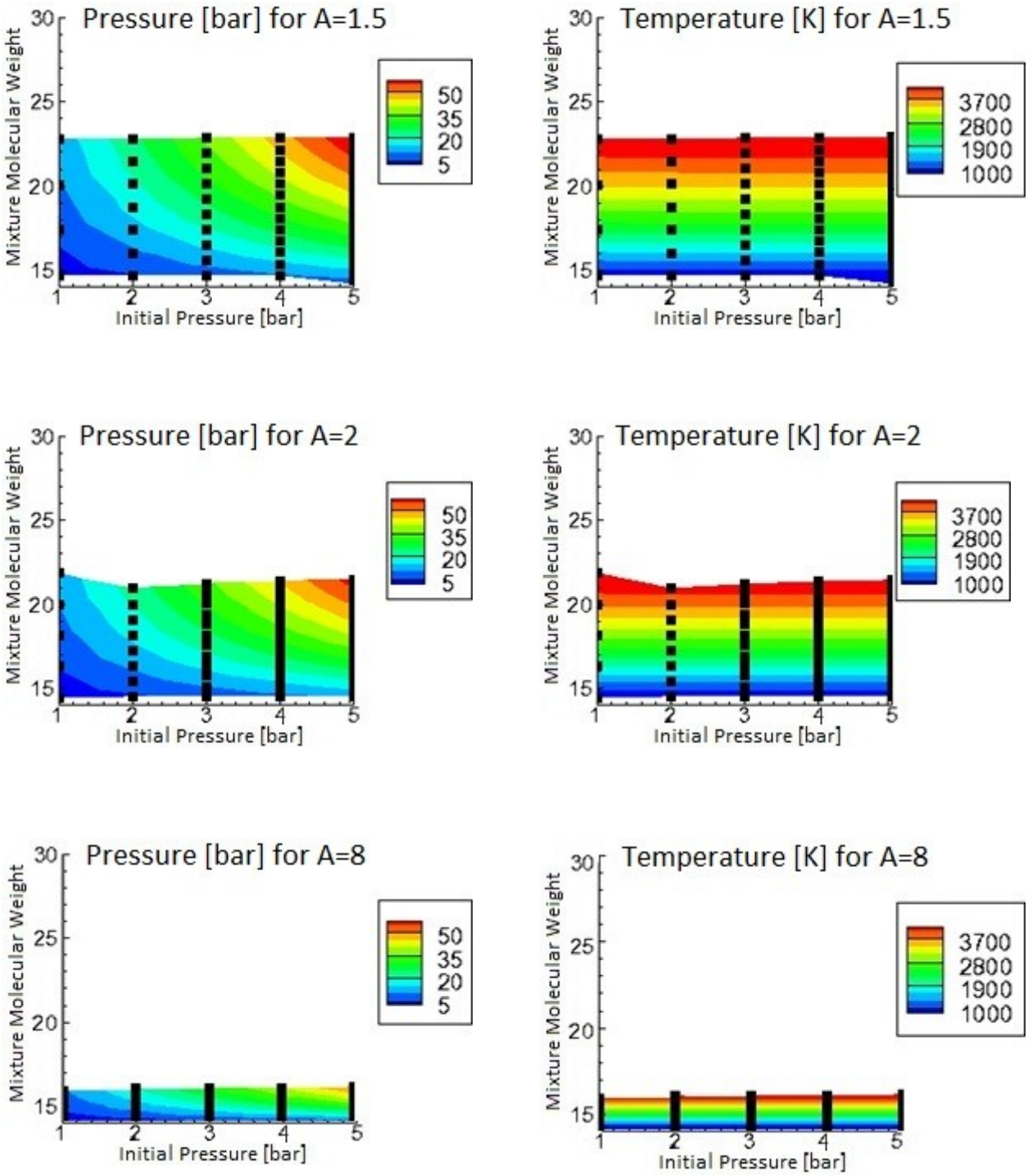

Figure 30 The left column presents the calculated post-combustion pressure and the right column the calculated adiabatic temperature of the post-combustion gases as a function of the initial pressure and mixture molecular weight. These graphs act as an operating map of the vessel.

4.3.2 Heat capacity

By definition the heat capacity of a gas at constant pressure is the partial derivative of enthalpy by temperature, for constant pressure:

$$C_p = \left(\frac{\partial h}{\partial T}\right)_p$$

For a mixture of gases with nSp number of species, the mixture enthalpy h is calculated as the molar concentration weighted average y_i of the enthalpies h_i of the components, or:

$$h = \sum_{i}^{nSp} (y_i h_i)$$

So the mixture heat capacity will be:

$$C_p = \sum_{i=1}^{nSp} (y_i C_{p,i})$$

In this section, it was assumed that the combustion was perfect, which means that the products were only CO_2, H_2O and N_2.

At top dead center of the piston, air heat capacity has a value of approximately 33 J/(mole K), as calculated in Appendix 2. This corresponds to dark blue of the colour map of Figure 31. As in the previous section, the horizontal axes represent the initial pressure of the pre-ignition mixture. The value of heat capacity seems to be insensitive to the increase of initial pressure, this is because from the definition of heat capacity, the mass of the gas is not taken into account. An easy way to understand this is by observing the units of heat capacity, i.e. J/(mole K) or J/(kg K), which are expressed per mole or per kilogram of the gas.

On the vertical axes of the plots of Figure 31, the molecular weight of the mixture is plotted. As the molecular weight increases, the heat capacity of the mixture increases too. But larger contribution in increasing the heat capacity comes from the increase of parameter A, due to the influence of vapour water, which has very high value of heat capacity as shown in Table 11.

Species (at STP)	Heat capacity [J/(mole*K)]	Thermal conductivity [W/(m*K)]
Air	29.19	0.025
Nitrogen	29.12	0.02583
Carbon Dioxide	36.94	0.0168
Water vapour at 100°C, 1 atm	75.33	0.02479

Table 11 Heat capacity and thermal conductivity of some combustion products

4.3.3 Thermal conductivity

The kinetic theory of gases allows for the accurate calculation of thermal conductivity of gases (Hirschfelder et al., 1964). The thermal conductivity of a single component gas can be accounted for the transport of translational energy λ' and the internal energy λ'', so:

$$\lambda = \lambda' + \lambda''$$

The first term on the right-hand-side of this definition is the translational contribution and can be calculated by:

$$\lambda' = \frac{15}{4}\frac{R}{M}\mu$$

Where R is the ideal gas constant, M the molecular weight and the viscosity μ of a pure component is given by:

$$\mu = 26.693\frac{\sqrt{MT}}{\sigma^2\Omega}$$

The viscosity units are in poise or $\frac{g}{cm \cdot s}$ and σ is the molecular diameter in angstroms and can be found on Table 12. Omega Ω is a dimensionless integral dependent on the force interaction during a collision, which is of the order of unity. For Lennard-Jones interaction (Hattikudur and Thodos, 1970), the Ω integral can be calculated as:

$$\Omega = 1.155\left(T^*\right)^{-0.1462} + 0.3945e^{-0.6672T^*} + 2.05e^{-2.168T^*}$$

Where T^* is a dimensionless temperature defined as:

$$T^* = \frac{kT}{\varepsilon}$$

k/ε can be acquired from Table 12 for the species of interest in this work. k is the Boltzmann's constant and ε is the maximum energy of attraction during the collision.

The Internal contribution can be approximated by:

$$\lambda'' = 0.88\left(\frac{2}{5}\frac{C_p}{R} - 1\right)\lambda'$$

Like-wise, for mixtures of gases, the heat conductivity can be calculated as a sum of the transport of translational energy and internal energy. However, in this work, the mixtures studied are not frozen, they are reacting mixtures, where the composition changes with pressure and temperature. There is a contribution to the thermal conductivity caused by the dissociation and recombination of molecules. So, as molecules fluctuate back and forth in the temperature gradient, they change the heat flux. This effect is accounted by this practical approximation:

$$\lambda_{mix} \approx \left(\lambda_{mix}' + \lambda_{mix}''\right)\frac{C_p}{C_{p,f}}$$

Where C_p is the equilibrium specific heat calculated in Section 4.3.2 and $C_{p,f}$ is the frozen specific heat, calculated as:

$$C_{p,f} = \sum_{i=1}^{nSp}\left(y_i C_{p,i}\right)$$

Similarly to the single component gas, the mixture translational contribution to the thermal conductivity is:

$$\lambda_{mix}{}' = \sum_i \frac{\lambda_i'}{1 + \sum_{\substack{j=1 \\ j \neq i}} \Psi_{ij} \frac{y_j}{y_i}}$$

Where:

$$\lambda_i' = \frac{15}{4} \frac{R}{M} \mu$$

And the coefficient is:

$$\Psi ij = \Phi ij \left[1 + 2.41 \frac{(M_i - M_j)(M_i - 0.142 M_j)}{(M_i - M_j)^2} \right]$$

Where:

$$\Phi ij = \frac{\left[1 + \left(\frac{\mu_i}{\mu_j} \right)^{1/2} \left(\frac{M_j}{M_i} \right)^{1/4} \right]^2}{2\sqrt{2} \left(1 + \frac{M_i}{M_j} \right)^{1/2}}$$

The mixture internal contribution to the heat conductivity is:

$$\lambda_{mix}{}'' = \sum_i \frac{\lambda_i''}{1 + \sum_{\substack{j=1 \\ j \neq i}} \Phi_{ij} \frac{y_j}{y_i}}$$

Where

$$\lambda_i'' = 0.88 \left(\frac{2}{5} \frac{C_p}{R} - 1 \right) \lambda_i'$$

species i	Molecular diameter $\sigma[\text{Å}]$	k/ε [K]
CO_2	3.941	195.2
H_2O	2.641	809.1
N_2	3.798	71.4
O_2	3.467	106.7
CO	3.690	91.7
H_2	2.827	59.7
H	2.708	37.0
O	3.050	106.7
OH	3.147	79.8
NO	3.492	116.7

Table 12 Collision parameters of the species accounted for in this work

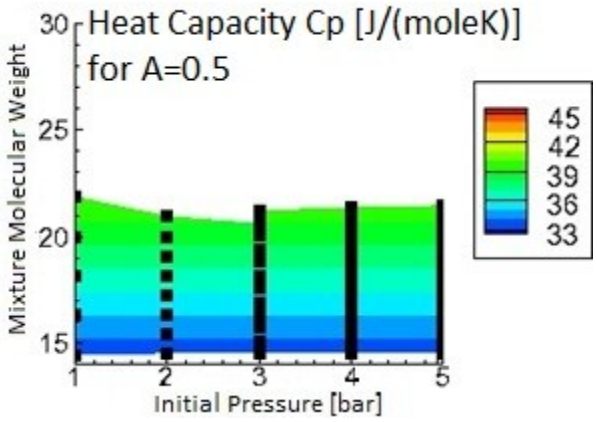

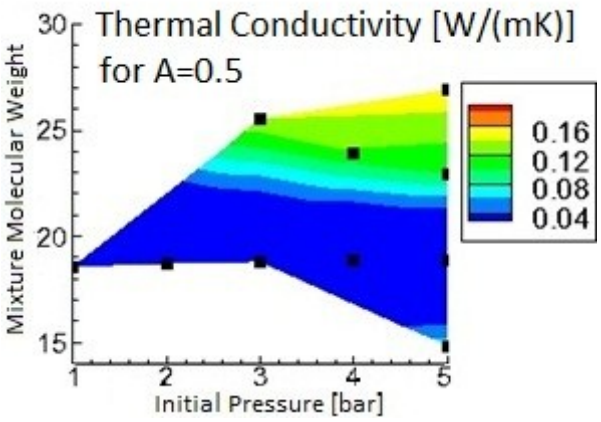

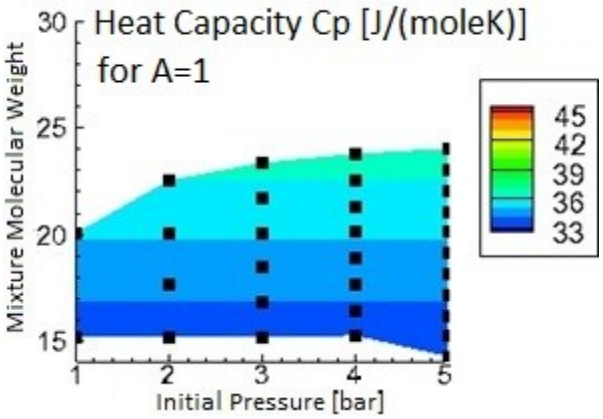
Heat Capacity Cp [J/(moleK)]
for A=1
Mixture Molecular Weight
Initial Pressure [bar]
45
42
39
36
33

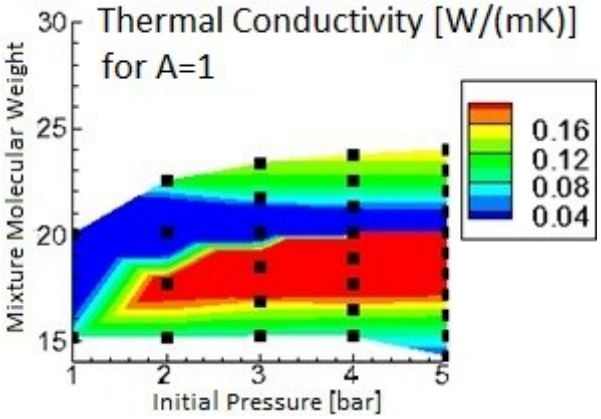
Thermal Conductivity [W/(mK)]
for A=1
Mixture Molecular Weight
Initial Pressure [bar]
0.16
0.12
0.08
0.04

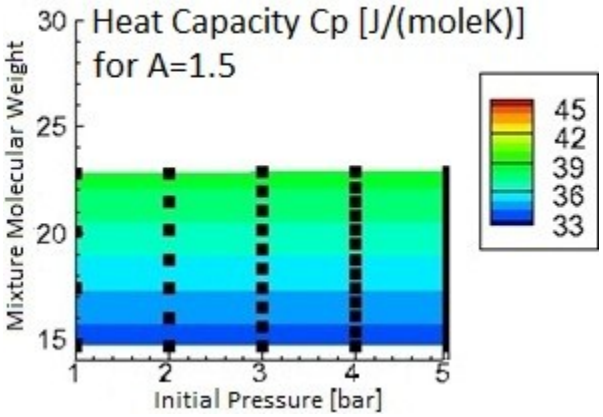
Heat Capacity Cp [J/(moleK)]
for A=1.5
Mixture Molecular Weight
Initial Pressure [bar]
45
42
39
36
33

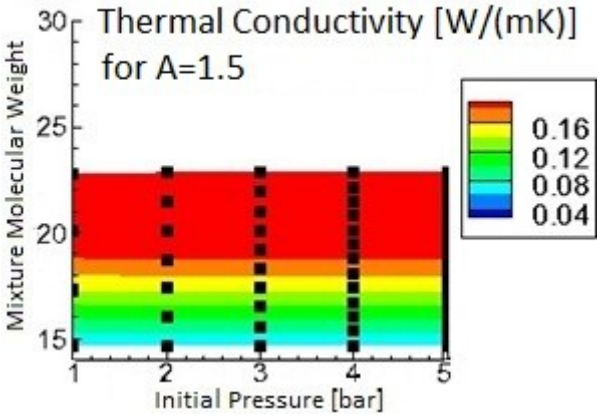
Thermal Conductivity [W/(mK)]
for A=1.5
Mixture Molecular Weight
Initial Pressure [bar]
0.16
0.12
0.08
0.04

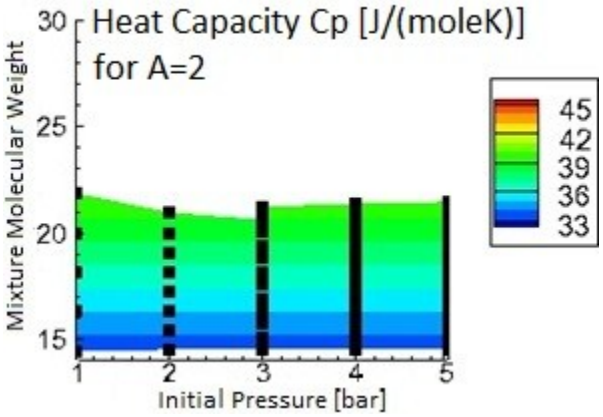
Heat Capacity Cp [J/(moleK)]
for A=2
Mixture Molecular Weight
Initial Pressure [bar]
45
42
39
36
33

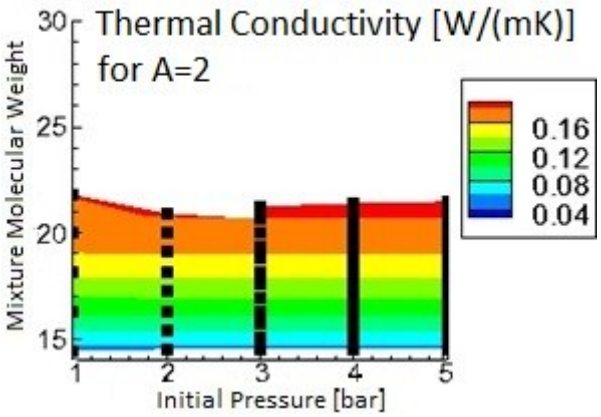
Thermal Conductivity [W/(mK)]
for A=2
Mixture Molecular Weight
Initial Pressure [bar]
0.16
0.12
0.08
0.04

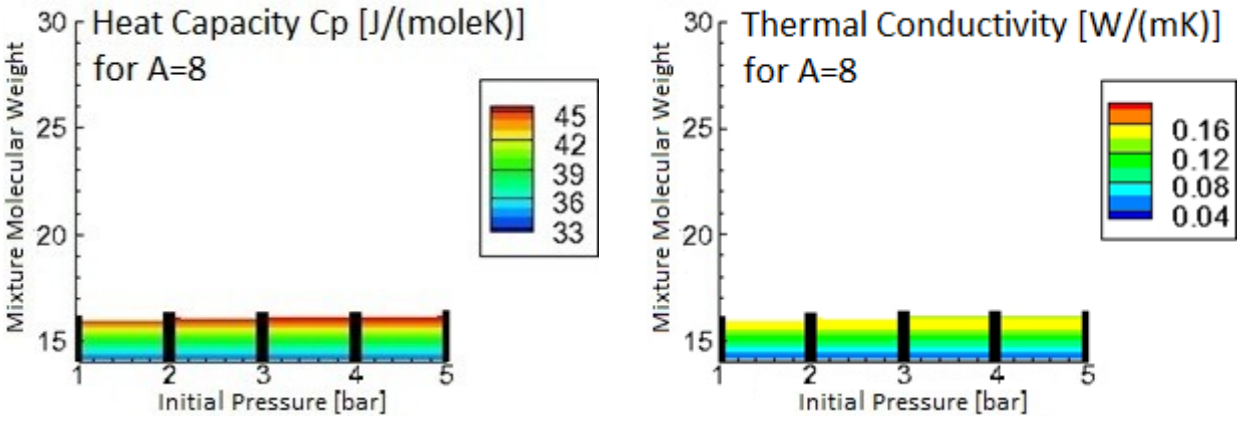

Figure 31 The left column presents the heat capacity and the right column the heat conductivity of the calculated post-combustion gases as a function of the initial pressure and mixture molecular weight. These graphs act as an operating map of the vessel.

The right-hand-side column of Figure 31 presents the thermal conductivity of the products of Acetylene, Hydrogen, Oxygen and Nitrogen conduction. From top to bottom the value of parameter A is increased. It is obvious that as the molecular weight of the reactants increases, the thermal conductivity increases. This is due to the lack of Carbon Dioxide, which has low thermal conductivity as presented in Table 11.

As presented in Appendix 2, typical values of the heat capacity and heat conductivity at the top dead-center of an engine are 33.05 J/(mole K) and $67.2*10^{-3}$ W/(m K) respectively. So engine-like values of heat capacity and heat conductivity can be achieved in the vessel using an Acetylene, Hydrogen, Oxygen and Nitrogen mixture at initial pressure up to 5 bar. Chapter 7 will demonstrate the importance of these two parameters on fuel evaporation. However, as the combustion in the vessel is not necessarily perfect, the next section will study the effect of chemical dissociation on the post-combustion environment in the vessel.

4.4 Chemically dissociative model of the pre-ignition

The previous section calculated the post-combustion pressure and adiabatic temperature based on the assumption of perfect combustion. However, in many engineering applications this assumption is not valid as some fuel/air mixture might remain unburnt.

Additionally, Acetylene is prone to forming soot. Also at high temperature Nitrogen bonds with Oxygen forming Nitric Oxides. It is also known that at elevated pressure and temperature conditions the combustion reaction is not a one way reaction, but behaves more like an equilibrium, in which ionic compounds separate or split into smaller particles, ions, or radicals, usually in a reversible manner (chemical dissociation). Imperfect combustion will result to conditions different to what has been calculated by the perfect combustion model, which in turn will alter the spray characteristics. For these reasons, it is important to investigate how the combustion in the vessel behaves, to this purpose, an extensively used technique of minimization of Helmholz free energy will be applied in the vessel combustion (Gordon and McBride, 1976).

The Helmholz free energy is defined as:

$$A = G - PV$$

Where P [Pascal] is the system pressure, V [m^3] the volume and G the Gibbs free energy defined as:

$$G(P,T) = U + PV - TS$$

Where U [J] is the internal energy, T [K] the temperature and S [J/K] the entropy of the system. On the right hand-side of the Gibbs energy definition, the middle term, which is the product of the system pressure times the Volume represents the work required to give to the system at the final volume V to have a constant pressure P. While the furthest-right term on the right-hand-side of the equation, is the product of Temperature times the Entropy of the system and shows the heat produced in the system. The internal energy U might be thought of as the energy required to create a system in the absence of changes in temperature or volume.

The definition of Gibbs free energy can be rewritten as:

$$G(P,T) = H - TS$$

where: H is the enthalpy of the system [J]. So the change in Gibbs free energy will be: $\Delta G = \Delta H - T\Delta S$. The change in Gibbs free energy, ΔG, in a reaction is a very useful parameter. It can be thought of as the maximum amount of work obtainable from a reaction. If ΔH<0, the reaction is producing heat and is known as exothermic, while if ΔH>0, the reaction is endothermic. In a similar way, for a reaction to have favourable conditions in terms of Entropy change ΔS, it should be ΔS>0, as shown on Table 13. If ΔH<0 and ΔS>0, the change in Gibbs free energy ΔG is lower than zero and the reaction is called spontaneous. While change in Gibbs free energy larger than zero, the reaction is non-spontaneous. The equilibrium constant for the reaction is related to ΔG by the relation: $K = e^{-\frac{\Delta G}{RT}}$. For a reaction to be in equilibrium, it should be $K = 1$. So if ΔG=0, the reaction is in equilibrium.

	Spontaneous ΔG<0	Non-spontaneous ΔG>0
ΔH	Favourable ΔH < 0	Unfavourable ΔH > 0
ΔS	Favourable ΔS > 0	Unfavourable ΔS < 0

Table 13 Map of spontaneous and non-spontaneous conditions of a reaction

The chemical potential μ of a species i is defined by:

$$\mu = \left(\frac{\partial G}{\partial x_i}\right)_{T,P,x_{i\neq j}}$$

Where G is the Gibbs free energy of the species i and x_i is the mole fraction of the species i in the system. If the species i is considered to be an ideal gas, then at pressure P, the chemical potential can be calculated as:

$$\mu = \mu^o + RTln\left(\frac{x_i}{\sum x_i}\right) + RTln\left(\frac{P}{P_o}\right)$$

Where μ^o is the chemical potential of species i at pressure P_o=1atm, $\sum x_i$ is the total number of moles in the system.

The equilibrium number of moles of species i is x_i (i = 1 to *nSp*), where nSp is the number of species accounted for in this analysis. For simplification of the problem, the species considered were N_2, H_2O, CO_2, CO, O_2, OH, H, O, H_2, NO. For a mixture of nSp species, the Helmholtz free energy is:

$$A = G - PV = \sum_{i=1}^{nSp} (\mu_i x_i) - PV$$

So, the Helmholtz Free Energy A of the mixture at pressure P is given by:

$$A = \sum_{i=1}^{nSp} \left(\frac{x_i G_i^o}{RT} + x_i ln\left(\frac{x_i}{\sum x_i}\right) + x_i ln(P) \right) RT - PV$$

where G_i^o is the molar free energy at 1 atmosphere of species i.

At equilibrium A is at a minimum, subject to the constrains imposed by atom conservation:

$$\sum_{i=1}^{nSp} a_{ij} x_i = b_j^o$$

$$b_j \ - b_j^o = 0$$

Where j represents the elements in the reaction, j has values from 1 to nEl, where nEl is the maximum number of elements accounted for in this analysis. The elements considered in this work were C, O, H and N. The number of atoms of element j in the reactants is b_j^o and in the

products b_j . The number of elements j in species i are given by a_{ij}. For each element *j* from 1 to *nEl:*

$$\sum_{i=1}^{nSp} a_{ij}x_i - b_j = 0$$

So the Gibbs energy term $\frac{G}{RT}$ needs to be minimised subject to the atom conservation constraints. To solve this problem, the Lagrangian multipliers λ_j *where* (*j*=1 to *nEl*) were introduced and F was defined as:

$$F = \sum_{i=1}^{nSp}\left(x_i G_i^o + x_i ln\left(\frac{x_i}{\sum x_i}\right)RT + x_i ln(P)RT - PV\right) - \sum_{j=1}^{nEl}\lambda_j \sum_{i=1}^{nSp}\left(a_{ij}x_i - b_j\right)$$

The required solution is when *F* is a minimum or $\delta F = 0$ for all species i from 1 to *nSp*. So:

$$\delta F = \sum_{i=1}^{nSp}\left(G_i^o + ln\left(\frac{x_i}{\sum x_i}\right)RT + ln(P)RT - \sum_{j=1}^{nEl}\left(\lambda_j a_{ij}\right)\right)\delta x_i - \sum_{i=1}^{nSp}\left(b_j - b_j^o\right)\delta\lambda_i$$

Treating δx_i and $\delta\lambda_i$ as independent, it should be:

$$G_i^o + ln\left(\frac{x_i}{\sum x_i}\right)RT + ln(P)RT - \sum_{j=1}^{nEl}\left(\lambda_j a_{ij}\right) = 0$$

and

$$b_j - b_j^o = 0 \xrightarrow{\sum_{i=1}^{nSp} a_{ij}x_i - b_j = 0} b_j = \sum_{i=1}^{nSp} a_{ij}x_i$$

For given temperature and pressure conditions the unknowns of the last two equations are the Lagrangian multipliers λ_j, (where j=1 to nEl), the number of moles of species i x_i,

(where i =1 to nSp) and the total number of moles in the system x. So in total the unknowns are nEl+nSp+1. If the system of the last two equations is expanded, it gives nEl+nSp number of equations, which are one less than the unknowns. The last equation to close the system of equations is $x = \sum_{i=1}^{nSp} x_i$. The equations are non-linear and need to be solved iteratively. In the literature there are many solvers for these equations, like GasEq, ECP, etc. This work was based on Gaseq (Morley, 2005).

The Gibbs energy of a species i at temperature T and pressure 1 atm can be found from the JANAF tables (Chase et al., 1985) as:

$$\frac{G_i^T}{RT} = \frac{(G^o - H_{298}^o)/T}{R} + \frac{\Delta H_{f,298}^o}{RT}$$

Where H_{298}^o and $\Delta H_{f,298}^o$ are respectively the enthalpy and the formation enthalpy of the species i at 298K

4.4.1 Pressure and Temperature results of the chemically dissociative combustion model

As described in the previous section, in the literature the preferred hydrocarbons for similar pre-ignition techniques are C_2H_2 and C_2H_4 because they support flame propagation even in lean mixtures and can be ignited relatively easy (Baert et al., 2009, Verhoeven et al., 1998, Naber and Siebers, 1996, Fujimoto et al., 2005a). In an early study by Oren et al. (1984), Acetylene was preferred over Hydrogen as it minimizes water production, as a result, less heating of the vessel windows was required to prevent condensation of water vapour on the cold windows. Sandia used a Hydrogen-Ethylene mixture of ratio $A \equiv \frac{X_{H_2}}{X_{C_aH_b}} = \frac{4}{1}$, which was later changed to 6 and then 11.4 (Verhoeven et al., 1998). In this section the influence of the Hydrocarbon in the post-combustion conditions will be investigated. In this direction, mixtures of Hydrogen with Acetylene, or Ethane, or Methane will be compared. To match the results of the current section to the experimental conditions and operation, which will be further

discussed in Section 4.5, the initial pressure of the mixture was set at 1 atm and the initial temperature at 350 K.

Figure 32 presents the adiabatic temperature and pressure, of a Hydrogen Acetylene fuel mixture as a function of parameter A, which is the ratio of moles of Hydrogen to Hydrocarbon. The selection of these axes (temperature and pressure on the vertical axes and parameter A on the horizontal), makes the plots easier to be used for vessel control. The user can easily observe the post-combustion conditions that correspond to different pre-ignition conditions. However, as the molecular weight of the pre-combustion mixture is not presented on the graphs, the amount of Nitrogen in the mixture has to be constant for all the points of the graphs. For this reason, the oxidizer used was Air.

The proportional linear relation between the adiabatic temperature and pressure, discussed in section 4.3, can be verified here, as the temperature and pressure curves are almost parallel. It is also observed that increasing the value of parameter A increases the value of adiabatic temperature and pressure, behavior observed in the previous section too.

Figure 33 and Figure 34 present the same information for Hydrogen Methane and Hydrogen Ethane mixtures respectively. Though these mixtures were not used in this work, they have been used in the past. As expected, because Ethane has lower calorific value than acetylene, the post-combustion values of pressure and temperature for the Hydrogen/Ethane mixtures are lower than the Hydrogen/Acetylene mixture.

The Acetylene/Ethane mixture in Figure 35, is the result of an investigation of using a mixture of two hydrocarbons rather than using the traditional mixture of Hydrogen and a hydrocarbon. The advantage of using a two hydrocarbons mixture is that the water vapour content of the post-combustion mixture will be much lower than using a Hydrogen/Hydrocarbon mixture. As the Hydrocarbon with the higher calorific value increases in the mixture, the post-combustion pressure and temperature increases. Even though the values of post-combustion pressure and temperatures are comparable to those produced by a Hydrogen/Hydrocarbon mixture, ingitability problems arise, especially at initial pressure higher than atmospheric.

Clearly and as expected, the Hydrogen/Acetylene mixture produces higher values of adiabatic temperature and pressure in the post combustion mixture than the Hydrogen-Ethane mixture. Last in post combustion temperature and pressure, comes the Hydrogen-Methane mixture. This is verified in Figure 35, where Acetylene was compared to Ethane.

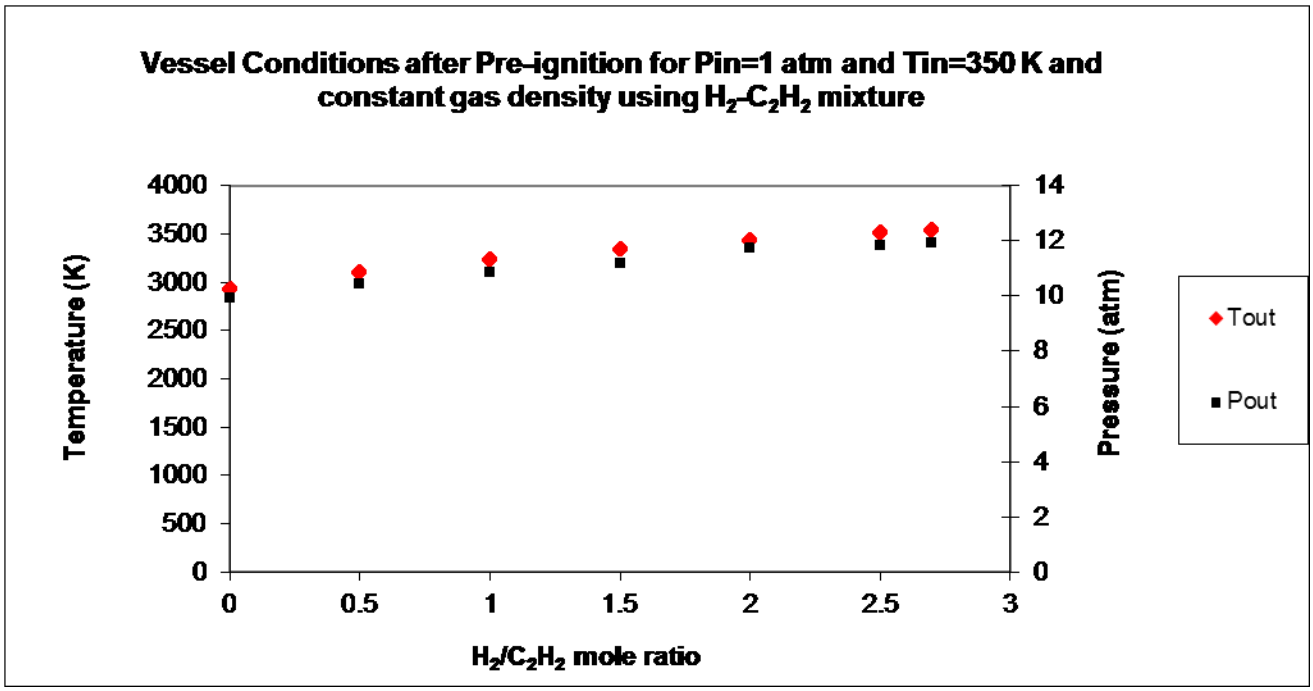

Figure 32 Post-combustion adiabatic temperature and pressure as a function of Hydrogen to Acetylene mole ratio for initial temperature 350 K and initial pressure 1 atm, calculated using the chemically dissociative model

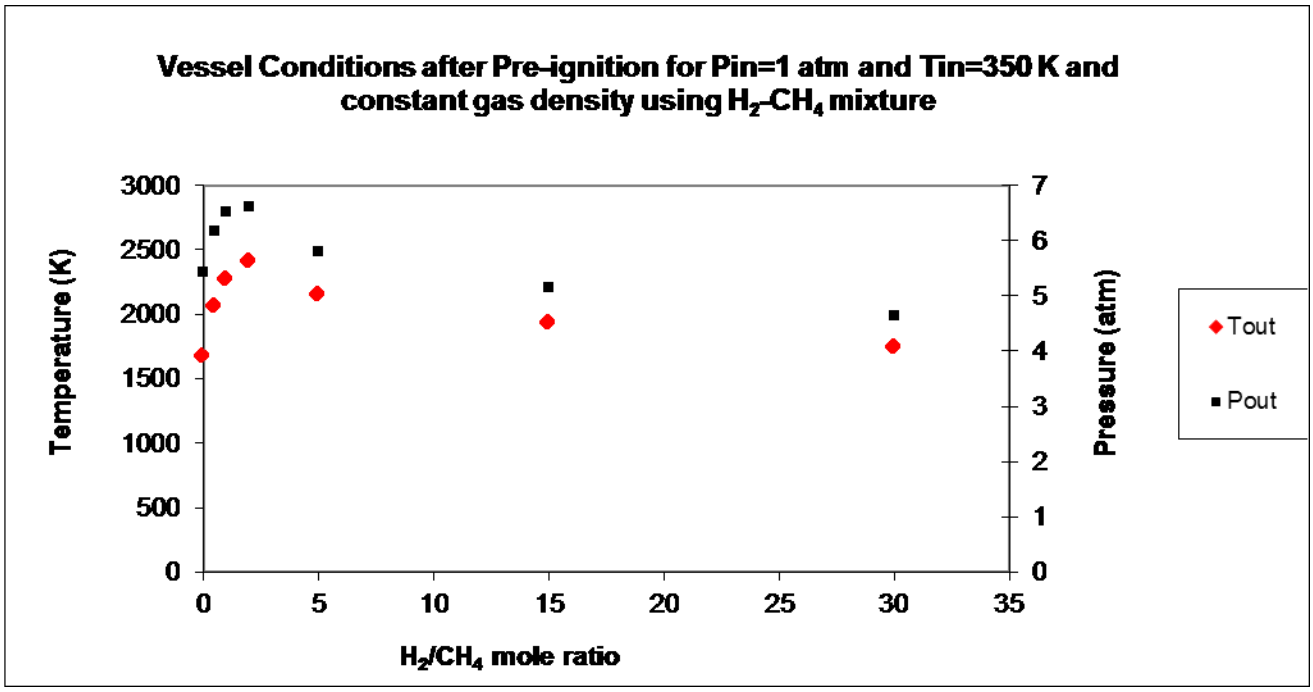

Figure 33 Post-combustion adiabatic temperature and pressure as a function of Hydrogen to Methane mole ratio for initial temperature 350 K and initial pressure 1 atm, calculated using the chemically dissociative model

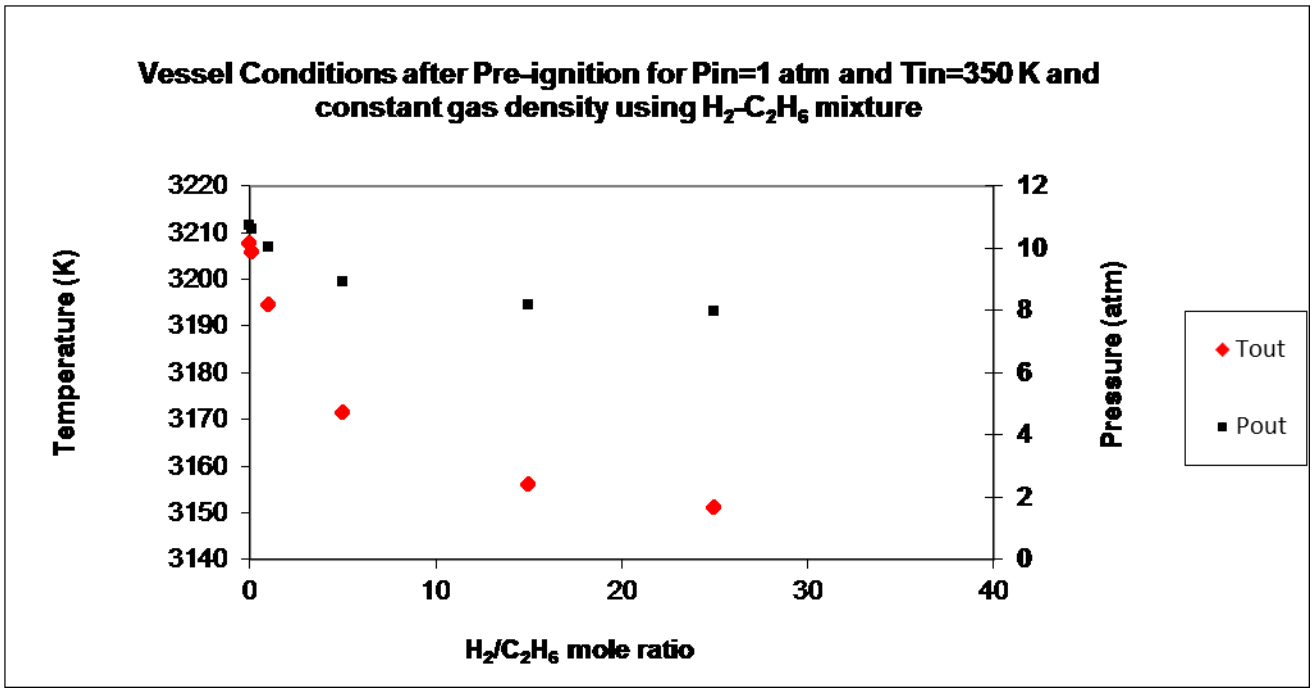

Figure 34 Post-combustion adiabatic temperature and pressure as a function of Hydrogen to Ethane mole ratio for initial temperature 350 K and initial pressure 1 atm, calculated using the chemically dissociative model

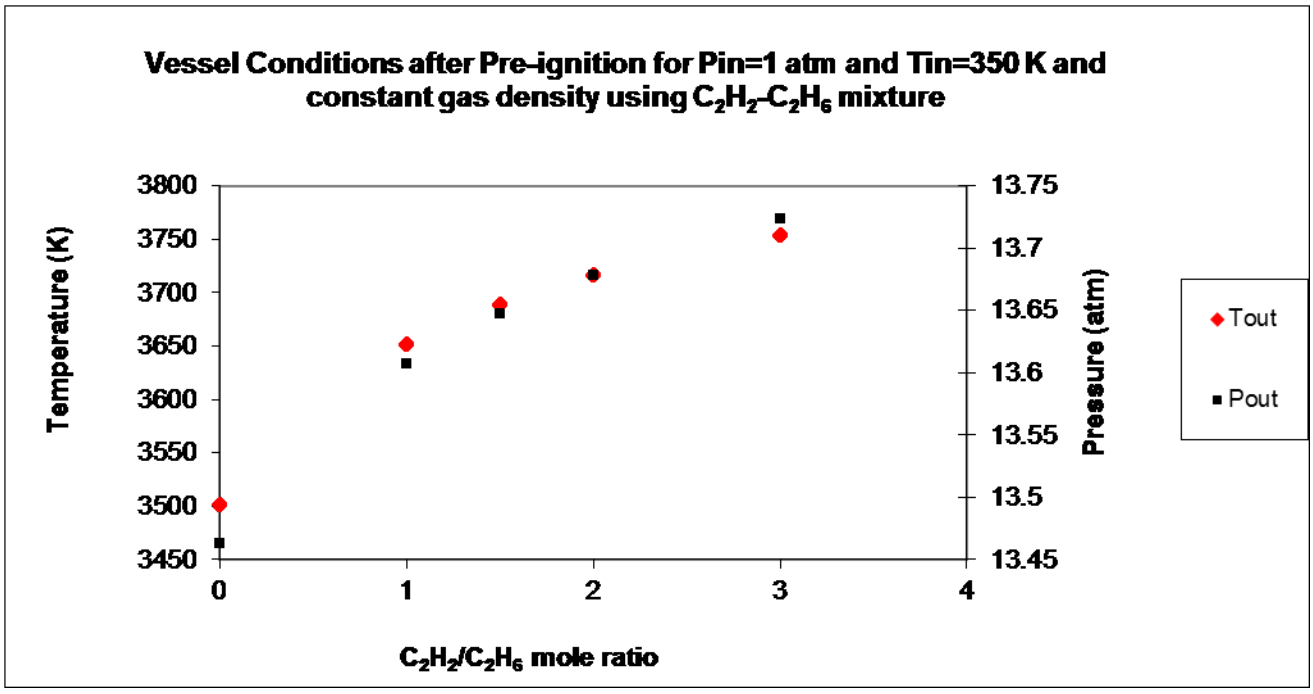

Figure 35 Post-combustion adiabatic temperature and pressure as a function of Acetylene to Ethane mole ratio for initial temperature 350 K and initial pressure 1 atm, calculated using the chemically dissociative model

4.4.2 Investigation of combustion dissociation

The previous section demonstrated why the pre-ignition mixture, that uses as fuel Acetylene and Hydrogen and as oxidizer an Oxygen and Nitrogen mixture at atmospheric air ratio, has been used extensively in the literature. This mixture has been used by Sandia and IFP labs, but never been investigated in terms of chemical dissociation, which as described in section 4.4, should not be overlooked. The perfect combustion equation would be:

$$3.245C_2H_2 + 0.515H_2 + 8.37O_2 + 89.75N_2 \rightarrow 89.75N_2 + 6.49CO_2 + 3.76H_2O$$

The hydrogen to hydrocarbon mole ratio can be easily calculated:

$$A = \frac{H_2}{C_2H_2} = \frac{0.515}{3.245} = 0.1587$$

The plots in Figure 36 investigate the chemical dissociation of the aforementioned reaction, accounting for CO, OH, NO and NO_2. Clearly more species will be formed, but these four species are the most molar fraction dominant. On the left-hand-side column of graphs, the

effect of initial pressure is investigated, while keeping the initial temperature at 300 K. On the right-hand-side column of graphs, the effect of initial temperature on the dissociative molecules is investigated, while maintaining the initial pressure at 5 bar. The initial pressure was kept at 5 bar, because as shown on the results of Section 4.3.1 in Figure 29, Figure 30 and Figure 31, an initial pressure of 5 bar is sufficient to simulate engine-like post-combustions conditions, without exceeding the specifications of the vessel.

It can be observed that with increasing the initial pressure of the pre-ignition mixture for initial pre-ignition temperature kept at room temperature, the CO, OH and NO mole fraction decreases. Even though the NO_2 mole fraction increases, increasing the initial pressure, the combustion process becomes more "perfect", as shown on the bottom-left graph. For instance, if the pre-ignition pressure is 1 bar 99.85% of the mole fraction in the post-combustion mixture is consisted of CO_2, H_2O and N_2, which are the "perfect" combustion products. While at 30 bar the same mole fraction is 99.95%. The percentage of the non-"perfect"-combustion products sounds small. However, as described in Section 4.3.3, this 0.05% to 0.15% of the non-"perfect"-combustion products results in a large change of the post-combustion heat conductivity. Heat conductivity affects the evaporation of the diesel spray.

On the right-hand-side column of graphs of Figure 36, as the initial temperature increases, the NO, NO_2 and OH mole fraction in the post-combustion mixture increase. The CO mole fraction has a minimum at initial temperature equal to room temperature and then follows the trend of NO, NO_2 and OH and increases as initial temperature increases. The effect of initial temperature is stronger on dissociation than pressure. As shown on the bottom right graph, at initial temperature of 150 K 99.9% of the post-combustion moles are CO_2 or H_2O or N_2, while at initial temperature of 650 K only 99.6%.

So it is obvious that as the initial temperature increases, the combustion becomes more perfect, which is the opposite effect of increasing initial temperature. Even though the percentage of non-"perfect"-combustion products is small, their influence on spray evaporation has to be investigated. Chapter 7 will study the evaporation of a single droplet in different

ambient conditions and thus will investigate the influence of the chemical dissociation phenomenon of the chemical-heating technique on the evaporation of the spray.

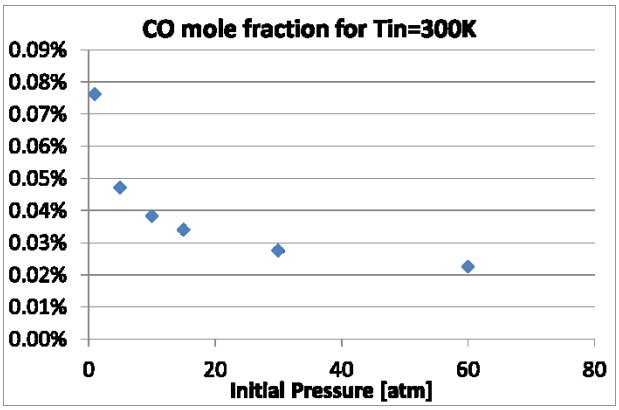

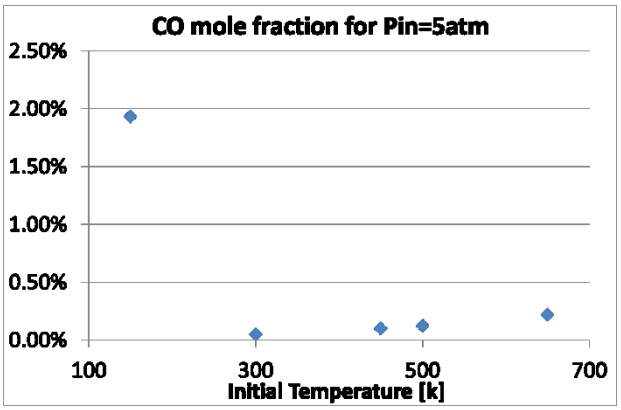

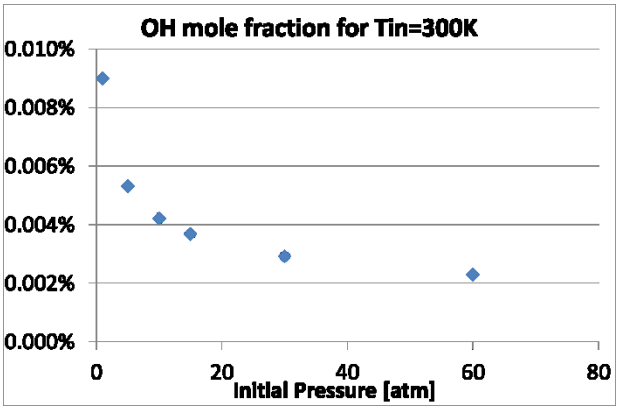

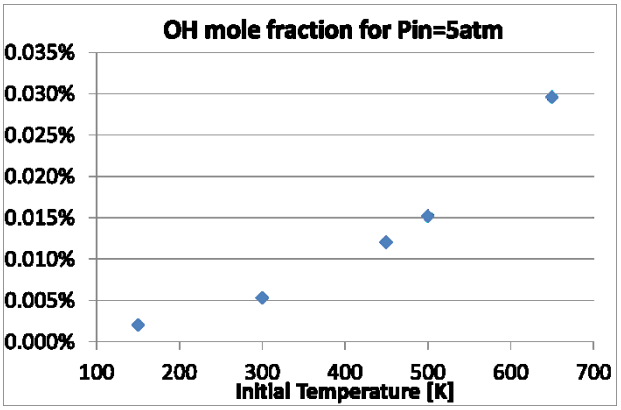

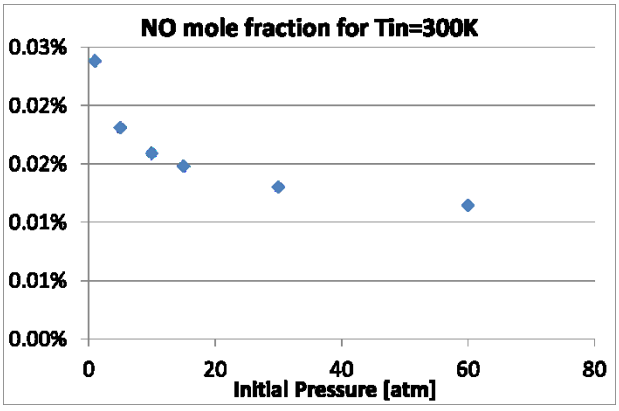

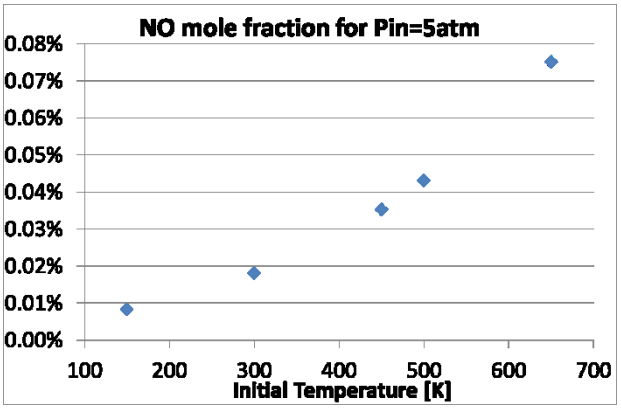

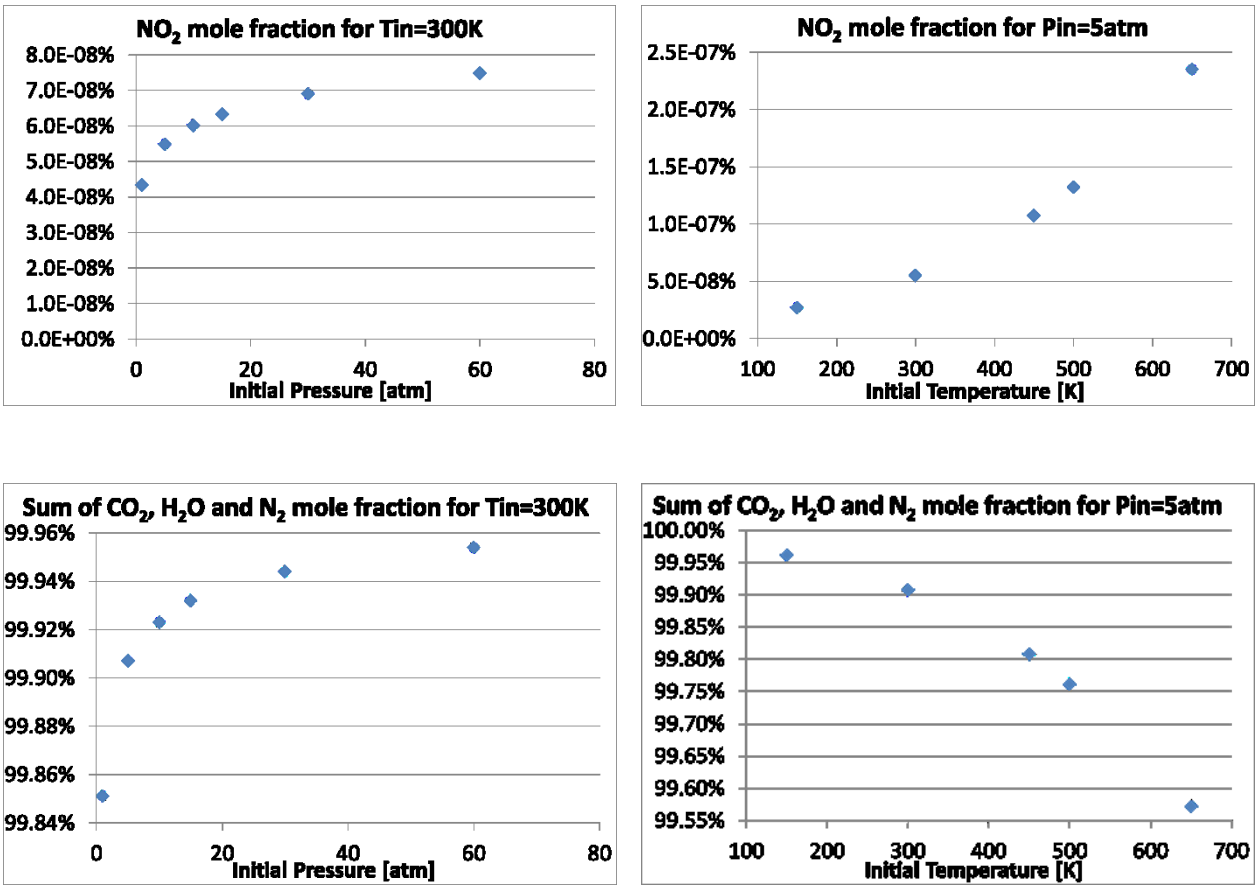

Figure 36 Molar fraction of CO, OH, NO, and NO_2 in the post-combustion gases and the accumulative molar fraction of the "ideal" products (CO_2, H_2O and N_2)

4.5 Pressure transducer experiments on the pre-ignition

Due to the window design, the vessel could not operate under vacuum. So to ensure sufficient removal of unwanted substances in the vessel, after different experimentation of the ignition processes, the purging technique of Chapter 3 was used. This purging technique also helped minimizing the errors in the delivered gas mass in the vessel, which would have been induced by a transitional operation of the Mass Flow Controllers (Chapter 3). So the vessel was purged with the combustible mixture. Then the inlet valve was shut off and then the outlet valve. So prior to combustion the vessel was filled with the combustible mixture at 1bar pressure.

As a consequence, no Hydrocarbon was used, as the Hydrocarbon reduces the peak pressure and temperature values that can be achieved by combustion. So only Hydrogen was used as pre-igniton fuel. Also the peak pressure was limited to 30 bar, which is dictated by the windows strength. This peak pressure value was found to be close to the peak pressure produced by an Oxyhydrogen perfect combustion ~20 bar. The drawback of this technique is that the ambient gas density (<0.82 kg/m^3) is lower than what is normally found at the top dead center of an engine (12-55 kg/m^3) (Appendix 2). The effect of gas density on the spray characteristics was investigated in Chapter 2. The current and the following sections will describe the experimental measurements on the pre-ignition combustion.

4.5.1 Dual pressure transducer technique

As described in the previous chapters, in the constant volume vessel, a combustible gas mixture is ignited to build up pressure and temperature. As the post-combustion hot gases cool down, pressure decreases and at a specific value of pressure and temperature the Diesel spray is injected into the vessel. It is therefore very important to know in real time the pressure and temperature in the vessel.

As presented in Chapter 3, in the literature thermocouples have been used to measure vessel wall temperature. However, this reading is not indicative of the core-gas temperature and thermocouples have a slow response time compared to the combustion timescale. In this work an RTD has been used to measure the temperature at the center of the vessel (drawings are available in Appendix 4). But still this reading cannot be used for real time control. So the monitoring of the conditions in the vessel cannot be based on the temperature reading.

The piezoelectric phenomenon was firstly observed in 1890 by Pierre and Marie Curie. When a material is subjected to a force, a charge is produced, proportional to the force and the piezoelectric constant of the material. Generally, Quartz crystals with parallel faces are usually packed with metallic electrodes to create a capacitor of 20 to 200 pF. This transducer is then connected in parallel to a charge amplifier through a cable of typical capacity from 70 to 100 pF/m (Allocca and Stuart, 1984).

The piezoelectric principle is primarily suitable for measuring rapid, dynamic and quasi-static pressure processes. Piezo pressure transducers have been used extensively to measure the pressure in the combustion chamber of IC engines, where high-frequency sampling is required. They have also been used into similar constant volume experiments in the literature. However, the piezoelectric pressure transducers measure relative pressures and not absolute ones. A reference value is therefore needed to convert the gauge pressure acquired to absolute pressure values.

In this work, the gauge pressure in the vessel was measured using a water-cooled piezoelectric pressure transducer (Kistler 6041AU20), which is suitable for high frequency pressure measurements, related to combustion in IC engines. The transducer was connected to a Kistler 5011B01Y50 charge amplifier. The sampling rate was set at 72 kHz. An Anologue Input card on the cRIO was connected to the amplifier to digitise the signal and use it for the vessel control as was shown in Chapter 3 in Figure 24.

Some researchers (Stein et al, 1987, Aleiferis, 2000) coated their sensor with a silicon rubber compound RTV, to protect the sensor from thermal shocks. However it seems that these compounds survive up to 180^{O}C, a low value considering that the average temperature of the wall of an engine's cylinder is 377^{O}C (Heywood, 1988, Aleiferis, 2000), a temperature easily achievable on the wall of a chemically pre-heated vessel wall, as demonstrated in Sections 3.3.9 and 4.5.3 as well as in previous work (Heitor and Moreira, 1993). Furthermore the instrument manufacturer does not advise in favour of this technique, but provides heat-shock correction coefficients for the readings. So in this work, the sensor was not protected by RTV, but the measurements were corrected for the shock environment, as recommended by the pressure-transducer manufacturer.

To find the abovementioned pressure reference value, to which the pressure, measured by the piezoelectric transducer is added, a different type of pressure transducer was used. The strain gauge is a device invented in 1938 by Edward Simmons and Arthur Ruge, to measure the deformation of an object. A strain gauge consists of a flexible metallic foil pattern, placed between two insulating layers. The gauge is attached to the object by a suitable adhesive. As

the object is deformed, the foil is deformed too, causing its electrical resistance to change. This resistance change is being measured using a Wheatstone bridge and is then related to the object deformation.

In a strain gauge pressure transducer, a strain gauge is attached to a diaphragm which is subjected to the pressure that needs to be measured. The diaphragm and the strain gauge are deformed due to pressure. The resistance change of the strain gauge, measured by the Wheatstone bridge, is then correlated to pressure.

In this work a Techni-measure PWF-10MPa strain gauge pressure transducer was used. The transducer was connected to a Wheatstone bridge and an SKG signal amplifier. The signal from the amplifier was then fed to the cRIO Analogue Input card.

4.5.2 Pressure transducers calibration

The strain gauge pressure transducer and its amplifier were initially calibrated using a General Electric Druck DPI portable pressure calibrator. The portable calibrator is equipped with a hand-pump that creates pressure and a screen that displays the pressure with an 0.025% accuracy of the full-scale value, which corresponded to an uncertainty of 0.1 mbar. The cRIO measured voltage value is then calibrated to the displayed pressure reading as shown in Figure 37. In the same way the calibration of the high-frequency Kistler pressure transducer was acquired, Figure 38.

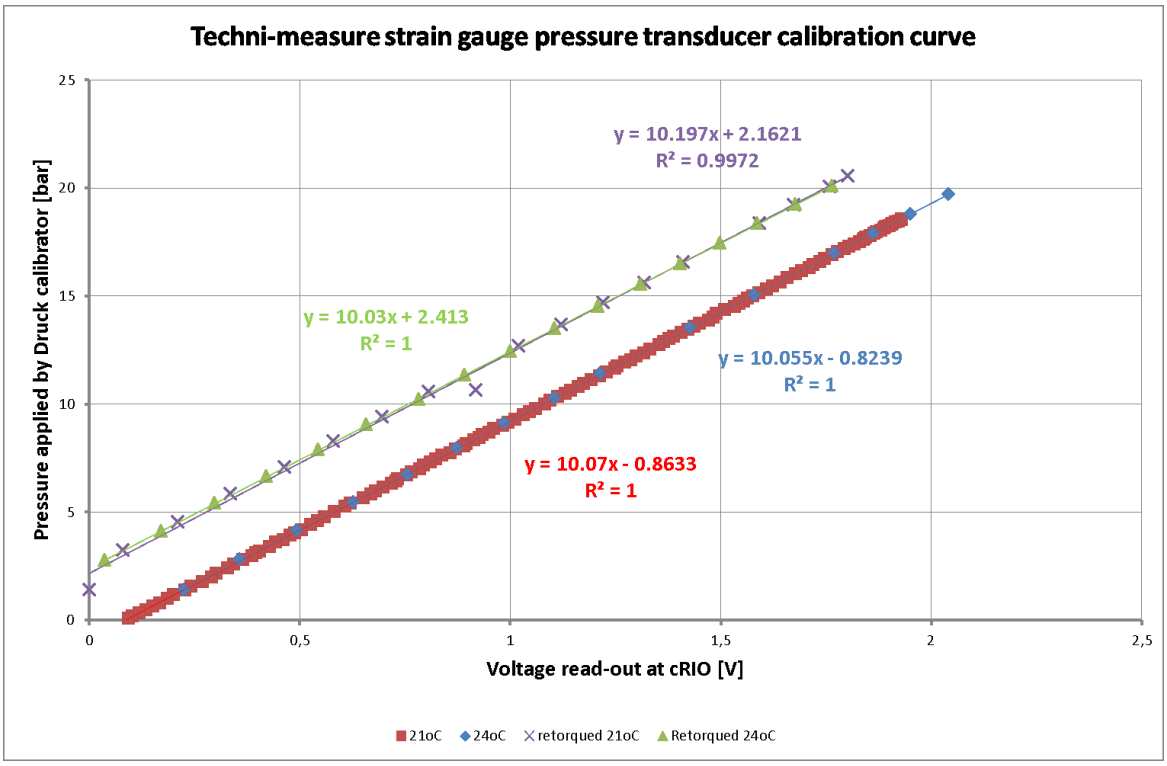

Figure 37 Techni-measure strain gauge pressure transducer dismounted-from-vessel calibration curve

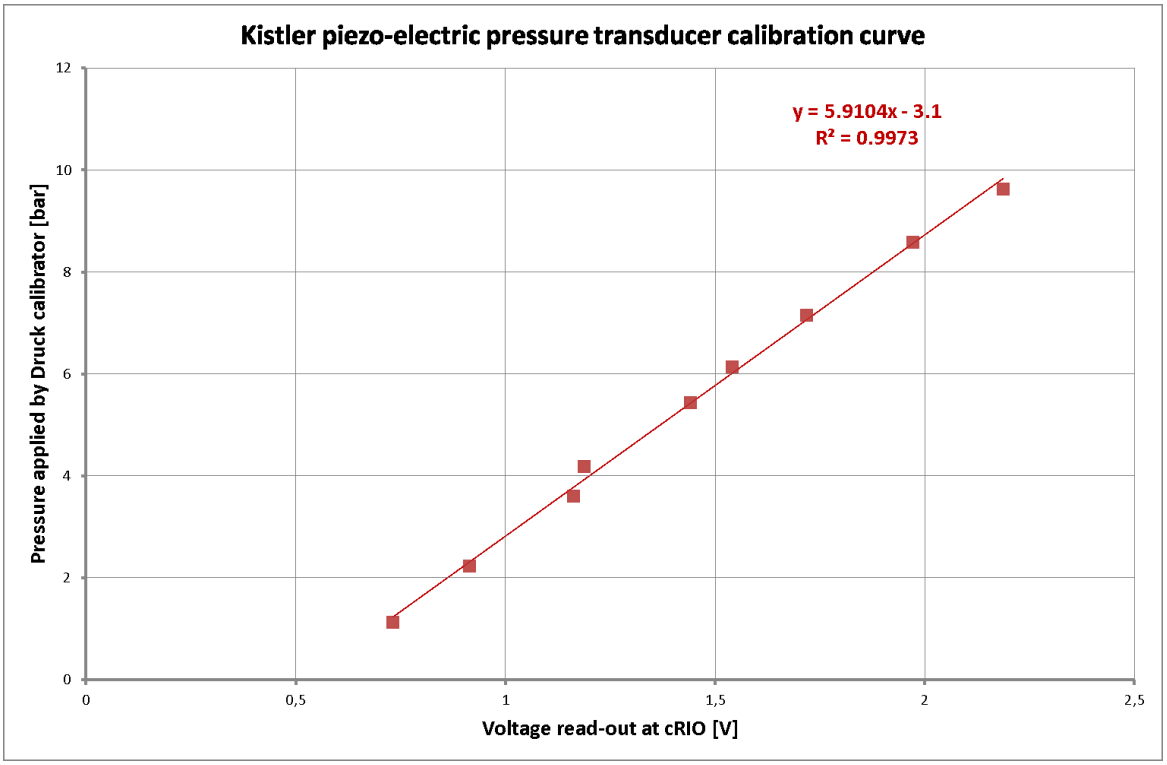

Figure 38 Kistler piezo-electric pressure transducer dismounted-from-vessel calibration curve

Figure 37 shows that the temperature effect on the techni pressure transducer is minimal, as expected from the literature (Doebelin, 2003, Aleiferis, 2000). More specifically, temperature affects the slope of the calibration curve, changing its value from 10.055 at 24^{o}C to 10.07 at 21^{o}C. The zero-drift of the sensor was expected to remain the same under different temperatures, but there was a negligible change.

The effect of the applied torque on the sensor, during installation, is demonstrated in Figure 37 on the zero-drift. The green line is the correctly torqued condition that prevents the sensor from leaking. Higher torque results in high-frequency noise. Less torque (red and blue lines) leads in major leaks.

In order to eliminate the dependency of the sensor's zero-drift to its installation torque, the sensor was calibrated after it was installed on the vessel. To achieve this, the portable Druck calibrator was connected to the vessel using a standard high-pressure tube. Pressure in the vessel was increased using the Druck's hand pump and pressure was read from the display screen. The calibration curves acquired with this technique are presented in Figure 39 and Figure 40. The high-frequency Kistler piezo-electric pressure transducer was calibrated in the same way as the strain-gauge Techni-measure pressure transducer, as shown in Figure 40, but as aforementioned, the off-set of this type of transducers is found from the strain gauge transducer. So, the slope for the Kistler transducer, calculated from this graph, is the important calibration parameter.

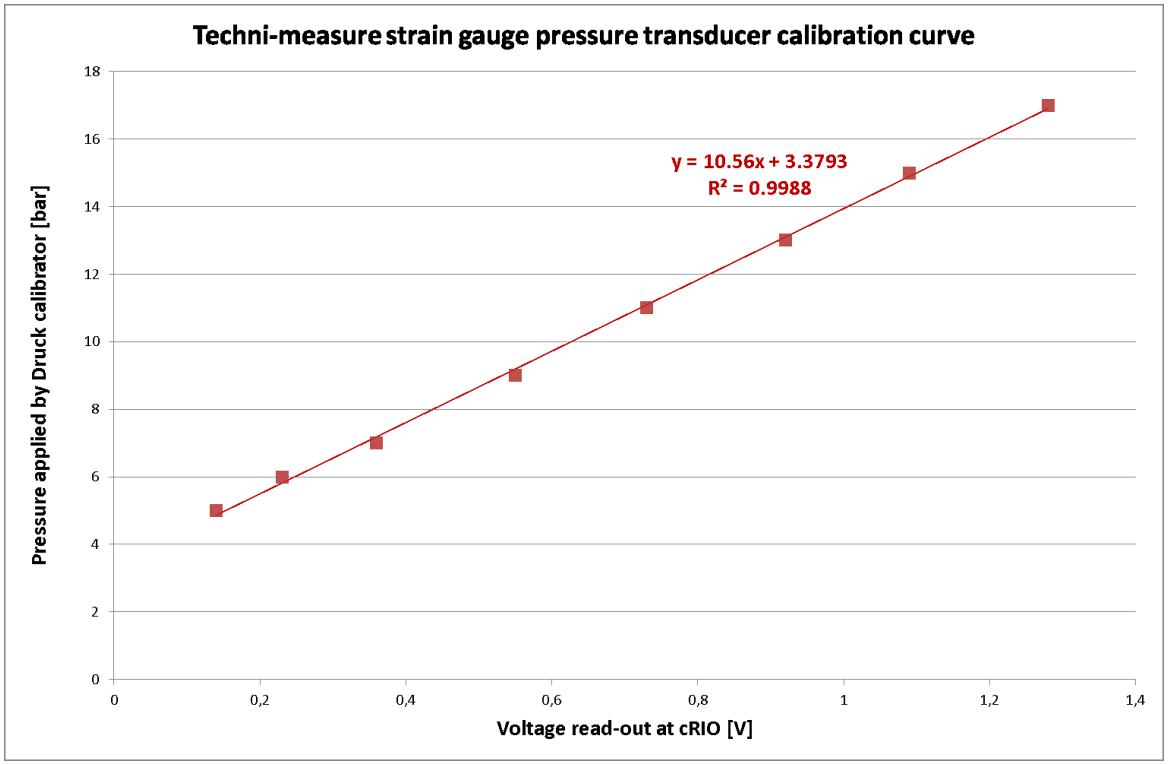

Figure 39 Techni-measure strain gauge pressure transducer mounted-on-vessel calibration curve

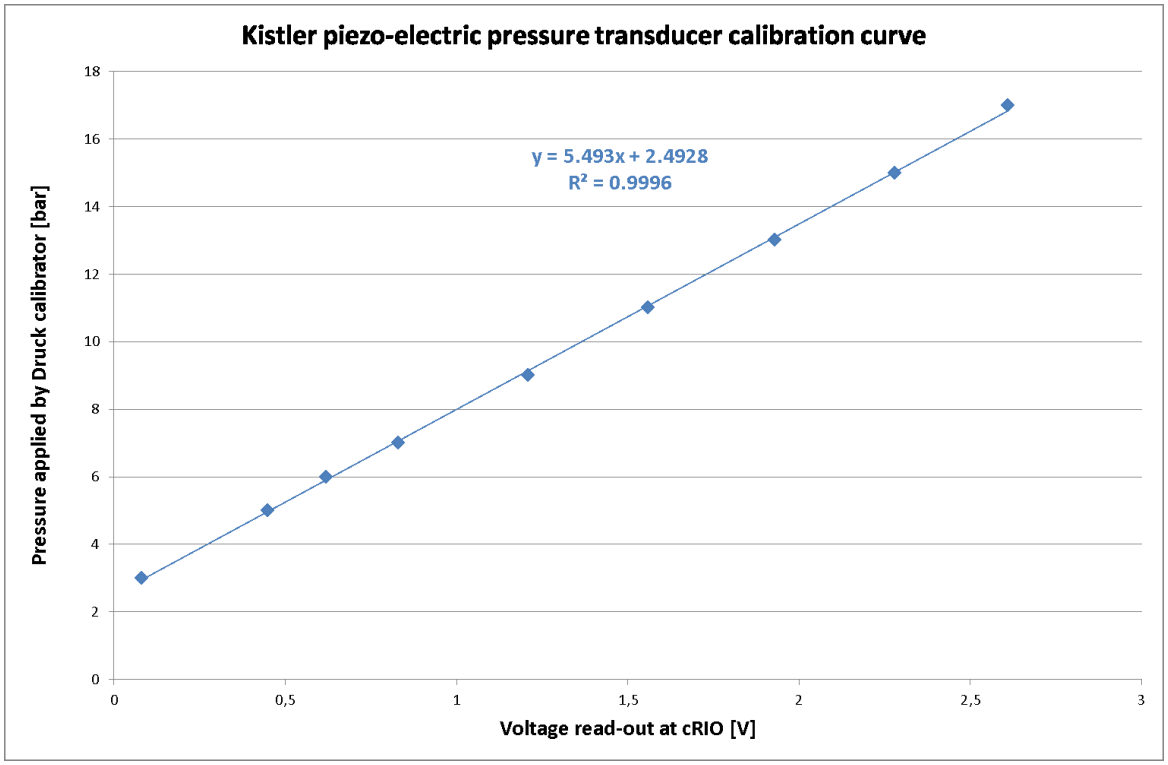

Figure 40 Kistler piezo-electric pressure transducer mounted-on-vessel calibration curve

With this calibration technique, which allows for calibration of the mounted transducers, the leak of the vessel can be quantified. This information is important for the safety of the experiment and for quantifying the experimental error. At 40 bar, the vessel was measured to leak 1 mbar every 3 minutes. The experiments of this work usually last of the order of a few seconds, so leaks from the vessel can be neglected.

4.5.3 Dual pressure transducer technique results

Figure 41 presents a typical pressure trace, as a function of time, as measured using the Kistler piezo-electric transducer and corrected for the initial pressure as measured by the Druck strain gauge pressure transducer. The base pressure corresponds to the pressure in the vessel, after it has been filled with the gas fuel mixture. Data logging begins when the glowplug is turned on. Some time passes from turning on the glowpplug/ start logging till pressure rises, as described in Chapter 3. This time corresponds to the ignition delay of the mixture, as will be presented later. On the pressure trace, following a rapid initial pressure rise, the pressure is reduced reaching exponentially the ambient pressure. The time to ignition is not well defined with the glowplug. Hence, the problem arises as to inclusion of time references and alternative ignition methods should be explored in future work as outlined below.

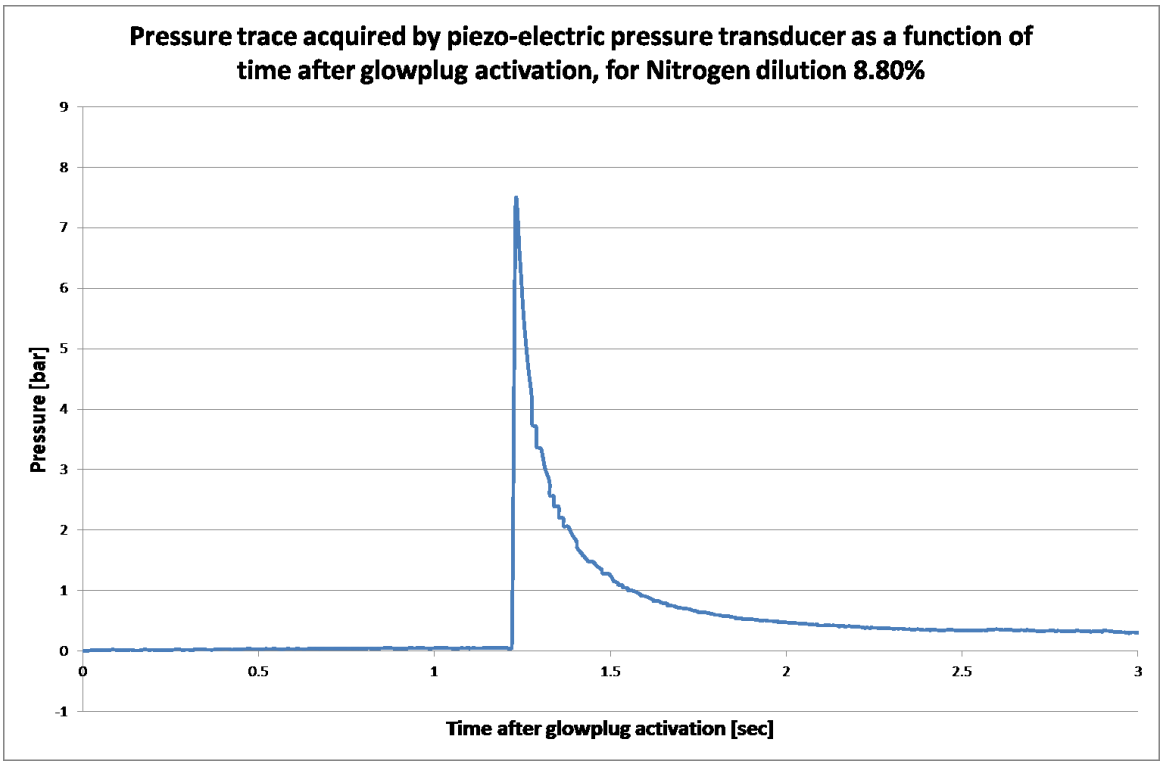

Figure 41 Pressure trace acquired by piezo-electric pressure transducer as a function of time after glowplug activation, for Nitrogen dilution 8.80%

Figure 42 shows the temperature measured by the RTD in the center of the vessel before the fuel gas mixture is ignited. This parameter is important because for given initial pressure, the initial temperature will correlate to the gas density of the pre-ignition mixture in the vessel. The ratio of gases is fixed by the MFCs and the diesel-spray injection is triggered by an appropriately selected pressure. So variation of the initial temperature will only affect the gas density and the temperature at the moment of injection. Figure 42 shows a small increase of the initial gas temperature from experiment to experiment, which could be the outcome of the previous deflagration warming up the vessel wall and then the walls warming up the gases of the following experiment. For example, experiments 1 to 9 took place on the same day and 10 to 20 on the following day, with a break after experiment 16. However, the initial gas temperature is constant within 2^{o}C, so the temperature difference in terms of initial gas density is negligible.

Figure 43 shows the gas bulk temperature as a function of time elapsed after initiation of the glowplug. The bulk gas temperature was calculated using the equation of state for ideal gas, which is a standard technique in the literature, as presented in Section 3.3.9. The temperature displayed is not the wall nor the core temperature, but a mass-averaged temperature. On the same plot, the pressure axis appears on the right. Pressure and temperature are proportional since the ideal gas law was considered.

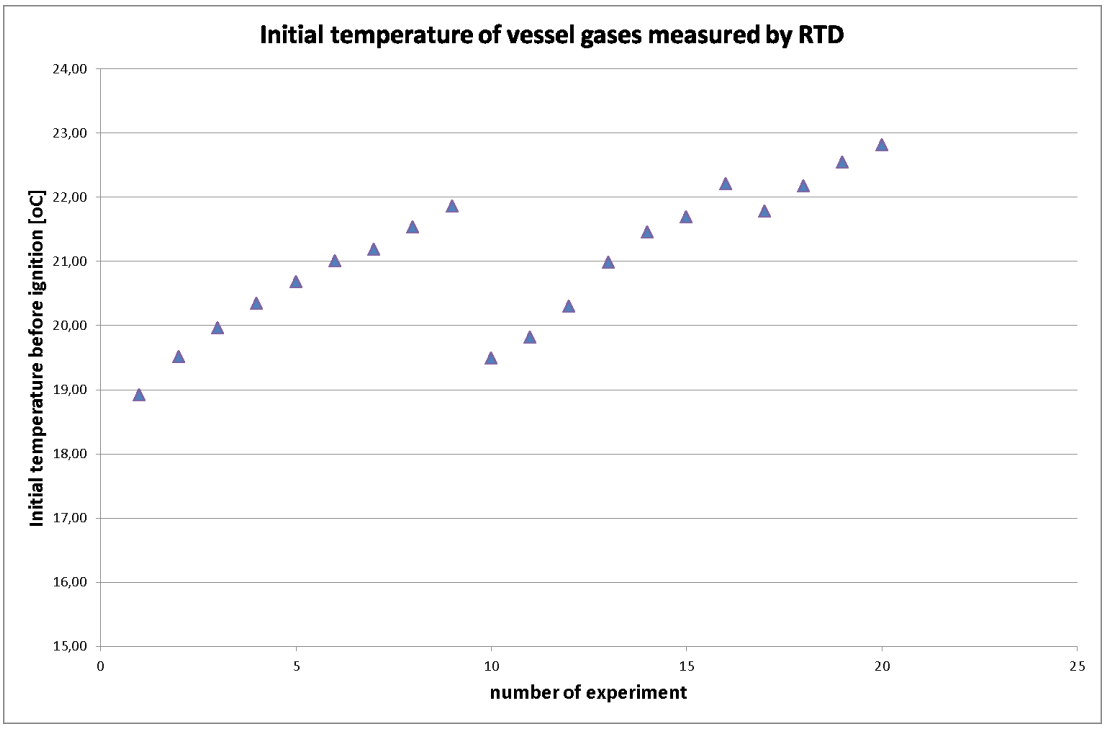

Figure 42 Initial temperature of vessel gases measured by RTD

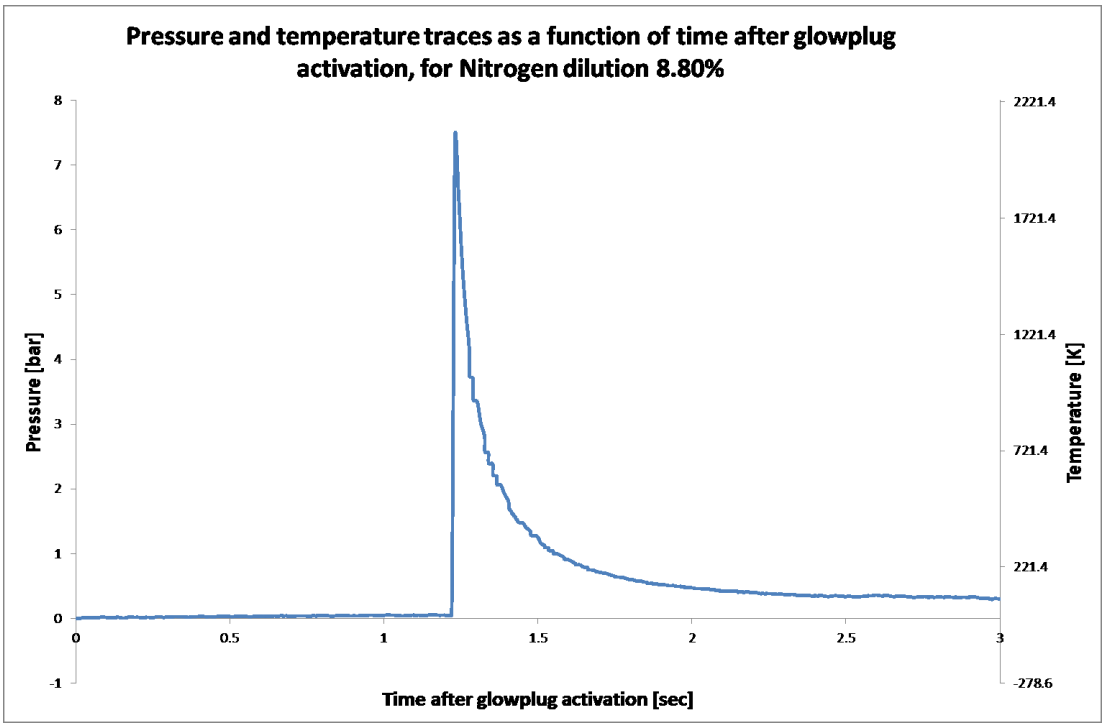

Figure 43 Pressure and temperature traces as a function of time after glowplug activation, for Nitrogen dilution 8.80% (same data as Figure 41)

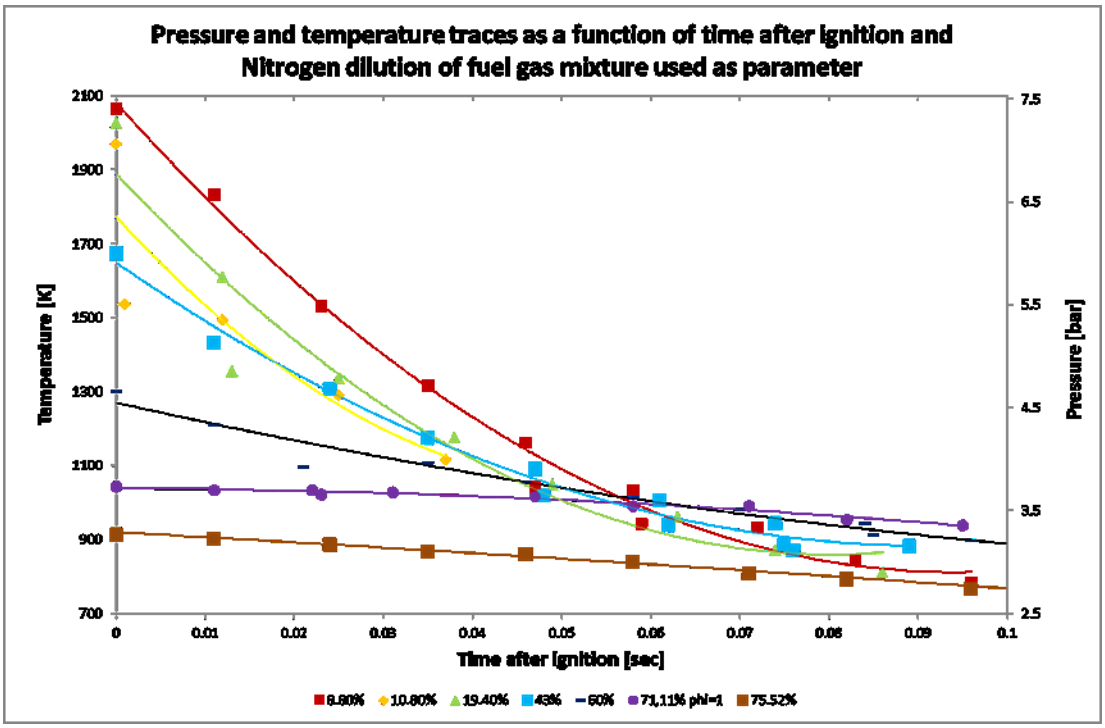

Figure 44 Pressure and temperature traces as a function of time after ignition and Nitrogen dilution of fuel gas mixture used as parameter

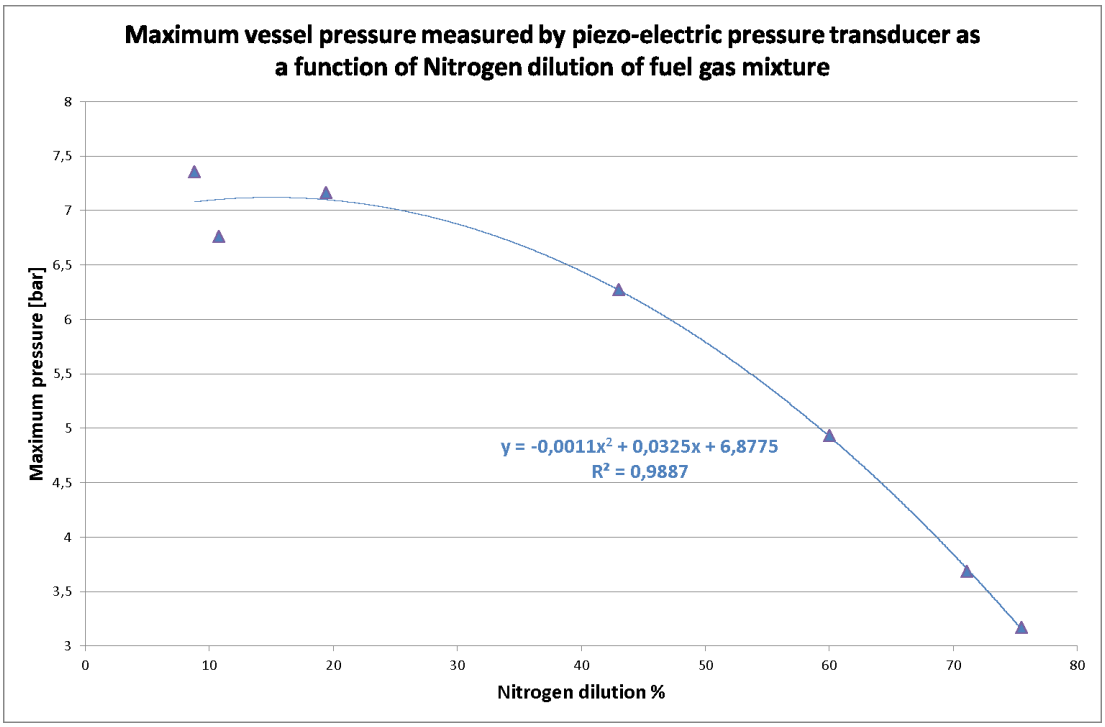

Figure 45 Maximum vessel pressure measured by piezo-electric pressure transducer as a function of Nitrogen dilution of fuel gas mixture

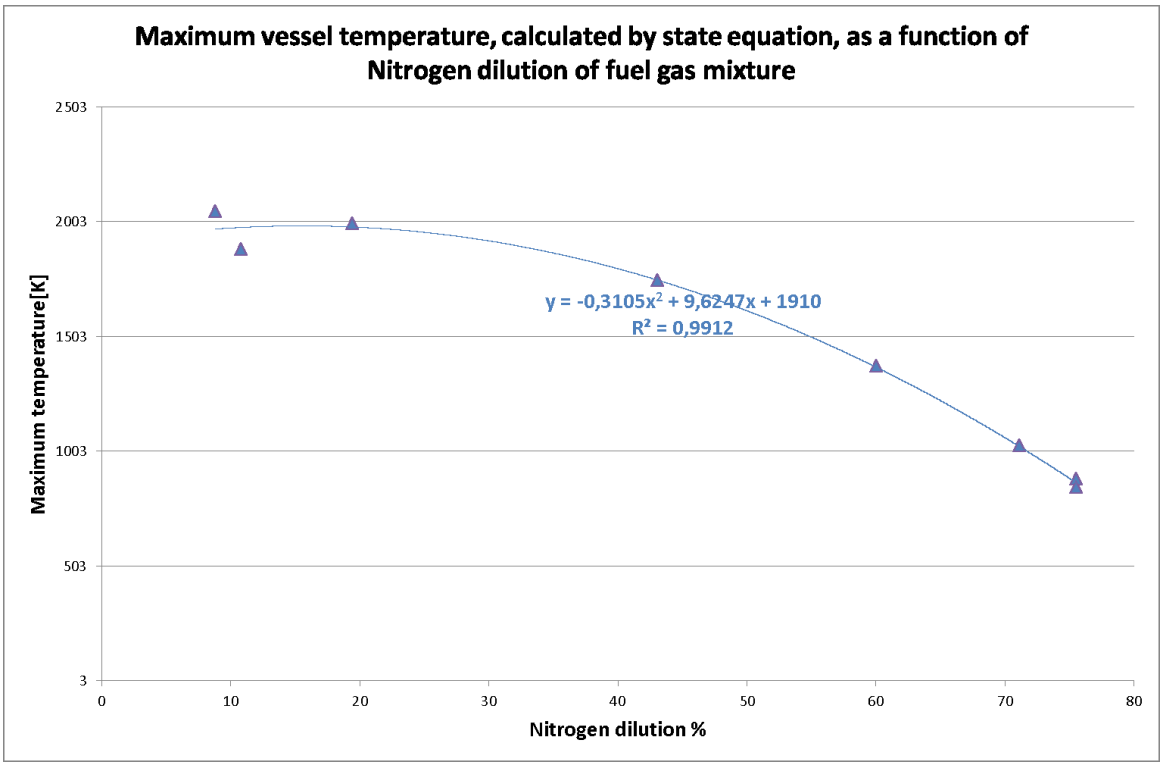

Figure 46 Maximum vessel temperature, calculated by state equation, as a function of Nitrogen dilution of fuel gas mixture

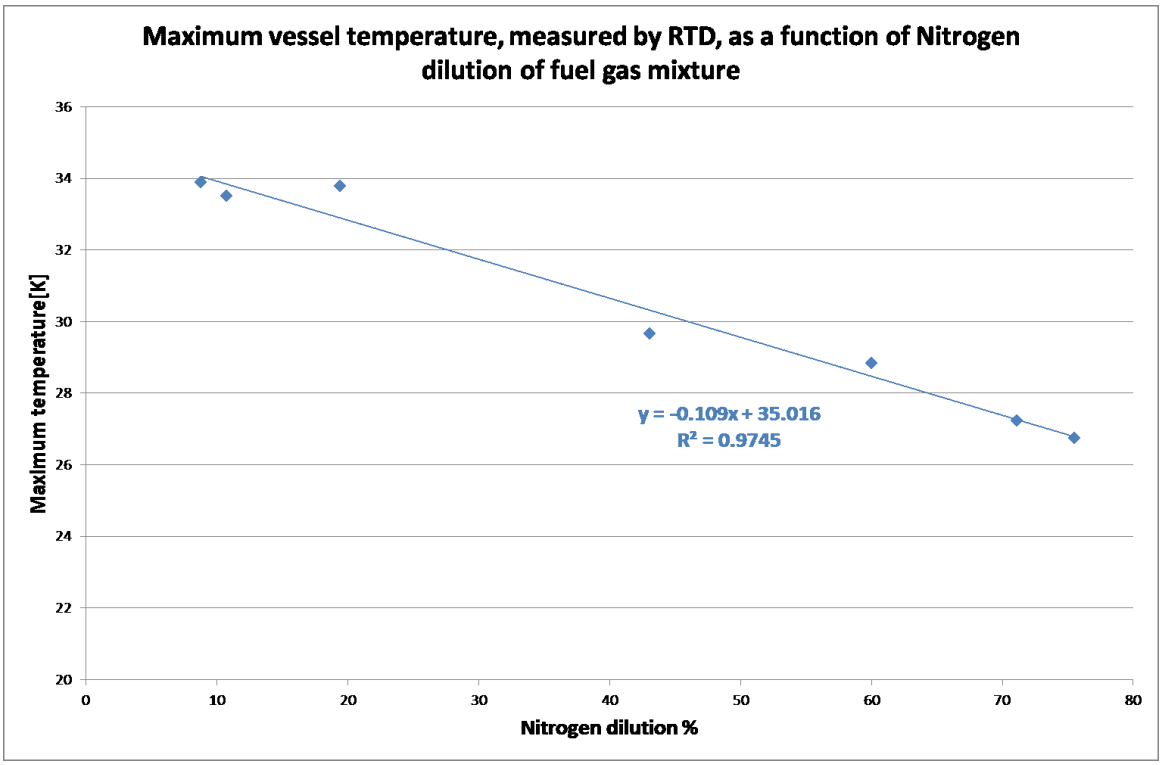

Figure 47 Maximum vessel temperature, measured by RTD, as a function of Nitrogen dilution of fuel gas mixture

Figure 44 presents the vessel temperature and pressure as a function of time after peak pressure. The Nitrogen dilution of the Hydrogen/Oxygen mixture was used as a parameter. This plot is important for allowing the user to decide what Nitrogen dilution should be used. After the user selects the Nitrogen dilution and the pressure at which the diesel injector will be triggered will inform the user for the vessel bulk gas temperature.

Figure 45 and Figure 46 show the maximum pressure and temperature of the vessel as a function of Nitrogen dilution. The user should make sure that the pressure never exceeds the maximum operational pressure.

Figure 47 shows the maximum temperature recorded by the RTD. Clearly the RTD has a slow response, as described in Section 3.3.9. So though it will not measure the actual gas core density, it will give an indication of the wall temperature. The temperature weakest components of the vessel are the PTFE o-rings which are certified up to 200^{o}C.

This section presented the pressure transducer technique used in this work. It is clear that this technique can be used for monitoring pressure and temperature conditions in the vessel and control further operations in the vessel, such as the fuel injection and the vessel structural integrity safety watchdog routines. It is evident that the Hydrogen/Oxygen/Nitrogen pre-ignition mixture can be used for the experiments of spray visualization that will be presented in Chapter 7. Finally this section provides a map of the post-combustion conditions produced by ignition of the Hydrogen/Oxygen/Nitrogen mixture. The next section will investigate optically the combustion process in the vessel, this is important to ensure uniform combustion with uniform post-combustion temperature distribution in the vessel.

4.6 Schlieren experiments on the pre-ignition

4.6.1 Introduction to Schlieren

In German Schlieren means streaks and as all nouns in the German language it is capitalized. Unlike to the reasonable common thinking, Schlieren, as a person, never existed. Hence it should be written with lower case in English. Schlieren techniques were firstly used by Toepler in 1864 to examine defects in lenses (Hecht, 2001). Schlieren techniques are based on the principle that if a beam of parallel light propagates uniformly through a media, whose density and thus refractive index are non-uniform, the light will "bent", as shown in Figure 48. This light deviation can produce localized brightening or darkening depending on the way the light deviates. In Schlieren flow visualization techniques, the deflection of light by the refractive index gradient of the fluid is directly related to the fluid density gradient. The deflected light is compared to the un-deflected light on a viewing screen. A knife edge is used to partially block the undisturbed light and one of the two directions of the deflected light, as shown in Figure 48. The light that is deflected by the inhomogeneity and not blocked by the knife edge, produces a shadow pattern on the viewing screen. This shadow pattern is a light-intensity representation of the refractive index gradient of the fluid, which can then be correlated to the density gradient of the fluid (Settles, 1949).

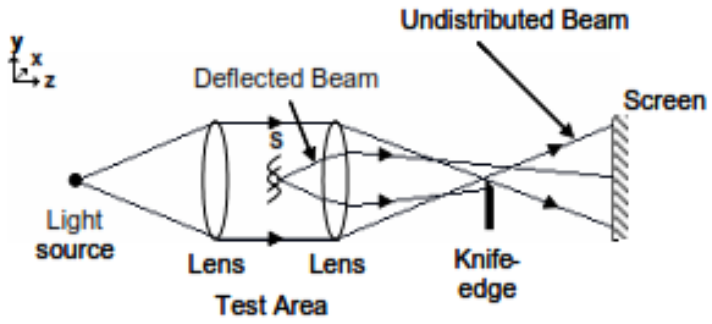

Figure 48 Demonstration of Schlieren principle

In this chapter a Z-type Schlieren technique is used to measure the spatial Line-Of-Sight (LOS) averaged location of “hot gases” in the vessel. In this way, the flame front of the pre-ignition combustion can be visualized. Figure 49 shows the experimental setup.

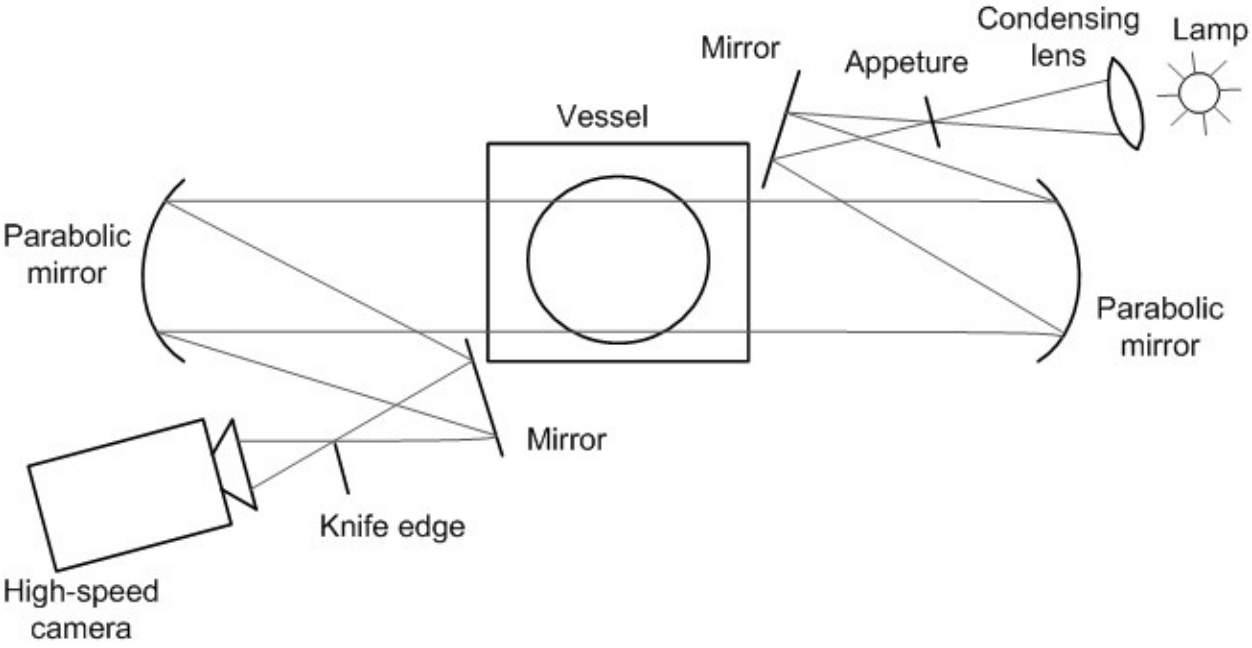

Figure 49 Schlieren experimental setup

A standard automotive 12 V 45 W light bulb was used as light source. A f=50 mm lens and a custom-built 2x6 mm pinhole were used to produce. From the optical properties of lenses one recognizes that the light source and the knife-edge plane are conjugate optical planes. It is of great importance then to have a well-defined effective light source. However, as the bulb is not a point source, a condensing lens and a pin hole, produce a uniform and effective light source. The quality of the projection of the light source on the knife-edge plane was verified prior to any measurement.

The light was collimated through the test area by using two parabolic mirrors of f=3m focal length and diameter of 15 cm. The minimum distance of the two mirrors is about $2f$. Longer distance between the mirrors in principle does not matter, but is restricted by the available lab space. Additionally, lens theory can demonstrate that increasing the distance of the two mirrors will reduce the image magnification, as presented in Figure 50. The

magnification m can be calculated as $m = f/s$, where the distance between the parabolic mirror and the test area is considered to be the sum of f and s.

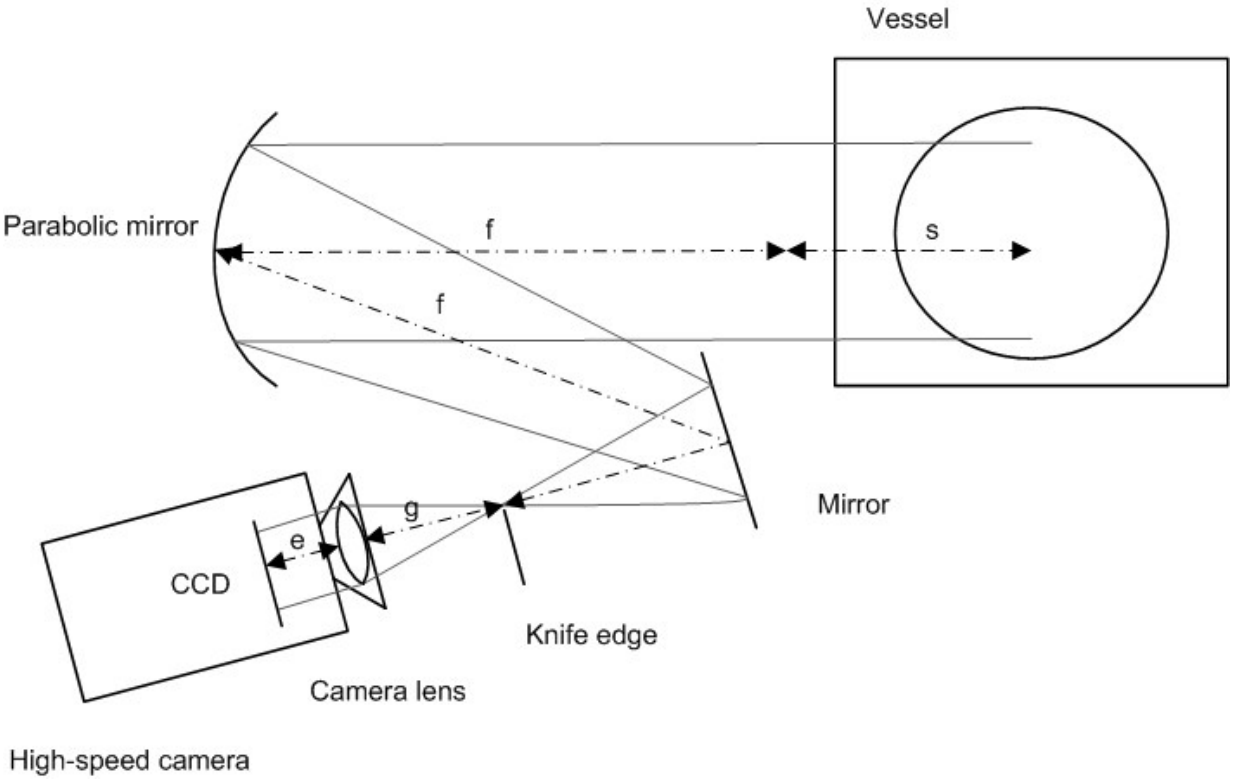

Figure 50 Light collecting mirrors of Schlieren setup

The parabolic mirrors used are figured for on-axis use, which means that their geometrical and optical axes are coincident. However, the Z-type Schlieren setup requires them to be used off-axis. So off-axis aberrations such as coma and astigmatism are introduced. Both lead to errors in the faithful production of the light-source at the knife-edge. Coma occurs when the direction of the light reflected from a mirror depends on the position of the point of reflection. As shown in Figure 51, coma aberration creates a line artifact from a point, which looks like a “comet”. Coma grows in proportion to the mirror offset angle and inverse of the mirror f# number for a given angle. So it can be minimized by minimizing the mirror angle and using long focal length mirrors. However, as coma is introduced on both mirrors, it can be

eliminated by tilting the two parabolic mirrors at equal angles in opposite directions from the central optical axis, thus forming a “Z” shape.

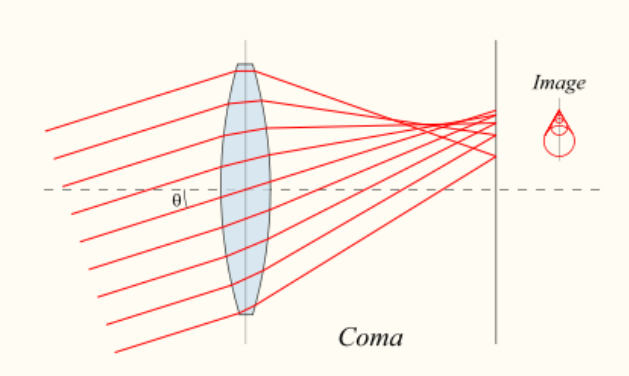

Figure 51 Demonstration of coma off-axis aberration

Astigmatism occurs when rays that propagate in two perpendicular planes have different foci, as shown in Figure 52. Astigmatism forms an artifact image of a cross, as the vertical and horizontal lines will be in sharp focus at two different distances. In Schlieren techniques, astigmatism is introduced due to the off-axis tilt of the parabolic mirrors. Since the path length along the optical centerline and the mirror periphery are different, this results in stretching the image of a point into two perpendicular lines spaced along the optical axis, forming the “cross” artifact. Astigmatism can be minimized by restricting the offset mirror-angles, and by using large f# number mirrors (typically 6 and higher). Unlike coma, astigmatism cannot be eliminated and is always present in Schlieren systems. In this work, the angle of the mirrors was kept at the minimum practically achievable angle of 6 degrees.

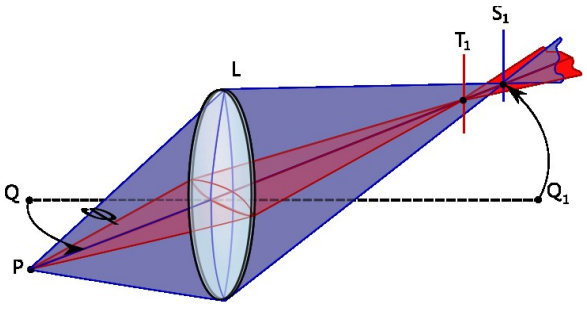

Figure 52 Demonstration of astigmatism off-axis aberration

Spherical aberrations occur due to the increased refraction of light rays when they strike a lens or a mirror near its edge, in comparison with those that strike nearer the center, Figure 53. In Schlieren techniques, spherical aberrations are not as important as the abovementioned off-axis aberrations because lenses and mirrors are usually well corrected for this aberration. Additionally in this setup the parabolic mirrors are of larger diameter than the vessel windows and the camera lens has a large f# number, which means that the light rays are more concentrated on the center of the optics thus minimizing the spherical aberrations.

To summarise, the effect of the three optical error sources on the experimental results can be neglected. Coma is introduced on both mirrors, but it was eliminated by tilting the two parabolic mirrors at equal angles in opposite directions from the central optical axis. Unlike coma, astigmatism cannot be eliminated and is always present in Schlieren systems. However, in this work, the angle of the mirrors was kept at the minimum practically achievable angle of 6 degrees. Finally the spherical aberrations are not as important as the abovementioned off-axis aberrations because lenses and mirrors are usually well corrected for this aberration. Additionally in this setup the parabolic mirrors are of larger diameter than the vessel windows and the camera lens has a large f# number, which means that the light rays are more concentrated at the center of the optics thus minimizing the spherical aberrations.

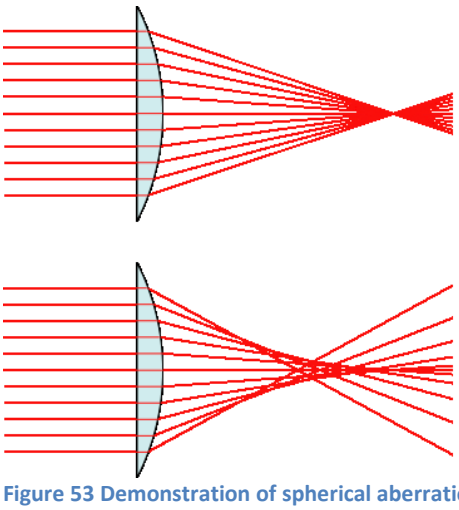

Figure 53 Demonstration of spherical aberration

4.6.2 Schlieren results on pre-ignition

A LaVision HighSpeedStar 6 was used to collect the light after the knife edge. The acquisition speed was set to 27000 frames per second and the spatial resolution was 64 by 328 pixels. A f=150 mm lens, where f is the focal length, was used to focus the CCD to the knife-edge plane. To overcome the natural flame luminosity of the flame front, the light bulb was set to maximum output. However, as that would damage the CCD sensor, three neutral density filters had to be used. The dynamic range of the camera is 16-bit, so the neutral density filters were chosen to facilitate the whole dynamic range of the CCD during imaging, without over- or under-exposing the CCD. Exposure time was empirically set to $1/99000$ to increase sharpness and reduce blurriness of the image. The camera has a limited amount of memory, 16 GBytes, so high speed images can be obtained for a limited amount of time, which means that the camera has to be triggered in parallel to the glowplug. This also gives the opportunity to measure the ignition delay time, within a time accuracy dictated by the camera recording speed, as will be presented later.

In the literature there is detailed description of different knife-edges. In this work a simple knife edge was used. Both horizontally and vertically placed. No visible difference was observed between the different positioning of the knife edge. So for experimental simplicity, the knife edge was placed horizontally.

The spatial resolution was 0.14 mm per pixel, so the flame speed can be easily calculated between consecutive images using the equation $S = \Delta x \cdot \mathrm{fps}$, where fps is the frame recording speed and Δx the flame front propagation between the two consecutive frames.

A 1951 USAF calibration target was used to focus the camera on the plane of the glowplug. Some consecutive example raw images of the flame propagation in the vessel are presented in Figure 54. The time interval between them is 1/27000 seconds, equal to the frame acquisition rate.

Figure 54 presents some raw images of the deflagration of the gaseous fuels in the vessel. The flame propagates radially from the glowplug, which is the ignition source, towards the walls of the vessel. The flame-front near the wall seems to propagate a bit faster than the rest of the flame-front. This happens because the vessel walls are slightly warmer than the ambient gases. It was shown in Figure 42, that after each experiment, the vessel wall temperature was slightly increasing. The gases being fed into the vessel are much colder than ambient, because they have undergone expansion from the high pressure gas cylinder to ambient pressure. The fan enhances heat transfer from the vessel walls to the gas mixture, but there is a small temperature difference between the wall and gases.

Initially the flame of Figure 54 is spherically shaped and smooth, but as the flame-front propagates, the part of the flame-front located closer to the hot wall, propagates faster than the part located closer to the colder unburnt gases. This temperature difference and subsequent velocity difference of the flame-front, introduces hydrodynamic (also known as Landau-Darrieus) instabilities. These instabilities appear initially in large dimensions and then cascade to the size of thermo-diffusive instabilities. Cellular or thermo-diffusive instabilities develop on the flame surface and, in general, make hard to measure the flame speed free of wrinkles. In this work as pressure was close to atmospheric and the fuel-air equivalence ratio (ϕ) close to unity, the thermo-diffusive instabilities were small. In general, as pressure and fuel-air equivalence ratio (ϕ) increase, the cellular instabilities increase too (Tse et al., 2000). This might be the reason why the images of the flames at later time and higher pressure have more cellular structures.

Figure 55 presents the time lag between the activation of the glowplug and the ignition of the mixture. This time was defined as “ignition delay”. Ignition delay was measured with two different ways. Firstly the ignition delay was measured as the time elapsed between the activation of the glowplug and the sudden increase in pressure, as measured by the Kistler high-frequency pressure transducer. The blue line in Figure 55 presents the results of this method and there is a minimum value of the ignition delay at oxy-hydrogen mixture with 35% Nitrogen molar fraction. The values of measured ignition delay are close to reported values in the

literature, the local minima trend is probably a measurement artifact, caused by the uncertainty in igniting a flammable mixture with a glowplug.

The second method used to measure the ignition delay, was to use the time-stamped imaged grabbed by the high-speed camera. As in similar work in the literature, the time of ignition of the mixture was considered to be the time at which the flame propagation was equal to the flame-thickness. The ignition delay measured with the camera, was in value always a bit smaller than the value measured using the pressure transducer. As with the previous method, the ignition delay measured with this method are close to the values reported in the literature. Unlike the previous method, the ignition delay seems to follow the trend reported in the literature with increasing ignition delay as the Nitrogen mole fraction increases (Zhang et al., 2012, Tang et al.).

The motivation for the measurement of the ignition delay is to quantify the time passed between initiation of the glowplug and actual deflagration of the mixture. This time could have consequently been used as a means of controlling the various operations involved in the experiment and described in Chapter 3. Such operations could have been for example, the injection of the spray, the activation of the camera, etc. However, the time delay between activation of the glowplug and mixture ignition, was not repeatable to nanosecond accuracy from ignition to ignition. The main reason for this behaviour is that a glowplug was used to ignite the mixture. Spark-plugs deliver higher energy density at shorter time, thus making ignition more repeatable. However, as described in Section 3.3.7, the option of using a spark-plug was not explored in this work.

Figure 56 presents the flame speed as measured by the high-speed camera. The edge of the flame front was detected using a threshold on the number of counts collected from each pixel of the CCD. As the intensity of the flame-front is darker than the rest of the image, the threshold for the edge detection was set to 40 camera counts. So the thin line with counts less than 40 is considered to be the flame front. From the movement of the flame-front, the flame speed was measured. A custom-made Matlab code was programmed to extract this information from the raw images. Values of oxy-hydrogen flame speed have not been reported

in the literature with parameter the Nitrogen molar fraction. However for atmospheric conditions flame speed measured here agrees with the literature (Kwon and Faeth, 2001, Aung et al., 1997). Also the trend of reducing flame speed as Nitrogen molar fraction increases, is in accordance to the literature (Tse et al., 2000).

This Chapter presented the chemically pre-heating technique used in this work to simulate engine-like conditions. Before presenting the measurements of the spray in Chapter 6 and Chapter 7, the tracer Laser Induced Fluorescence technique used to measure fuel vapour has to be presented. So, Chapter 5 will explain the reasons for the selection of the LIF technique and the associated tracer.

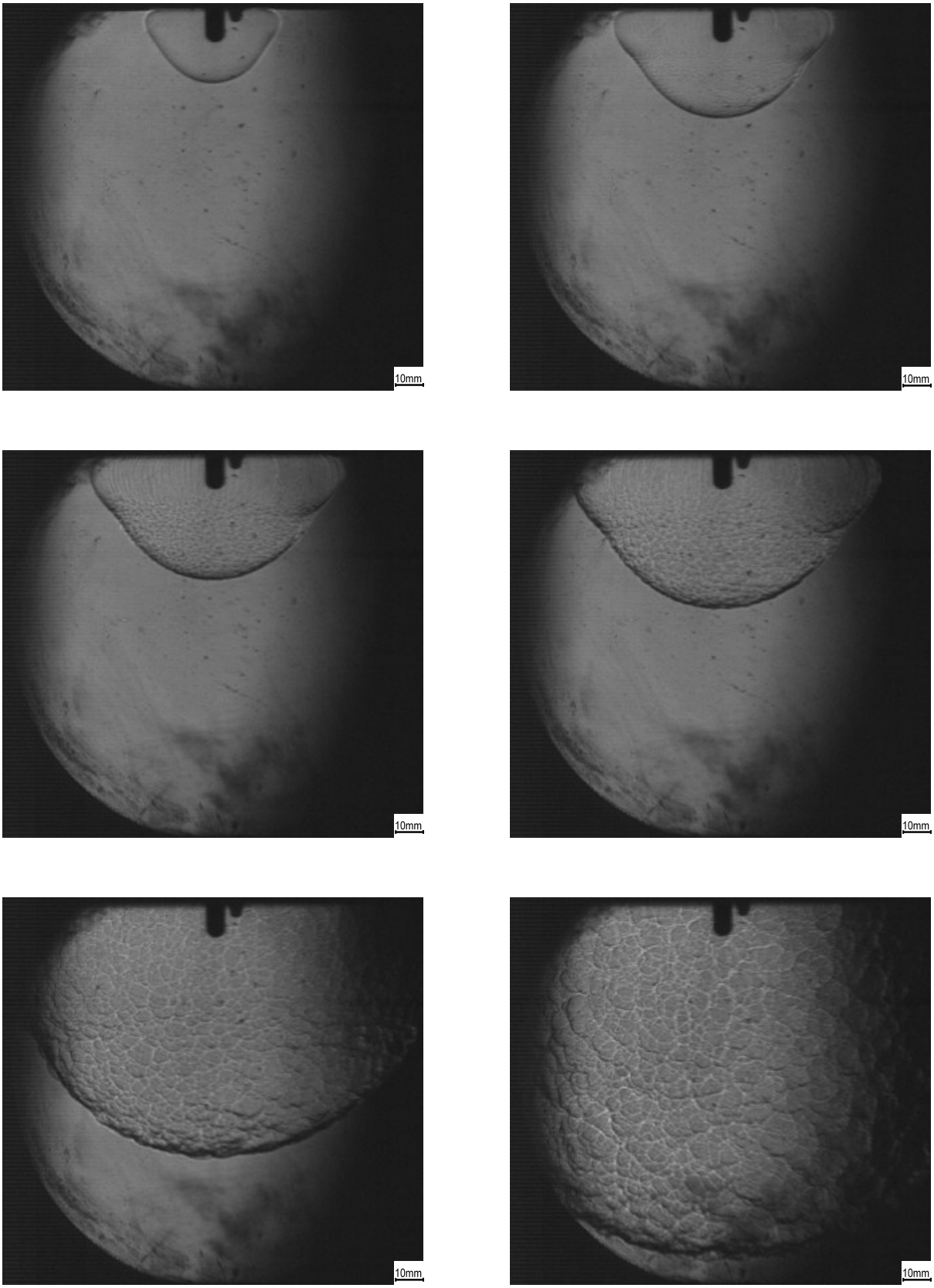

Figure 54 High-speed Schlieren imaging of fuel gas deflagration in the vessel

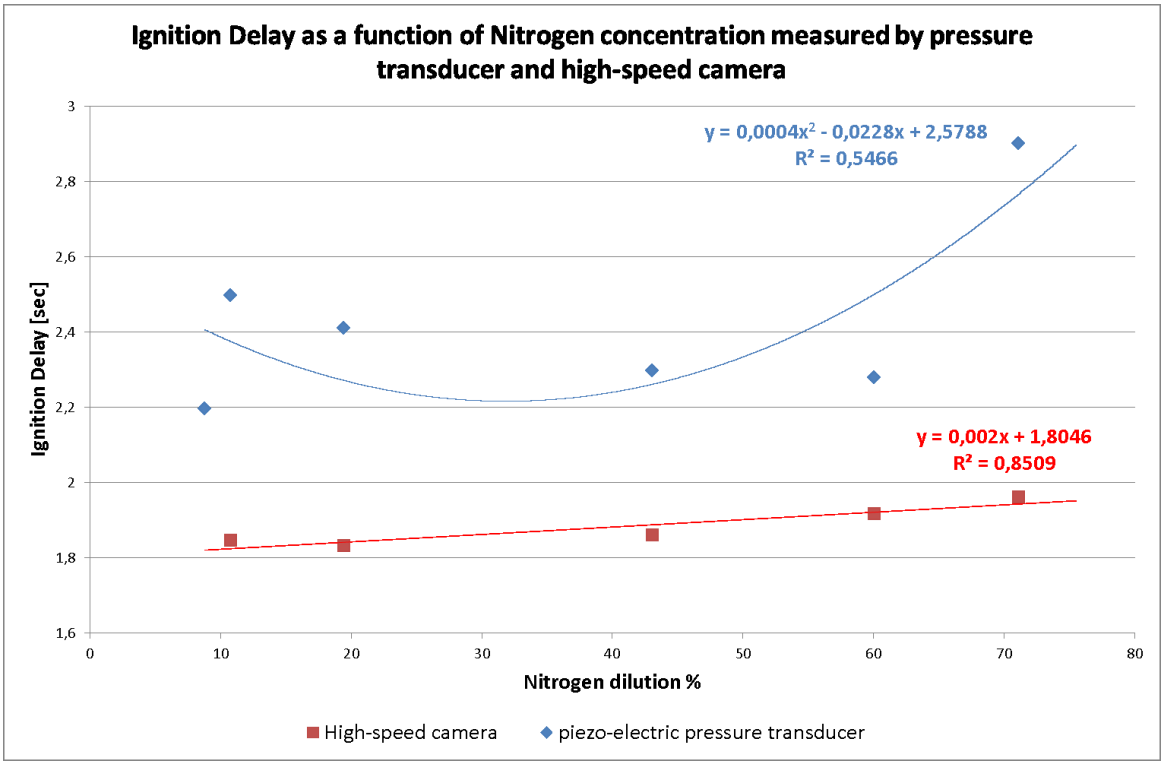

Figure 55 Ignition delay as a function of Nitrogen concentration measured by pressure transducer and high-speed camera

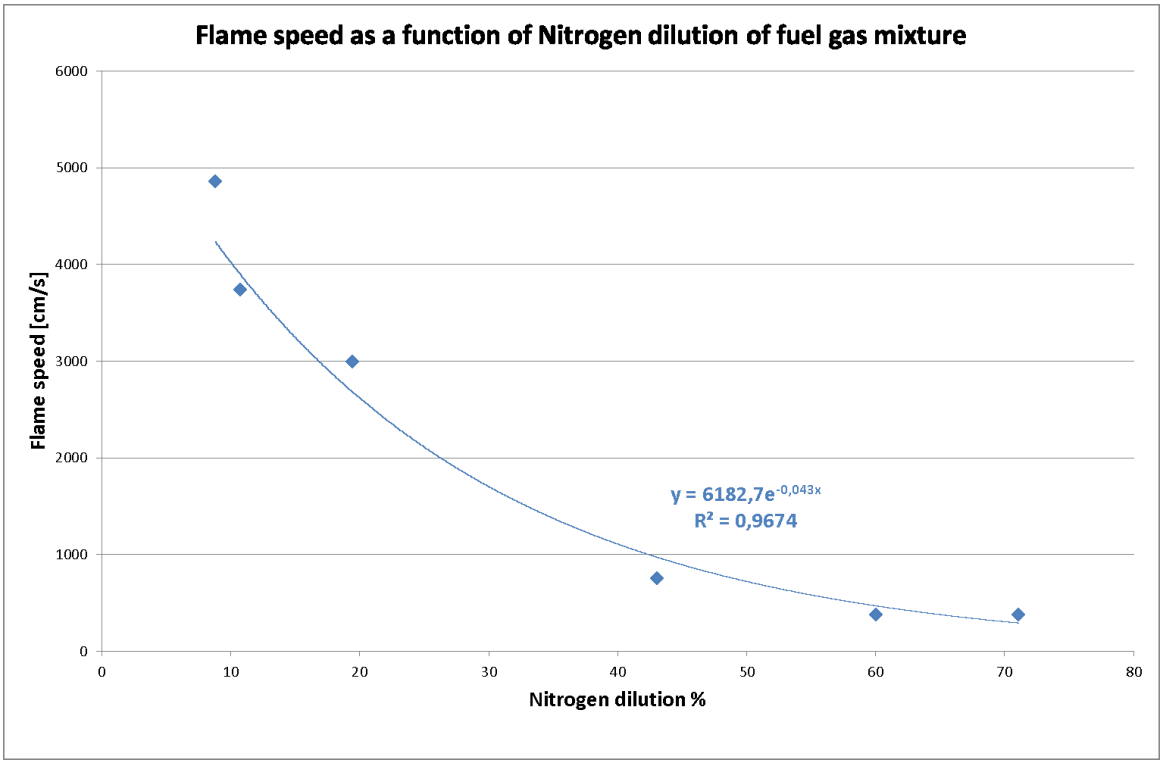

Figure 56 Flame speed as a function of Nitrogen dilution of fuel gas mixture

5. Laser Induced Fluorescence

5.1 Introduction

Laser Induced Fluorescence is a very general term used to describe experimental techniques, where a laser beam is used to excite an atom or molecule and a receiver is used to receive its de-excitation emission. This chapter will initially present the fundamentals of LIF, offer a literature survey on LIF-techniques and then present the LIF technique used in this work to measure the fuel vapour concentration.

5.2 Fundamentals of LIF

Fluorescence is the light emitted from an atom or molecule after it has been excited by electron bombardment or heating or chemical reaction (chemiluminescence) or photon absorption. In the case of Laser Induced Fluorescence, the light emission may be shifted in wavelength relative to the incident light, or occur at the same wavelength (resonance fluorescence). In general, it is desirable to examine shifted emission to avoid potential interferences from particle (Mie) or spurious laser scattering. The fluorescence lifetime is the time that the emission lasts and may vary between 10^{-10} and 10^{-5} seconds.

As will be explained later, in this study the fluorescence originates from a fluorescent dye, or tracer, added in the studied fluid. The experimental setup used in this work is shown in Figure 61. A Nd:Yag laser was used to excite a fluorescence dye and a camera, fitted with an optical filter to cut-off the laser wavelength, was used to collect the fluorescence emission. So assuming a low intensity laser sheet at wavelength λ propagating in the x direction and a single absorbing and emitting species, the total photon emission per unit of longitudinal sheet area, per unit time is:

$$N(x,y,t,\lambda) = \int N\iota(y,z,t)e^{-\sigma(\lambda)\int C(x,y,z)dx}\sigma(\lambda)C(x,y,z)\Phi(\lambda)dz$$

Where:

z is the coordinate transverse to the laser sheet;

y is the coordinate along the laser sheet thickness;

$N\iota(y,z,t)$ is the incident photon flux, which is proportional to the number of photons per unit time per unit transverse area incident on the flow;

$\sigma(\lambda)$ is the molecular absorption cross-section of the tracer in cm^{-1};

$C(x,y,z)$ is the absorbing species concentration in the lower energy level in cm^{-3};

$\Phi(\lambda)$ is the species 'quantum efficiency' for emission (or Stern-Volmer factor) for this transition, which is the ratio of photons emitted to photons absorbed.

Derivation of the above equation will give the following correlation for the collected signal F:

$$F = \frac{hv}{c}\frac{\Omega}{4\pi} lAN_1^0 B_{12} I_v \frac{A_{21}}{A_{21}+Q_{21}}$$

hv photon energy, h Plank's constant, v frequency of emitted fluorescence,

Ω collection solid angle,

l axial extent along the beam from which fluorescence is observed

A focal area of the laser sheet,

$A_{21}/A_{21}+Q_{21}$ fluorescence efficiency

I_v incident laser irradiance

N_1^0 tracer population

A_{21} Einstein coefficient for absorption of the tracer

B_{12} Einstein coefficient for spontaneous emission of the tracer

Q_{21} quenching rate

So the tracer population will be:

$$N_1^0 = \frac{Fc4\pi}{h\nu\Omega lAB_{12}I_\nu}\frac{A_{21}+Q_{21}}{A_{21}}$$

But an excited molecule will not necessarily emit light, it could also lead to dissociation, ionization, energy transfer to another molecule, energy transfer to another internal energy state within the molecule and chemical reaction. These processes, competitive to fluorescence, are termed quenching processes and they reduce the amount of fluorescence and obscure the interpretation of data. If all the quenching data were constant and known, then, in principle analytical corrections could be applied. But quenching data are rarely known, so research in fluorescence is focusing in eliminating or in-situ correcting quenching, ie: saturation, predissociation.

Oxygen causes strong quenching of the fluorescence signal. Quantification of quenching is difficult because it depends on many parameters. So during an experimental study, quenching will vary according to temperature, pressure and species concentration, and as a consequence the relationship between fluorescence intensity and tracer concentration is not constant.

5.2.1 Planar LIF disadvantages

Due to the nature of planar LIF, large optical windows are needed to capture a planar image. Depending on the considered geometry, these large windows could disturb the flow.

Also due to the low intensity of fluorescence signal, an Intensified CCD camera is needed thus limiting the frequency of the framing rate to no higher than 1 Hz.

In order to have quantitative measurements using a LIF technique, quenching from Oxygen will need to be eliminated. The best way to eliminate quenching from oxygen is to obtain measurements in the absence of oxygen, but this limits the technique from being applied in reacting flows (Bruneaux, 2007, Frieden et al., 2002, Koban et al., 2005c, Luong et al., 2008, Schulz and Sick, 2005).

5.2.2 Planar LIF advantages

In general, it is desirable to examine shifted emission to avoid potential interferences from particle (Mie) or spurious laser scattering (Preussner et al., 1998). This is a major advantage of LIF, as the fluorescence signal is of different wavelength than the incident laser light that is used to induce the fluorescence.

The fluorescence emission is independent of the droplet size (since it depends on the tracer concentration) and the direction of detection. However, a high number of droplets, in the irradiated measurement volume of the spray, can cause a big part of the laser irradiance to be Mie-scattered and to excite fluorescence outside of the measurement volume. Thus, no quantitative information of the mass distribution of highly atomized sprays can be drawn (Preussner et al., 1998).

5.3 Tracer-Planar LIF

5.3.1 Need for tracer

Diesel contains many impurities; some of them are aromatic compounds which fluoresce. Many researchers have used this natural fluorescence of Diesel to obtain

measurements. But diesel consists of many different compounds with different behavior both thermodynamically and photophysically, also the proportion of these compounds in the mixture is not constant. So natural fluorescence can only offer semi-quantitative measurements.

5.3.2 The perfect tracer

The ideal tracer should have exactly the same "fluid properties" as the fluid to which it is added and also have good "fluorescence behavior". Also due to the high temperatures and pressures that the measurements are taking place, the tracer should also have good resistance to pyrolysis.

The term "fluid properties" refers to the viscosity, density, thermodynamic behavior, surface tension of the tracer. So the tracer should ideally not affect the droplet formation, convection, evaporation, diffusion, reactivity and reaction rate as the fluid. In the case where the evaporation of the fluid is of interest, the transition from liquid to gas should happen at the same time both for the fuel and the tracer. This can be checked either by the distillation curves of the tracer and fluid, or by using a simple model based on their boiling points.

The ideal tracer would have very strong fluorescence yield Φ directly proportional to the studied property and not be affected by the ambient conditions. So there should be very low sensitivity to quenching.

If autoignition of diesel is to be studied, the cetane number (CN) of the tracer is of major importance. Cetane number of a fuel is defined as the percentage by volume of normal cetane in a mixture of normal cetane and alpha-methyl-naphthalene which has the same ignition characteristics (ignition delay) as the test fuel when combustion is carried out in a standard engine under specified operating conditions. Usually the tracer tends to have a much lower CN than the pure fuel, so the auto-ignition delay of the mixture fuel-tracer would be longer than the auto-ignition delay of pure fuel (Bruneaux, 2007).

Numerous tracers have been used to visualize mixing and reacting phenomena occurring in fuel-sprays. Some of the most popular tracers are acetone, toluene, biacetyl, 3-pentanone and naphthalene. It is very important to clarify at this point that tracer's fluorescence characteristics change with temperature and pressure, as will be presented.

5.3.3 Tracers applied at low temperature and pressure conditions

Dimotakis et al. (1983) studied the structure and the dynamics of a round turbulent jet by a tracer-LIF technique. Rhodamine 6G or sodium fluorescein was used as a tracer in an air jet and the obtained images demonstrated the dominance of large-scale vertical structures in the dynamics of fully developed turbulent jets. Researchers from Heidelberg University (Duwel et al., 2004b) studied rhodamine doped evaporating water droplets, which were heated by a CO_2 laser. The authors noticed the importance of oxygen-quenching and faster evaporation of water than the rhodamine tracer. Also Guillard et al (Guillard et al., 1998) doped a turbulent water jet with rhodamine 610 chloride to study air entrainment while the jet impinges onto a flat surface. Post-processing of the collected image was applied to acquire quantitative data.

Because of its simplicity in use, non-toxicity and availability, acetone is one of the most favored molecules used as a tracer in LIF techniques. Franke et al (Franke et al., 2005) applied LIF to image the acetone seeded fuel and the distribution of hydroxyl and nitric oxide of the burned gas. LIF data were used to explain measurements from an ionization sensor. The cooling of the burned gases by the ionization sensor was observed and the NO mole fraction was correlated to the sensor signal. Acetone was also used by Lund Institute of Technology (Nygren et al., 2002) seeded in ethanol in an attempt to visualize three-dimensional fuel iso-concentration surfaces for different crank-angle positions in an HCCI engine. It was proved that HCCI combustion relies on distributed reactions and not on flame propagation. Also, the spatial structure of the oxidation process was revealed in greater detail. An interesting technique combining simultaneous two-plane Rayleigh scattering from propane and LIF from seeded acetone was presented by Su and Clemens (1999), in order to measure three-dimensional

scalar gradient and scalar energy dissipation rate of a gas-phase turbulent flow. A “knife-edge” technique was applied to correct for the laser sheet energy profile.

Some researchers experimented with many tracers before finally choosing the best tracer for the application. For example, Le Coz et al. (1994) applied a quantitative LIF technique to measure the thickness of liquid fuel layers formed on intake pipe walls of port-injection spark-engine engines. Iso-octane was used as fuel and 3-pentanone, 4-methyl 2-pentanone, 2-hexanone, 2,3-butanedione, 2,3-pentanedione and 2,3-hexanedione were tested under various conditions. Phenomena like the impact of spray and deposition of fuel and the displacement of liquid waves were observed. They concluded that out of the tested tracers, ketones, 2-hexanone and 2,3-hexanedione were the best for observing the liquid phase of the fuel.

Koban et al. (2002) introduced a double-tracer LIF technique, in which toluene and 3-pentanone were used to measure oxygen concentrations in vapour-fuel/air mixtures, by taking advantage of the different responses of toluene and 3-pentanone to collisional quenching by molecular oxygen. Toluene has also been used by Hoffmann et al, who developed a LIF technique for three-dimensional concentration measurements that applied to a nitrogen/air mixing flow seeded with toluene and to a methane/air flame where OH concentration was measured. The authors were satisfied by the high spatial resolution but still some artifacts occurred when the observed structures were close to parallel to the observed intersection line.

Many exotic tracers have been used but not proved to be effective. Munsterer and Jahne (1998) used a tracer HCl LIF technique to measure one-dimensional vertical concentration profiles of dissolved gases in the aqueous mass boundary layer at a wavy interface. Van Cruyningen et al. (1990) observed an atmospheric nitrogen spray seeded with biacetyl using LIF and quantitative concentration measurements were made. Hasegawa et al. (2007) applied a LIF technique to measure two-dimensional gas-phase temperature of phosphor seeded air in an optical engine with 5% accuracy in the region of 600-1200 K. In Hokkaido University, a technique for simultaneous measurement of temperature and concentration was applied to an argon jet injected in hot argon-iodine ambient environment. Iodine was excited by a Nd Yag laser and visualized at 580 and 625nm. The error in

measurements was estimated to be less than 15% for temperatures up to 200°C (Kido et al., 1998).

5.3.4 High pressure and temperature TRACER-LIF

At high pressure and temperature the photo-physical properties of tracers are altered. In general, with increasing temperature the fluorescence emission wavelength tends to shift towards the "red" and with increasing pressure the fluorescence intensity tends to decrease. But this is a very general rule that depends on the tracer-molecule and the excitation wavelength. This section reviews previous work done at high pressure and temperature, regarding tracer-LIF and the modification of the fluorescing properties of tracers.

5.3.4.1 Rhodamine

Duwel used a diode-pumped Nd:YAlO3 laser system emitting at 671 nm and tested Rhodamine 800 and Atto 680 as tracers for LIF concentration measurements in a diesel/ethanol mixture. Though Atto 680 was found to have higher quantum yield, its fluorescence intensity dependency with tracer concentration was non-linear! However, Rhodamine 800 as a fluorescent tracer was found to have shown promising results(Duwel et al., 2004a).

5.3.4.2 3-Pentanone

The photophysics of 3-pentanone is intensively studied for application as a LIF tracer. Ossler and Alden measured the fluorescence behavior of 3-pentanone and acetone at temperatures between 323 K and 723 K and at pressures of nitrogen and air between 0.001 MPa and 1.0 MPa in a cell, using a picosecond laser radiation at 266 nm. Nitrogen was found to have a stabilizing effect on the fluorescence as the effective lifetimes seem to reach asymptotic value with increasing pressure, while oxygen and temperature were found to have a quenching effect on the fluorescence emission. It was found, that for the studied conditions, acetone was more sensitive to temperature and pressure than 3-pentanone (Ossler, 1997).

Researchers from Bosch (Preussner et al., 1998) used iso-octane seeded with diethylketone (3-Pentanone) injected in an optical engine and in a combustion vessel. The importance of the shape of the combustion chamber was emphasized. The vessel reached up to 5.6 bar and 180^{o}C. Davy et al. (2003) studied numerically and experimentally the evaporation characteristics of the 3-Pentanone-iso-octane mixture with application to LIF techniques and they observed that the evaporation characteristics of the 3-Pentanone-isooctane mixture was controlled by the relative mole fractions of the two components contained within the liquid phase.

Some applications of 3-pentanone high pressure temperature and pressure LIF are by Graf et al. (2001), who studied a mixture of iso-octane/n-heptane doped with 3-pentanone in an optically accessible 4-stroke engine. Simultaneously with the tracer LIF, the Formaldehyde molecule produced during combustion was observed using a Formaldehyde-LIF technique. Tracer decomposition and signal attenuation were also noticed. Richter et al used an endoscope to collect LIF images from a reciprocating engine fueled with iso-octane doped with 3-pentanone. The need of sufficient light entering the cylinder head was stressed, but the technique seemed to give promising results (Richter et al., 1998). Einecke et al. (2000) used a two-line LIF technique on iso-octane doped with 3-pentanone that was used in a two-stroke optical engine to quantitatively measure concentration, temperature and fuel/air equivalence ratio. Two dimensional planar temperature was measured with an accuracy of 4% and could be used to remove the temperature-dependency of the tracer for concentration measurements. Ekenberg and Johansson (2000) applied a Planar LIF technique using iso-octane doped with 3-pentanone that was injected in an optical engine to study the fuel distribution in the cylinder of the air assist direct injection engine with central injector and spark-plug. It was found that it is difficult to get significant stratification of the fuel around the spark-plug during ignition if the piston is flat. Koban et al. (2005c) studied in an optical engine and in a cell and modeled the photo-physics of 3-pentanone in the range of 0.45 to 8 bar and 328-600 K.

5.3.4.3 Toluene

Toluene is a widely used tracer at high temperatures and was applied by Koban et al in a temperature range of 300-650 K and pressure of 1 bar in a nitrogen/oxygen bath to study the oxygen-quenching. It was concluded that toluene-emission signal was not proportional to the fuel to air LIF-signal for engine-like conditions. A single-wavelength excitation, two-color detection toluene LIF technique was applied to measure in-cylinder temperature distributions in a motored spark-ignition engine (Koban et al., 2005b). The simultaneous measurement of two-colors of toluene emission made unnecessary any correction for laser pulse energy, sheet profile and tracer concentration (Luong et al., 2008). Koban et al. (2005a) also developed a photo-physical model for toluene and found that oxygen quenching is not the dominant de-excitation path for high pressure and temperature conditions thus the FARLIF signal is erroneous. Later, Koban and Schulz (2008) measured the absorption and emission characteristics of toluene at 1 bar in the temperature range of 300-700 K in a cell placed in a furnace. Measurements took place in the presence of oxygen and was found that intermolecular non-radiative decay increase strongly with temperature and cannot be neglected. Zimmermann et al. (2006) measured the fluorescence lifetime of toluene excited at 248 nm in a nitrogen bath at 1 bar but in the temperature range of 296-625 K. It was observed that fluorescence lifetimes decrease with increasing temperature and a time-correlated single-photon counting LIF technique was suggested for temperature measurements of tracer concentration-independent gas phase. At higher pressures, 0.45 to 8bar and 328-600 K, Koban et al. (2005c) studied and modeled the photo-physics of toluene.

5.3.4.4 Acetone

Extensive work has been done on acetone as a LIF tracer at high pressure and temperature. Thurber et al. (1998) measured and modeled the absorption and fluorescence of acetone from 300 to 1000 K at atmospheric pressure with application to LIF temperature diagnostics. Tran et al. (2008) measured and modeled the fluorescence emission of vapor and liquid acetone to temperature up to 600 K and pressure up to 60 atm. An interesting result was

that oxygen quenching does not affect liquid fluorescence as compared to vapor fluorescence. Tamura et al. (2001) applied acetone and OH LIF in an optical engine to investigate effects of valve timing, back pressure and ignition time. Methane was used as fuel and was doped with acetone that acts as tracer for the unburned fuel. It was found that the in-cylinder flow changes suddenly with opening of the exhaust valve and oxidation of the crevice flow is affected. In Leeds University (Clarkson et al., 2001) acetone LIF was applied to measurements in a rapid compression machine. Acetone was either seeded in inert gases when non-reacting flow was studied or was the product of the exothermic decomposition of di-t-butyl peroxide vapor. It was concluded that no quantitative data could be measured for the exothermic decomposition of di-t-butyl peroxide because there are no iso-thermal conditions, as heat was produced during the decomposition. But more vital to this work was their observation of thermal decomposition of acetone at temperatures above 900 K.

5.3.4.5 Other tracers

Many researchers have tried many molecules for high pressure and temperature conditions. Researchers from University of Hiroshima (Yoshizaki et al., 1996) doped n-hexane with pyrene $C_{16}H_{10}$ and, using a LIF technique, measured the temperature of the liquid phase of the injected mixture in a combustion bomb. It was shown that laser-based technique could be used for thermometry at high temperature environments. Davy et al applied two-dimensional Mie-scattering and laser-induced-fluorescence techniques to investigate the effects of fuel composition on mixture formation in an optically accessible direct injection spark ignition engine. 2,3-Butanedione was used as a tracer in iso-octane fuel and in a three-component research fuel composed of iso-pentane, iso-octane and n-nonane. It was found that composition of the fuel influences the development of the spray (Davy et al., 2000).

5.3.4.6 Mixture of tracers

Some researchers have experimented with a mixture of tracers at high temperature and pressure, for example Gervais et al. (2002) used an optically accessible engine to apply a FARLIF

technique based on iso-octane doped with benzene and tri-ethyl-amine(TEA) mixture. Blotevogel et al. (2004) used triethylamine (TEA) LIF to study quantitatively the mixture formation process in a hydrogen engine. The LIF technique was verified by simultaneous Raman scattering measurements. Dawson and Hochgreb (1998) applied a qualitative LIF technique to study the liquid fuel flow in the intake-valve region of an optical engine. Iso-octane fuel was doped with acetone and 3-pentanone. But these techniques are sensitive to quenching among the tracers.

5.3.4.7 Tracer-LIF in combination to conventional techniques

Many researchers combine a tracer-LIF technique with another technique to test the LIF technique. Depussay et al. (1998) used a Catalytic Hot Wire Probe in an optical engine to compare results from a LIF technique and good agreement was found. Bruneaux (2007) used a tracer-Planar-LIF technique combined with high-speed chemiluminescence imaging in the presence of oxygen in a high pressure and temperature combustion vessel to study mixing and autoignition processes of Diesel sprays. It was concluded that due to the high fluorescence quantum yield of 5-nonanone, visualization of the fuel was possible in the presence of oxygen with global illumination and in conditions of a typical engine. However, due to these reasons, the technique was not quantitative.

5.3.4.8 Nonanone

Nonanone is a promising tracer at high pressure and temperature conditions: Duwel et al. (2004b) applied 5-Nonanone LIF doped in n-decane in a combustion vessel to measure fuel vapor distribution. However, as Nonanone is a ketone and the number of Carbon atoms in the Nonanone molecule is smaller than that of the typical Diesel, Nonanone has a boiling point lower than the typical Diesel, as shown in Table 14. This means that Nonanone cannot be used to study the Diesel fuel evaporation.

5.3.4.9 Naphthalene

The pyrolytic behavior of naphthalene molecules has been studied extensively by many researchers (Kinney and DelBel 1953; Kjell and Sheridan 1985; Klusmeier et al. 1989; Lang and Buffleb 1958; Ondruschka et al. 1990; Somers, McClaine, and Wornat 2007; Taylor et al. 1993; Herbinet et al. 2007). Since diesel spray injection is of the order of 1 ms at most, pyrolysis of the naphthalene tracer is not a significant factor in this work.

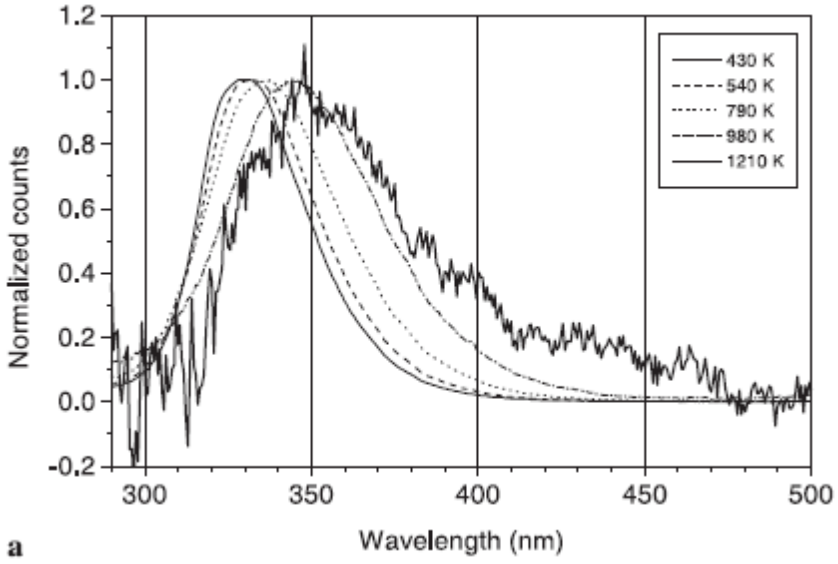

Figure 57 emitted fluorescence for naphthalene (Ossler et al., 2001)

Methyl-naphthalene has been chosen as a fluorescence tracer for this work because of the high energy absorption at Nd:Yag laser wavelengths (266 nm), the boiling temperature close to the Dodecane pure fuel boiling temperature, the high quantum yield the long fluorescence life-time at high temperature and pressure conditions (Bruneaux et al., 1999). Ossler et al. (2001) took measurements of naphthalene and other aromatic hydrocarbons in a cell at atmospheric pressure at a temperature range of 400-1200 K, Figure 57. They noticed that at low temperature the emitted fluorescence spectrum is a smooth function with a peak at about 325 nm. As temperature is increased, the peak of the emitted fluorescence spectra is red-shifted. They noticed that for temperatures above 1000 K the fluorescence signal had

strong noise. Ossler et al. (2001) did not comment on the origin of the noise, but Kaiser and Long observed that as temperature is increased the intensity of the fluorescence signal of methyl-naphthalene decreases, Figure 58. So, the Signal-to-Noise-Ratio will decrease, probably causing the high noise observed in Figure 57 for high temperatures (Kaiser and Long, 2005). In conclusion, Ossler et al. (2001) observed that a small change in temperature has a large effect on fluorescence.

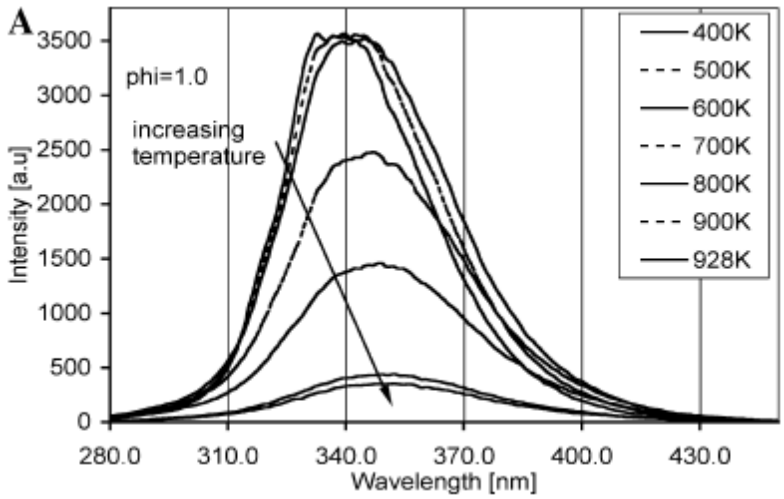

Figure 58 Fluorescence spectra of Methyl-Naphthalene (Kaiser and Long, 2005)

Ossler et al. (2001) also observed that naphthalene emitted fluorescence is affected by the concentration of the tracer in the fuel as shown in Figure 59. In the literature there is a lack of data of fluorescence on Naphthalene as a function of pressure. In general, however, “large” ketone and aromatic molecules (3-pentanone, toluene) reach a plateau of fluorescence signal at high pressure due to collisional transfer of the excess vibrational energy (Ossler et al., 2001, Kaiser and Long, 2005, Koban et al., 2005c) Figure 59.

The behaviour of Methyl-naphthalene tracer described above has been used in the literature for quantitative images. However, the conditions under which this quantification took place, were conditions of constant temperature and constant tracer concentration. The next section will investigate the feasibility of quantifying the LIF images taken in the vessel.

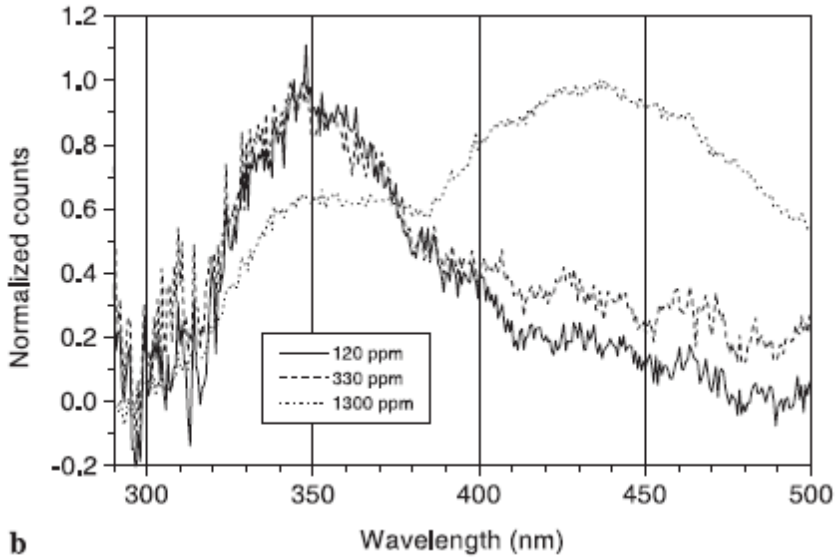

Figure 59 Fluorescence spectra of Methyl-Naphthalene (Ossler et al., 2001)

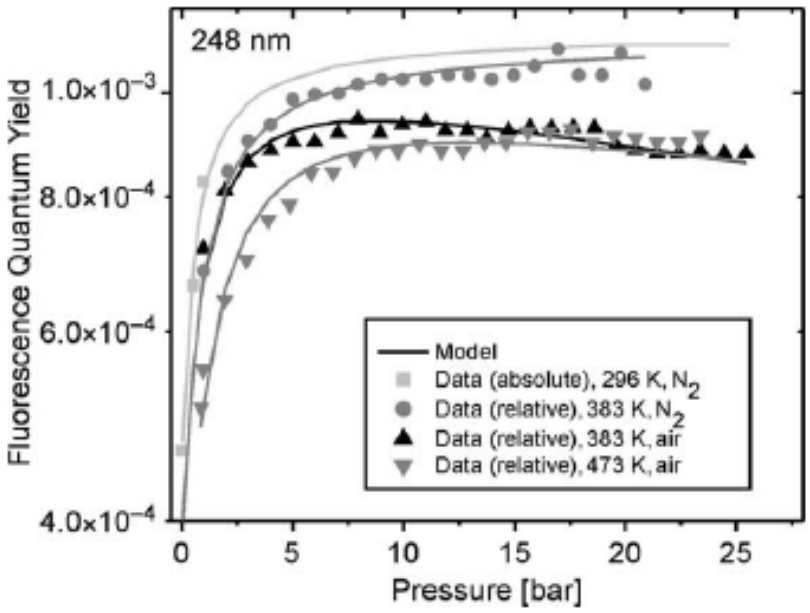

Figure 60 Fluorescence quantum yield of 3-Pentanone as a function of pressure (Koban et al., 2005c)

	Boiling °C	MW	Density (g/cm^3)	Viscosity
Acetone	56			
Anthracene	340	178	1.25	
Azulene	242	128	1.037	
Benzene	99			
DEA	217			
DMA	193			
Fluorene	295	166	1.202	
Naphthalene	218	128	1.14	-
Methyl-naphthalene	240	142	1.001	
Nonanone	192	142		
3-Pentanone (diethylketone)	99			
Pyrene	404	202	1.27	
TEA (triethylamine)	89			
TMPD	260			
Toluene	111			
Typical Diesel	200-350	148		
Hexadecane	287	226		
Dodecane	216	170	0.75	1.34 at 25°C
Decane	174	142	0.73	0.92 at 20 °C
Octane	125	114	0.7	0.542 at 20 °C
Iso-Octane	99.3	114	0.68	
Heptane				

Table 14 Properties of tracers and pure fuels

5.4 Quantifying LIF

5.4.1 Experimental technique

A Nd:Yag laser with doubled frequency was used to produce a laser beam at 266 nm that was formed in a sheet of thickness 0.5 mm and height 15 mm. A Schott BG3 bandpass filter was fitted in front of the camera to block the laser frequency. An Andor Intensified CCD camera was used to capture images. Images were processed by a custom-made C++ code. A time-averaged intensity profile of the laser beam was measured by the knife-edge technique and the beam profile was following a Gaussian distribution, with intensity being higher in the center. The laser was operating in a pulsed mode with a repetition rate of 10 Hz. The average pulse energy was measured to be 60 mJ. As will be shown later, this was sufficient to produce a LIF signal adequately collected by the camera.

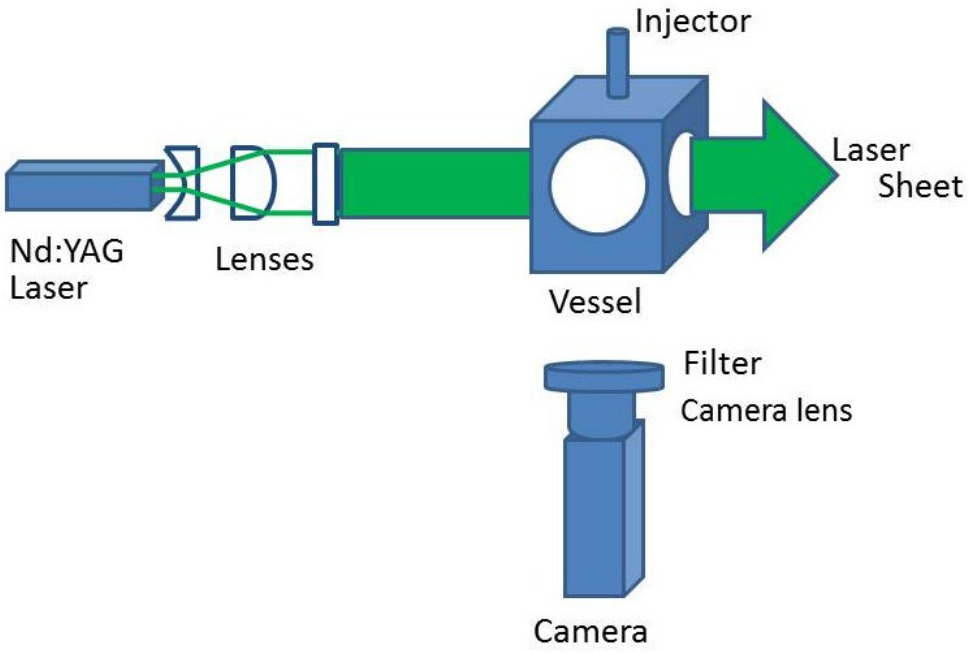

Figure 61 LIF experimental setup

In this work, measurements will take place in absence of Oxygen, in order to avoid combustion of the spray and to avoid interaction of the heat produced from combustion, with spray development. Also avoiding combustion of the fuel spray, avoids the interference of

combustion light with the fluorescence signal. Finally, as in the test volume there will be no oxygen, oxygen quenching of the fluorescence is avoided. However, no simultaneous measurements of air-entrainment and combustion will be possible (Bruneaux, 2007).

5.4.2 Image corrections

The images taken by the camera do not faithfully represent the measured flow property; some corrections are required before the camera-images can represent quantitative information. So if $S_{tot}(x, y, t_i)$ is the signal acquired on the (x, y) location of the CCD array, $S_{tot}(x, y, t_i)$ is proportional to the number of photons incident on (x, y) and is a function of the exposure time ti and of the array readout time t_{ro}. The information of interest $S_e(x, y)$ is thereby given by the equation:

$$S_{tot}(x, y, t_i) = w(x, y)[L(x, y)S_e(x, y) + S_{back}(x, y, t_i)] + S_{dark}(x, y, t_{ro})$$

$$S_e(x, y) = \frac{S_{tot}(x, y, t_i) - [w(x, y)S_{back}(x, y, t_i) + S_{dark}(x, y, t_{ro})]}{w(x, y)L(x, y)}$$

where S_{back} is the signal from the unwanted background, S_{dark} is the signal from a dark image, which is a fixed image taken with all the lenses mounted on the camera but covered so that no light "enters the camera", $w(x, y)$ is the "white-field" response function which describes the signal variation on a uniformly white object.

In the beginning of the experiment a "black image" was taken. Black image is the image taken with all the lenses mounted on the camera but covered so that no light "enters the camera". At the beginning of every set of measurements, a background image was taken, this is an image of the focusing plane, illuminated with the laser sheet, but without any flow.

5.4.3 Laser sheet intensity profile (Dye cell)

When the laser is operating in pulsed mode, it is known that the produced pulses are not exactly the same. This is an important factor that has to be taken into account for quantitative measurements (Hult et al., 2005, Seitzman et al., 1994). In order to experimentally "visualize" the laser sheet intensity profile, a dye cell was purpose-build. As shown in Figure 62, this is a box with two quartz windows so that the laser sheet can pass through. The cell was filled with acetone vapour, which has very high fluorescing yield, so the acetone fluorescence signal was collected by a CCD camera and provided the intensity distribution of the laser sheet. The sheet was Gaussian in intensity but not necessarily with the same energy from pulse-to-pulse.

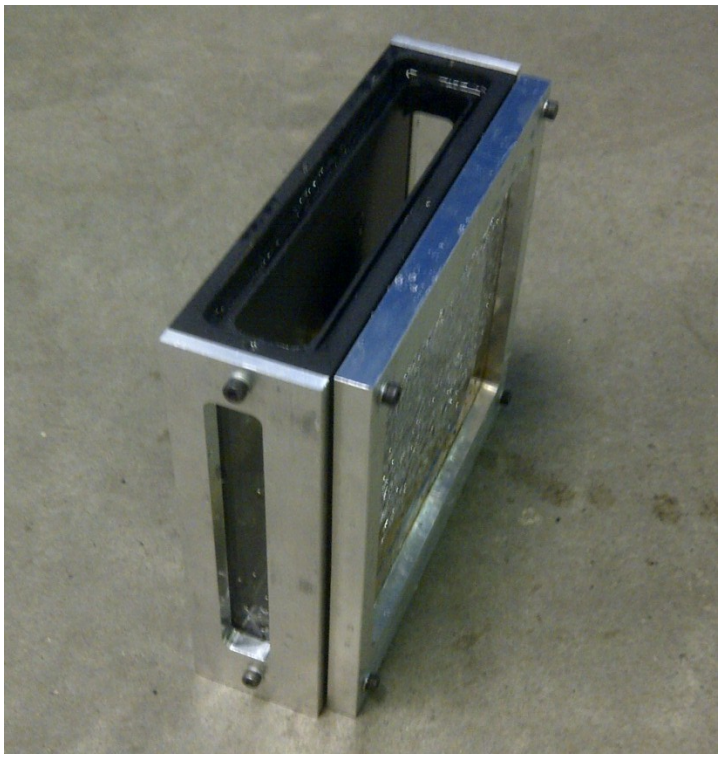

Figure 62 Photo of purpose-built dye cell

Figure 63 presents the average laser sheet intensity profile of 100 laser pulses. This profile was produced by exciting, with the Nd:YAG laser sheet, the saturated acetone vapour

environment in the dye cell presented in Figure 62. The laser sheet propagates from the right of the photo to the left, the laser absorption is quite visible. Laser absorption is defined by the Beer-Lambert law and many researchers are taking this absorption into account, however for the scope of this work and the lean in tracer mixture, the laser absorption is not an issue. Some horizontal lines appear, which are due to experimental flaws in the optics and laser. These lines are typical in LIF measurements and are removed from the final photos as described in Section 5.4.2. This profile in very important in distinguishing which part of the measured LIF signal is due to tracer concentration and which part is due to different intensity along the horizontal axis. To this end, Figure 64 presents the average vertical laser sheet intensity profile of the 100 images along the horizontal laser sheet axis.

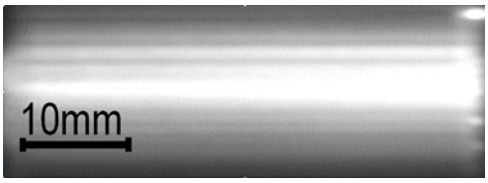

Figure 63 Photo of laser sheet profile in the dye cell

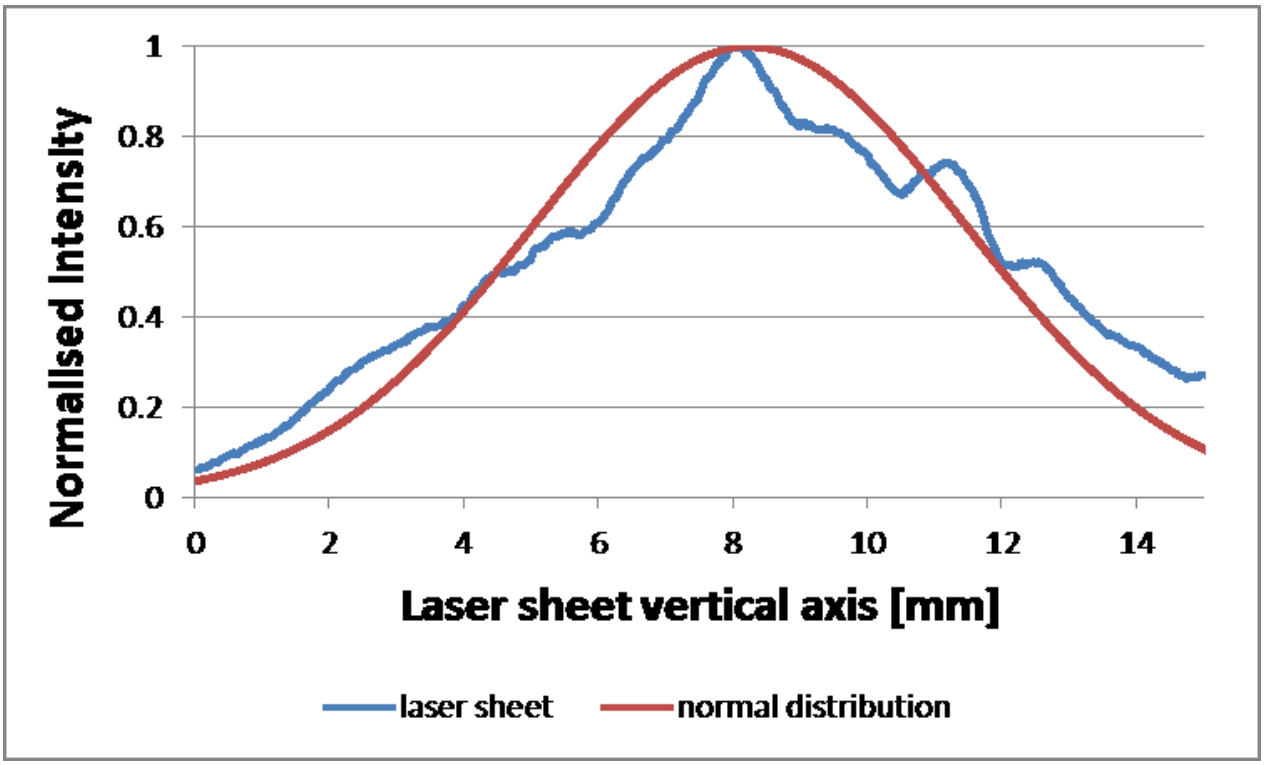

Figure 64 Average laser sheet intensity distribution along the vertical axis

A pulse-to-pulse monitoring of the sheet energy would require a more complicated experimental setup with a percentage of the pulse energy being diverted to the dye cell, thus reducing the spray LIF-signal, and a second CCD dedicated to imaging the dye cell. Also the knowledge of the energy of the sheet would not provide extra information.

5.4.4 Laser sheet attenuation

As the laser sheet propagates through the tracer, photons are absorbed by the trace according to Beer-Lambert Law, so from the initial laser sheet intensity, a small fraction will be absorbed by the tracer. Stoffels et al. (2008) presented a method for correction of local non-uniform laser attenuation in Planar LIF techniques. Duwel et al. (2004b) also presented interesting techniques correcting for beam steering and laser attenuation. However, because the concentration of the tracer is very low and the absorption cross-section small, the laser

sheet attenuation can be ignored in this setup. Though some researchers have taken it into consideration with little or no effect at their results (Haudiquert et al., 1997).

5.4.5 Temperature, pressure and tracer concentration

Section 5.3.4.9 quantified the fluorescence behaviour of Methyl-naphthalene tracer with pressure and temperature. However, these quantifications took place under constant conditions of temperature, pressure and tracer concentration. In this work, the spray is injected into a high pressure and temperature environment. The ambient pressure and temperature are known, also the temperature of the injected liquid is known. However, the temperature of the spray is unknown, as it absorbs heat from the ambient both for warming up and evaporating, as will be presented in Chapter 7. Additionally, the boiling temperatures of Dodecane and Methyl-naphthalene are not matched exactly, as presented in Table 14. The Dodecane with boiling temperature of 216^{o}C will evaporate earlier than the Methyl-naphthalene with boiling point of 240^{o}C. This will result in an un-even concentration of the tracer in the vapour mixture.

To overcome these problems and produce quantitative measurements of the vapour concentration, even if the pressure after injection is considered constant and uniform, quantitative information is needed on the temperature distribution and the tracer concentration distribution in the vapour mixture. In the literature there has been some effort recently to simultaneously acquire information about spray temperature and vapour concentration (Tea et al., 2011). However, this is done under the assumption of uniform distribution of the tracer in the pure-fuel vapour. Based on this assumption, a two colour measurement had been suggested to provide quantitative measurements of the vapour concentration. Additionally, these two-colour techniques require the use of double cameras or of an image doubler on one camera. As a result, the counts collected on each pixel of each camera or camera sub-area, need to be calibrated to count for the same number of photons. This calibration introduces a large experimental uncertainty, thus making the technique semi-quantitative.

For the scope of this work, which is the study of the spray evaporation under different ambient environment, such a method would introduce great complexity and not offer any advantage over the use of a single-colour tracer semi-qualitative imaging. The next chapter will present the case of a non-evaporative spray and, in particular, Section 6.5 will present the images produced using this technique. Later in Chapter 7, the measurement of an evaporating spray will be presented.

6. Non-Evaporating Spray

6.1 Introduction

In Chapter 2 there was no distinction between evaporating and non-evaporating spray. In general it is difficult to make such a distinction, but in the literature, sprays at ambient temperature and pressure sprays are referred to as non-evaporating. As shown in Chapter 2, the ambient pressure influences the spray penetration and droplet break-up. However, for fixed ambient pressure, this work will demonstrate in this chapter and in Chapter 7 that temperature is the main parameter influencing spray evaporation. For this reason in this chapter, measurements on sprays at ambient temperature will be presented. Pressure was regulated by a high pressure regulator.

6.2 Back illumination

6.2.1 Experimental setup

The Schlieren technique can visualise the second derivative of the refractive index as was presented in Chapter 4. In this section, to visualise the non-evaporative spray, a different technique was used and Figure 65 shows the experimental setup used for the back illumination measurements of the spray. The spray was back illuminated using a standard 12 V 45 W automotive light bulb and a paper diffuser was used to even out luminosity. Homogeneity of light source after the diffuser was optically checked in the grabbed images.

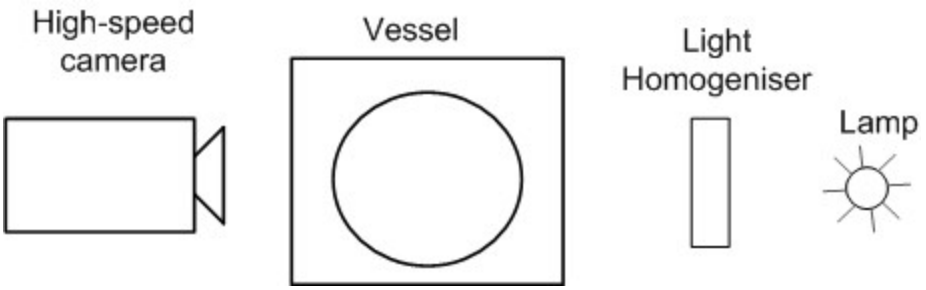

Figure 65 Back illumination high-speed experimental setup

As the spray injection lasts for a very short time, of the order of 1 ms, to obtain good temporal resolution of the injection process, a high speed camera was used. In this work, a high speed camera (LaVision HighSpeedStar 6) was used to grab images of the spray. The acquisition speed was set to 15000 frames per second. However as there is a trade off between temporal and spatial resolution, the resolution was set to 512 by 512 pixels, which was considered sufficient to capture clear images of the sprays using a f=150 mm lens, where f is the focal length. The spatial resolution was 0,14 mm per pixel. Some consecutive instanteneous sample raw images appear in Figure, the time interval between them is 1/15000 seconds.

The camera was triggered by the cRIO and acquisition paused at the end of every spray, allowing for the vessel's nitrogen atmosphere to be purged and reheated. When the 16 GBytes camera memory was full, the images were copied to the computer's hard drive and the process continued.

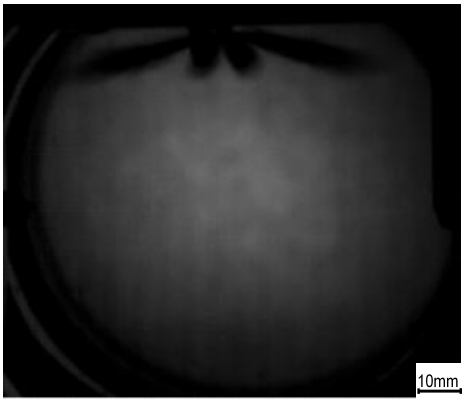

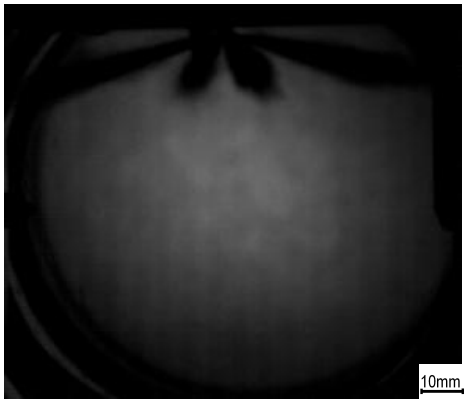

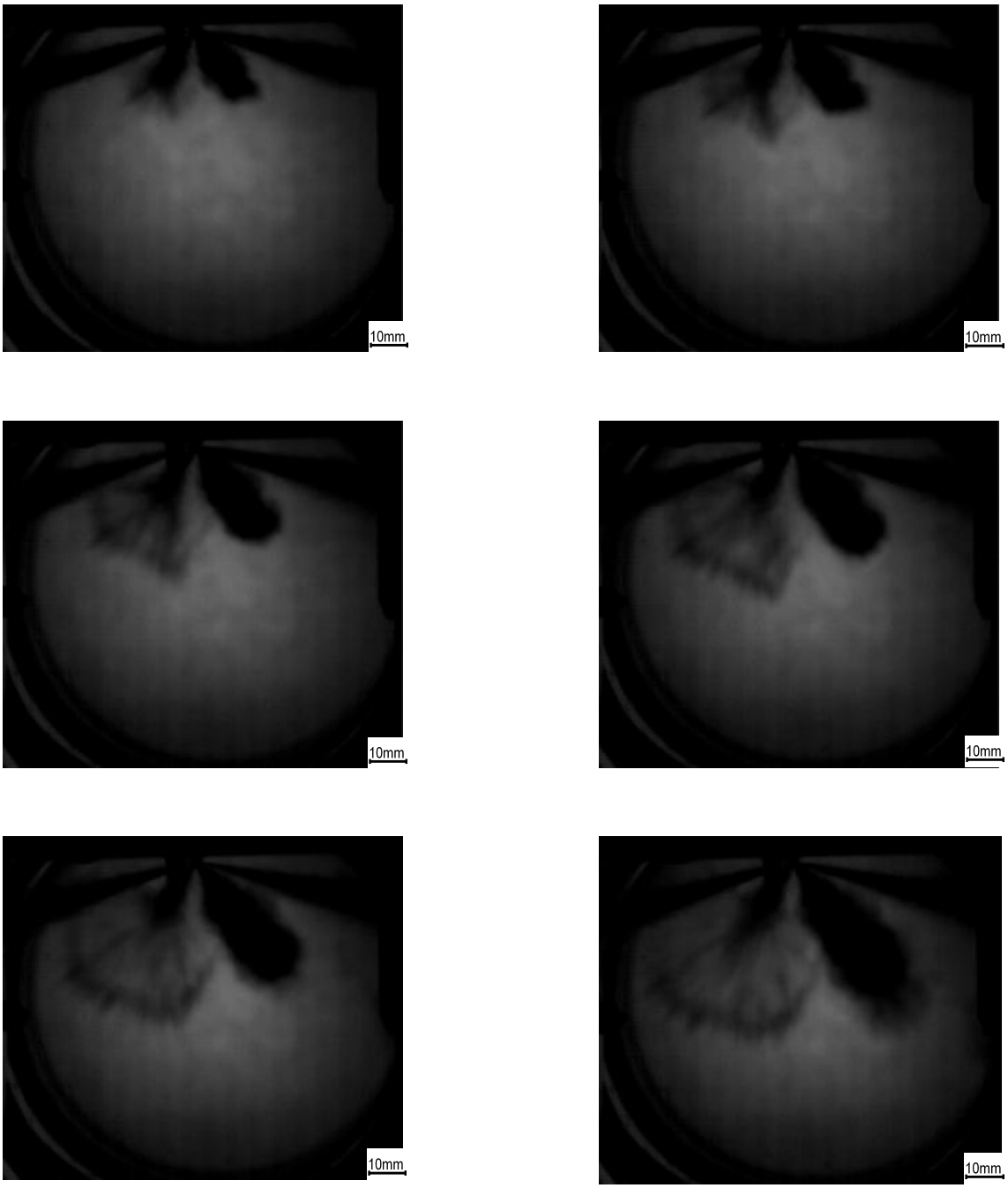

Figure 66 Typical back illumination imaging raw photos of non-evaporative spray at 9bar ambient pressure

The injector and injector mount were described in Chapter 3. The nozzle produces six sprays, with two aligned to perpendicularly impact the windows not seen by the camera. The angle between the vessel ceiling and the spray centreline is 20^{o}. Figure 66 shows the raw images of a diesel spray at 9 bar ambient pressure and room temperature. Clearly the injector is mounted on the top and a temperature RTD probe is visible on the far right of every frame. The

two large circle structures at the periphery of the images are the front and back windows of the vessel. Especially on the first frame, on the left of the injector on the top plate, a small tubular structure appears, which is a glowplug. On the following frames, one of the sprays impinges on the glowplug. The temporal succession is from left to right and top to bottom. The time interval between the frames is 1/15000 s and the first image was shot 0.26 ms±5 ns after the SOI (Start of Injection) signal. On the images four sprays appear but the injector has six holes. The two sprays appearing in the middle are hiding two more sprays on the background. Spray number two from the left and its equivalent background spray are impinging on the glowplug and back window respectively. As spray number three from the left is the projection of two sprays, it cannot offer any valuable information. However, the far left and far right sprays are single uninterrupted sprays and therefore were used to gain quantitative information.

6.2.2 Image correction and processing

Images were processed using a combination of DaVis software and purpose programmed codes in C++. A LaVision calibration target was used to match pixels to length on the focal plane and dewarp the edges of the image. Prior to measurements, a dark image was shot and was then subtracted from the acquired images.

The grabbed images of the spray represent the projection of the spray on the camera plane, as shown in Figure 67. In order to acquire useful information on the actual spray geometry, the spray characteristics measured on the images have to be corrected for the inclination of the spray to the camera CCD plane. It can be easily shown that:

$$L_P = L'_P / \cos\theta$$

Where L'_P is the projection tip penetration of the spray, L_P the actual tip penetration and θ the angle between the spray plane and the CCD-surface. Angle θ was kept small in order to keep the spray in the depth of field of the camera-lens arrangement.

To acquire the projection tip penetration, images were rotated and the tip penetration length was measured along the centreline of the spray, using a threshold of 40 counts to differentiate between the fuel and the nitrogen environment. Then equation above was used to compensate for the off-plane inclination of the spray.

Similarly the projection of the spray centreline on the CCD φ' can be correlated to the actual

$$\varphi = \operatorname{atan}(\tan\varphi'/\sin\theta)$$

Cone angle can be calculated by measuring the spray width at a distance of 50mm from the injector tip. A similar technique has been used by other researchers in the past (Delacourt et al., 2005).

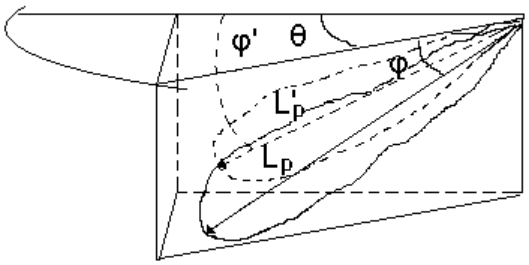

Figure 67 Cartoon representation of spray, with marked tip penetration length and angles of spray centreline

6.2.3 Spray characteristics

Timing uncertainties are of the order of 5 ns, which is negligible in the injection timescale. Pressure drop in the common rail during injection is compensated by the FPGA controller. The uncertainty in common rail fuel pressure was observed to be of the order of ±30 bar, which corresponds to ±1.7%. The uncertainty of the ambient pressure is calculated as half of the minimum subdivision of the scale of the pressure regulator, so it is ±1 bar. The vibration of the vessel and the subsequent moving of the image was measured to be less than 2 pixels, so considering that each pixel corresponds to 0.14 mm on the plane of imaging, these vibrations add an uncertainty of ±0.28 mm on the lengths measured on the images.

Similarly to past work (Atzler et al., 2007, Yeom et al., 2002, Reitz and Bracco, 1979), this work also observed decrease of the spray liquid length with increasing ambient pressure. Figure 68 presents the tip penetration as a function of time at various ambient pressures. The spray tip penetration was measured from the high-speed camera images using a custom-made Matlab code and a threshold of 200 camera counts to distinguish between the dark spray and the brighter background. Time was given from the timestamp of each image. Unlike past work, where spray tip penetration for the initial stages of injection is proportional to the square root of injection time (Yeom et al., 2002), this work did not observe a similar behaviour, as seen in Figure 69. This could be the result of the higher injection pressure used in this work, 1700 bar or of the lower ambient pressure, 10 bar instead of 50 bar in the literature.

The cone angle measured in this work was in accordance to the literature both in values and in trend. So, the cone angle was relatively constant as a function of time, as seen in Figure 70. The cone angle was measured in a similar way to the tip penetration. As in the literature, at a distance of 20 mm from the spray exit, two lines were plotted tangent to the spray sides and the angle between them was measured.

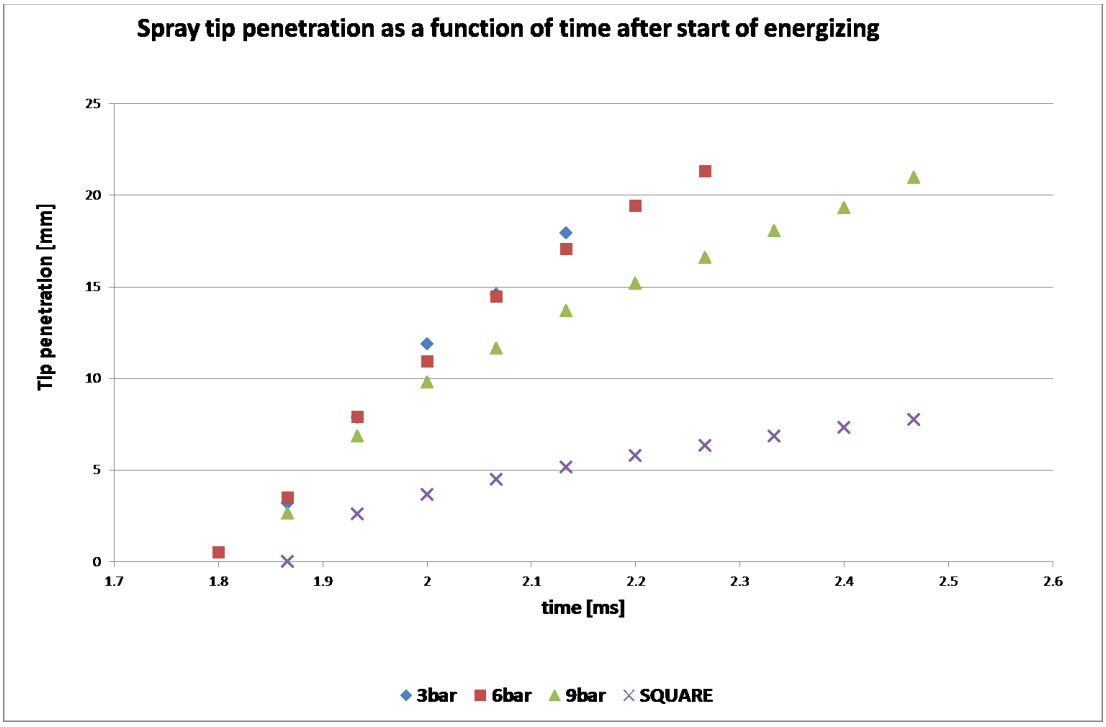

Figure 68 Spray tip penetration as a function of time elapsed after initiation of injection signal

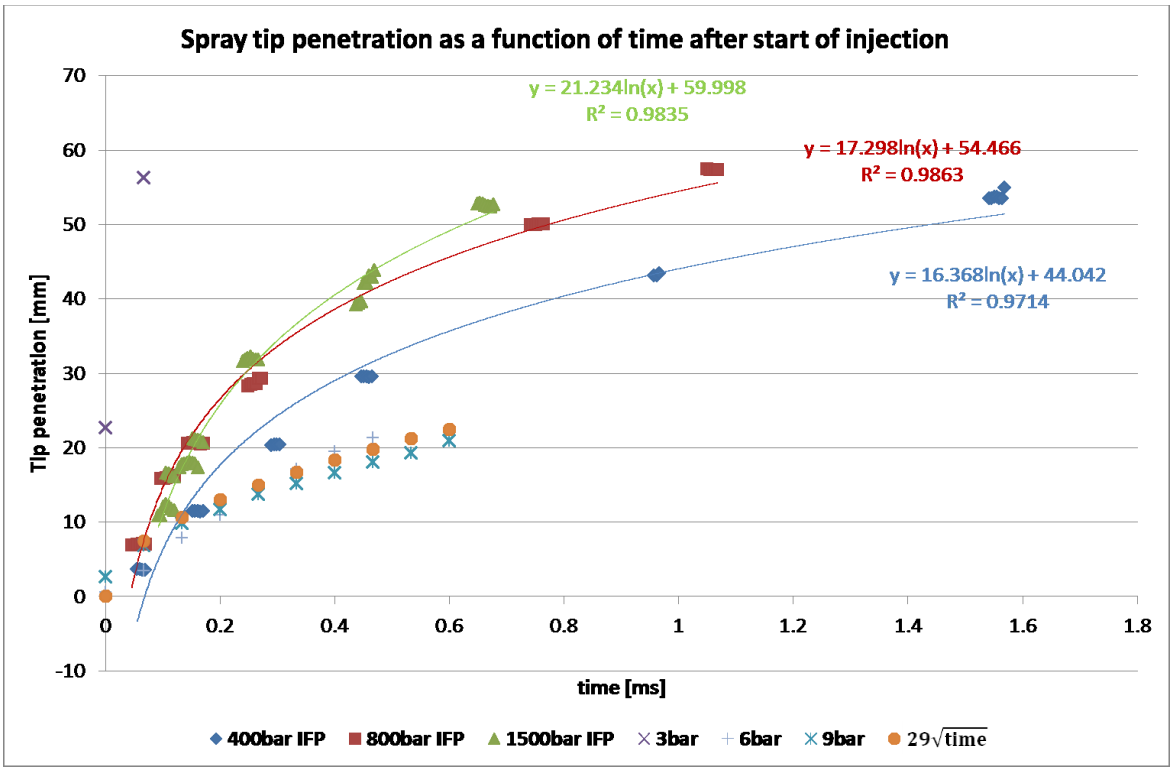

Figure 69 Spray tip penetration as a function of time elapsed after initiation of injection signal

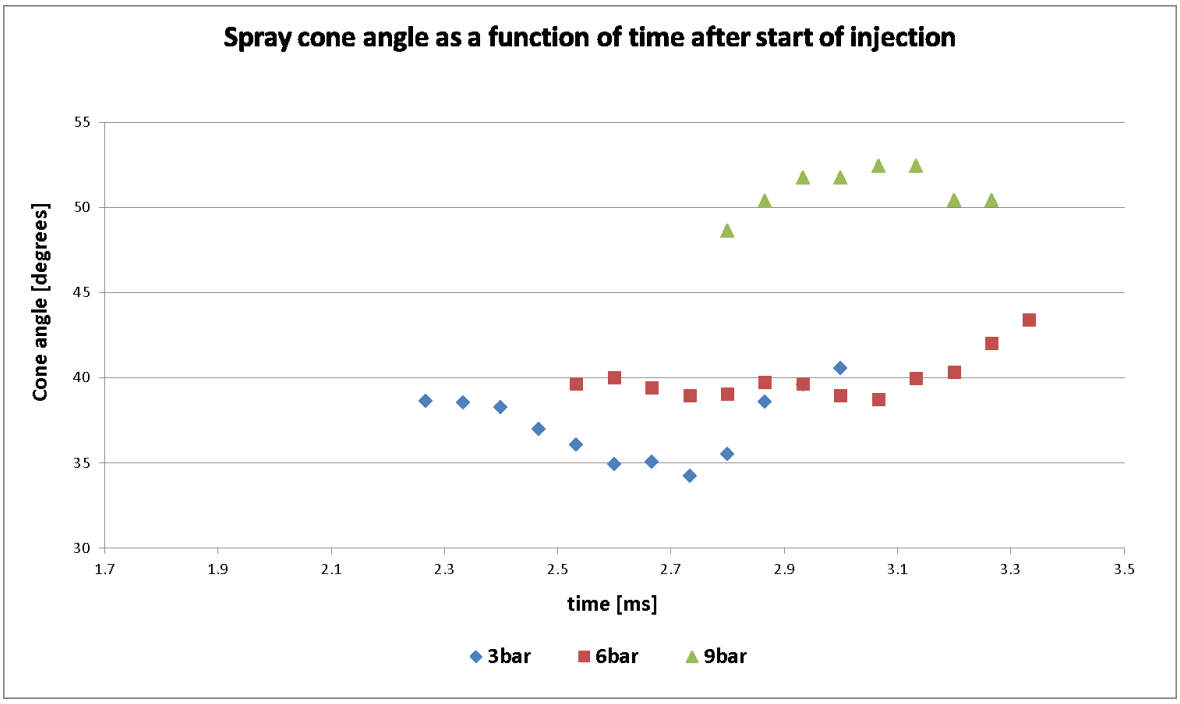

Figure 70 Spray cone angle as a function of time elapsed after initiation of injection signal

6.3 High-Speed Schlieren

6.3.1 Experimental setup

The experimental setup used in this section for the Schlieren High-Speed cinematography of the spray, was identical to the setup used in Section 4.6. However, as the spray does not produce natural luminosity, the exposure time had to be increased to 1/60000 seconds. Apart from the exposure time, all the other parameters and setup were identical to Section 4.6.

6.3.2 Results and spray characteristics

Figure 71, Figure 72 and Figure 73 present some typical raw images of the High-Speed Schlieren cinematography of the spray at Nitrogen environment at 8 bar, 10 bar and 14 bar respectively. In each figure, the images presented, from the top image to the bottom were taken at 300 μs, 374 μs, 448 μs, 522 μs and 596 μs after activation of injection respectively.

It is apparent that the spray tip penetration is a function of the time elapsed after initiation of injection. The spray tip penetration was observed to follow a square root relation with time, as in the literature described in Chapter 2.

It would have been expected that the ambient pressure would not affect the spray tip penetration considerably, as the ambient pressure (8-14 bar) is two orders of magnitude lower than the injection pressure (1700 bar). However, similarly to the results reported in the literature and presented in Chapter 2, as the ambient pressure increases, the spray tip penetration reduces. This reduction of spray tip penetration with increasing ambient pressure has a decreasing rate as the ambient pressure increases, as shown in Figure 74.

Similarly to the literature presented in Chapter 2 and the experimental observations of Section 6.2.3, the cone angle is relatively constant as a function of time. Clearly, some time is needed for the spray to develop and after the injection has stopped, the spray breaks up into smaller droplets. So the cone angle has a slight increasing trend in the beginning of the injection

and a decreasing trend at the end of the injection. This trend is observed quite clearly in Figure 75. However, the cone angle is constant within one degree. Ambient pressure has a stronger influence on the cone angle. As expected, as the ambient pressure increases, the cone angle of the spray increases. As in the case of spray tip penetration, the rate of increase of the cone angle with ambient pressure, is reducing as the value of ambient pressure increases.

The next section will study, with the means of the laser induced fluorescence technique discussed in Chapter 5, a Dodecane/Metyl-naphthalene spray. For the back-illumination and high speed Schlieren images, commercial Diesel fuel was used. So, the next section will, not only test the LIF technique, but will also allow for the comparison of a pure tracer fuel to the engine-like Diesel spray.

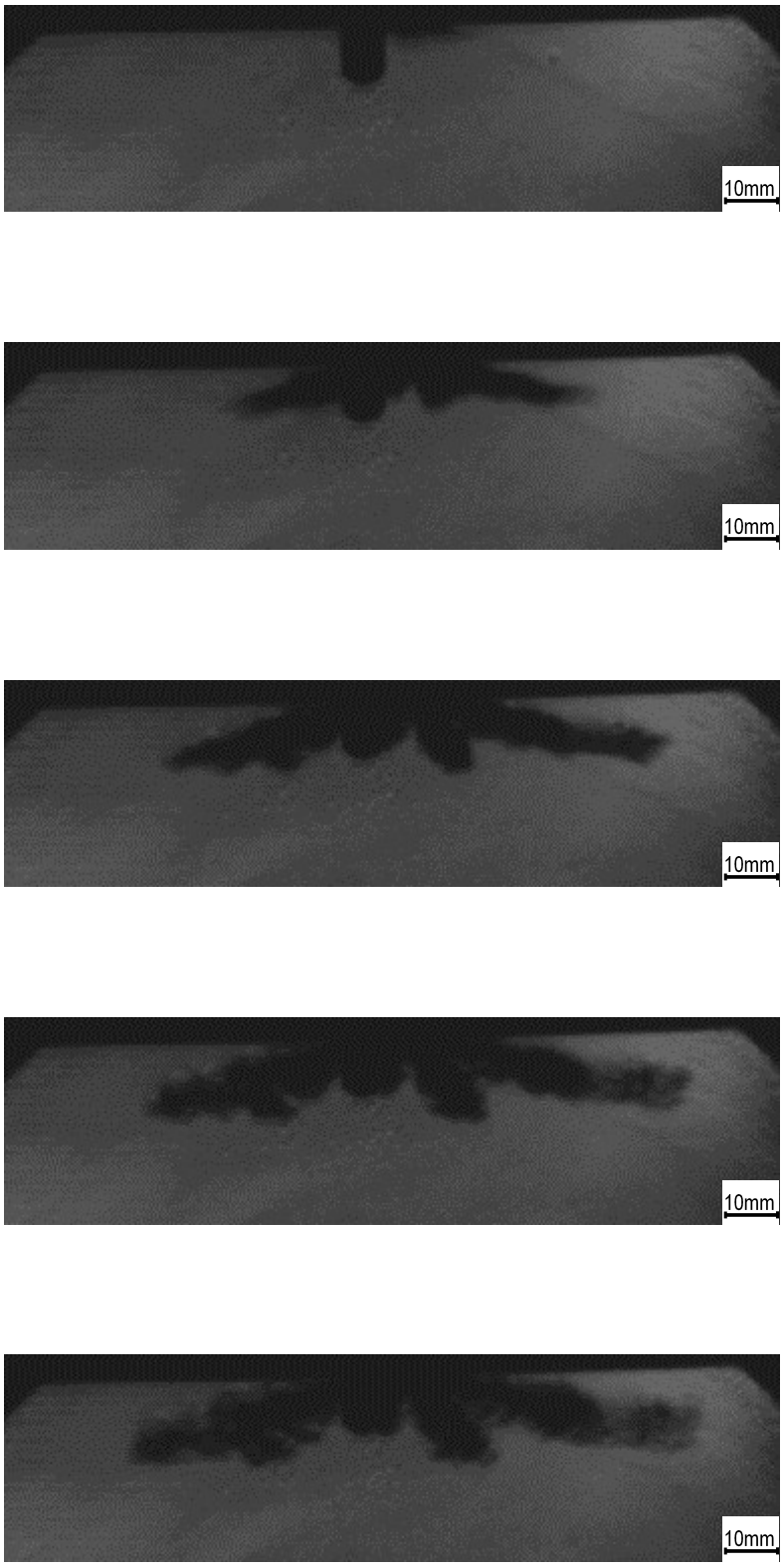

Figure 71 High-Speed Schlieren cinematography of spray at Nitrogen environment at 8 bar, images taken at 300 µs, 374 µs, 448 µs, 522 µs and 596 µs after activation of injection from the top image to bottom respectively

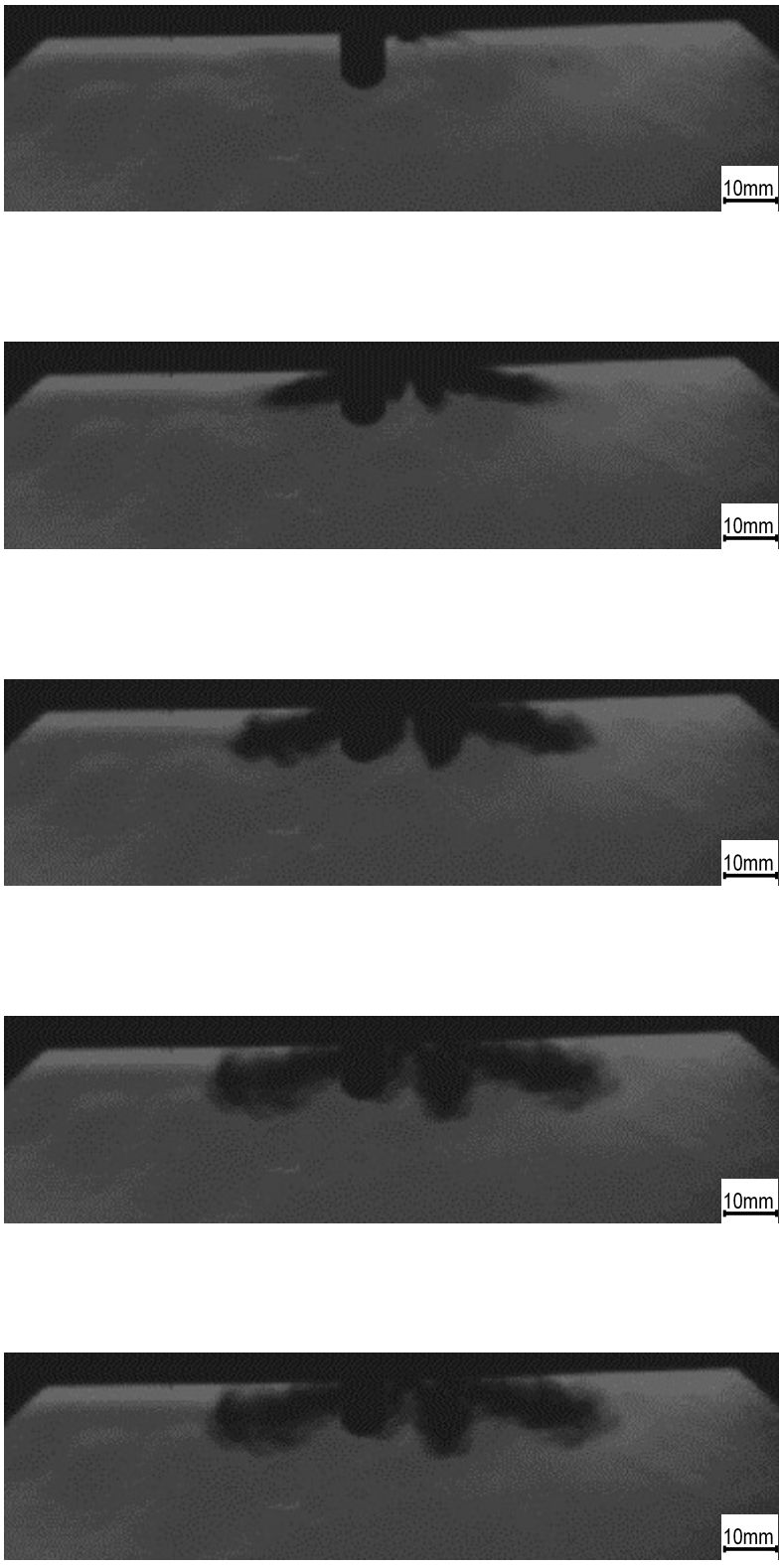

Figure 72 High-Speed Schlieren cinematography of spray at Nitrogen environment at 10 bar, images taken at 300 µs, 374 µs, 448 µs, 522 µs and 596 µs after activation of injection from the top image to bottom respectively

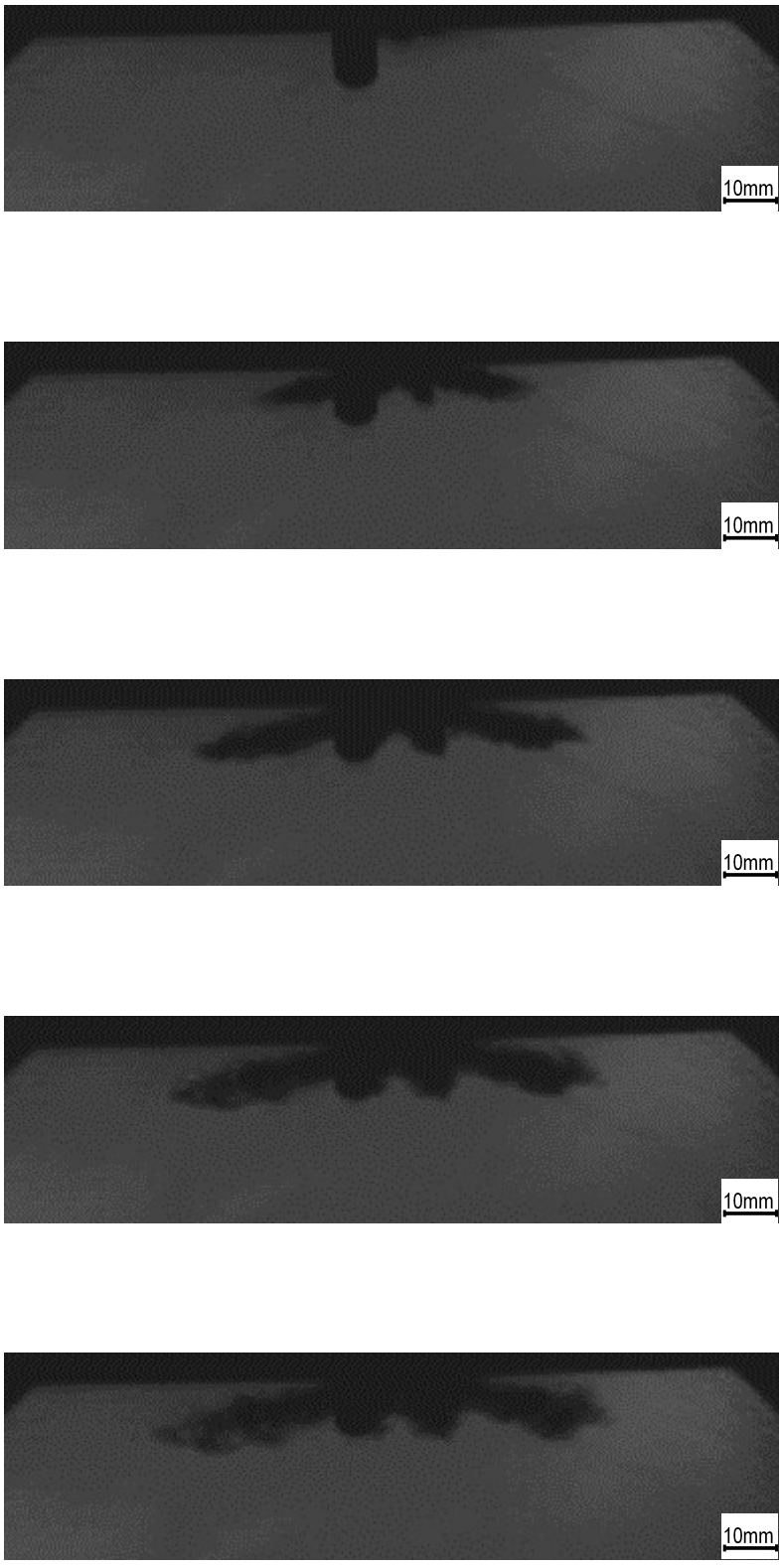

Figure 73 High-Speed Schlieren cinematography of spray at Nitrogen environment at 14 bar, images taken at 300 µs, 374 µs, 448 µs, 522 µs and 596 µs after activation of injection from the top image to bottom respectively

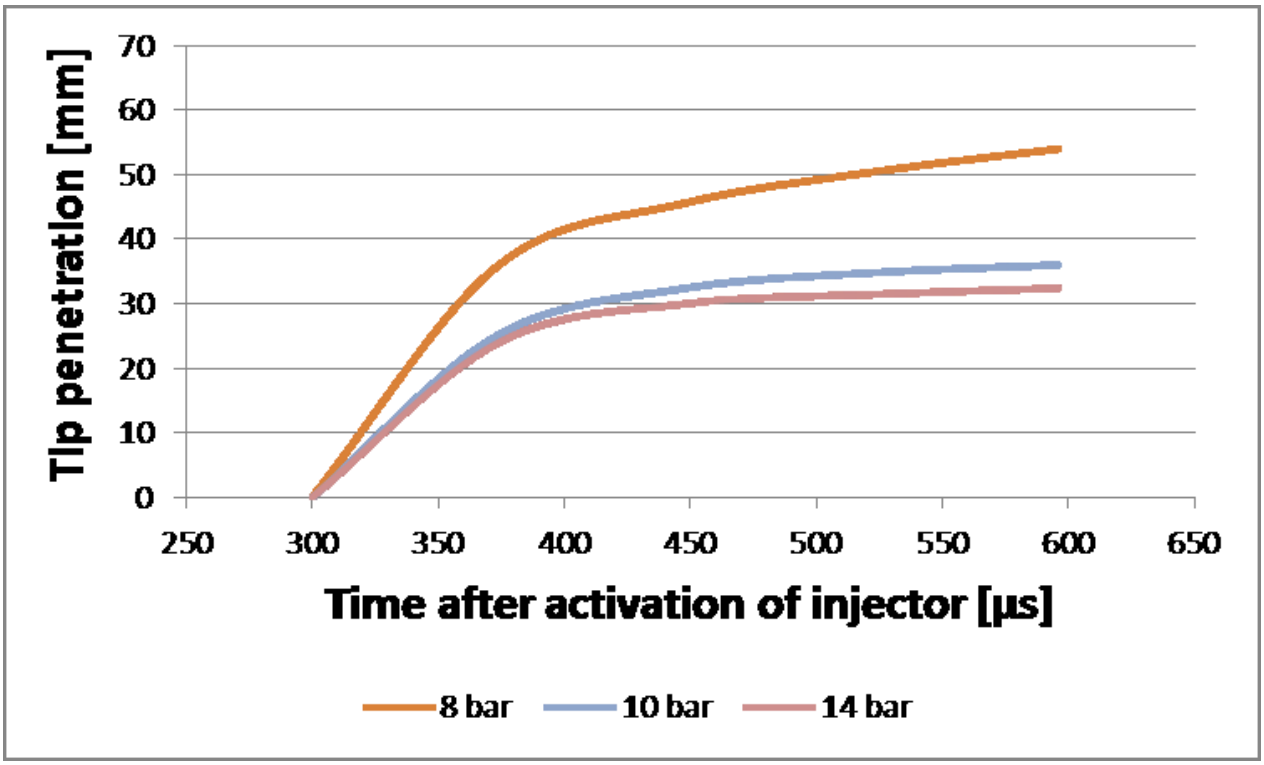

Figure 74 Tip penetration, as a function of time with ambient pressure used as parameter in Nitrogen environment at 300 K measured by high-speed Schlieren imaging

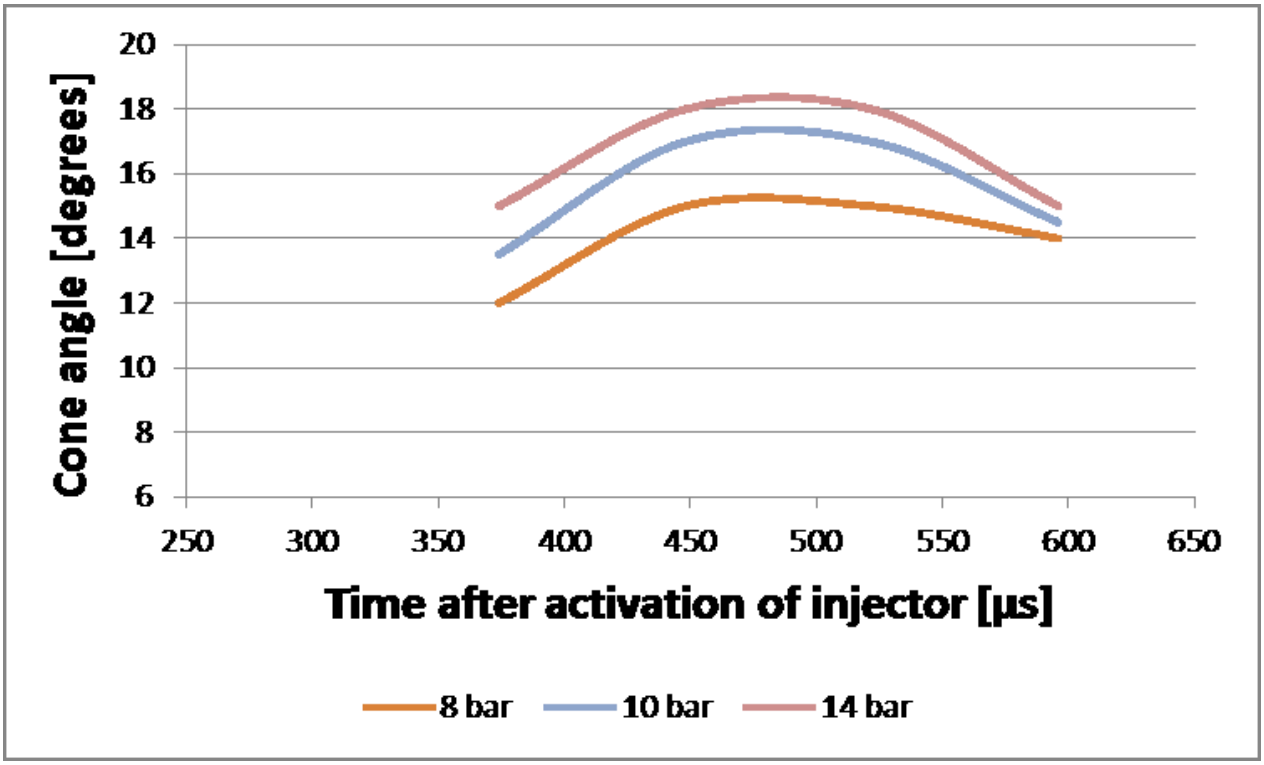

Figure 75 Cone angle, as a function of time with ambient pressure used as parameter in Nitrogen environment at 300 K, measured by high-speed Schlieren imaging

6.4 Laser Induced Fluorescence at room temperature and elevated pressure

6.4.1 Experimental Setup

The experimental setup, the tracer selection and the image corrections applied, have been thoroughly described in Chapter 5, which was dedicated to the LIF technique used in this work. This section will present the images and discuss the results of the LIF technique applied at room temperature Nitrogen environment at elevated pressure.

6.4.2 Results and discussion

Figure 78 presents LIF raw images at 5 bar ambient pressure, in a Nitrogen environment. At the rows from top to bottom, the images were grabbed at 300 μs, 340 μs, 380 μs and 560 μs after activation of injection. The two columns are two consecutive experiments, to demonstrate repeatability of the spray characteristics. It is quite clear that the automotive injector used in this work is capable of producing repeatable spray both temporally and spatially.

On the left side of each image, a cylindrical "thimble" appears. This thimble was created to isolate the five sprays from the one that is being visualised. A side cross-section of the thimble is presented in Figure 76. The thimble looks like a pipe which guides the five sprays at the bottom of the vessel, away from the imaging area, where the fuel can be safely extracted from the vessel at the end of every measurement, as presented in Chapter 3. Figure 77 presents a top view cross-section of the thimble, it is obvious that a stripe has been removed from the pipe-looking thimble, in order to allow for one spray to fully develop. The stripe that has been removed from the cylindrical tube, forms a 60 degree angle, which is large enough to allow for the uninterrupted propagation of even the widest spray that this injector can produce. The wall thickness is only 0.1 mm but the high strength of stainless steel, makes the thimble resistant to the high pressure sprays impinging on the internal wall of the thimble.

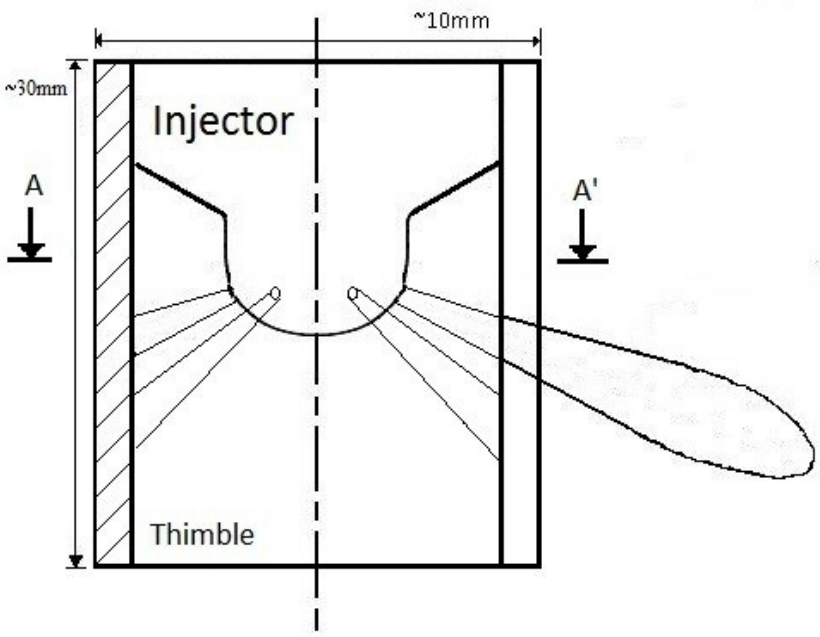

Figure 76 Side cross-section of thimble

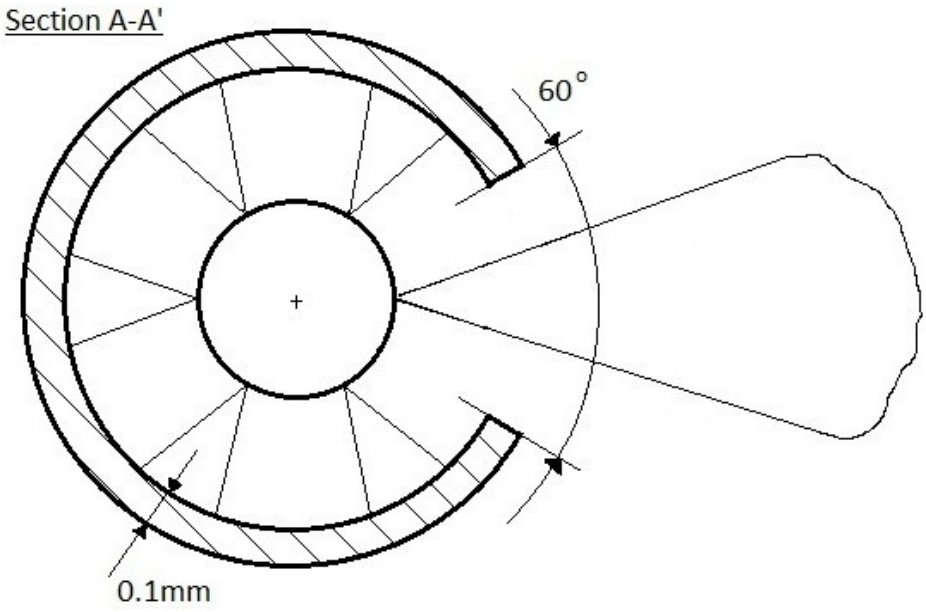

Figure 77 Top view cross-section of thimble

Similarly to Figure 78, Figure 79 presents the same Dodecane Methyl-naphthalene spray in high pressure, room temperature, Nitrogen environment, but at ambient pressure of 15 bar. Likewise, Figure 80 is referring to 25 bar ambient pressure. Five out of the six sprays produced by the injector nozzle are captured by the thimble and led at the bottom of the vessel. The sixth spray is excited by the laser sheet and the produced fluorescence captured by the camera. The fluorescence signal in all three pressure conditions seems to be of the same luminosity, supporting what has been reported in the literature and in Chapter 5, that the fluorescence signal is almost unaffected by the ambient pressure and mainly affected by the ambient temperature. The effect of ambient temperature on the fluorescence luminosity will be demonstrated in Chapter 7.

Table 15 presents the number of experimental samples taken at different pressure conditions and different time after activation of the injector. Five samples were taken at each pressure point and time point. It is known that for an experiment with confidence level 1- a and confidence interval half-width δ, the required sample size is given by $n = \left(\frac{z_{a/2}\,\sigma_x}{\delta}\right)^2$, where σ_x is the sample standard deviation (Mathews, 2010). In the current experiment, a confidence level of 95% was considered sufficient, so for example for the case of 15 bar and 380 μs after activation of injector, the 5 measured tip penetration lengths were 38.12, 37.99, 38.35, 38.20 and 38.74. The sample standard deviation is σ_x=0.26 mm and the confidence interval half-width δ=0.38mm. So for 95% confidence, the number of samples needed is $n = \left(\frac{1.96 \cdot 0.26}{0.38}\right)^2 = 1.78 \approx 2$. The above simple analysis is based on the assumption of normal distribution, which is extensively assumed for spray distribution and the quantity $z_{a/2}$ is the z-score value, which can be found on tables.

Similarly to the High-Speed Schlieren images, the tip penetration is a function of the time elapsed after initiation of injection. As the ambient pressure increases, the spray tip penetration reduces. This reduction of spray tip penetration with increasing ambient pressure has a decreasing rate as the ambient pressure increases, as shown in Figure 81.

In Figure 82 the cone angle is relatively constant as a function of time, within one degree precision. As in Section 6.3, because some time is needed for the spray to develop and after the injection has stopped, the spray breaks up into smaller droplets, the cone angle has a slight increasing trend in the beginning of the injection and a decreasing trend at the end of the injection. As the ambient pressure increases, the cone angle of the spray increases. As in the case of spray tip penetration, the rate of increase of the cone angle with ambient pressure, is reducing as the value of ambient pressure increases.

The spray shown in the high-speed Schlieren images was a Diesel spray with injection duration 1 ms, injection time which was too long for the specific injector. The long injection time overheated the coil of the solenoid injector and as a consequence destroyed many injectors. In this section, the spray studied was a mixture of Dodecane and Methyl-naphthalene, with injection duration of 300 μs, which was the design operational condition for this model of injector. As a consequence of the different injection times, the results from the two sections may not be directly comparable. However, this section showed that the macroscopic behaviour of a Diesel spray is almost identical to the macroscopic behaviour of the Dodecane Methyl-naphthalene mixture. This is probably because the two mixtures have almost identical densities. This chapter presented measurements in room temperature and Chapter 7 will investigate the case of an evaporative spray.

Time after initiation of injection [μs]	Ambient Pressure [bar]		
	5bar	15bar	25bar
300μs	5	5	5
340μs	5	5	5
380μs	5	5	5
420μs	5	5	5

Table 15 Number of experimental Laser Induced Fluorescence samples at 300K and high ambient pressure

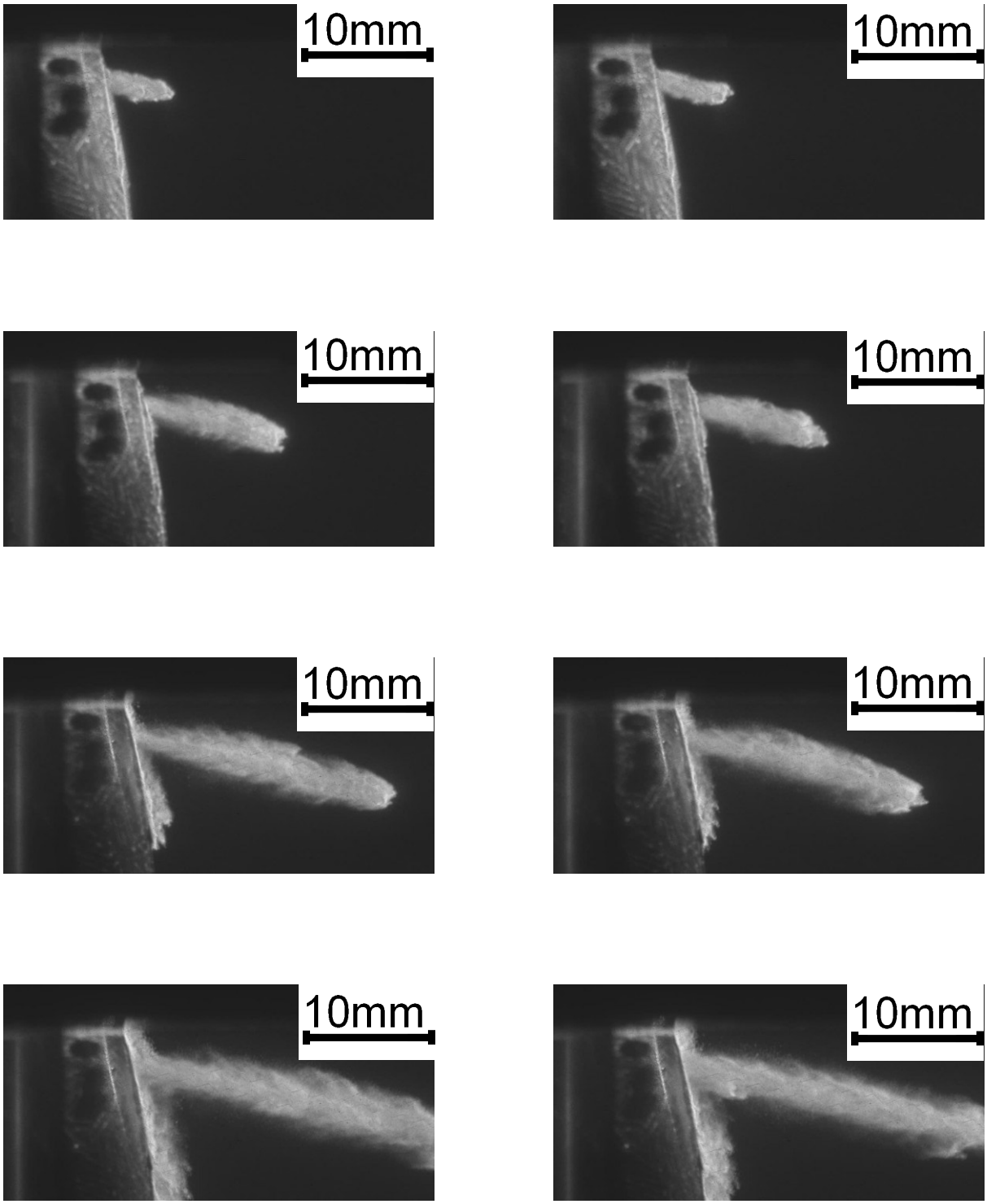

Figure 78 LIF raw images at 5 bar ambient pressure, in Nitrogen environment. At the rows from top to bottom, the images were grabbed at 300 μs, 340 μs, 380 μs and 560 μs after activation of injection. The two columns are two consecutive experiments, to demonstrate repeatability of the spray characteristics

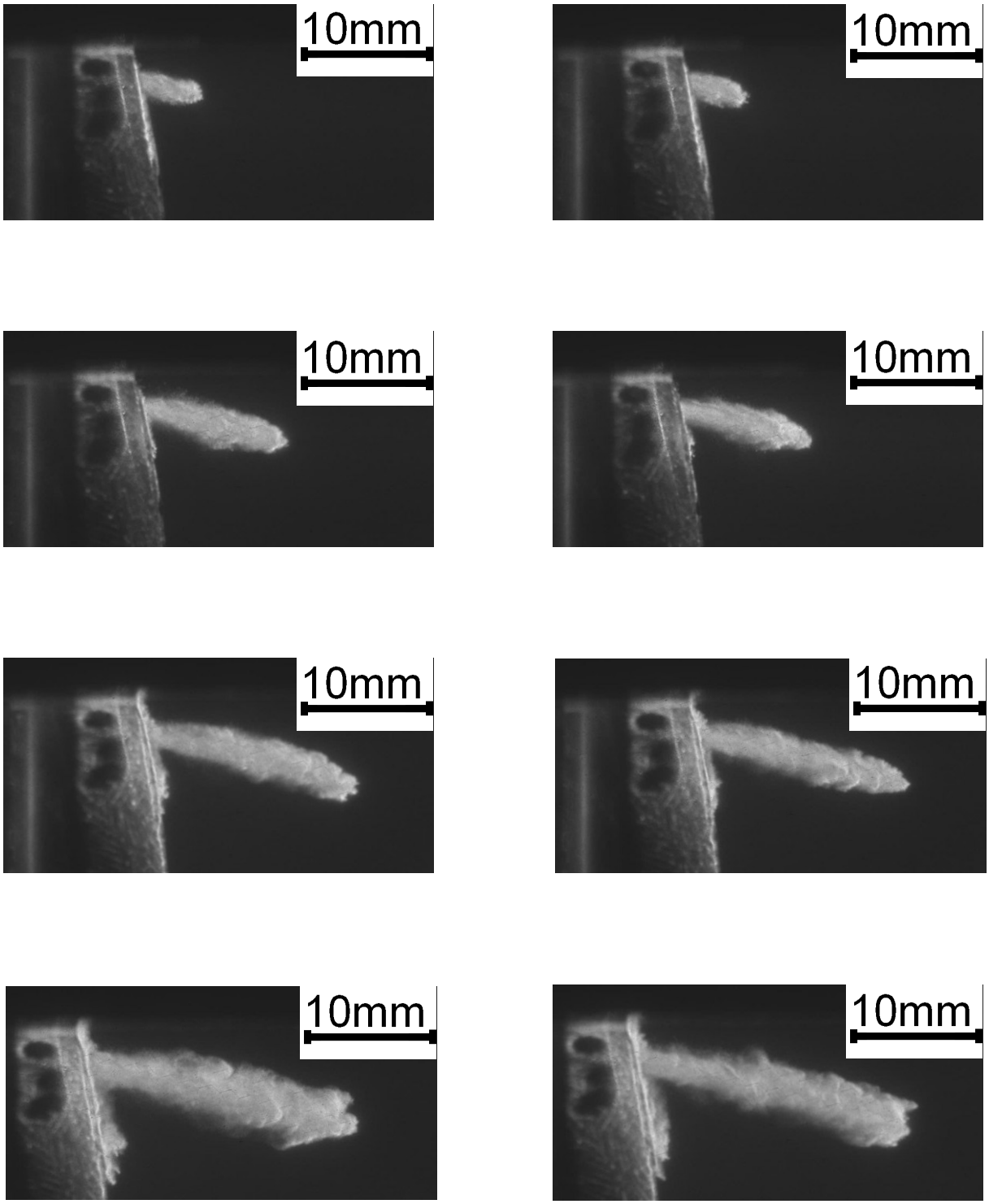

Figure 79 LIF raw images at 15 bar ambient pressure, in Nitrogen environment. At the rows from top to bottom, the images were grabbed at 300 μs, 340 μs, 380 μs and 560 μs after activation of injection. The two columns are two consecutive experiments, to demonstrate repeatability of the spray characteristics

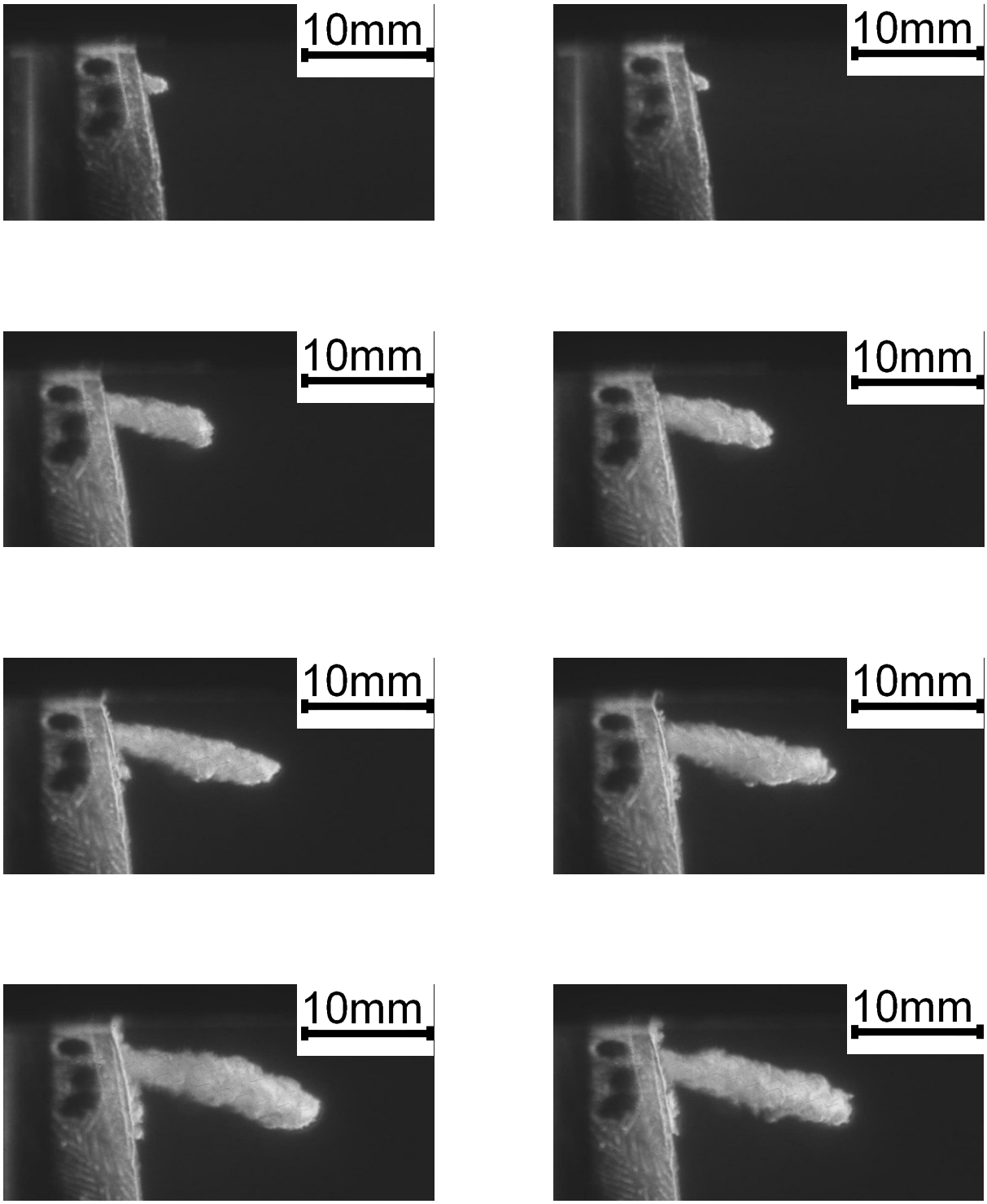

Figure 80 LIF raw images at 25 bar ambient pressure, in Nitrogen environment. At the rows from top to bottom, the images were grabbed at 300 µs, 340 µs, 380 µs and 560 µs after activation of injection. The two columns are two consecutive experiments, to demonstrate repeatability of the spray characteristics

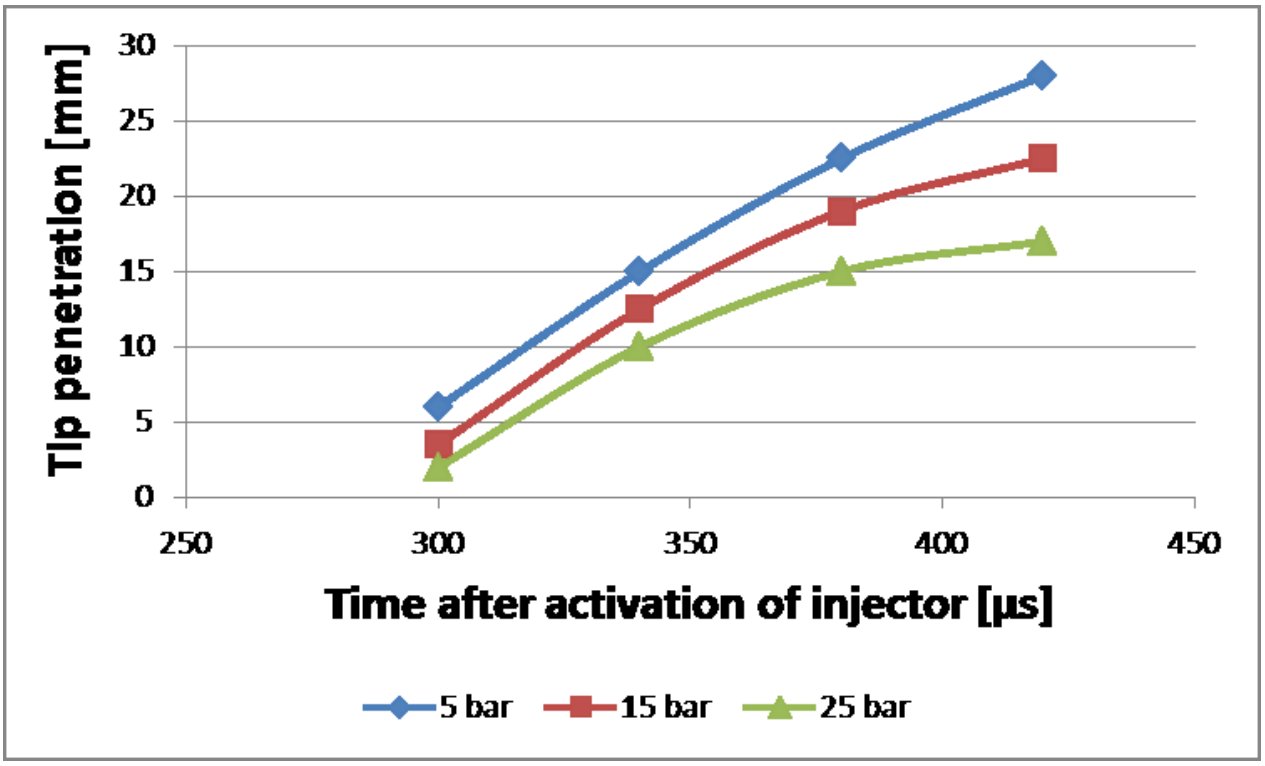

Figure 81 Tip penetration, as a function of time with ambient pressure used as parameter in Nitrogen environment at 300 K, measured using the tracer Laser Induced Fluorescence technique

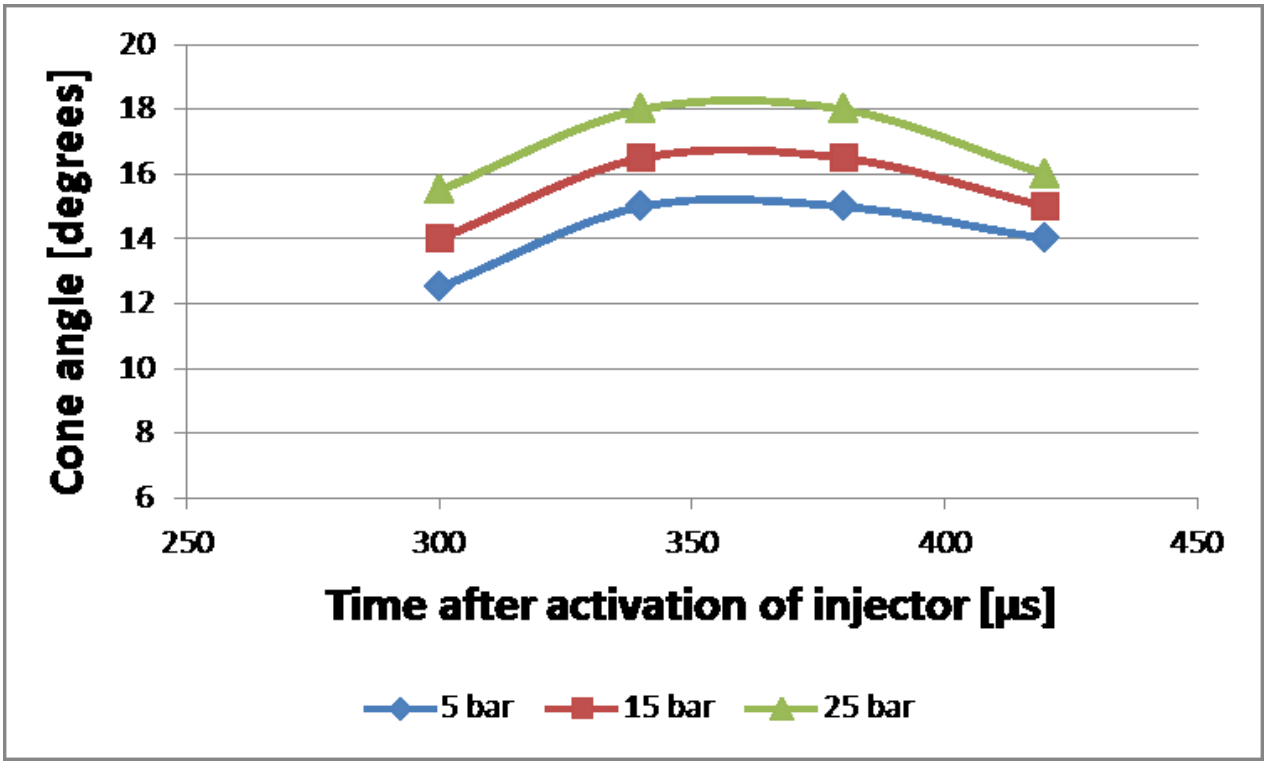

Figure 82 Cone angle, as a function of time with ambient pressure used as parameter in Nitrogen environment at 300 K ambient temperature, measured using the tracer Laser Induced Fluorescence technique

7. Evaporative spray

7.1 Introduction

In Chapter 6, the case of a spray not undergoing evaporation was studied. Temperature was kept at room conditions and pressure was increased using a high pressure regulator. In this Chapter, both temperature and pressure values will be increased, using the pre-ignition technique that was described and calculated in Chapter 4. A numerical evaluation will be presented first followed by an experimental study. The chapter will conclude with discussing the evaporation behavior of a diesel spray.

7.2 Droplet D^2 evaporation model

As was presented in Chapter 1, droplets are formed on the periphery and between the break-up length of the liquid core and the liquid length of the spray. To improve our understanding on the evaporation of a spray and to correlate the spray evaporation to the vessel environment studied in Chapter 4, the case of a single evaporating droplet at high pressure and high temperature environment is simulated here.

A single droplet in a stagnant environment is considered and is treated as a constant source of single-component fuel vapour. This implies that heat and mass transfer in the interior of the droplet are ignored. The external forces and natural convection are ignored. The droplet regression rate is considered slower than the gas-phase transport processes. Droplet evaporation is investigated from the point of view of mass diffusion, dictated by Fick's law, and from the point of view of thermal conduction, dictated by Fourier's law. Figure 83 shows the schematic of the model (Spalding, 1979, Law, 2006).

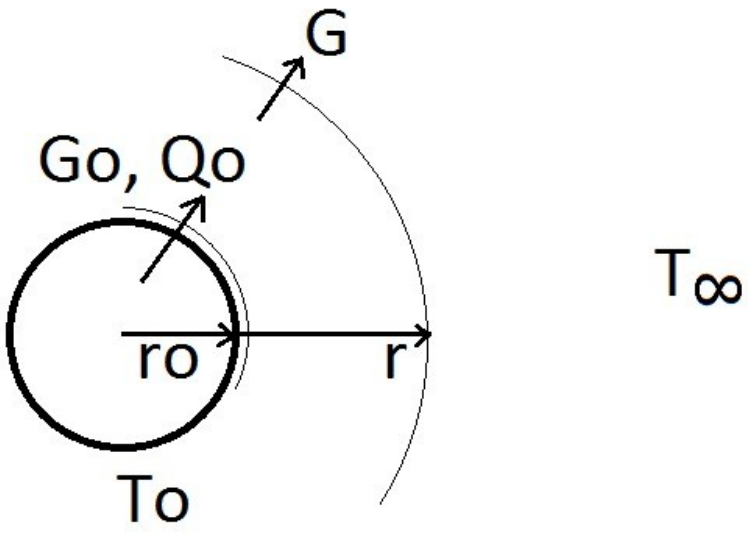

Figure 83 Droplet evaporation model of mass diffusion and thermal conduction

7.2.1 Mass conservation

Mass flux at the droplet surface should be conserved at any spherical shell of radius r, so:

$$Gr^2 = G_o {r_o}^2$$

Conservation of vapour

Because the total vapour velocity at a radius larger than the droplet diameter is the convective vapour velocity minus the diffusive mass velocity, from Fick law it is:

$$\left(m_{vap} G - \Gamma_{vap} \frac{dm_{vap}}{dr}\right) r^2 = G_o {r_o}^2$$

It should be noted that at this point non-constant transport properties are considered because the value of the exchange coefficient, Γ_{vap}, varies with temperature.

The boundary conditions are:

$$r = r_o : m_{vap} = m_{vap,o}$$

$$r = \infty : \; m_{vap} = m_{vap,\infty}$$

7.2.2 Conservation of energy

Spalding (1979), using the assumptions considered so far in this work (single spherical droplet in a stagnant environment, no heat and mass transfer in the interior of the droplet and droplet regression rate slower than the gas-phase transport processes) plus the assumption of a uniform vapour heat capacity c_{vap}, derived this equation of energy conservation:

$$r^2 \lambda \frac{dT}{dr} = G_o \left[c_{vap}(T - T_o) - \frac{Q_o}{G_o} \right] r_o^2$$

However, for non-constant vapour heat capacity c_{vap}, Spalding's equation of energy conservation, taking into account that $c_{vap} = \left(\frac{\partial h_{vap}^{(T)}}{\partial T} \right)_p$ needs to be changed to:

$$r^2 \lambda \frac{dT}{dr} = G_o \left[h_{vap}^{(T)} - h_{vap}^{(T_o)} - \frac{Q_o}{G_o} \right] r_o^2$$

Where Q_o is the heat flux through gas phase close to the liquid surface, which is consumed both in the form of latent heat of vapour and droplet heating. Therefore, the term $-\frac{Q_o}{G_o} \equiv L_{eff}$ is called “effective latent heat” of the droplet and is expressed as:

$$L_{eff} = L - \frac{q''}{G_o}$$

Where L is the latent heat of droplet per unit of mass, and q'' is the magnitude of the conductive heat flux into the droplet.

The boundary conditions are:

$$r = r_o : \; T = T_o$$

$$r = \infty : \; T = T_\infty$$

7.2.3 Phase equilibrium at the droplet surface

At the droplet surface, the phase equilibrium is achieved according to the Clausius-Clapeyron relation (Law, 2010), where the partial pressure of the vapourising liquid p_{vap} at a specific temperature T, can be expressed as:

$$p_{vap}(T) = p_n exp\left[\frac{L}{R^o}\left(\frac{1}{T_{BP,n}} - \frac{1}{T}\right)\right]$$

Where L is the molar latent heat of vaporization, $T_{BP,n}$ is the boiling point of the liquid at a reference pressure p_n, which was 1 atmosphere in this work. Using Dalton's law, the mole fraction of vapour on the droplet surface, with temperature T_o, can be expressed as:

$$Y_{vap,o} = \frac{p_{vap}(T_o)}{p_\infty}$$

The mole fraction Y_{vap} and the mass fraction m_{vap} of the vapour can be expressed as a function of each other as:

$$m_{vap} = \frac{Y_{vap} MW_{vap}}{Y_{vap} MW_{vap} + (1 - Y_{vap}) MW_{amb}}$$

$$Y_{vap} = \frac{m_{vap}/MW_{vap}}{m_{vap}/MW_{vap} + (1 - m_{vap})/MW_{amb}}$$

7.2.4 Evaporation rate derived from vapour conservation

The evaporation rate on the droplet surface G_o, can be calculated from the equation of vapour conservation as:

$$\frac{dm_{vap}}{m_{vap} - 1} = G_o r_o^2 \frac{dr}{\Gamma_{vap} r^2}$$

Integration from droplet surface to infinity,

$$\int_{m_{vap,o}}^{m_{vap,\infty}} \frac{dm_{vap}}{m_{vap} - 1} = G_o r_o^2 \int_{r_o}^{\infty} \frac{dr}{\Gamma_{vap} r^2}$$

$$ln\left(\frac{1-m_{vap,\infty}}{1-m_{vap,o}}\right) = G_o r_o^2 \int_{r_o}^{\infty} \frac{dr}{\Gamma_{vap} r^2}$$

Introduction of Spalding number of mass transfer $B_M = \frac{m_{vap,o} - m_{vap,\infty}}{1 - m_{vap,o}}$ and of the transformation $\Phi = 1 - \frac{r_o}{r}$ with boundaries $\Phi = 0 : \ r = r_o$ and $\Phi = 1 : \ r = \infty$, results in:

$$ln(1 + B_M) = G_o r_o \int_0^1 \frac{d\Phi}{\Gamma_{vap}}$$

Defining the average exchange coefficient as $\overline{\Gamma_{vap}} = \left(\int_0^1 \frac{d\Phi}{\Gamma_{vap}}\right)^{-1}$, the evaporation rate on the droplet surface is given by:

$$G_o = \frac{\overline{\Gamma_{vap}}}{r_o} ln(1 + B_M)$$

7.2.5 Evaporation rate derived from energy conservation

Similarly, the evaporation rate on the droplet surface G_o, can be calculated from the equation of energy conservation as:

$$r^2 \lambda \frac{dT}{dr} = G_o \left[h_{vap}^{(T)} - h_{vap}^{(T_o)} - \frac{Q_o}{G_o}\right] r_o^2$$

$$\frac{dT}{h_{vap}^{(T)} - h_{vap}^{(T_o)} - \frac{Q_o}{G_o}} = \frac{G_o r_o^2 dr}{r^2 \lambda}$$

$$\int_{T_o}^{T_\infty} \frac{dT}{\frac{-Q_o/G_o}{\frac{h_{vap}^{(T)} - h_{vap}^{(T_o)}}{-Q_o/G_o} + 1}} = \int_{r_o}^{\infty} \frac{G_o r_o^2}{r^2 \lambda} dr$$

Introducing the heat transfer number as $B_H = \frac{h_{vap,\infty} - h_{vap,o}}{-Q_o/G_o}$ and because by definition $c_{vap} = \frac{dh_{vap}}{dT}$, it is:

$$ln(1+B_M) = \int_{r_o}^{\infty} \frac{G_o r_o^2}{r^2\left(\lambda/c_{vap}\right)} dr$$

As in the previous section, introducing the transformation $\Phi = 1 - \frac{r_o}{r}$ with boundaries $\Phi = 0 : r = r_o$ and $\Phi = 1 : r = \infty$, it is:

$$ln(1+B_M) = \int_{0}^{1} \frac{G_o r_o}{\left(\lambda/c_{vap}\right)} d\Phi$$

By defining $\overline{\lambda/\mathrm{c}_{vap}} = \left(\int_0^1 \frac{d\Phi}{\lambda/\mathrm{c}_{vap}}\right)^{-1}$, the evaporation rate on the droplet surface is given by:

$$G_o = \frac{\overline{\lambda/\mathrm{c}_{vap}}}{r_o} ln(1+B_H)$$

7.2.6 Comments on evaporation rate

In the assumption of unity Lewis number, the Spalding mass transfer number B_M and the heat transfer number B_H are equal. As the vapour formed originates from the droplet, the rate of droplet radius change is proportional to the evaporation rate G_o, so:

$$\frac{dr_o}{dt} = -\frac{G_o}{\rho_{liq}}$$

Or expressed as a function of the droplet diameter D_o:

$$\frac{dD_o}{dt} = -\frac{2G_o}{\rho_{liq}}$$

Substituting any of the previous derivation of G_o into any of the last two equations, leads to an equation of the form $dD_o{}^2/dt = const$, this is why this model is called D^2 evaporation model.

7.2.7 Distribution of vapour mass fraction and temperature

By integrating the expressions of G_o from the droplet surface to an arbitrary position r, the distribution of vapour mass fraction and temperature can be obtained as:

$$1 + \frac{m_{vap,o} - m_{vap}}{1 - m_{vap,o}} = (1 + B_M)^{\overline{\Gamma_{vap}} \int_0^{\Phi} \frac{d\Phi'}{\Gamma_{vap}}}$$

$$1 + \frac{h_{vap} - h_{vap,o}}{L_{eff}} = (1 + B_H)^{\overline{\lambda/c_{vap}} \int_0^{\Phi} \frac{d\Phi'}{\lambda/c_{vap}}}$$

As the local value of enthalpy is known, the equivalent local temperature value can be calculated using the reverse operation of $h_{vap}(T)$.

7.2.8 Droplet heating

Assuming a uniform droplet temperature (infinite conductivity model) and that the temperature within the droplet is uniform, the energy (heat) balance on the droplet gives:

$$-Q_o 4\pi r_o^2 = \frac{4}{3}\pi r_o^2 \rho_{liq} c_{liq} \frac{dT_o}{dt} + G_o L 4\pi r_o^2$$

The first term, which is the product of the droplet surface times the heat flux through gas phase close to the droplet surface, represents the heat flux reaching the droplet. The second term, which is the volume of the droplet times its heat capacity times the temperature raise of the droplet, equals to the heat required to increase the droplet temperature. The last term is the product of the liquid latent heat times the evaporation rate times the surface of the droplet and represents the latent heat required to change the phase of the liquid to vapour.

Solving for the temporal change of temperature on the surface of the droplet is:

$$\frac{dT_o}{dt} = \frac{3}{r_o \rho_{liq} c_{liq}} (-Q_o - G_o L)$$

7.3 Results of single droplet evaporation

The liquid of the droplet was considered to be Dodecane with properties shown in Table 16. Dodecane was chosen because it has boiling point close to that of a typical Diesel blend and was also used in the Laser Induced Fluorescence measurements as the pure fuel, Chapter 5 and Chapter 7. The initial droplet diameter was 5 μm, typical of a modern diesel injector.

Liquid characteristic	Value	Units
Latent heat	61510	J/mole
Boiling point (at 1bar)	489	K
Density	0.78	g/(cm^3)
Heat capacity (Specific heat)	2.21	J/(gK)
Critical pressure	18.60	Bar
Critical temperature	634.98	K

Table 16 Droplet fuel characteristics (NIST, 2013)

The ambient environment in which the droplet is evaporating was considered to be the products of Hydrogen and Air perfect stoichiometric combustion, unless specified otherwise. The pressure and temperature ambient conditions are specified on the graphs.

On the graphs of Figure 84, the ambient post-combustion peak temperature, at which the droplet was exposed, was used as a parameter. The equivalent post-combustion ambient peak pressure was kept as a constant at 1 bar by altering the pre-ignition mixture. The temperature values plotted were 300, 600, 800 and 1000 K corresponding to the blue, green, red and purple lines respectively. On all four graphs of Figure 84 time is the independent variable on the horizontal axis. Figure 84a presents the droplet diameter, Figure 84b presents the dimensionless square of the ratio of the droplet diameter to the initial droplet diameter, Figure 84c presents the evaporation rate on the droplet temperature and Figure 84d presents the droplet temperature. Likewise, the same graphs appear in Figure 85, but with ambient pressure used as a parameter and post-combustion peak temperature kept constant at 1000 K

by altering accordingly the pre-ignition mixture. The values of pressure plotted were 1, 10, 20 and 30 bar, which correspond to the purple, red, green and blue lines respectively.

Exactly like in the case of droplets created by an automotive diesel injector, the single droplet examined here, when subjected to a high temperature environment, has an initially low evaporation rate. This is because most of the energy transferred to the droplets is used to increase their temperature (heating up period). As the droplet liquid temperature increases, the amount of fuel vapour evaporating from the droplet surface increases and gradually larger part of the energy is used as latent heat for the phase change. Considering no radiation of heat, the droplet reaches an equilibrium or 'wet-bulb' temperature and the evaporation rate increases to a maximum, holding that maximum value until the liquid is completely evaporated. This is shown in Figure 84a, where the droplet diameter initially decreases slowly and then it reduces in a parabolic manner. This behavior can be observed more clearly, in Figure 84b, where the dimensionless square of the ratio of the droplet diameter to the initial droplet diameter, initially has a flat slope and then reduces linearly, justifying the D^2 dependence of this model.

In Figure 84c, it can be observed that the evaporation rate on the droplet surface starts from a very low value (10^{-3} g/cm^{2}s), as the droplet is at low temperature. As the droplet temperature increases, so does the evaporation rate on the drop surface. When the droplet reaches the wet-bulb temperature, the evaporation rate on the surface, increases in a parabolic-type manner, this is because heat is now used only for the vapour phase change. On the graph it can be observed that after the parabolic-increase, the evaporation rate increases very rapidly, almost vertically on the graph, this is due to the droplet recession. Finally the evaporation rate stops when the droplet has evaporated.

In Figure 84d, the droplet surface temperature is plotted as a function of time. Initially there is a transient period, during which the droplet temperature has not reached the "wet-bulb" temperature and the heat flux through the liquid phase close to the droplet surface is used to increase the temperature of the droplet. When the droplet has reached equilibrium

temperature, the heat flux through the liquid phase close to the droplet surface is used as phase-changing latent heat of liquid evaporation.

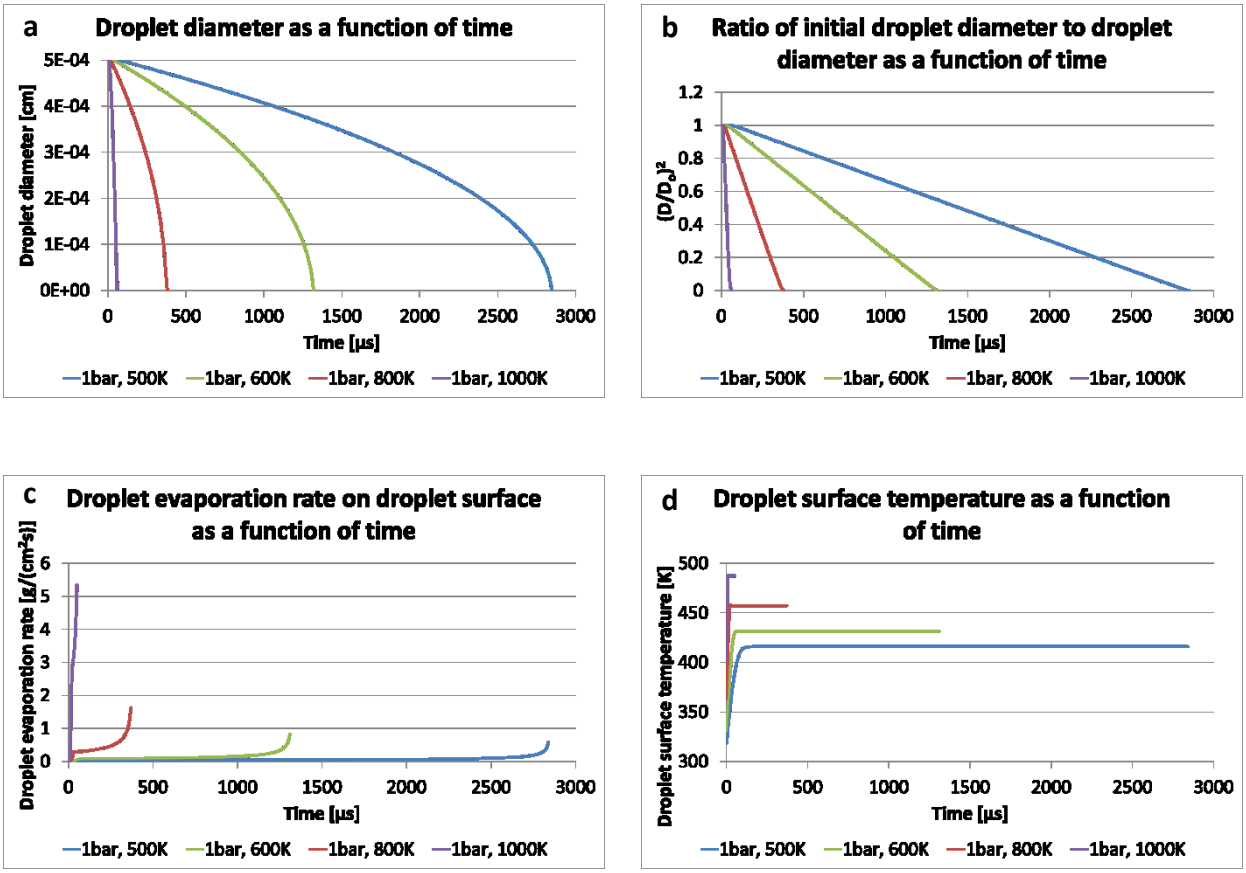

Figure 84 Influence of temperature on droplet evaporation, with temperature used as a parameter, a)droplet diameter, b)droplet square ratio of diameter to initial diameter, c)evaporation rate on droplet surface, d)temperature on droplet surface

Overall, Figure 84 shows that as the ambient temperature increases, droplet evaporation is promoted. So as temperature increases, the droplet lifetime decreases and the evaporation rate increases. The opposite behaviour is observed for increasing ambient pressure in Figure 85. So, as ambient pressure increases, the droplet lifetime increases and the evaporation rate on the surface of the droplet decreases. This however, is to be expected from the Clausius-Clapeyron relation, as an increase in ambient pressure increases the boiling point, which in turn demotes evaporation. A simplistic example of the Clausius-Clapeyron relation is

water boiling at 100°C at sea level, but having a lower boiling point on the top of a mountain. Thus, according to English tradition, tea prepared on Mount Everest does not taste as good as tea prepared in England.

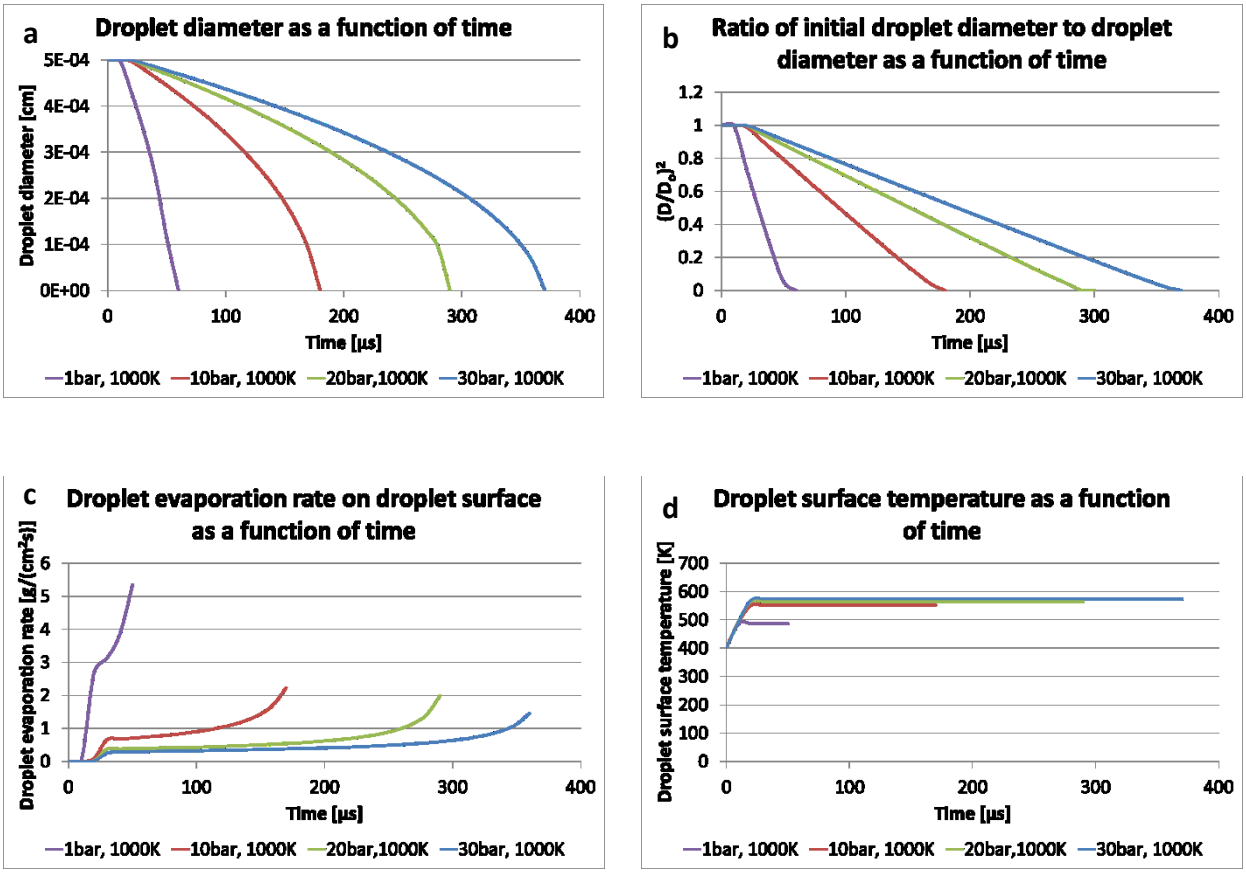

Figure 85 Influence of temperature on droplet evaporation, with pressure used as a parameter, a)droplet diameter, b)droplet square ratio of diameter to initial diameter, c)evaporation rate on droplet surface, d)temperature on droplet surface

Figure 86 demonstrates the influence of ambient temperature and pressure on the droplet evaporation. The influence of temperature is stronger than the influence of pressure and as temperature increases, the influence of pressure becomes even smaller. It can even be observed that at 1000 K, the difference on the droplet lifetime between 1 and 30 bar ambient pressure is almost negligible. So for simulating droplet evaporation in the vessel, it is more important to achieve the ambient temperature present in an automotive cylinder, rather than the pressure in the cylinder. This can now justify better the selection of pure Hydrogen as fuel

in the vessel and the exclusion of the Hydrocarbon, which would lower the post-combustion temperature and pressure.

However, excluding the Hydrocarbon from the pre-combustion mixture, results in a post-combustion mixture which consists only of water vapour and Nitrogen and has no Carbon Dioxide. So, the ambient gas heat capacity and heat conductivity are different to what would normally be found in a Diesel engine cylinder. Chapter 4 calculated the values of these thermal properties of the post-combustion ambient gas. However, the influence of those characteristics on the spray evaporation will be studied here using the single droplet model. Figure 87 demonstrates how the droplet life-time changes for different pre-ignition mixtures. Perfect combustion with Air was considered for Hydrogen, Methane, Acetylene and mixtures of Hydrogen with Methane and Hydrogen with Acetylene, with unity Hydrogen to Hydrocarbon mole ratio (parameter A, Chapter 4). The horizontal axis of the graph is the post-combustion peak temperature for post-combustion ambient pressure of 1 bar, conditions at which the droplet was exposed. It is clear that the post-combustion mixture composition has a negligible effect on the droplet life-time.

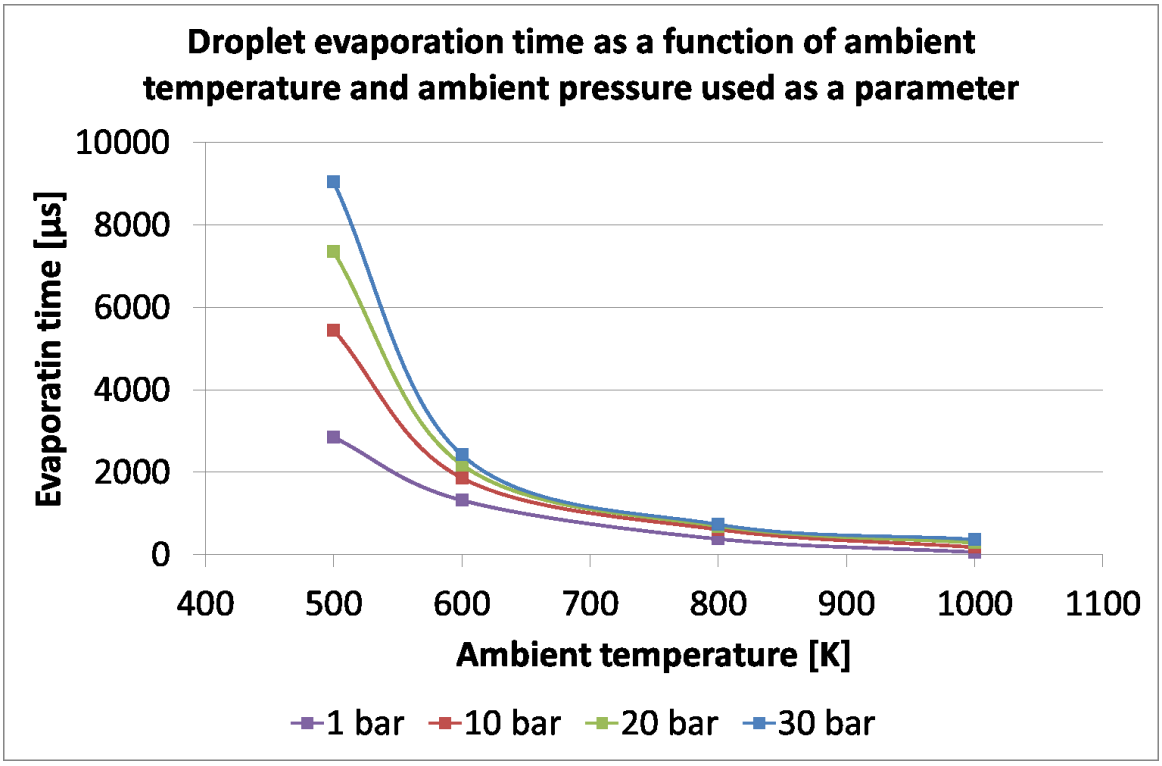

Figure 86 Pressure and temperature influence on droplet evaporation time

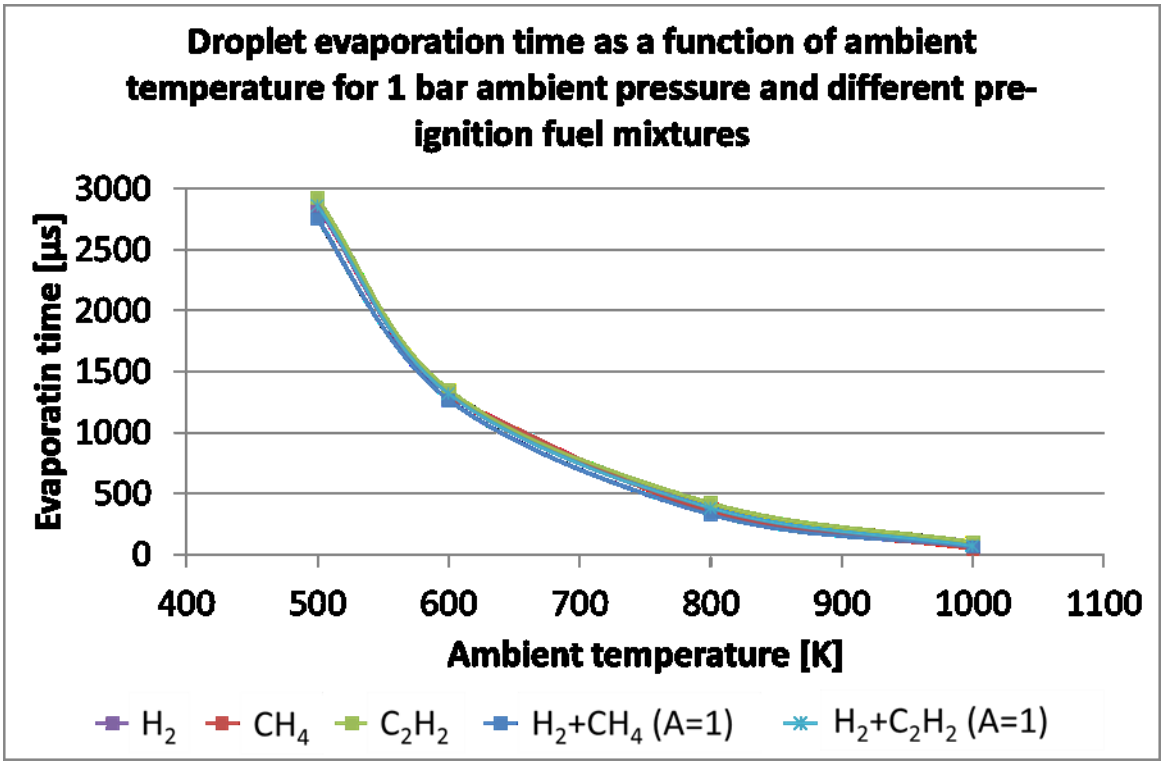

Figure 87 Ambience gas composition influence on droplet evaporation time

7.4 LIF on evaporative spray

7.4.1 Experimental setup

Similarly to Section 7.4.1, the experimental setup, the tracer selection and the image corrections applied, have been thoroughly described in Chapter 5, which was dedicated to the LIF technique used in this work. This section will present the spray images and discuss the results of the LIF technique applied at elevated pressure and temperature.

Table 17 presents the number of experimental samples taken at different pressure conditions and different time after activation of the injector. Like Section 6.4, five samples were taken at each pressure point and time point, which provided confidence level above 95% as demonstrated earlier.

Time after initiation of injection [μs]	Ambient Temperature [K]		
	300 K	1500 K	1800 K
300 μs	5	5	5
340 μs	5	5	5
380 μs	5	5	5
420 μs	5	5	5

Table 17 Number of experimental Laser Induced Fluorescence samples at high temperature and pressure environment created using the chemical pre-heating technique

7.4.2 Discussion

Figure 88 presents some LIF raw images at 5 bar ambient pressure and 1500 K ambient temperature. This environment was created with the chemical heating technique described in Chapter 4. More specifically, Hydrogen and composed air were ignited in the vessel at atmospheric pressure. Pressure and temperature followed the trace shown in Figure 44. When pressure had reached 5bar and the equivalent temperature was 1500 K, the LIF images of the spray were taken. At the rows from top to bottom, the images were grabbed at 300 μs, 340 μs,

380 μs and 560 μs after activation of injection. The two columns are two consecutive experiments, to demonstrate repeatability of the spray characteristics. Similarly Figure 89 presents the same results for 5 bar and 1800 K.

The most obvious difference to the LIF measurements presented in Section 6.4 is that in these conditions of higher temperature, the fluorescence luminosity is lower than the fluorescence at high pressure but low temperature. This verifies the discussion of Chapter 5, that temperature affects the fluorescence signal more than pressure.

The tip penetration of the spray as a function of time, as shown in Figure 90, is uninfluenced by the ambient temperature. At ambient pressure of 5 bar and ambient temperature altered to 300, 1500 and 1800 K, the tip penetration was identical. This justifies section 2.2, where the main factor influencing the spray penetration was the injection pressure. Also, Figure 90 in combination to Figure 81, presents the small but important influence of ambient pressure in tip penetration propagation.

Another observation is that even though the spray cone angle is relatively constant with time, as in Section 6.4, in the case of high temperature measurements, the cone angle values are slightly smaller than for the high pressure and room temperature cases. This indicates better evaporation from the periphery of the spray. As shown in Figure 91, for constant ambient pressure, as ambient temperature increases, the cone angle of the spray decreases.

Finally, comparing the times calculated for evaporating a single Dodecane droplet in the vessel post-combustion environment in Section 7.2, to the spray lifetime scales observed in the vessel in Section 7.3, it is quite clear that the calculations over-predict droplet lifetime by a factor of 1000. This could be the result of a false assumption in the D2 evaporation models. These models assume that a droplet absorbs heat for warming-up and then keeps absorbing heat to cover the necessary latent heat for evaporation. This model would absolutely make sense in subcritical conditions. However, as shown on Table 16, the critical temperature and pressure of Dodecane are 634.98 K and 18.6 bar respectively. In a modern engine, at the top-dead center, the ambient pressure and temperature are higher than the critical point of fuel. In the current work the mass-averaged ambient temperature was above critical. So, the super-

critical temperature is not local but throughout the volume of the vessel. It is known that the injected spray cools down the vessel gases. So, the spray is not in super-critical temperature. To this direction in the literature, optical temperature techniques are being applied to measure the temperature field in the spray. It is obvious that only the very edge of the tip and the periphery of the spray, the temperature is supercritical (Trost et al., 2013). So the assumption of supercritical evaporation cannot be valid for the whole spray area and cannot explain the shorter experimentally observed evaporation time. To this direction maybe a supercritical and a subcritical evaporation model could be combined to produce more accurate results.

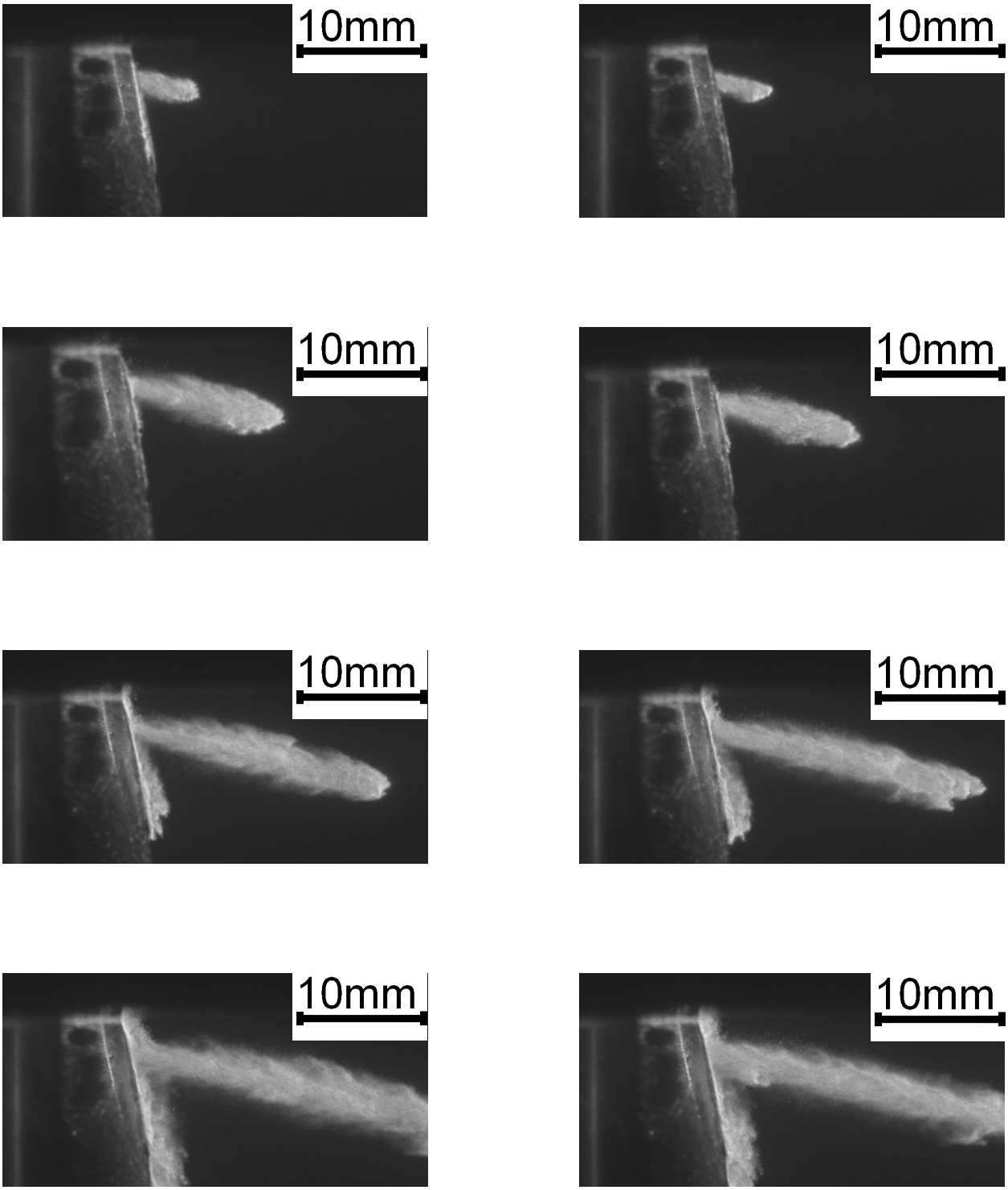

Figure 88 LIF raw images at 5 bar ambient pressure and 1500 K ambient temperature. At the rows from top to bottom, the images were grabbed at 300 μs, 340 μs, 380 μs and 560 μs after activation of injection. The two columns are two consecutive experiments, to demonstrate repeatability of the spray characteristics

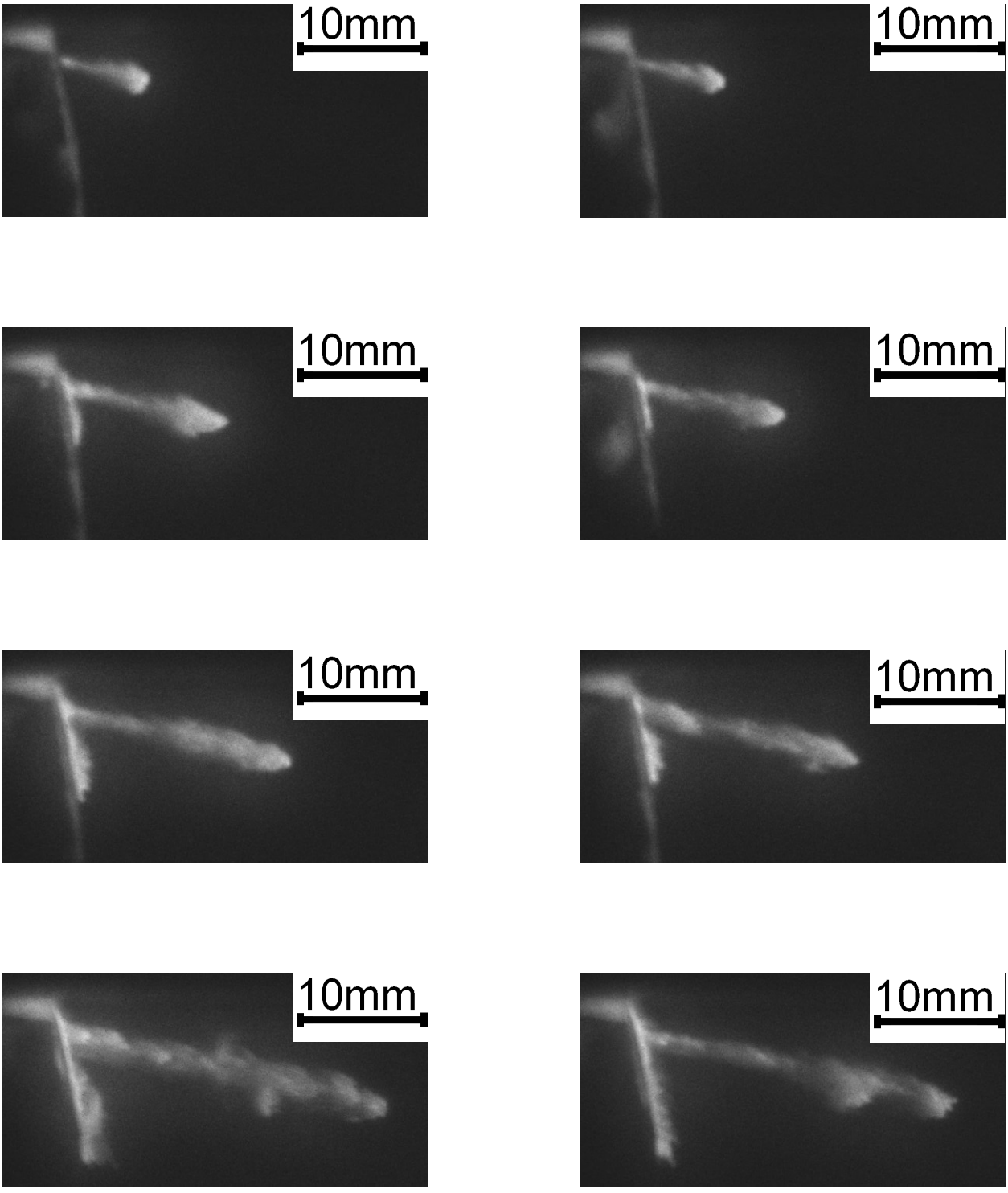

Figure 89 LIF raw images at 5 bar ambient pressure and 1800 K ambient temperature. At the rows from top to bottom, the images were grabbed at 300 μs, 340 μs, 380 μs and 560 μs after activation of injection. The two columns are two consecutive experiments, to demonstrate repeatability of the spray characteristics

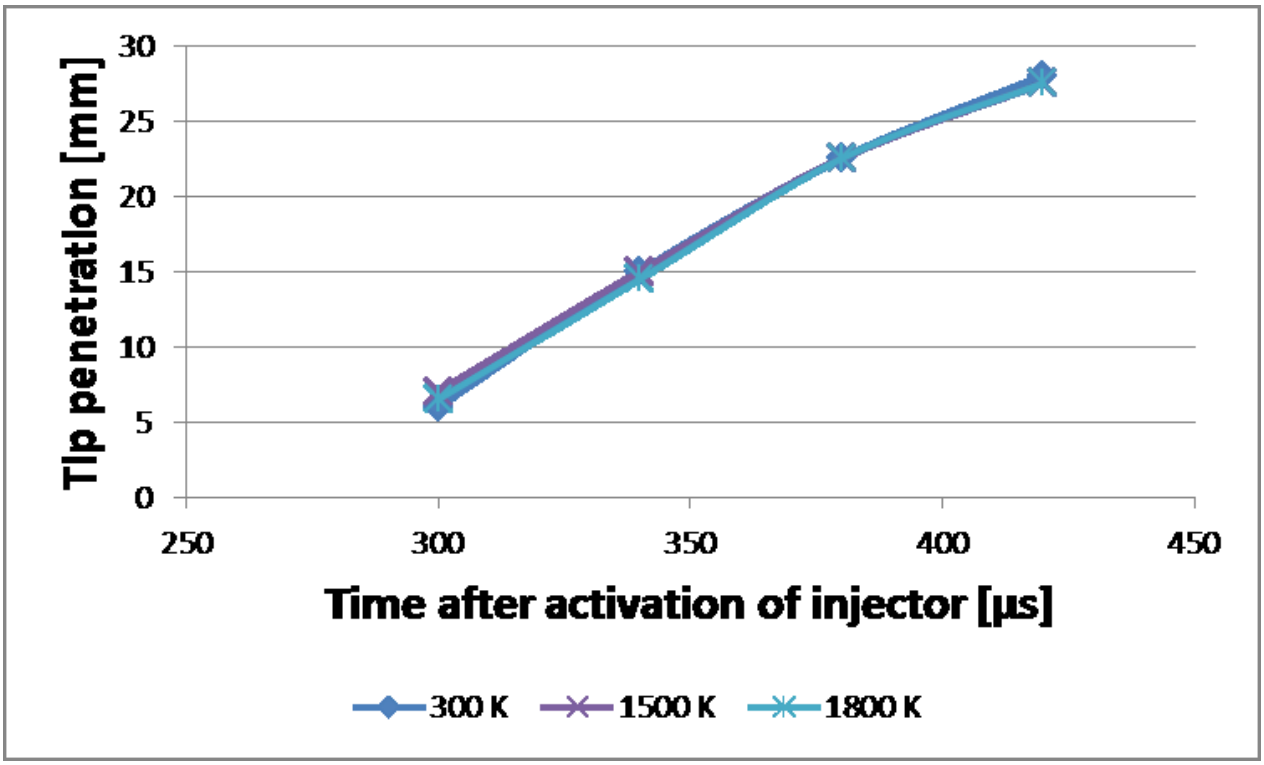

Figure 90 Tip penetration, as a function of time with ambient temperature used as parameter at 5 bar ambient pressure, measured using the tracer Laser Induced Fluorescence technique

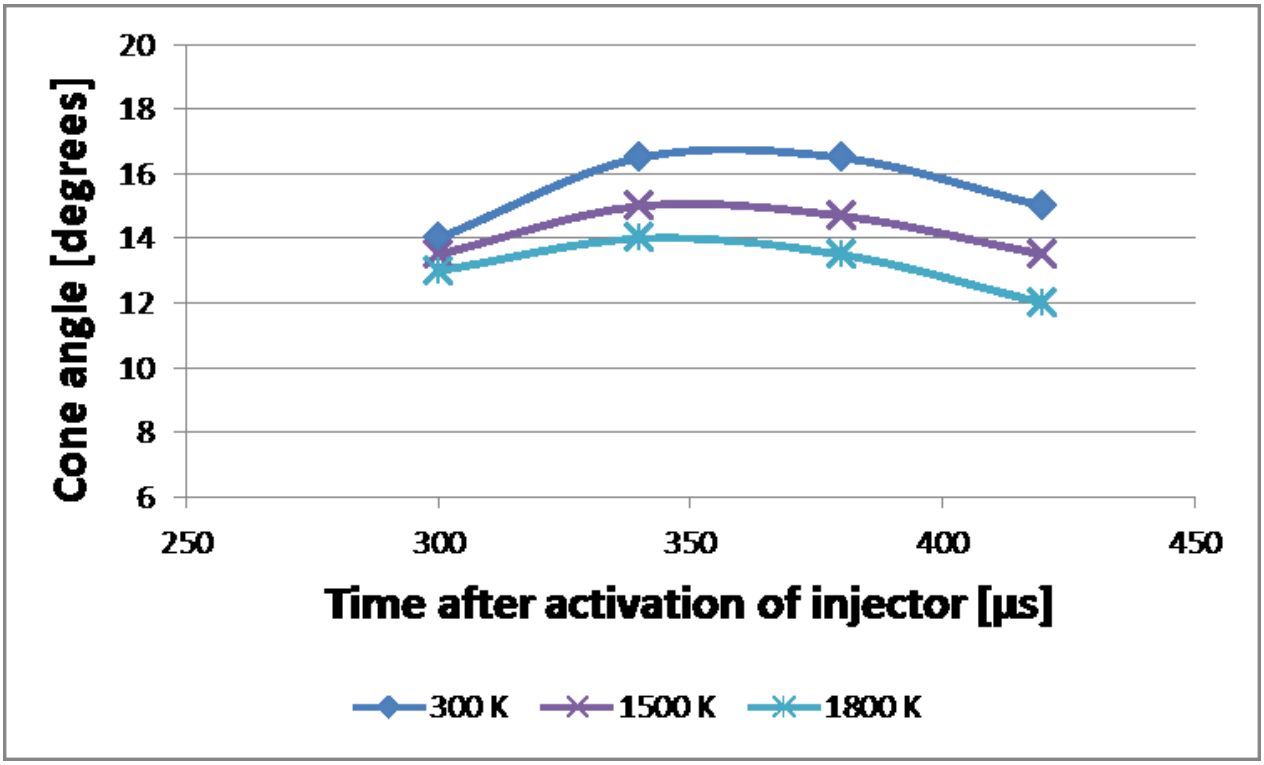

Figure 91 Cone angle, as a function of time, with ambient temperature used as parameter at 5 bar ambient pressure, measured using the tracer Laser Induced Fluorescence technique

8. Conclusion, contributions of this work and future work

8.1 Introduction

As the title implies, the purpose of this chapter is to summarize the conclusions and contributions of this work. Additionally some ideas for future work targeted to better understanding evaporating spray phenomena will be described.

8.2 Conclusions and Contributions of this work

Similar experiments carried out in the past, had none or primitive electronic control of the setup. In this work, real-time multilevel-architecture monitoring and controlling equipment was custom-built. A reprogrammable NI FPGA connected to a Real-Time-Controller was programmed in LabView, to receive information from sensors and send commands to a series of actuators. This improved control of the rig allowed for better control of the experimental conditions as described below. In this work, Bronkhorst mass flow meters, coupled with LabView purpose-programmed controllers were used for gas mixing as the constant volume vessel could not be evacuated. This is a paramount measurement, as the post-combustion conditions were calculated based on the amount of gases in the vessel.

So, because of the flow meters, the amount of pre-combustion gases entering the vessel can be better controlled and combined with chemical equilibrium calculations based on minimization of Gibbs energy, the exact post-combustion conditions can be predicted. In similar, previous work, perfect combustion of gases was being assumed in the vessel. However it is well known that dissociation of chemical reactions is promoted at higher pressures. In the vessel high pressures are reached and it was calculated that, though in small scale, dissociation of the pre-ignition gases does take place.

In this work, effort has been put in trying to maintain heat capacity and thermal conductivity of post-combustion gases at the same levels as in a diesel engine. Many

researchers ignore these parameters, as their influence in fuel evaporation is not of great importance. But combined with combustion free-radicals appeared from dissociation of the pre-ignition technique, values of Cp and k can reach very high, non-realistic values. To overcome this problem, light gases, which have low heat properties, were added in greater proportion in the pre-ignition mixture. Future plans could include the addition of Argon.

Additionally, in this work it is the first time that the effect of chemical dissociation in a similar rig is being investigated. It was concluded that dissociation is a phenomenon taking place in chemical heating techniques, but can however be neglected.

From the Fuel Injection Equipment point of view, this work has introduced a dual common rail system. The older common rail systems were equipped with a pressure control valve. In the newer common rail systems, to save energy from pressurizing and then returning to tank excess fuel, a by-pass valve is being installed prior to the high-pressure pump and is being controlled by a pressure sensor on the rail. However with the later configuration the control of pressure in the common rail suffers from a time-lag. As in this work a new type common rail system is to be tested, the pressure in the rail was measured by the pressure sensor on the new-type rail and a dummy old-type common rail was used to control the fuel pressure by the pressure regulating valve. Both pressure regulating valve and low-pressure by-pass valve were controlled by custom made National Instruments electronics to ensure stable pressure in the rail during injections. Clearly, it was not in the scope of this work to program the FIE system to save energy, but it could be easily done with this dual-rail configuration.

Similar macroscopic measurements in sprays have been performed in the past and in particular it has been observed that the cone angle of a spray remains constant with time. However, a novel observation of this work, which was only possible by the high-speed controlling software and camera, was the trend of slightly increasing and then decreasing cone angle. This was explained as the spray needs some time to fully develop, thus the increasing trend and after the injection has stopped, the spray needs some time to break into smaller structures, thus the decreasing trend.

In terms of the spray evaporation, it has been suggested in this work that a supercritical mechanism takes place. So far, all computational work is based on the assumption of latent heat absorption evaporation, as described by the D^2 law. The fuel injector produces fuel droplets with different values of diameters. So under the latent heat evaporation assumption, larger droplets would take longer time to evaporate. However, in this work it was experimentally observed that the evaporation of a spray takes place roughly on the same distance from the nozzle exit, thus all droplets evaporate on the same time, Figure 89. Clearly, at engine-like conditions ambient pressure and temperature values are greater than the critical pressure and temperature of typical hydrocarbons usually found in the diesel fuel blend. It is known that supercritical evaporation of a mixture composed of liquid and vapour phase, takes place without latent heat absorption, but as an instant transition from the two phase mixture to the vapour phase. However, the fuel injected in the cylinder through the injector is in liquid phase and is instantly being surrounded by supercritical ambient pressure. Even though the ambient temperature is supercritical, the spray cools down the ambient. In order for the supercritical transition to commence, the droplets will firstly have to be at supercritical temperature. Some time is required to warm up the spray. This might be the reason why in the spray images droplets appear for some time after injection and then evaporate all together. Maybe supercritical transition of the liquid phase is the reason why pre-injection in diesel engines promotes fuel evaporation and decreaces emissions, as the pre-injection increases the in-cylinder temperature. Even if the pre-injection fuel does not combust, it significantly reduces the fuel quantity of the main injection, so the main injection spray needs less time to warm up and evaporate.

8.3 Future work

To investigate the hypothesis of supercritical evaporation, the fuel vapour distribution needs to be quantitatively measured. This was achieved using an LIF technique based on the fluorescence of a naphthalene tracer, added in a pure Dodecane fuel. Methyl-naphthalene and Dodecane were chosen because they have evaporation characteristics similar to the average

diesel fuel, as demonstrated with the use of High-Speed Schlieren and back-illumination cinematography.

The hypothesis of supercritical evaporation needs to be further investigated by experimental means. For example, in this work the spray temperature was not measured, but referred from past work. High speed two colour LIF thermometry would provide the temporal and spatial temperature distribution field in the spray. Also, High-speed LIF with telescopic lens should be able to verify the sudden supercritical evaporation hypothesis, as a sudden change of tracer concentration would appear.

Finally, in this work, though the ambient temperature was well above the critical temperature of the typical Diesel and Dodecane, the ambient pressure was below the critical pressure of the fuel liquid. This was due to the structural integrity of the vessel. As demonstrated, in order to increase the post-combustion pressure, the pre-combustion pressure has to be increased. This, however, is a very dangerous task, as a minor increase of the pre-ignition pressure, will lead to a major increase of the post combustion pressure, Figure 29. By the end of the experimental measurements, the windows were damaged on the internal surface by the impinging spray and the combustion and on the external surface and their interior by the laser beam. So, further increase of the post-combustion vessel pressure requires structural and software modifications.

References

ALEIFERIS. 2000 PhD Thesis

ARAI, M., TABATA, M., HIROYASU, H. & SHIMIZU, M. 1984. Disintegrating process and spray characterization of fuel jet injected by a diesel nozzle. *SAE*, 840275.

ATZLER, F., WEIGAND, A., ROTONDI, R. & KASTNER, O. 2007. Emissions reduction potential of high EGR rates in D.I. Diesel engines. *SAE*, 2007-24-0024.

AUNG, K. T., HASSAN, M. I. & FAETH, G. M. 1997. Flame stretch interactions of laminar premixed hydrogen/air flames at normal temperature and pressure. *Combustion and Flame,* 109, 1-24.

BAE, C. & KANG, J. 2000. Diesel spray development of VCO nozzles for high pressure direct injection. *SAE.*

BAERT, R. S. G., FRIJTERS, P. J. M., SOMERS, B., LUIJTEN, C. & DE BOER, W. A. 2009. Design and operation of a high pressure, high temperature cell for HD diesel spray diagnostics: guidelines and results. *SAE*.

BAIK, S., BLANCHARD, J. & CORRADINI, M. 2001. Development of micro-diesel injector nozzles via MEMS technology and effects on spray characteristics. *SAE*, 2001-01-0528.

BAYVEL, L. & ORZECHOWSKI, Z. 1993. *Liquid atomization*.

BLOTEVOGEL, T., EGERMAN, J., LEIPERTZ, A., HARTMANN, M., SCHENK, M. & BERCKMULLER, M. 2004. Developing planar laser induced fluorescence for the investigation of the mixture formation process in hydrogen engines. *SAE.*

BOSCH, R. G. 2005. *Diesel-Engine Management*.

BOUGIE, B., TULEJ, M., DREIER, T., DAM, N. J., TER MEULEN, J. J. & GERBER, T. 2005. Optical diagnostics of diesel spray injections and combustion in a high-pressure high-temperature cell. *Applied Physics B: Lasers and Optics,* 80, 1039-1045.

BOWMAN, C.T. and HANSON, R.K. "Shock Tubes and Lasers: New Opportunities for High Temperature Kinetics Studies," Invited Plenary Lecture, 16 th Inter. Symp. on Gas Kinetics, Cambridge, UK, July 2000. BRADLEY, J. 1962. *Shock waves in chemistry and physics*.

BRUNEAUX, G. 2001a. LIQUID AND VAPOR SPRAY STRUCTURE IN HIGH-PRESSURE COMMON RAIL DIESEL INJECTION. 11, 24.

BRUNEAUX, G. 2001b. A Study of Soot Cloud Structure In High Pressure Single Hole Common Rail Diesel Injection Using Multi-Layered Laser-Induced Incandescence. *Proceedings of Comodia*, 622-630.

BRUNEAUX, G. 2007. Study of the correlation between mixing and auto-ignition processes in high pressure diesel jets. *SAE.*

BRUNEAUX, G., AUGE, M. & LEMENAND, C. 2004. A Study of Combustion Structure in High Pressure Single Hole Common Rail Direct Diesel Injection Using Laser Induced Fluorescence of Radicals (Spray Technologies, Mixture Formation). *The...international symposium on diagnostics and modeling of combustion in internal combustion engines,* 2004, 551-559.

BRUNEAUX, G., VERNOEVEN, D. & BARITAUD, T. 1999. High pressure diesel spray and combustion visualization in a transparent model diesel engine. *SAE.*

CHARALAMPOUS, G., HARDALUPAS, Y. & K. P. TAYLOR, A. M. 2009. Novel Technique for Measurements of Continuous Liquid Jet Core in an Atomizer. *AIAA Journal,* 47, 2605-2615.

CHASE, M., DAVIES, C., DOWNEY, J., FRURIP, D., MCDONALD, R. & SYVERUD, A. 1985. *NIST-JANAF Thermochemical Tables* [Online]. http://kinetics.nist.gov/janaf/: NIST.

CLARKSON, J., GRIFFITHS, J. F., MACNAMARA, J. P. & WHITAKER, B. J. 2001. Temperature fields during the development of combustion in a rapid compression machine. *Combustion and Flame,* 125, 1162-1175.

COMMISSION, E. 2006. Impact Assessment for Euro 6 emission limits for light duty vehicles.

CORPORATION, N. I. 2009. CompactRIO Developers Guide, Recommended LabVIEW Architectures and Development Practicesfor Machine Control Applications.

COUNCIL, T. E. P. A. 1997. On the approximation of the laws of the Member States concerning pressure equipment.

CROWE, C. 2006. *Multiphase flow handbook*.

CRUA, C., KENNAIRD, D. A. & HEIKAL, M. R. 2003. Laser-induced incandescence study of diesel soot formation in a rapid compression machine at elevated pressures. *Combustion and Flame,* 135, 475-488.

DAVY, M., WILLIAMS, P. & ANDERSON, R. 2000. Effects of fuel composition on mixture formation in a firing direct- injection spark-ignition (disi) engine: an experimental study using mie- scattering and planar laser-induced fluorescence (plif) techniques. *SAE.*

DAWSON, M. & HOCHGREB, S. 1998. Liquid fuel visualization using laser-induced fluorescence during cold start. *SAE.*

DELACOURT, E., DESMET, B. & BESSON, B. 2005. Characterisation of very high pressure diesel sprays using digital imaging techniques. *Fuel,* 84, 859-867.

DENT, J., C. 1971. A basis for the comparison of various experimental methods for studying spray penetration. *SAE*, 710571.

DEPUSSAY, , E., ROUSSELLE, C., BURNEL, , S. & RICORDEAU, V. 1998. Comparative measurements of local iso-octane concentrations by planar laser induced fluorescence and catalytic hot wires probe in SI engine. *SAE.*

DESANTES, J. M., PAYRI, R., SALVADOR, F. J. & GIL, A. 2006. Development and validation of a theoretical model for diesel spray penetration. *Fuel,* 85**,** 910-917.

DOEBELIN, E. 2003. *Measurement Systems : Application and Design*.

DONOVAN, M. T., HE, X., ZIGLER, B. T., PALMER, T. R., WOOLDRIDGE, M. S. & ATREYA, A. 2004. Demonstration of a free-piston rapid compression facility for the study of high temperature combustion phenomena. *Combustion and Flame,* 137**,** 351-365.

DUWEL, I., SCHORR, J., PEUSER, P., ZELLER, P., WOLFRUM, J. & SCHULZ, C. 2004a. Spray diagnostics using an all-solid-state Nd : YAlO3 laser and fluorescence tracers in commercial gasoline and diesel fuels. *Applied Physics B-Lasers and Optics,* 79**,** 249-254.

DUWEL, I., SCHORR, J., WOLFRUM, J. & SCHULZ, C. 2004b. Laser-induced fluorescence of tracers dissolved in evaporating droplets. *Applied Physics B-Lasers and Optics,* 78**,** 127-131.

EINECKE, S., SCHULZ, C. & SICK, V. 2000. Measurement of temperature, fuel concentration and equivalence ratio fields using tracer LIF in IC engine combustion. *Applied Physics B-Lasers and Optics,* 71**,** 717-723.

EJIM, C. E., FLECK, B. A. & AMIRFAZLI, A. 2007. Analytical study for atomization of biodiesels and their blends in a typical injector: Surface tension and viscosity effects. *Fuel,* 86**,** 1534-1544.

EKENBERG, M. & JOHANSSON, B. 2000. Fuel distribution in an air assist direct injected spark ignition engine with central injection and spark plug measured with laser induced fluorescence. *SAE.*

ELKOTB, M. M. 1982. Fuel atomization for spray modelling. *Progress in Energy and Combustion Science,* 8**,** 61-91.

EPA 2009. Integrated Science Assessment for Particulate Matter, EPA/600/R-08/139F.

FERGUSON, C. 1985. *Internal combustion engines*.

FERRI, A. 1961. *Fundamental data obtained from shock-tube experiments.*

FRANKE, A., KOBAN, W., OLOFSSON, J., SCHULZ, C., BESSLER, W., REINMANN, R., LARSSON, A. & ALDÉN, M. 2005. Application of advanced laser diagnostics for the investigation of the ionization sensor signal in a combustion bomb. *Applied Physics B: Lasers and Optics,* 81**,** 1135-1142.

FRIEDEN, D., SICK, V., GRONKI, J. & SCHULZ, C. 2002. Quantitative oxygen imaging in an engine. *Applied Physics B-Lasers and Optics,* 75**,** 137-141.

FROBA, A. P., RABENSTEIN, F., MUNICH, K.-U. & LEIPERTZ, A. 1998. Mixture of TEA and Benzene as a new seeding material for quantitative two-dimensional laser-induced exciplex fluorescence imaging of vapor and liquid fuel inside SI engines. *Combustion and Flame.*

FUJIMOTO, H., HIGASHI, K., YAMASHITA, T. & SENDA, J. 2005a. Effects of Ambient Temperature and Oxygen Concentration on Soot Behavior in Diesel Flame. *SAE***,** 2005-24-007.

FUJIMOTO, H., MYONG, K., SUZUKI, H., UEDA, K. & SENDA, J. 2005b. Characteristics of a Transient Spray of Fuel with Multiple Components. *SAE***,** 2005-01-3846.

FUJIMOTO, H., OURA, S., MORINAGA, S., HASHIMOTO, Y., YAMASHITA, T. & SENDA, J. 1999. Combustion phenomena in IDI diesel engine detected by optical methods. *SAE.*

FUJIMOTO, H., SENDA, J., KOMEMUSHI, Y. & KUGE, T. 2006. Soot generation in spray of oxygenated fuel. *SAE.*

GAYDON, A. 1963. *The shock tube in high-temperature chemical physics*.

GERVAIS, D & GASTALDI, P. 2002. A comparison of two quantitative laser-induced fluorescence techniques applied to a new air-guided direct injection SI combustion chamber. *SAE.*

GILL, S. S., TSOLAKIS, A., DEARN, K. D. & RODRÍGUEZ-FERNÁNDEZ, J. 2011. Combustion characteristics and emissions of Fischer–Tropsch diesel fuels in IC engines. *Progress in Energy and Combustion Science,* 37**,** 503-523.

GRAF, N., GRONKI, J., SCHULZ, C., BARITAUD, T., CHEREL, J., DURET, P. & LAVY, J. 2001. In-cylinder combustion visualization in an auto-igniting gasoline engine using fuel tracer- and formaldehyde-LIF imaging. *SAE.*

GRANT, R. P. & MIDDLEMAN, S. 1966. Newtonian jet stability. *AIChE Journal,* 12**,** 669-678.

GUILLARD, F., FRITZON, R., REVSTEDT, J., TRÄGÅRDH, C., ALDÉN, M. & FUCHS, L. 1998. Mixing in a confined turbulent impinging jet using planar laser-induced fluorescence. *Experiments in Fluids,* 25**,** 143-150.

HANSON ,R.K., 1997, Advanced Laser-Based Diagnostics for Shock Tube/Tunnel Flows, plenary paper, Proceedings of the 21st Int"l. Symp. on Shock Tubes and Waves, July 20-25, 1997, Australia.

HANSON, R.K., 2013, Advances in Shock Tube/Laser Absorption Techniques for Studies of Combustion Kinetics, 8th International Conference on Chemical Kinetics, Seville, Spain, from 8th to 12 th of July 2013.

HATTIKUDUR, U. R. & THODOS, G. 1970. Equations for the Collision Integrals Omega 21[sup (1,1)]* and Omega([sup 2,2]). *The Journal of Chemical Physics,* 52**,** 4313.

HAUDIQUERT, M., CESSOU, A., STEPOWSKI, D. & COPPALLE, A. 1997. OH and soot concentration measurements in a high-temperature laminar diffusion flame. *Combustion and Flame,* 111**,** 338-349.

HECHT, E. 2001. *Optics* Addison-Wesley.

HEITOR, M. V. & MOREIRA, A. L. N. 1993. Thermocouples and sample probes for combustion studies. *Progress in Energy and Combustion Science,* 19**,** 259-278.
HELIN, X., YUSHENG, Z. & HUIYA, Z. 2006. Experimental and numerical study of the characteristics of liquid phase LPG and diesel fuel sprays. *SAE.*
HEYWOOD, J., B 1988. *Internal Combustion Engine Fundamentals*.
HIGGINS, B., MUELLER, C. & SIEBERS, D. 1999. Measurements of fuel effects on liquid-phase penetration in DI Sprays. *SAE***,** 1999-01-0519.
HIGGINS, B. & SIEBERS, D. L. 2001. Measurement of the flame lift-off location on DI sprays using OH chemiluminescence. *SAE.*
HILDENBRAND, F. & SCHULZ, C. 2001. Measurements and simulation of in-cylinder UV-absorption in spark ignition and Diesel engines. *Applied Physics B: Lasers and Optics,* 73**,** 173-180.
HIROYASU, H. 2000. Spray breakup mechanism from the hole-type nozzle and its applications. *Atomization and Sprays,* 10**,** 511-527.
HIROYASU, H. & ARAI, M. 1990. Structures of fuel sprays in diesel engines. *SAE.*
HIRSCHFELDER, J. O., CURTISS, C. F. & BYRON BIRD, R. 1964. Molecular Theory of Gases and Liquids Nueva York, EUA : Wiley.
HULT, J., MEIER, U., MEIER, W., HARVEY, A. & KAMINSKI, C. F. 2005. Experimental analysis of local flame extinction in a turbulent jet diffusion flame by high repetition 2-D laser techniques and multi-scalar measurements. *Proceedings of the Combustion Institute,* 30**,** 701-709.
HWANG, J. S., HA, J. S. & NO, S. Y. 2003. SPRAY CHARACTERISTICS OF DME IN CONDITIONS OF COMMON RAIL INJECTION SYSTEM (II). *International Journal of Automotive Technology,* 4**,** 119-124.
JANNA, W., S. 2009. *Engineering heat transfer*.
KADOTA, T. & HIROYASU, H. 1981. Combustion of a fuel droplet in supercritical gaseous environments. *Eighteenth Symposium (International) on Combustion*.
KAISER, S. A. & LONG, M. B. 2005. Quantitative planar laser-induced fluorescence of naphthalenes as fuel tracers. *Proceedings of the Combustion Institute,* 30**,** 1555-1563.
KAMIMOTO, T., YOKOTA, H. & KOBAYASHI, H. 1987. Effect of high pressure injection on soot formation processes in rapid compression machine to simulate diesel flames. *SAE***,** 871610.
KARIMI, K. 2007. *Characterisation of Multiple-Injection Diesel Sprays at Elevated Pressures and Temperatures.*
KIDO, A., KUBOTA, S., OGAWA, H. & MIYAMOTO, N. 1998. Simultaneous measurements of concentration and temperature distributions in unsteady gas jets by an iodine LIF method. *SAE.*
KLEIN-DOUWEL, R. J. H., FRIJTERS, P. J. M., SOMERS, L. M. T., DE BOER, W. A. & BAERT, R. S. G. 2007. Macroscopic diesel fuel spray shadowgraphy using high speed digital imaging in a high pressure cell. *Fuel,* 86**,** 1994-2007.
KNIGHT, B. 1955. The Performance of a Type of Swirl Atomizer. *Proc. Inst. Mech. Eng.,* 169**,** 104.
KOBAN, W. & C, S. 2008. Toluene Laser-Induced Fluorescence (LIF) Under Engine-Related Pressures, Temperatures and Oxygen Mole Fractions. *SAE.*
KOBAN, W., KOCH, J. D., HANSON, R. K. & SCHULZ, C. 2005a. Oxygen quenching of toluene fluorescence at elevated temperatures. *Applied Physics B-Lasers and Optics,* 80**,** 777-784.
KOBAN, W., KOCH, J. D., HANSON, R. K. & SCHULZ, C. 2005b. Toluene LIF at elevated temperatures: implications for fuel-air ratio measurements. *Applied Physics B-Lasers and Optics,* 80**,** 147-150.
KOBAN, W., KOCH, J. D., SICK, V., WERMUTH, N., HANSON, R. K. & SCHULZ, C. 2005c. Predicting LIF signal strength for toluene and 3-pentanone under engine-related temperature and pressure conditions. *Proceedings of the Combustion Institute,* 30**,** 1545-1553.
KOSTAS, J., HONNERY, D. & SORIA, J. 2009. Time resolved measurements of the initial stages of fuel spray penetration. *Fuel,* 88**,** 2225-2237.
KUNKULAGUNTA, K. 2000. Video imaging and analysis of common rail sprays in an optical engine using shadowgraphy technique. *SAE.*
KWON, O. C. & FAETH, G. M. 2001. Flame/stretch interactions of premixed hydrogen-fueled flames: measurements and predictions. *Combustion and Flame,* 124**,** 590-610.
L.HERMANT, J. F. L. C. A. 2001. Quantification of fuel concentrations and estimation of liquid/vapor ratios in direct injection sprays by laser-induced fluorescence. *SAE.*
LABS, J. E. & PARKER, T. E. 2007. A comparison of single shot diesel spray combustion emissions with trends predicted by a conceptual model. *Combustion Science and Technology,* 179**,** 1159-1182.
LACOSTE, J. 2006. *Characteristics of diesel sprays at high temperatures and pressures.*
LAW, C. K. 2010. *Combustion Physics*, Cambridge University Press.
LEE, S., KUSAKA, J. & DAISHO, Y. 2001. Spray characteristics of alternative fuels in constant volume chamber (comparison of the spray characteristics of LPG, DME and n-dodecane). *JSAE Review,* 22**,** 271-276.
LEE, S., TANAKA, D., KUSAKA, J. & DAISHO, Y. 2002. Effects of diesel fuel characteristics on spray and combustion in a diesel engine. *JSAE Review.*
LEFEBVRE, A., H 1989. *Atomization and Sprays*.

LIM, J., KIM, Y. & MIN, K. 2004. Characteristics of the Spray and Combustion Process of DME under Engine Conditions.
LÓPEZ, J. J. & PICKETT, L. M. 1. Jet/wall interaction effects on soot formation in a diesel fuel jet. *Fuel,* 7**,** T70.
LUONG, M., ZHANG, R., SCHULZ, C. & SICK, V. 2008. Toluene laser-induced fluorescence for in-cylinder temperature imaging in internal combustion engines. *Applied Physics B-Lasers and Optics,* 91**,** 669-675.
MATHEWS, P. 2010. *Sample Size Calculations: Practical Methods for Engineers and Scientists*, Mathews Malnar and Bailey, Inc.
MCGLASHAN, N. R. 1997. *Design and testing of a high pressure chamber for diesel spray studies.* PhD, Imperial College London (University of London).
MEROLA, S. S. & VAGLIECO, B. M. 2004a. Analysis on Common Rail diesel engine combustion process by optical diagnostics. *International Conference on Energy and Automotive Technologies*.
MEROLA, S. S. & VAGLIECO, B. M. 2004b. Analysis on Common Rail diesel engine combustion process by optical diagnostics. *N/A*.
MINETTI, R., RIBAUCOUR, M., CARLIER, M., FITTSCHEN, C. & SOCHET, L. R. 1994. Experimental and modeling study of oxidation and autoignition of butane at high pressure. *Combustion and Flame,* 96**,** 201-211.
MITTAL, G. & SUNG, C. J. 2006. Aerodynamics inside a rapid compression machine. *Combustion and Flame,* 145**,** 160-180.
MORLEY, C. 2005. Gaseq.
MYONG, K. J., SUZUKI, H., SENDA, J. & FUJIMOTO, H. 2008. Spray inner structure of evaporating multi-component fuel. *Fuel,* 87**,** 202-210.
NABER, J. D. & SIEBERS, D. 1996. Effects of gas density and vaporization on penetration and dispersion of diesel sprays. *SAE***,** 960034.
NABER, J. D. & SIEBERS, D. L. 1998. Hydrogen combustion under diesel engine conditions. *International Journal of Hydrogen Energy,* 23**,** 363-371.
NASR, G., G., YULE, A. J. & BENDIG, L. 2002. *Industrial sprays and atomization, design, analysis and applications*, Springer.
NIST. 2013. *NIST webbook* [Online]. Available: http://webbook.nist.gov/cgi/cbook.cgi?ID=C112403&Units=SI&Mask=7.
NYGREN, J., HULT, J., RICHTER, M., ALDÉN, M., CHRISTENSEN, M., HULTQVIST, A. & JOHANSSON, B. 2002. Three-dimensional laser induced fluorescence of fuel distributions in an HCCI engine. *Proceedings of the Combustion Institute,* 29**,** 679-685.
OSSLER, F., METZ, T. & ALDÉN, M. 2001. Picosecond laser-induced fluorescence from gas-phase polycyclic aromatic hydrocarbons at elevated temperatures. I. Cell measurements. *Applied Physics B,* 72**,** 465-478.
OSSLER, F. A., M. 1997. Measurements of picosecond laser induced fluorescence from gas phase 3-pentanone and acetone: Implications to combustion diagnostics. *Applied Physics B: Lasers and Optics.*
PARK, S., W., KIM, J., W. & LEE, C., S. 2006. Effect of injector type on fuel-air mixture formation of high-speed diesel sprays. *Proc.Instn.Mech.Engrs,* 220.
PAYRI, R., SALVADOR, F. J., GIMENO, J. & DE LA MORENA, J. 2008a. Macroscopic behavior of diesel sprays in the near-nozzle field. *SAE***,** 2008-01-0929.
PAYRI, R., SALVADOR, F. J., GIMENO, J. & ZAPATA, L. D. 2008b. Diesel nozzle geometry influence on spray liquid-phase fuel penetration in evaporative conditions. *Fuel,* 87**,** 1165-1176.
PICKETT, L. M. & SIEBERS, D. L. 2002. An investigation of diesel soot formation processes using micro-orifices. *Proceedings of the Combustion Institute,* 29**,** 655-662.
PICKETT, L. M. & SIEBERS, D. L. 2004. Soot in diesel fuel jets: effects of ambient temperature, ambient density, and injection pressure. *Combustion and Flame,* 138**,** 114-135.
PLACKMANN, J., KIM, T. & GHANDHI, J. 1998. The effects of mixture stratification on combustion in a constant volume combustion vessel. *SAE.*
PREUSSNER, C., DORING, C., FEHLER, S. & KAMPMANN, S. 1998. GDI: Interaction between mixture preparation, combustion system and injector performance. *SAE.*
RAYLEIGH, L. 1878. On the instability of jets. *Proceedings of the London Mathematical Society*.
REITZ, R. & BRACCO, F. 1979. On the dependence of spray angle and other spray parameters on nozzle design and operating conditions. *SAE***,** 790494.
REITZ, R. & BRACCO, F. 1982. Mechanism of atomization of aliquid jet. *Phys.Fluids,* 25**,** 1730-1742.
RICHTER, M., AXELSSON, B. & ALDEN, M. 1998. Engine diagnostics using laser induced fluorescence signals collected through an endoscopic detection system. *SAE.*
SASAKI, S., AKAGAWA, H. & TSUJIMURA, K. 1998. A study on surrounding air flow induced by diesel sprays. *SAE.*
SCHULZ, C., GRONKI, J. & ANDERSSON, S. 2004. Multi-species, laser-based imaging measurements in a diesel spray. *SAE.*
SEITZMAN, J. M., HANSON, R. K., DEBARBER, P. A. & HESS, C. F. 1994. Application of Quantitative 2-Line Oh Planar Laser-Induced Fluorescence for Temporally Resolved Planar Thermometry in Reacting Flows. *Applied Optics,* 33**,** 4000-4012.
SETTLES, G., S. 1949. *Schlieren and shadowgraph techniques : visualizing phenomena in transparent media*.
SIEBERS, D. L. 1998. Liquid phase fuel penetration in diesel sprays. *SAE.*
SIEBERS, D. L. & HIGGINS, B. 2001. Flame lift-off on direct-injection diesel sprays under quiescent conditions. *SAE.*
SIRIGNANO, W. 1999. *Fluid Dynamics and Transport of Droplets and Sprays*, Cambridge University Press.

SORENSON, S., GLENSVIG, M. & ABATA, D. 1998. Dimethyl ether in diesel fuel injection systems. *SAE,* 981159.
SOTERIOU, C., ANDREWS, R. & SMITH, M. 1998. Diesel injection - laser light sheet illumination of development of cavitation in orifices. *I.Mech.E.Conf.Proc.London*.
SPALDING, D. 1979. *Combustion and mass transfer*.
SPIEKERMANN, P., JERZEMBECK , S., FELSCH , C., VOGEL , S., GAUDING, M. & PETERS , N. 2009. EXPERIMENTAL DATA AND NUMERICAL SIMULATION OF COMMON-RAIL ETHANOL SPRAYS AT DIESEL ENGINE-LIKE CONDITIONS. *Atomization and Sprays,* 19**,** 99.
STOFFELS, G., STOKS, S., AM, N. & EULEN, J. 2008. Methods to Correct Planar Laser-Induced Fluorescence Distributions for Local Nonuniform Laser Attenuation. *Applied Optics.*
STONE, R. 1985. *Introduction to internal combustion engines*.
TAMAKI, N., SHIMIZU, M. & HIROYASU, H. 2001. Enhancement of the atomization of a liquid jet by cavitation in a nozzle hole. *Atomization and Sprays,* 11**,** 125-137.
TAMURA, M., SAKURAI, T. & TAI, H. 2001. A study of crevice flow in a gas engine using laser-induced fluorescence. *SAE.*
TANASAWA, Y. & TOYODA, S. 1954. (in Japanese). *Trans. JSME,* 20**,** 7.
TANG, C., MAN, X., WEI, L., PAN, L. & HUANG, Z. Further study on the ignition delay times of propane–hydrogen–oxygen–argon mixtures: Effect of equivalence ratio. *Combustion and Flame*.
TAYLOR, S. G. 1949. The instability of liquid surfaces when accelerated in a direction perpendicular to their planes I. *Proceedings of the Royal Society*.
TEA, G., BRUNEAUX, G., KASHDAN, J. T. & SCHULZ, C. 2011. Unburned gas temperature measurements in a surrogate Diesel jet via two-color toluene-LIF imaging. *Proceedings of the Combustion Institute,* 33**,** 783-790.
TENNISON, P., GEORJON, T., FARRELL, P. & REITZ, R. 2009. An experimental and numerical study of sprays from a common rail injection system for use in an HSDI diesel engine. *SAE***,** 980810.
THURBER, M. C., GRISCH, F., KIRBY, B. J., VOTSMEIER, M. & HANSON, R. K. 1998. Measurements and modeling of acetone laser-induced fluorescence with implications for temperature-imaging diagnostics. *Applied Optics.*
TRAN, T., KOCHAR, Y. & SEITZMAN, J. 2008. Acetone photophysics at near critical to supercritical conditions. *AIAA.*
TROST, J., ZIGAN, L. & LEIPERTZ, A. 2013. Quantitative vapor temperature imaging in DISI-sprays at elevated pressures and temperatures using two-line excitation laser-induced fluorescence. *Proceedings of the Combustion Institute,* 34**,** 3645-3652.
TSE, S. D., ZHU, D. L. & LAW, C. K. 2000. Morphology and burning rates of expanding spherical flames in H2/O2/inert mixtures up to 60 atmospheres. *Proceedings of the Combustion Institute,* 28**,** 1793-1800.
TSUJIMURA, T., MIKAMI, S., ACHIHA, N., TOKUNAGA, Y., SENDA, J. & FUJIMOTO, H. 2003. A study of direct injection diesel engine fueled with hydrogen. *SAE.*
VAN DE SANDE, E. & SMITH, J. M. 1976. Jet break-up and air entrainment by low velocity turbulent water jets. *Chemical Engineering Science,* 31**,** 219-224.
VERGNES, C., FOUCHER, F., MOUNAÏM-ROUSSELLE, C., JEANNE, B., BARBEAU, B. & DADIREAU, F. 2007. Cold start physical phenomena in diesel engines. *Proceedings of the 21th ILASS-Europe Meeting.*
VERHOEVEN, D., VANHEMELRYCK, J. & BARITAUD, T. 1998. Macroscopic and ignition characteristics of high-pressure sprays of single-component fuels. *SAE.*
VOGEL, S., HASSE, C., GRONKI, J., ANDERSSON, S., PETERS, N., WOLFRUM, J. & SCHULZ, C. 2005. Numerical simulation and laser-based imaging of mixture formation, ignition, and soot formation in a diesel spray. *Proceedings of the Combustion Institute,* 30**,** 2029-2036.
WAKURI, Y., FUJI, M., AMITANI, R. & TSUNEYA, R. 1960. Studies on the penetration of fuel spray in a diesel engine. *Bull.Jap.Soc.Mech.Engrs,* **13**, 9.
WEBER, J., PETERS, N., PAWLOWSKI, A., KNEER, R., HERGART, C. A., EL TAHRY, S. H. & LIPPERT, A. 2006. 2006-01-1115 Diesel Spray Characterization Using a Micro-Genetic Algorithm and Optical Measurements. *SAE SP,* 2010**,** 49.
WRIGHT, J. 1961. *Shock tubes*.
YEH, C.-N., KAMIMOTO, T., KOBORI, S. & KOSNKA, H. 1993. 2-D imaging of fuel vapor concentration in a DI diesel spray via exciplex-based fluorescence technique. *SAE.*
YEOM, J., ASHIDA, K., SENDA, J., FUJIMOTO, H. & DAN, T. 2001. Analysis of diesel spray structure by using a hybrid model of TAB breakup model and vortex method. *SAE.*
YEOM, J. K., KANG, B. M., LEE, M. J., CHUNG, S. S., HA, J. Y. & FUJIMOTO, H. 2002. A study on the mixture formation process of evaporating diesel spray by offset incidence laser beam. *Journal of Mechanical Science and Technology,* 16**,** 5.
YOON, W. H., KIM, J. Y., KIM, D. H., KIM, K. D. & HA, J. S. 2004. Optimization of Fuel Injection Nozzles for the Reduction of NOx Emissions in Medium-Speed Marine Diesel Engines.
YOSHIZAKI, T., TAKEMURA, Y., HISAEDA, T., NISHIDA, K. & HIROYASU, H. 1996. Planar measurements of the liquid phase temperature in diesel sprays injected into high-pressure and high-temperature environments. *SAE.*
YU, J. & BAE, C. 2003. Dimethyl ether (DME) spray characteristics in a common-rail fuel injection system. *Proc.Instn.Mech.Engrs,* 217 Part D.

YULE, A. J. & FILIPOVIC, I. 1992. On the break-up times and lengths of diesel sprays. *International Journal of Heat and Fluid Flow,* 13**,** 197-206.

ZEL'DOVICH, Y. & RAIZER, Y. 1962. *Physics of shock waves and high-temperature hydrodynamic phenomena*.

ZHANG, L., TSURUSHIMA, T., UEDA, T., ISHII, Y., ITOU, T., MINAMI, T. & YOKOTA, K. 1997. Measurement of liquid phase penetration of evaporating spray in a DI diesel Engine. *SAE***,** 971645.

ZHANG, Y., HUANG, Z., WEI, L., ZHANG, J. & LAW, C. K. 2012. Experimental and modeling study on ignition delays of lean mixtures of methane, hydrogen, oxygen, and argon at elevated pressures. *Combustion and Flame,* 159**,** 918-931.

ZHU, Y., DAVIDSON, D. F. & HANSON, R. K. Pyrolysis and oxidation of decalin at elevated pressures: A shock-tube study. *Combustion and Flame*.

ZIMMERMANN, F. P., KOBAN, W., ROTH, C. M., HERTEN, D. P. & SCHULZ, C. 2006. Fluorescence lifetime of gas-phase toluene at elevated temperatures. *Chemical Physics Letters,* 426**,** 248-251.

Appendix 1 Some basic dimensionless numbers used in this work

Dimensionless number	
Ohnesorge number relates the viscous and surface tension force. $$Oh = \frac{\mu}{\sqrt{\rho\sigma L}} = \frac{\sqrt{We}}{Re}$$	μ is the liquid viscosity ρ is the liquid density σ is the surface tension L is the characteristic length scale (typically-drop diameter) Re is the Reynolds number We is the Weber number
Reynolds number is a measure of the ratio of inertial forces ($V\rho$) to viscous forces (μ / L) $$\mathrm{Re} = \frac{\rho V D}{\mu} = \frac{V D}{\nu} = \frac{Q D}{\nu A}$$	V is the mean fluid velocity (SI units: m/s) D is the diameter (m) μ is the dynamic viscosity of the fluid (Pa·s or N·s/m²) v is the kinematic viscosity (v = μ / ρ) (m²/s) ρ is the density of the fluid (kg/m³) Q is the volumetric flow rate (m³/s) A is the pipe cross-sectional area (m²)
Weber number is a measure of the relative importance of the fluid's inertia compared to its surface tension $$We = \frac{\rho v^2 l}{\sigma}$$	ρ is the density of the fluid. v is its velocity. l is its characteristic length, typically the droplet diameter. σ is the surface tension

Appendix 2 Typical diesel engine conditions

Though there is no such thing as a "typical" diesel engine, as every engine has different characteristics. As this work is focusing on light-duty automotive diesel engines, data are drawn from Honda Civic diesel 2.2Liter engine and the Ford 2.0Liter TDCi diesel engine. Some "typical" characteristics are presented in the table below

Characteristic	Typical Value
Compression ratio	19-22
Orifice diameter	100-200 μm
Warm running	
Intake Temperature	45-120 ^{o}C
Intake Pressure	0.7-2.2 atm
Fuel Temperature	100 ^{o}C
Top Dead Center	
Pressure[1]	43-160 atm
Temperature[2]	625-900 ^{o}C
Gas Density[3]	12-55 kg/m^{3}
If warm TDC 50bar, 700^{o}C, air thermodynamic propertie:	
Heat Conductivity	67.2*10^{-3} W/(m*K)
Heat Capacity	33.05 J/(mole*K)

[1] For adiabatic compression it is $P_2 = P_1\left(\frac{V_1}{V_2}\right)^{\gamma}$

[2] For adiabatic compression it is $T_2 = T_1\left(\frac{P_2}{P_1}\right)^{\frac{\gamma-1}{\gamma}} \rightarrow T_2 = T_1\left(\frac{V_1}{V_2}\right)^{\gamma-1}$

[3] From ideal gas law it is $\mathrm{PV} = nRT \rightarrow \mathrm{PV} = \frac{m}{MW}RT \rightarrow \mathrm{P} = \frac{m}{V}\frac{1}{MW}RT \rightarrow \rho = \frac{P \cdot MW}{RT}$

Appendix 3 Some heat-transfer calculations

On this appendix, using a simple steady state one dimensional heat transfer model, the heat loses of the vessel will be calculated. In Figure 92, a sketch of the heat transfer through the window of the vessel is presented. We can consider the temperature at the center of the vessel to be 1300K, a value reasonable for adiabatic combustion, as shown in Chapter 2, and the room temperature to be 290K. As presented in Chapter 2, fused silica has heat conductivity of 1.3W/mK and a typical value of the convective heat-transfer of air in natural convection is around 25W/m^{2}K (Janna, 2009).

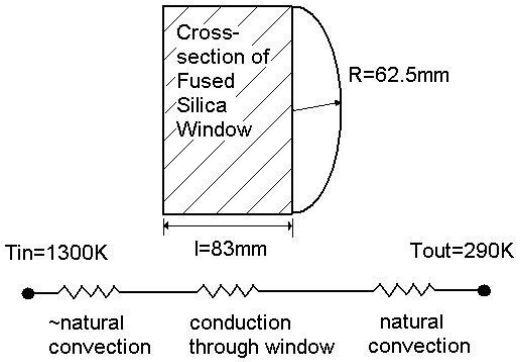

Figure 92 Sketch of heat transfer through vessel's window

The surface area of the window is $A = \pi R^2 = \pi 0.0625^2 = 0.0123\text{m}^2$

So the heat loses through the window are: $Q = \frac{\Delta T}{\frac{1}{h_o A} + \frac{l}{kA} + \frac{1}{h_o A}} = \frac{(1300-290)K}{\frac{2}{25\frac{W}{m^2K}0.0123\text{m}^2} + \frac{0.083m}{1.3\frac{W}{mK}0.0123\text{m}^2}} = 86.36W$

The same methodology is applied for the stainless steel part of the vessel, considering the same dimensions as the window and the electrically heated metal to have reached 500K, value very close to the experimental conditions. The heat loses through the metal part of the vessel are:

$$Q = \frac{\Delta T}{\frac{l}{kA} + \frac{1}{h_o A}} = \frac{(500-290)K}{\frac{0.083m}{16.3\frac{W}{mK}0.0123\text{m}^2} + \frac{1}{25\frac{W}{m^2K}0.0123\text{m}^2}} = 46.88W$$

Appendix 4 Vessel Engineering Drawings and photographs

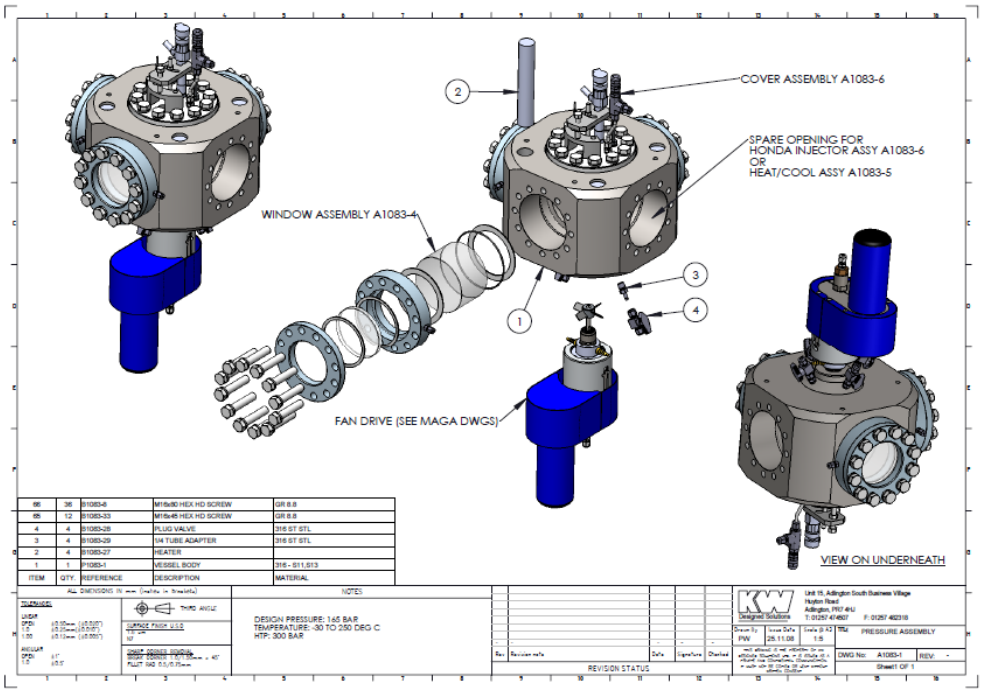

Figure 93 Drawing of the vessel assembly

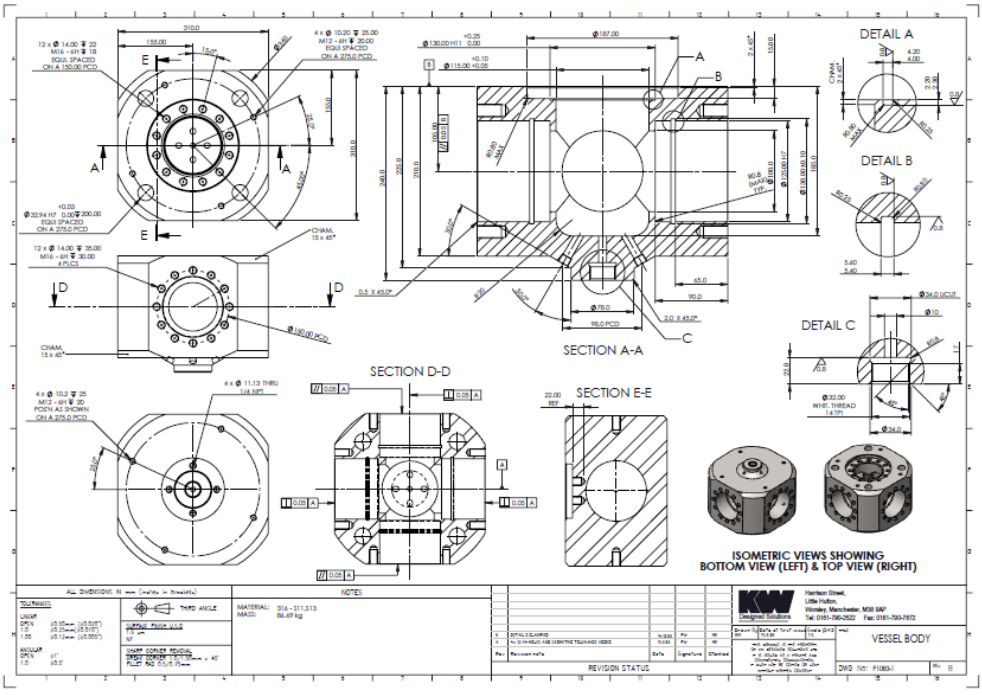

Figure 94 Drawing of the core of the vessel

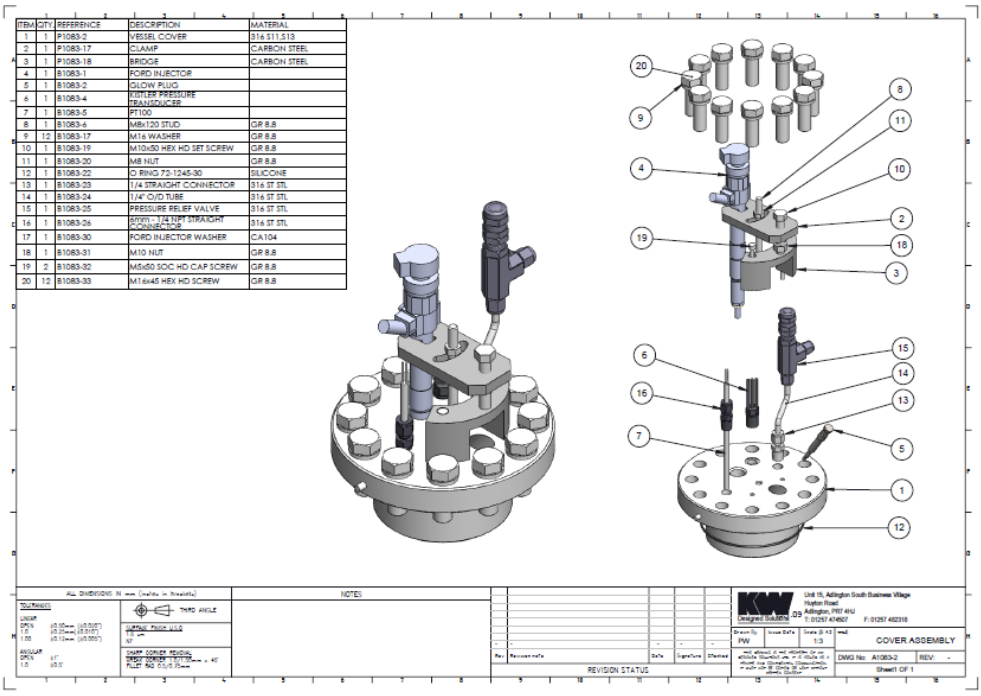

Figure 95 Drawing of the injector mounting port

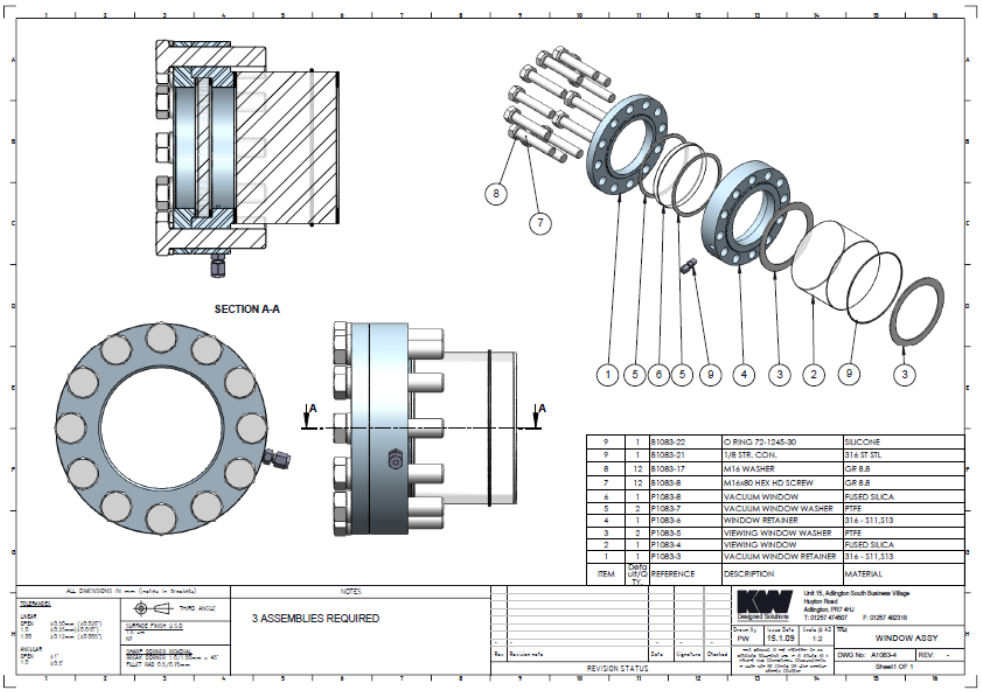

Figure 96 Drawing of the window assembly

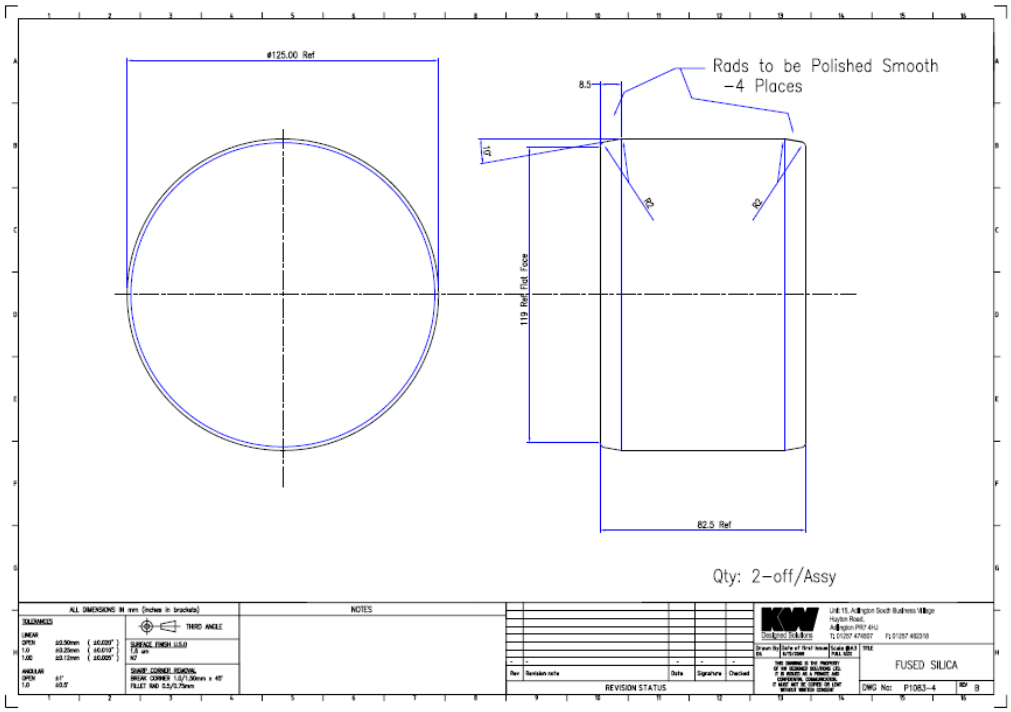

Figure 97 Drawing of the window glass

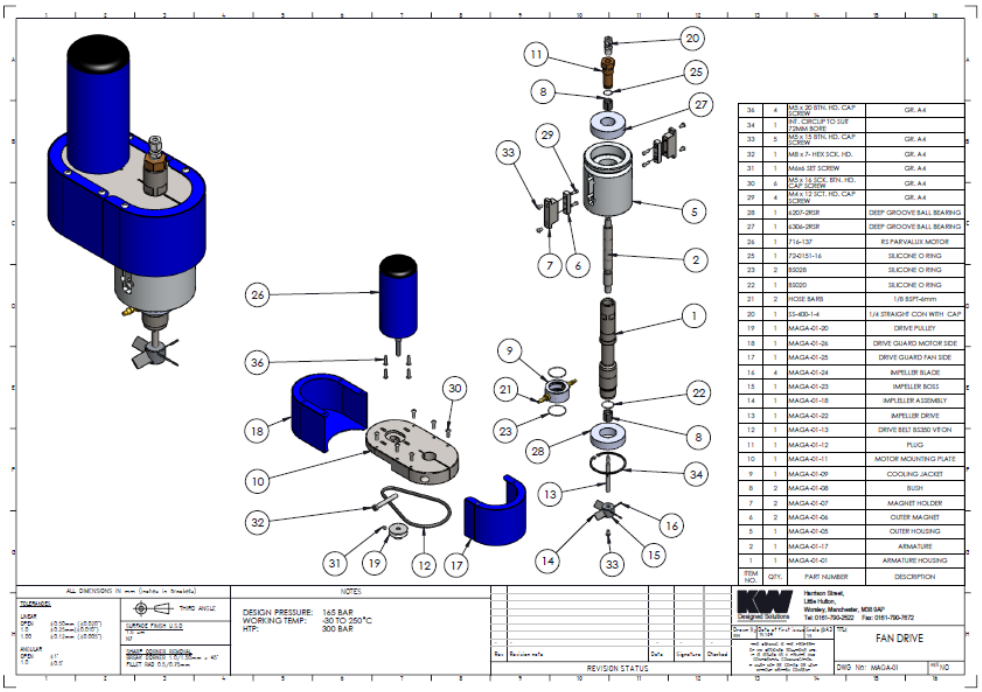

Figure 98 Drawing of the magnetic stirrer assembly

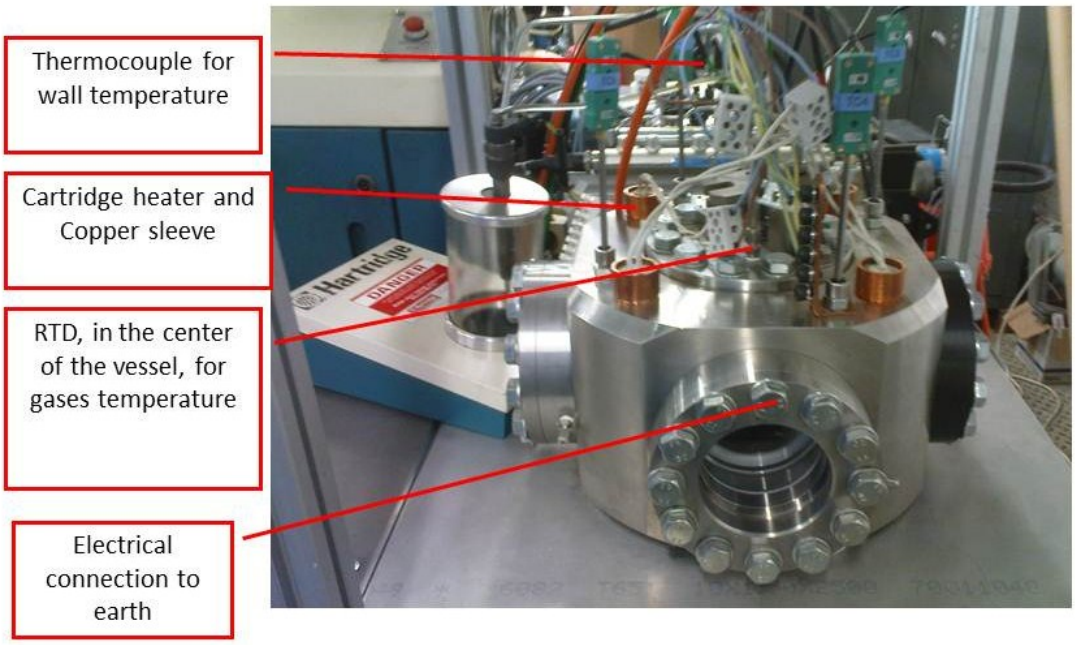

Figure 99 Photograph of Constant Volume Vessel

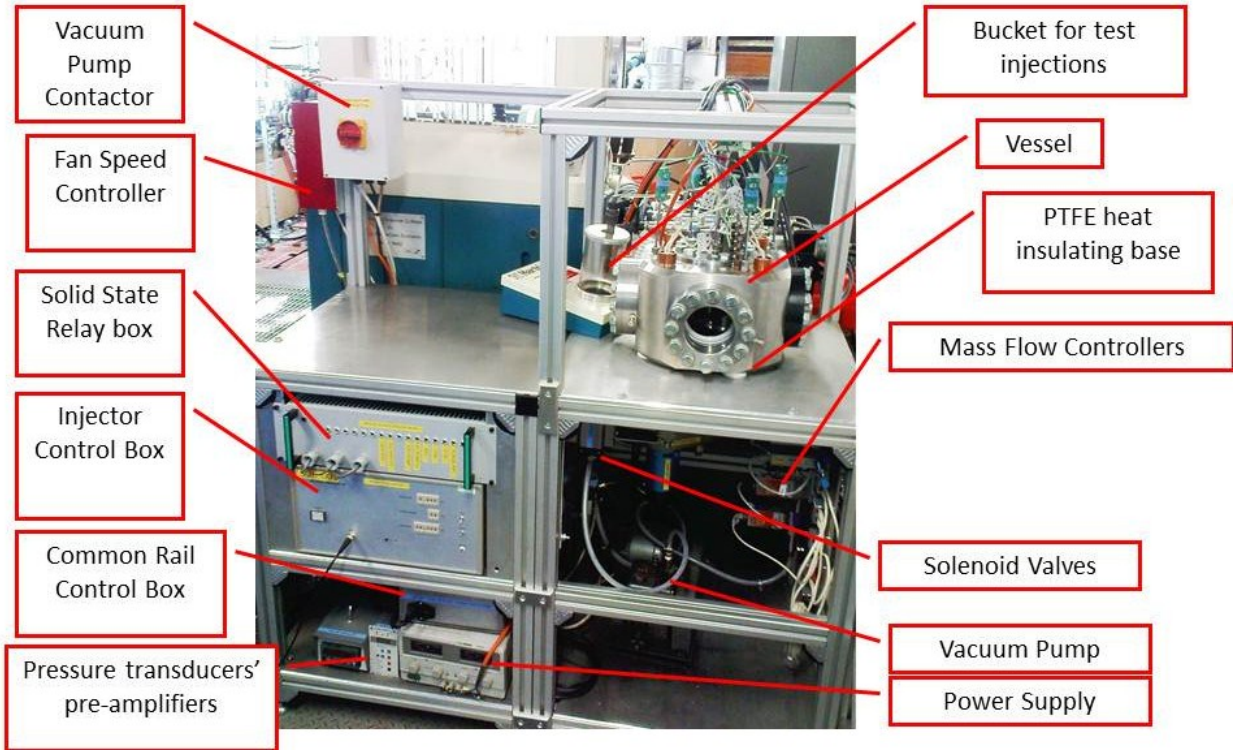

Figure 100 Photograph of Constant Volume Vessel Assembly

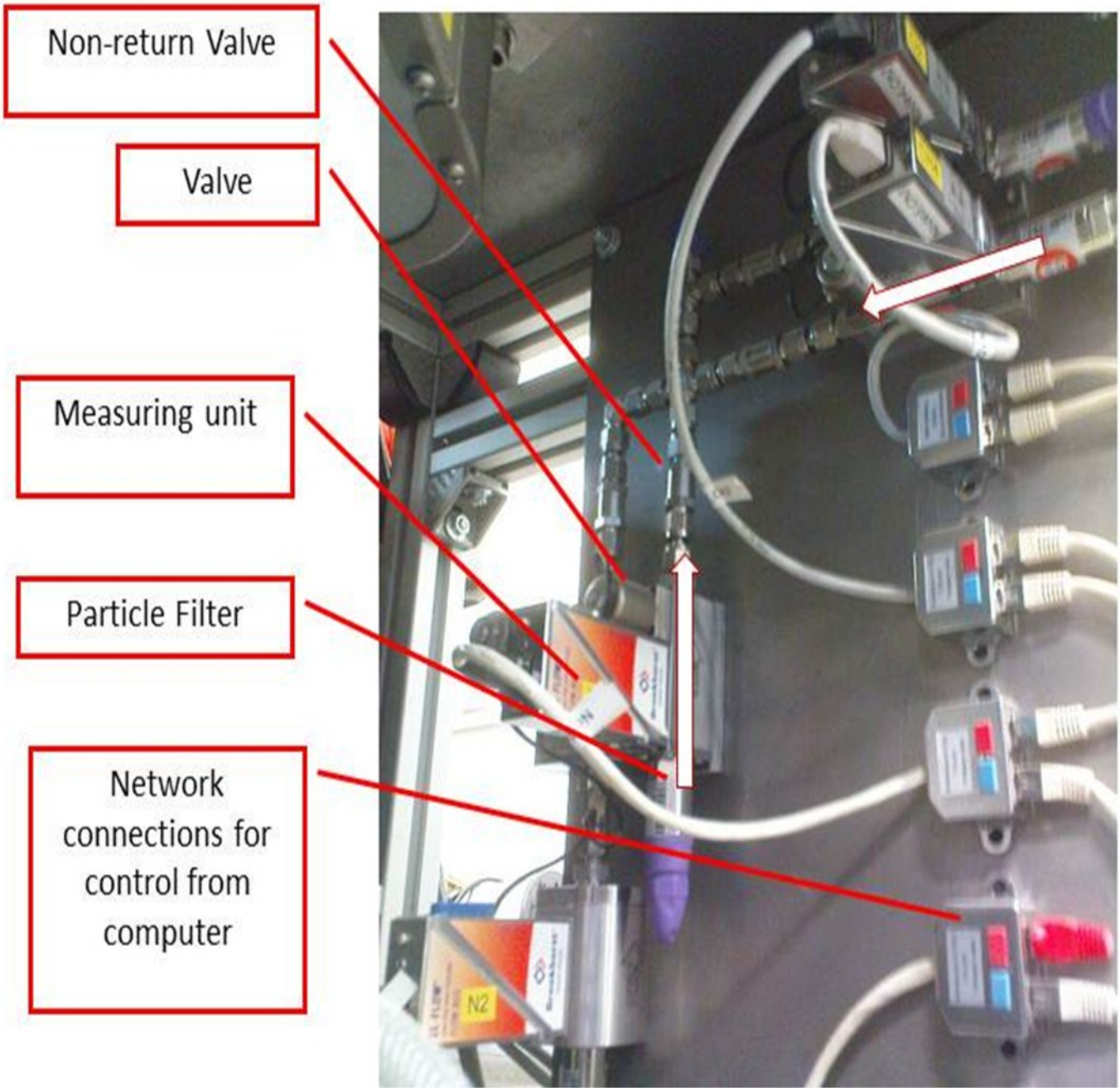

Figure 101 Photograph of Mass Flow Control of pre-ignition gases

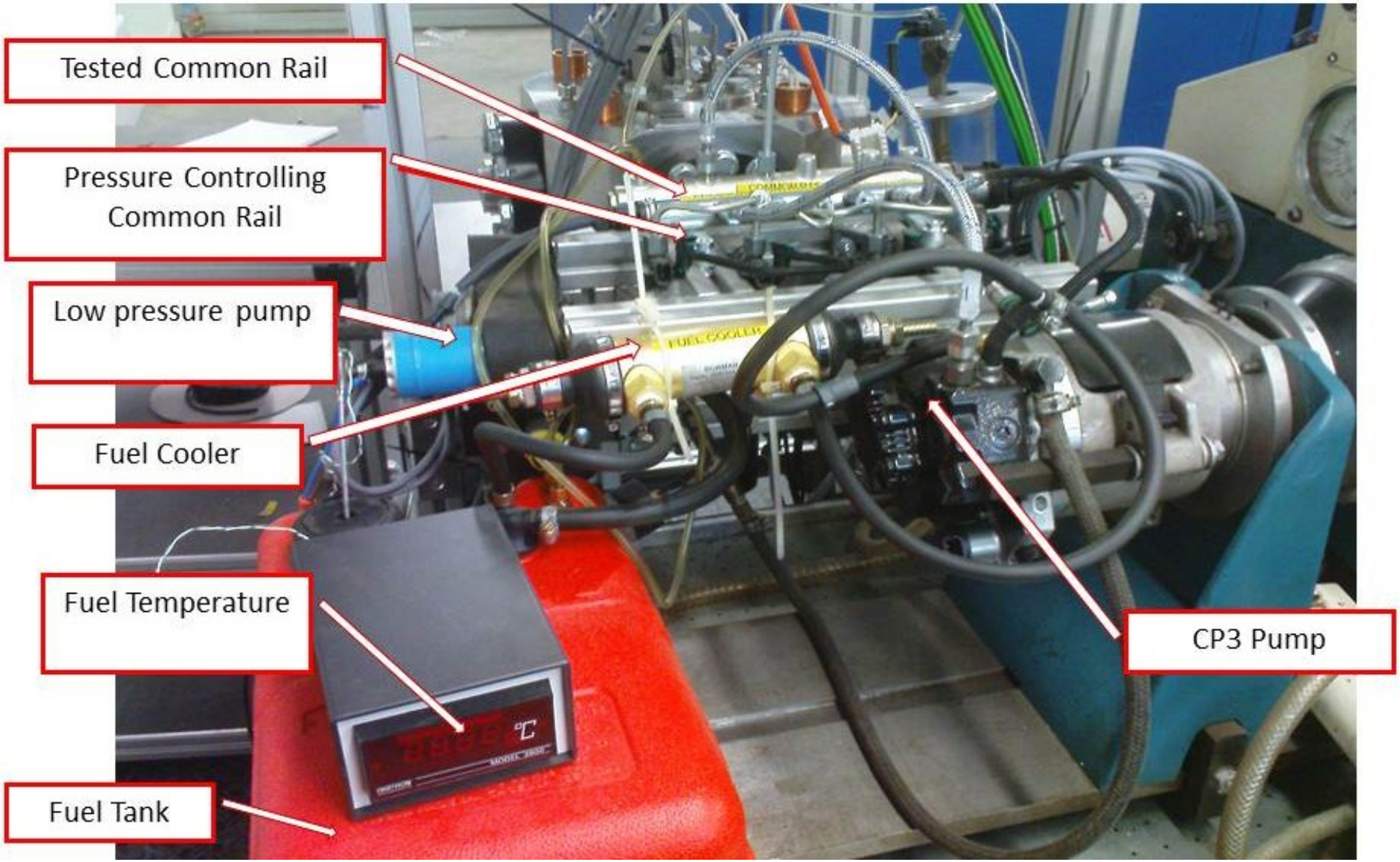

Figure 102 Photograph of Fuel Injection Equipment

Appendix 5 Parameter A

In this work, for the first time in the constant volume combustion chemistry, the parameter A was introduced as the ratio of Hydrogen moles to the hydrocarbon moles:

$$A \equiv \frac{X_{H_2}}{X_{C_aH_b}}$$

The molecular weight of the pre-combustion mixture is:

$$MW = X_{C_aH_b} MW_{C_aH_b} + X_{H_2} MW_{H_2} + X_{O_2} MW_{O_2} + X_{N_2} MW_{N_2}$$

$$\frac{MW}{X_{C_aH_b}} = MW_{C_aH_b} + A\, MW_{H_2} + \left(\frac{A}{2} + a + \frac{b}{2}\right) MW_{O_2} + X_{N_2} MW_{N_2}$$

It is clear thereafter, that the mixture molecular weight is a linear function of the Nitrogen mixture fraction for a given initial pressure and temperature.